INVESTIGATING THE EXTENT OF DAMAGE FROM A SINGLE BLASTHOLE

by

Kirk Brandon Erickson

A thesis submitted to the faculty of
The University of Utah
in partial fulfillment of the requirements for the degree of

Master of Science

Department of Mining Engineering

The University of Utah

May 2014

The University of Utah Graduate School

STATEMENT OF THESIS APPROVAL

The thesis of **Kirk Brandon Erickson**

has been approved by the following supervisory committee members:

Michael K. McCarter	, Chair	**6/20/2013** Date Approved
Dale S. Preece	, Member	**6/20/2013** Date Approved
Paul W. Jewell	, Member	**6/20/2013** Date Approved

and by **Michael G. Nelson** , Chair/Dean of

the Department/College/School of **Mining Engineering**

and by David B. Kieda, Dean of The Graduate School.

ABSTRACT

An ever-present challenge at most active mining operations is controlling blast-induced damage beyond design limits. Implementing more effective wall control during blasting activities requires (1) understanding the damage mechanisms involved and (2) reasonably predicting the extent of blast-induced damage. While a common consensus on blast damage mechanisms in rock exists within the scientific community, there is much work to be done in the area of predicting overbreak.

A new method was developed for observing near-field fracturing with a borescope. A field test was conducted in which a confined explosive charge was detonated in a body of competent rhyolite rock. Three instrumented monitoring holes filled with quick-setting cement were positioned in close proximity to the blasthole. Vibration transducers were secured downhole and on the surface to measure near-field vibrations. Clear acrylic tubing was positioned downhole and a borescope was lowered through it to view fractures in the grout. Thin, two-conductor, twisted wires were placed downhole and analyzed using a time-domain reflectometer (TDR) to assess rock displacement.

Fracturing in the grout was easily observed with the borescope up to 3.78 m (12.4 ft) from the blasthole, with moderate fracturing visible up to 2.10 m (6.9 ft). Measured peak particle velocities (PPV) at these distances were 310 mm/s (12.2 in./s) and 1,490 mm/s (58.5 in./s), respectively, although no fracturing was observed near the depth of the

vibration transducers located 3.78 m (12.4 ft) from the blasthole. TDR readings were difficult to interpret but indicated rock displacement in two of the monitoring holes.

Three methods were used to predict the radial extent of tensile damage around the blasthole: a modified Holmberg–Persson (HP) model, a shockwave transfer (SWT) model, and a dynamic finite element simulation using ANSYS Autodyn™. The extent of damage predicted by the HP and SWT models is similar to field measurements when using static material properties of the rock, but is underestimated using dynamic material properties. The Autodyn™ model significantly overpredicted the region of damage but realistically simulated the zones of crushing and radial cracking. Calibration of material parameters for the Autodyn™ model would be needed to yield more accurate results.

TABLE OF CONTENTS

ACKNOWLEDGEMENTS

This work would not have been possible without assistance from several individuals. Special thanks to Dr. Michael McCarter, professor of mining engineering, for originally proposing the idea for my research and serving as my graduate advisor. His advice, expertise, and tireless efforts were invaluable to the progress of this thesis. Gratitude is extended to Dr. Paul Jewell, associate professor of geology and geophysics, and Dr. Dale Preece, senior research fellow with Orica USA Inc., for their willingness to serve as members of my committee. Additional thanks is made to Dr. Dale Preece for his recommendations on the Autodyn^{TM} finite element modeling. Sincere appreciation goes to Robert Byrnes, technician, for his assistance in conducting tests with the triaxial testing machine and to Hossein Changani, fellow graduate student, in performing tests with the split Hopkinson pressure bar. Acknowledgement is due for the indiduals at the mine where the field test was conducted, whose support made this project feasible.

Recognition for financial support is made to the William C. Browning Graduate Fellowship administered by the University of Utah through the Mining Engineering Department and to the Best in the West Scholarship administered by the International Society of Explosives Engineers. Many thanks are owed to encouragement given by family, friends, student colleagues, and professors who have also been mentors. And last but not least, I am indebted to the continual, loving support of my parents throughout my university education and to Providence for guiding me.

1. INTRODUCTION

Rock blasting is a process that has been and continues to be widely used in mining and civil construction activities. Starting with the incorporation of gunpowder in the late 17th century and later with the introduction of modern blasting agents with the creation of dynamite in the 19th century, the use of explosive chemical compounds in rock breakage applications has become a staple among a wide gamut of mining methods (Darling 2011). Blasting currently offers the most cost-effective means to reduce rock to a form that can then be excavated and yet remains acceptably safe when proper controls are implemented.

1.1 Blasting in a mining context

The primary goal in most production-related blasting activities at a mining operation is to achieve a target fragmentation size. The size constraints are dictated by diggability, and in the case of ore, capabilities of downstream comminution activities in the mine-to-mill path. A significant amount of effort has been and continues to be dedicated to designing, implementing, and refining blast patterns that will achieve a desirable fragment size distribution. Three factors primarily control this distribution: explosive energy quantity, explosive energy distribution, and rock structure (Persson et al. 1994). While the rock structure cannot be controlled, the other two factors can through varying a number of pattern design factors. These include the following:

- Explosive type,

- Degree of coupling,
- Hole diameter,
- Hole depth,
- Burden and spacing,
- Stemming,
- Subdrill,
- Timing, and
- Decking.

In addition to achieving fragmentation goals, there are other objectives that the blasting practitioner must consider:

- Vibration control,
- Wall control,
- Airblast control,
- Flyrock mitigation,
- Abatement of noxious fumes,
- Ore dilution control, and
- Displacement of broken material.

The contribution of each design variable to the outcomes of a particular blast design can be significant in several ways. Ascertaining the manner and degree of influence for a variable to arrive at an optimal solution is not always straightforward due to the complex physical processes that occur during blasting. A change in one parameter, although intended to alter a characteristic of a blast pattern in a specific manner, may create unwanted or unintended side effects. For instance, changing the timing scheme on

a pattern with hopes of decreasing ore dilution may produce larger ground vibrations. Increasing stemming to direct a greater portion of the explosive energy into the rock mass may expand the region of damage beyond the design limits of the blast, adversely affecting ground integrity and stability.

1.2 Blast damage and backbreak

The detonation of an explosive charge in a solid medium will create what may be referred to as a zone of damage. In the context of rock breakage by blasting, the extent of the damaged zone is often referred to as backbreak or overbreak. Within this region of backbreak, the rock is deemed incompetent due to the damage incurred.

Damage does not have a specific, unique definition—the criteria for delineating damaged rock apart from sound rock will vary from site to site and even application to application. For instance, one site may characterize damage as rock that has been fragmented to the point at which it can be excavated. Another site may label damage as the formation of large cracks extending into a bench so that unstable features are formed. Yet another site may classify damage as shifting of rock blocks along preexisting faults or joint structures.

While there is no one definition of damage, the overall consensus seems to share common attributes. Oriard (1982) defines damage in his discussion of blasting as including "not only the breaking and rupturing of rock beyond the desired limits of excavation but also an unwanted loosening, dislocation, and disturbance of the rock mass the integrity of which one wishes to preserve." For the purpose of this thesis, damage in a rock mass is generally characterized by an increase in both the density and extent of fractures and similar discontinuities, disturbance and/or weakening of geological features,

and an alteration of physical properties such as reduced rock strength or changes in elastic moduli. Damage also possesses the properties of being cumulative and irreversible.

The above definition, however, fails to make an important distinction regarding the scale of damage. Blasting induces damage both on a macroscale and a microscale, both of which may be the focus of different emphases. On the one hand, the geotechnical engineer is concerned with damage on a macroscale, which manifests itself in the form of large cracks and unstable blocks that have potential for causing ground instability. On the other hand, the metallurgical engineer is concerned with damage on a microscale, as microfractures and reductions in the rock stiffness affect breakage energies during comminution. The importance of both must be recognized by the blasting engineer. This work focuses mainly on that which can be observed directly, which is macroscale damage.

1.3 Application of blast damage to wall control

Before delving into the body of this work, the following question must be discussed: what is the practical importance of studying blast-induced damage? Due to the ubiquitous use of blasting, backbreak is a widespread phenomenon among many mining operations and certain construction projects. Damaged rock is a contributor to ground instability. Thus, backbreak is of paramount importance in geotechnical analysis and safety considerations. With regard to structures and buildings, maintaining an intact foundation when blasting in close proximity can be crucial. For underground excavations, blasting practices can influence the stability of openings and dictate the degree of support needed. At surface mines, implementing good wall control can be a significant task with

a large payback. By blasting in a manner that leaves pit slopes competent, batter angles can be increased and thus, stripping costs are reduced.

Currently, the measurement, quantification, and prediction of backbreak constitute an area of ongoing extensive research. A better understanding of blast damage will lead to greater ability in designing better blast patterns and implementing more effective wall control.

A scientific investigation of blast-induced damage from a single blasthole is here presented. While the overall scope of this project may appear limited, the collected data and observations are a valuable contribution to the existing literature on near-field blast measurements. A new method is presented for directly observing the fracture network created by the explosive charge. Numerical modeling is conducted to correlate field measurements associated with blast-induced damage and compare simulation results with experimental data.

For the reader interested in further study of rock breakage by explosives, vibration analysis, and measuring blast damage, additional material is provided in the appendices. A detailed description of theory of rock blasting is presented in Appendix A. Seismic wave propagation, vibration predictions using the scaled distance concept, and frequency analysis are reviewed in Appendix B. A summary of methods for measuring blast-induced damage is given in Appendix C. Since much of the computer programming for this thesis was done using Python, it was considered appropriate to give a brief introduction to Python in Appendix D.

2. PREDICTION APPROACHES TO BLAST DAMAGE

In this section, a brief overview of techniques developed for predicting near-field blast damage will be presented. While numerous, valuable contributions have been made in these areas towards predicting blasting, only sparse attention will be paid to individual results. The intent is not to extensively cover these findings, but rather to acquaint the reader with the variety of approaches that have been attempted. References made in regards to each approach are meant to provide an example from literature, in lieu of an all-inclusive compilation. Only items of pertinent interest to research efforts later in this thesis will be discussed in detail.

2.1 Predicting blast-induced damage

An extensive body of literature exists on endeavors to quantitatively predict the limits of blast-induced damage. Approaches developed encompass everything from simple analytical expressions and rules of thumb to advanced analytical expressions and numerical models. While a consensus exists within the scientific community regarding the common damage mechanisms that occur during blasting, little consensus exists on how to appropriately predict backbreak. As is discussed in Appendix A, explosive-induced rock breakage involves the interaction of several complex physical phenomenon. In developing a prediction method, the tendency is to make certain simplifying assumptions in hopes that the overall solution will not be detrimentally affected.

Oversimplification easily results, however, particularly with analytical expressions. With the continual advances in computational ability using computers, numerical methods offer a means for incorporating high model complexity and coupled interactions while staying true to fundamental laws regarding conservation of mass, momentum, and energy. However, a numerical simulation is only as good as its input parameters, constitutive material models, and equations of state. Numerical methods are also subject to additional constraints and sources of error such as floating point precision, computational stability, and numerical artifacts that can occur (i.e., element errors, boundary effects, solution nonconvergence, and limited model resolution).

Most nonnumerical prediction methods tend to focus only on one or two key variables in the blasting process. Thus, selection of a method requires considering the variables of choice. This is particularly true when comparing computational results to field measurements.

In a comparative review of several damage limit models, Iverson et al. (2010) posed a set of key issues that needs to be addressed in backbreak prediction. Several of these are listed here, for not only are they applicable to most damage models, but they have potential to significantly affect the outcome. Among them are

- Deciding on a definition or definitions of damage in a blasting environment;
- Knowing how to best measure damage;
- Determining what variables should be used in calculating damage, such as gas pressure, wave energy, etc.;
- Determining whether quasistatic or dynamic assumptions are appropriate;

- Knowing whether to use static or dynamic properties of rocks, and how to best measure them, especially dynamics properties; and
- Determining if basic explosive properties are sufficient.

Hand-in-hand with backbreak prediction is fragmentation prediction. The two fields are often treated separately in the modeling process, but the breakage mechanisms involved are the same. While the following summary of prediction approaches focuses on blast damage limits, some of these tools may well have usefulness in predicting fragmentation.

With everything said, there is one additional benefit of modeling to keep in mind. Hustrulid (1999) makes the valid point that even if a model or simulation does not reflect the physics of the real world as accurately as hoped, it may still lend itself useful for comparative studies. As long as a damage prediction tool produces reasonable results, it can provide the blasting practitioner or researcher with information regarding relative changes between, say, blast designs or field conditions.

The following list of methods for predicting the extent of blast-induced damage represents those encountered during a fairly extensive review of literature. Some techniques have been utilized extensively, while others have only a marginal presence or have only recently been developed. The author has attempted to cite those contributions that seem to be most relevant.

2.1.1 Vibration

Perhaps the most common prediction tool of all is damage limits based on vibration. Predictions of near field vibrations have ranged from empirical correlation of site-specific limits to variations using scaled distances to advanced analytical solutions.

2.1.1.1 Usefulness of vibration as a predictor

The reasons why vibration has attained a broad presence in damage prediction are threefold, in the author's estimation.

1. The practice of recording blast-induced vibrations makes damage criteria via vibration a natural choice. A sizeable body of experimental data is available in this area.
2. As discussed in Section C.1.1 in Appendix C, vibration measurements either record strain directly or can be easily converted to strain or strain rate using the mechanical properties of the medium through which the seismic wave is passing. The relationships are (Yang et al. 1993)

$$\varepsilon = \frac{du}{dx} = \frac{du}{dt}\frac{dt}{dx} = v\frac{1}{c} \tag{2.1}$$

$$\dot{\varepsilon} = \frac{dv}{dx} = \frac{dv}{dt}\frac{dt}{dx} = a\frac{1}{c} \tag{2.2}$$

where

ε and $\dot{\varepsilon}$ are the strain and strain rate, respectively,

u is the particle displacement,

v is the particle velocity,

a is the particle acceleration,

t is the time from detonation of the explosive charge,

c is the seismic wave velocity, usually equal to the P-wave velocity c_P, and

$x = ct$ is the distance from the explosive charge.

Note that these strain relationships are based on the small strain assumption. Assuming linear elastic behavior of the transmitting medium, Hooke's law for one dimension ($\sigma = E\varepsilon$) can be combined with Equation 2.1 to produce an equation relating vibration velocity and stress,

$$\sigma = E\frac{v}{c} \tag{2.3}$$

where σ is the stress induced by vibration and E is Young's modulus. If the strength of the rock is known, Equation 2.3 can be used to determine a damage limit based on either the compressive strength σ_c, shear strength σ_s, or tensile strength σ_t. Typically the tensile strength σ_t is used. Equation 2.3 is useful for determining a dynamic increase factor of the rock strength based on the strain rate. Jimeno et al. (1995) provided the relationship $\sigma = \rho vc$, which gives the user the option of inserting the rock density ρ in place of E.

3. Some of the available methods for applying vibration limits, especially particle velocity, are relatively simple to use. The most common one, as discussed in Section B.4.2 in Appendix B, is the scaled distance relationship presented in Equation B.32. Another commonly used approach, which incorporates scaled distance, is the Holmberg–Persson model, discussed later in Section 2.1.1.4.

When using Equations 2.1 and 2.2, the wave propagation velocity is typically set equal to the P-wave velocity of the transmitting medium. The reader may ask why this is. After all, the P-wave amplitude and thus energy content in a set of seismic waves may

not be the largest component. Furthermore, since P-waves possess the largest velocity of all seismic wave velocities, dividing the particle velocity by c_P would seem to give a smaller value of strain than if using the S-wave (c_S) or Raleigh wave velocities (c_R). The reasons apparent to the author are

- Equation 2.3 is mostly useful to determine the tensile damage limit, since the tensile strength of rock is smallest and dictates the extent of rock fracturing. Tensile failure is mostly caused by P-wave action that either stretches the rock during the rarefaction phase of the wave or induces spalling at a free face. Shear motion that is present in S-waves and Raleigh waves does not induce tensile failure, and the longitudinal motion component of a Raleigh wave does not appear to be significant in comparison to the motion in a P-wave.
- A shear damage limit could conceivably be determined by using the shear strength σ_s and S-wave velocity c_S in Equation 2.3. However, σ_s is usually several times larger than σ_t. Even if the S-wave amplitude is larger than that of the P-wave, any increase in strain from dividing the particle velocity by a smaller wave velocity would be more than compensated for by the greater value of σ_s. In other words, a shear damage limit would not extend out as far as a tensile damage limit.
- In the near-field region of an explosive charge detonating in rock, the main initial particle motion results from the compressive shock/stress wave emanating from the blast. Thus, within the fracture zone,

longitudinal wave motion dominates, and the most favorable failure mode from ground response beyond the crushing zone is tensile.

2.1.1.2 Near-field vibration modes

An important aspect of near-field blast vibration analysis is knowing the resulting modes of vibration. The dilatational wave dominates the initial vibration event that takes place, as the majority of near-field vibration investigations will show. Contrasting with far-field measurements, the P-wave, S-wave, and surface wave motions can usually be distinctly separated as they each travel at different velocities (ISEE 2011). This would seem to indicate that longitudinal wave motion is of primary origin, and shear wave motion is of secondary origin. However, an analytical elastic solution by Heelan (1953) shows that both dilatational and shear waves are generated from a cylindrical explosive charge. Furthermore, the shear wave amplitudes can, at certain orientations, exceed the dilatational wave amplitudes as Figure 2.1 shows. Confirmation of this has been accomplished using dynamic finite element analysis (Blair and Minchinton 1996).

Most vibration models that account for the direction of particle motion only consider dilatational wave motion. Although the largest portion of ground motion does indeed take place initially as a shock wave in close proximity to the explosive charge, as indicated by field measurements, a full description of near-field strains and therefore damage cannot be made without analyzing shearing as well as volumetric change. That is not to discredit models that do not include shear wave motion. A number of models that assume only dilatational motion have been used with success in predicting vibration levels. Such a simplification, though, is bound to have limitations under certain circumstances.

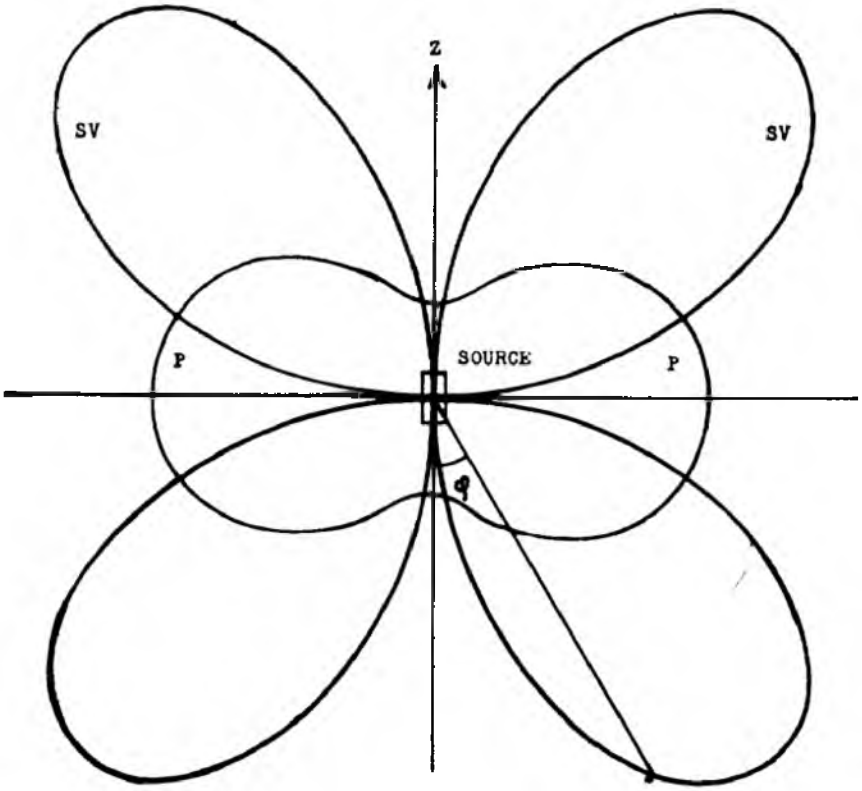

Figure 2.1 Resultant P-wave and S-wave amplitude potentials from a cylindrical charge (Source: Heelan 1953. Reprinted with the permission of the Society of Exploration Geophysicists).

2.1.1.3 Peak particle velocity criteria

Peak particle velocity (PPV) has been used as criterion for evaluating rock damage in the vicinity of the explosive charge. Oriard (1982) presented the following guidelines for correlating PPV and rock damage:

- 51–102 mm/s (2–4 in./s) – falling of loose rocks,
- 127–381 mm/s (5–15 in./s) – shifting of stable sections of rock,
- >635 mm/s (25 in./s) – damage to unsound rock, and
- >2540 mm/s (100 in./s) – damage to sound rock.

Vibration amplitudes in the majority of studies correlating vibration and damage are in

this general range. When using PPV as an indicator of damage, distinctions need to be made as to what kinds of damage correspond with each vibration level, as there are multiple modes of rock failure. Figure 2.2 shows one such comparison by McKenzie and Holley (2004) from a field study. A large quantity of research has been conducted using PPV. For the interested reader, a sample of field studies is listed as follows: Adamson and Scherpenisse (1998), Dey and Murthy (2013), LeBlanc et al. (1996), Liu et al. (1998), Murthy et al. (2004), Rorke and Milev (1999), and Yang et al. (1993).

In order to correlate PPV and damage, there needs to be a technique in place to interpolate vibrations. The next section will present some approaches that have been developed.

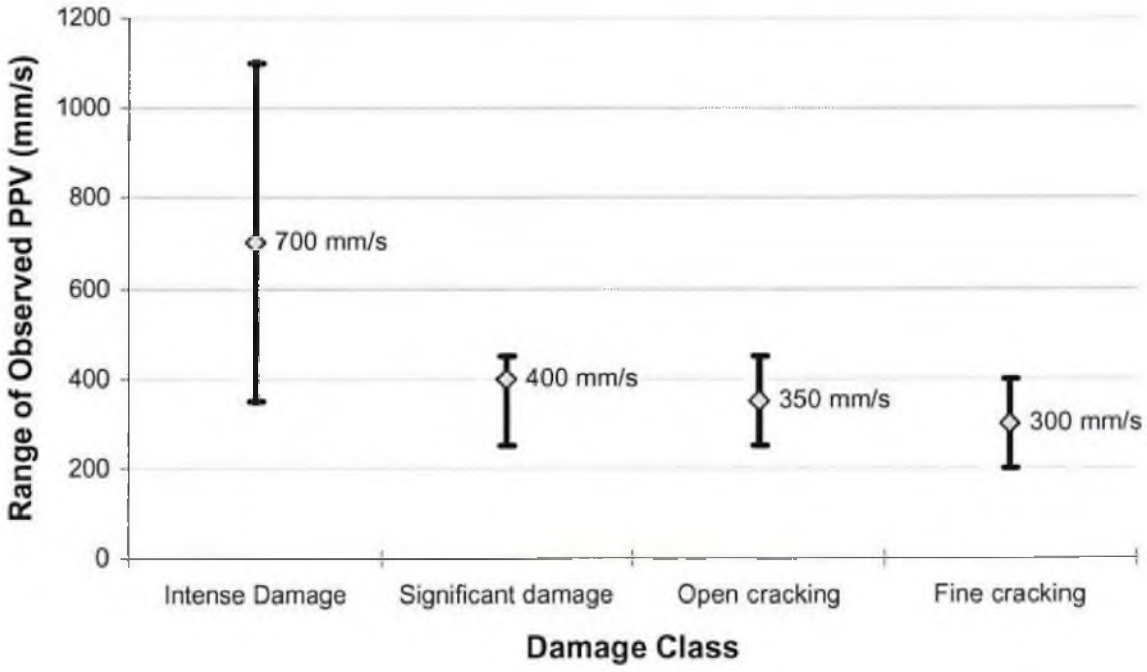

Figure 2.2 Field measurements correlating peak particle vibrations and damage intensity (Source: McKenzie and Holley 2004. Reprinted with the permission of the International Society of Explosives Engineers).

2.1.1.4 Vibration prediction models

One of the most widely-used near-field vibration models is the Holmberg–Persson (HP) model (Persson et al. 1994). The HP model is an adaptation of the scaled distance method. It breaks down the explosive column into segments and numerically sums the contribution of each segment at a point according to the scaled distance attenuation relationship. Using the aid of Figure 2.3, the HP formula is

$$PPV = k\left[q\int_{T}^{H}\frac{dZ}{[r_0^2+(z-z_0)^2]^{\beta/2\alpha}}\right]^{\alpha} \tag{2.4}$$

where

q is the loading density of the explosive per unit length,

H is the depth to the bottom of the explosive column,

T is the depth to the top of the explosive column,

dZ is an incremental charge length, evaluated from T to H, and

(r_0, z_0) are the coordinates of the point in space under consideration.

The constants k, β, and α are site specific values based on the scaled distance concept as explained in Section B.4.2 in Appendix B. For completeness, the scaled distance equation is given here:

$$PPV = k\left(\frac{R}{W^{\frac{\alpha}{\beta}}}\right)^{-\beta} \tag{2.5}$$

According to Hustrulid and Lu (2002), Equation 2.4 contains an error. The α term outside of the integral should be moved to the inside. The corrected forms of the HP formula, in

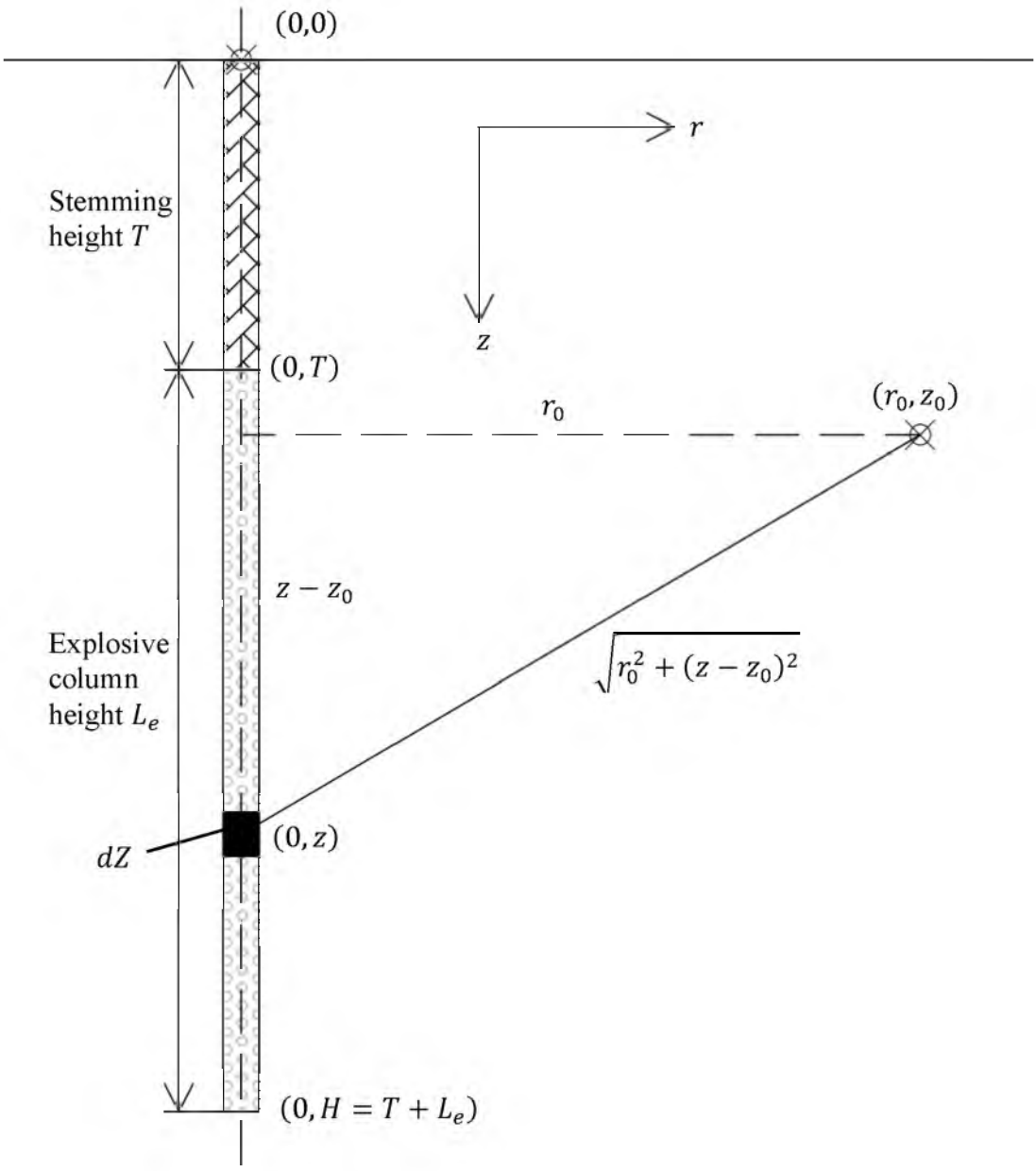

Figure 2.3 Schematic of Holmber-Persson near-field vibration model
After Persson et al. (1994).

both integral and discrete formulations, are

$$PPV = kq^{\alpha} \int_{T}^{H} \left(\frac{dZ}{[r_0^2 + (z - z_0)^2]^{\frac{\beta}{2\alpha}}} \right)^{\alpha} \tag{2.6}$$

$$PPV = kq^{\alpha} \sum_{T}^{H} \left(\frac{dZ}{[r_0^2 + (z - z_0)^2]^{\frac{\beta}{2\alpha}}} \right)^{\alpha} \tag{2.7}$$

The HP model has been used with varying degrees of success. Its popularity lies in its incorporation of the widely-used scaled distance concept and its relative ease of implementation. Several modifications of the HP model have also been proposed to enhance its accuracy (Arora and Dey 2013; Iverson et al. 2008; Smith 2003). Figure 2.4 shows a typical set of vibration contours generated by the HP model around a blasthole.

There are a few items of concern that have been brought forth, however (Blair and Minchinton 1996; Ouchterlony et al. 2001). Chief among these are the manner in which charge increments are summed. No attempt is made either to (1) account for differences in arrival of the strain pulse originating from each charge increment or (2) resolve into components each arrival based on its incoming direction. Regarding the first issue, Persson et al. (1994) claimed that the peak particle velocity does not occur when the wavefronts arrive, but when the rock mass as a whole starts to move. Thus, the difference in arrival times are insignificant compared to the timescale of rock motion. Regarding the second issue, a case study by Arora and Dey (2013) claimed improved results when resolving individual velocity vectors and then calculating a resultant net velocity. However, Blair and Minchinton (1996) argued that superposition of the incremental

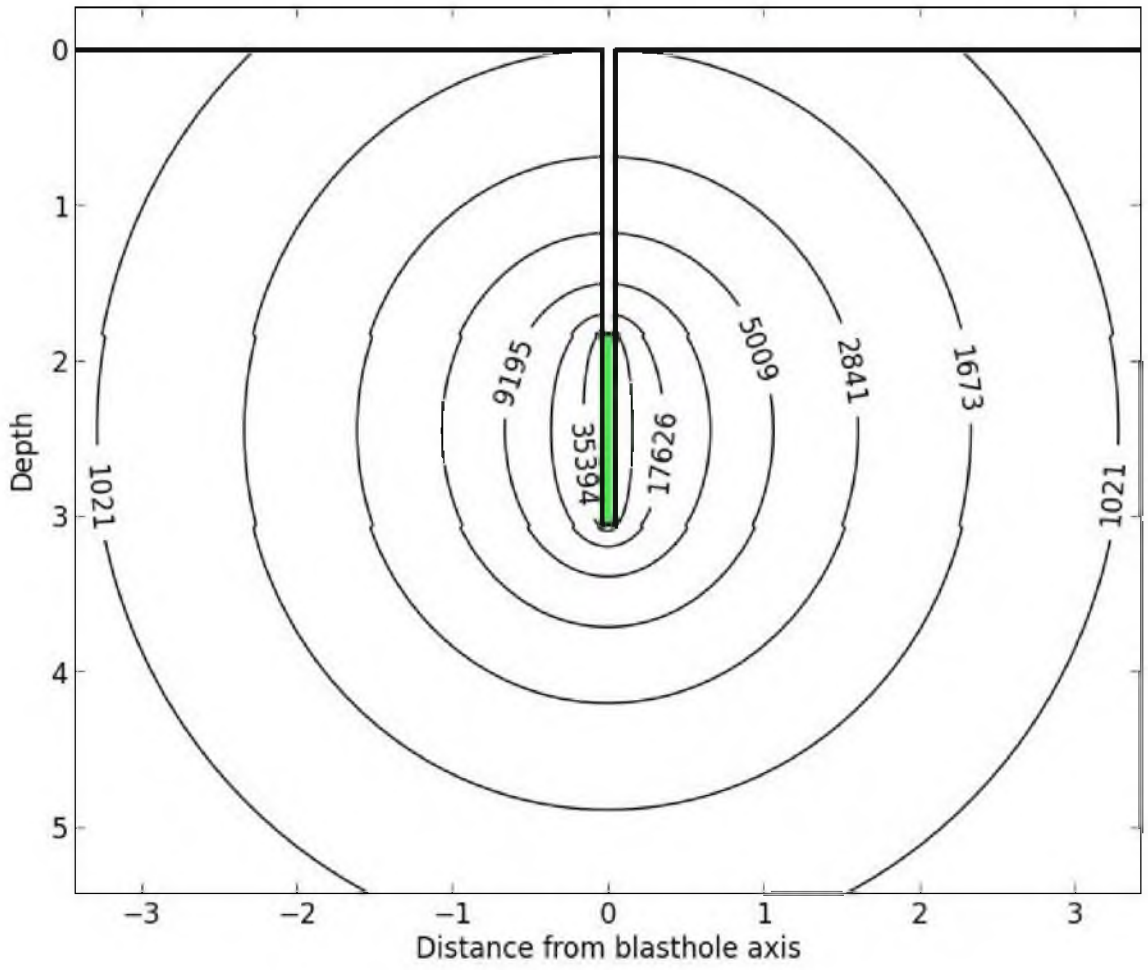

Figure 2.4 Vibration contours in mm/s generated by the HP model around a single blasthole

charges does not solve a fundamental issue of vibrations from different wave types. Both dilatational and shear waves originate from a cylindrical charge, but the HP model does not distinguish between the two. Thus, the usual assumption is that all vibrations are from longitudinal wave motion.

The HP also assumes instantaneous detonation of the explosive column. As pointed out by Blair and Minchinton (1996), even more accurate solutions such as that developed by Heelan (1953) can err from this assumption when compared to numerical simulations that incorporate a finite velocity of detonation.

One of the earlier analytical solutions to blast-induced vibrations was developed by Favreau (1969). Favreau calculated elastic solutions for strains and vibrations from an explosive charge within a spherical cavity. His work later became the basis for vibrations models developed by Harries (1983) and Hustrulid's CSM model (Hustrulid and Lu 2002).

As has been mentioned earlier, Heelan (1953) calculated elastic solutions for vibrations from a cylindrical explosive charge in terms of two displacement potentials.* His work was later modified by Abo-Zena (1977), who found errors in Heelan's work. However, the differences are miniscule (Hustrulid and Lu 2002). Heelan (1953) came to the interesting result that as much as 60% of the seismic energy from near-field vibrations is comprised of shear waves, and only 40% dilatational waves. Heelan's solution, however, requires the pressure function applied to the wall of the cavity to be assumed, limiting its theoretical soundness (Hustrulid and Lu 2002). Instantaneous detonation of the explosive column is implied.

Jordan (1962) solved the case for a cylindrical explosive column with a finite detonation velocity in an elastic medium. He made the observation that during the peak compressive phase of the outgoing dilatational phase, the elastic solution indicates all three of the stress components (radial, tangential, and axial) are compressive. This brings into question the commonly-accepted tensile "hoop stress" phenomenon that occurs in the radial fracture zone as discussed in Section A.2 in Appendix A. Jordan states

---

* A potential function is a function that satisfies Lapaces equation $\nabla^2\phi = \frac{\partial^2\phi}{\partial x^2} + \frac{\partial^2\phi}{\partial y^2} = 0$. With potential functions, irrotational motion is assumed. Potential functions can be used to establish equipotential, or constant, lines of a quantity such as velocity.

that this tensile phase instead occurs near the tail-end of the outgoing strain pulse, and that all three stress states are tensile at the same time.

A number of studies were conducted by the U.S. Bureau of Mines on strain wave decay from "approximately spherical" charges in Lithonia granite (for examples, see Atchison and Pugliese 1964; Atchison and Roth 1961; Atchison and Tournay 1959; Duvall and Petkof 1959; Fogelson et al. 1959). By "approximately spherical," the charges were actually cylindrical with length-to-diameter ratios of less than eight (Hustrulid 1999). Strain gauges were bonded to rock cores and secured downhole with cement. Strain measurements from different explosives and at different distances were obtained, such as those shown in Figure 2.5. The exponential or power attenuation laws described in Equations B.13 and B.14 in Appendix B were fit to the data. Figure 2.6 shows one such plot. In one report, a comparison was made between strain energy and distance (Fogelson et al. 1959). Scaling was also performed according to both distance and charge weight so comparisons could be made between different distances and charges.

Starfield and Pugliese (1968) developed the seed waveform model for simulating cylindrical charges that is easily implemented and can return quite reasonable results (Hustrulid 1999; Hustrulid and Lu 2002). Like the HP model, the explosive column is subdivided into charge increments. A seed waveform is assumed for each increment, and the results are summed up at a point to give the overall vibration history. A finite detonation velocity is accounted for. Starfield and Pugliese (1968) used idealized strain seed waveforms based on experimentally obtained strain data from the U.S. Bureau of Mines. These seed waveforms were resolved using simplified strain rotation formulas.

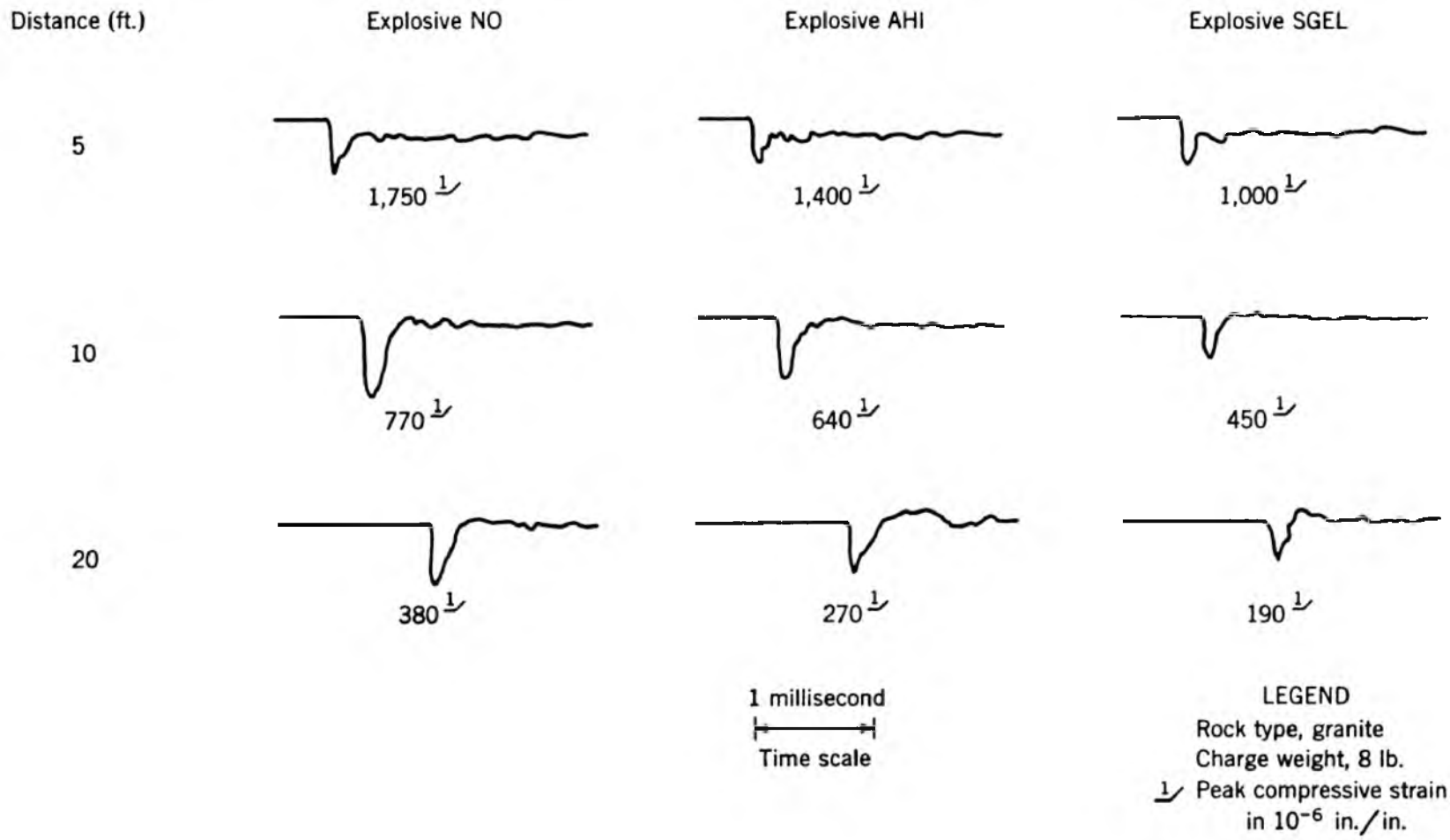

Figure 2.5 Sample field strain records
(Source: Atchison and Tournay 1959. Courtesy of the U.S. Bureau of Mines).

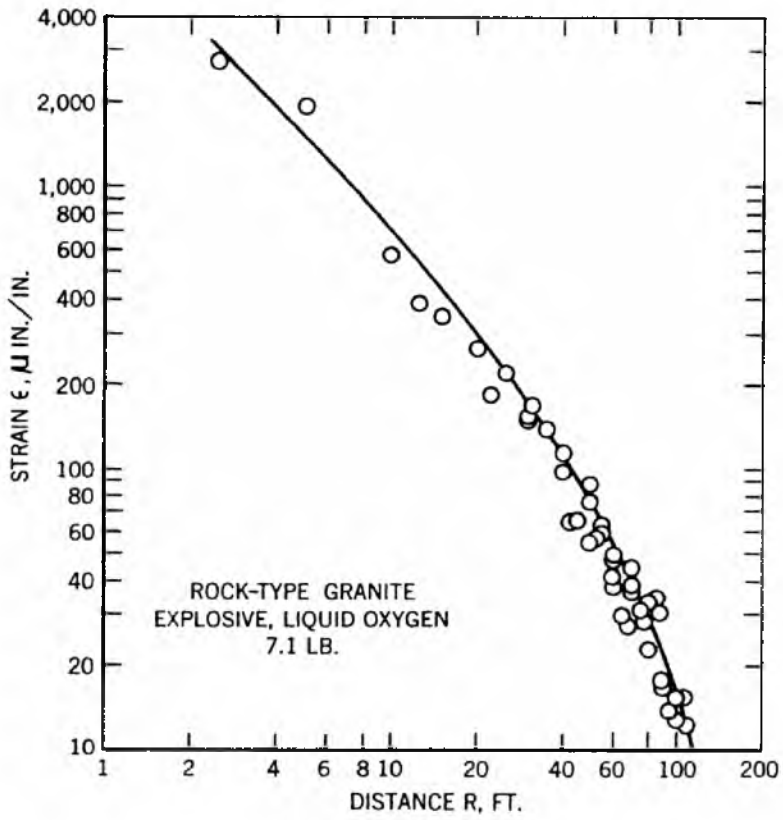

Figure 2.6 Sample strain with distance for an explosive charge (liquid oxygen = LOX) (Source: Duvall and Petkof 1959. Courtesy of the U.S. Bureau of Mines).

A limitation of this approach is that the characteristic seed waveform must be assumed (Hustrulid and Lu 2002).

Harries (1983) employed the solution developed by Favreau (1969) to cylindrical charges. He subdivided the explosive column into equivalent spherical charges and summed up the vibrations from each sphere, accounting for both the orientation of the vibration and a finite velocity of detonation. He also employed Q-based attenuation using the approach developed by Kjarntansson (1979). Harries's approach is theoretically more reasonable, but in actual application will not give reasonable results (Hustrulid and Lu 2002). At distances greater than a few meters from the blasthole, a permanent positive amplitude dominates the vibration waveform, which is unrealistic.

Hustrulid's CSM model (Hustrulid and Lu 2002) also employs the solution developed by Favreau (1969) to cylindrical charges by subdividing the explosive column into spheres. Instead of summing the resulting vibrations from each charge increment like Harries did, Hustrulid concluded that the duration of the initial strain pulse is sufficiently short that there is no need to perform superposition of the vibrations. Thus, only radial PPVs are accounted for.

Hustrulid and Lu (2002) developed a hybrid approach which combines together Heelan's (1953) elastic solutions, a pressure function proposed by Blair and Minchinton (1996), and the scaled distance formulation. The hybrid approach closely approximates the HP model under certain condition, but compares reasonably well with a finite difference simulation performed using Itasca's FLAC® software, using the same input pressure function.

2.1.2 Stress and strain

Stress, strain, vibration, and energy are closely related to each other. Thus, some of the models discussed in Sections 2.1.1.4 and 2.1.3 could very well be included here. Using stress or strain as a damage predictor requires the use of a failure model. A plethora of failure models exist, ranging from popular rock mechanics failure criteria such as Mohr–Coulomb and Hoek–Brown to advanced models such as the RHT (Reidel et al. 1999) and JH2 (Johnson and Holmquist 1993) models which are usually only employed with numerical methods. In addition, several models have been developed specifically for blasting. For specific examples see Hamdi et al. (2011), Liu and Katsabanis (1997), Yang et al. (1996), Yang et al. (2002), and Yang and Wang (1996). All of these models include a damage accumulation mechanism. Since there is an

extensive body of literature on various failure models, a discussion of these is not included here.

Drukovanyi et al. (1976) derived boundaries for the crushing and radial fissuring zones for a cylindrical charge. They used an analysis of quasistatic gas pressures within an expanding borehole cavity. A comparison with published field data indicates the approach produces comparative results (Drukovanyi et al. 1976). A laboratory study by Iverson et al. (2010) indicated, however, that the model developed by Drukovanyi et al. (1976) slightly underestimates the zone of crushing and significantly overestimates the extent of radial fractures.

An approach for estimating zones of rock mass damage from decay of the shock/stress wave was presented by Atchison et al. (1964). Three zones were identified as shown in Figure 2.7: (1) the source zone where high pressure gases from the explosive reaction expand and impact the borehole wall, (2) the transition zone where crushing and fracturing of the rock occurs, and (3) the seismic or undamaged zone. Johnson (2010) expanded the number of regions to five, separating the source zone into the explosive and the decoupled zones and the transition zone into crushing and radial fracture zones. Johnson also developed a modification of the split Hopkinson bar called the Hustrulid bar for measuring these regions of decay in rock samples.

2.1.3 Pressure and energy

Several pressure and energy-based models have been developed by considering the interaction between the gas-induced borehole pressure on the blasthole walls. Some are based on empirical rules, others on a more rigorous analysis of the thermodynamics and material physics involved. A few of these are presented below.

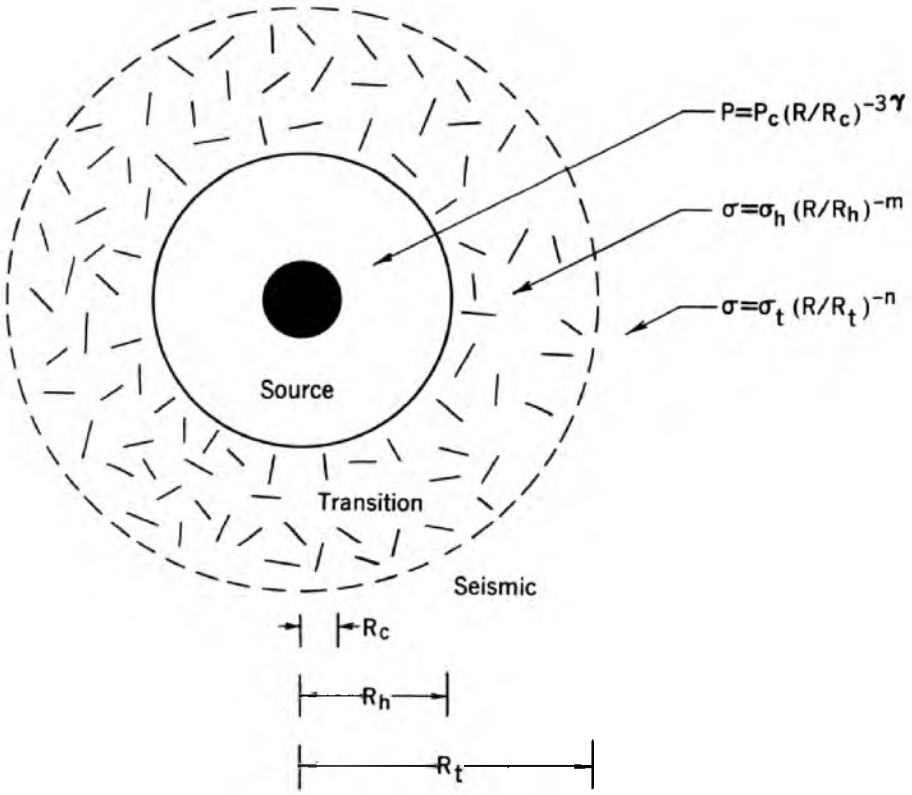

Figure 2.7 Zones of damage for a decoupled charge
(Source: Atchison et al. 1964. Courtesy of the U.S. Bureau of Mines).

Hustrulid and Johnson (2008) developed a pressure-based methodology for estimating the radius of damage in drift rounds. The end result, as originally derived by Hustrulid (1999), is

$$\frac{R_d}{r_h} = 25\sqrt{\frac{\rho_e s_{ANFO}}{\rho_{ANFO}}}\sqrt{\frac{2.65}{\rho_{rock}}} \tag{2.8}$$

where

R_d is the radius of damage in the surrounding rock,

r_h is the diameter of the blasthole,

ρ_e is the density of the explosive,

s_{ANFO} is the relative weight strength of ANFO,

ρ_{ANFO} is the density of ANFO, and

ρ_{rock} is the density of the rock.

Ouchterlony (1997) considered both the pressure-based behavior of the gaseous explosive products and the properties of the rock to arrive at a set of formulas that incorporate the following parameters:

- Explosive density, velocity of detonation (VOD), and adiabatic expansion constant;
- Borehole diameter and coupling ratio between the explosive and borehole walls; and
- Rock density, acoustic velocity, and fracture toughness.

Comparing with experimental results, Ouchterlony's predictions are reasonable with low-VOD explosives, but do not hold up well with high-VOD explosives (Ouchterlony 1997).

Bastante et al. (2012) developed a blast-induced damage similar to those of Hustrulid and Johnson (2008) and Ouchterlony (1997), but with only three parameters needed. These parameters are

- Explosive energy of the charge,
- Coupling factor and rock constant between the explosive and rock, and
- Mean gas isentropic expansion factor.

Comparison of this prediction method with published field data indicates a reasonably good fit (Bastante et al. 2012).

Sun (2013) developed a shock wave transfer (SWT) model that attempts to theoretically account for the gas-rock interaction. By using Hugoniot relationships for

both the explosive and the rock and enforcing force and velocity continuity between the two, the gas pressure on the borehole wall is estimated. The response of the rock is divided into two regions: a crushing zone and a tensile cracking zone. The size of each zone is dictated by the dynamic compressive and tensile strengths, respectively, of the rock. When entering static strengths, a dynamic increase factor is applied. Both fully coupled and decoupled charges are considered. For decoupled charges, the interaction between the explosive and air is accounted for using a Hugoniot relationship before determining the combined effect on the borehole wall. Sun compared his model with multiple blast damage models and types of field data, both published by others and his own set of tests at a mine. There was reasonable agreement with the SWT model in almost every case. However, Sun's own laboratory experiments, in which explosive charges of different sizes were detonated inside a cast concrete cylinder, did not produce satisfactory results. Sun attributed this to the small scale of the laboratory experiment, in which a free face was present in close vicinity to the charge.

2.1.4 Hydrodynamics

Hydrodynamics is a subset of fluid mechanics that concerns the motion of liquids (National Oceanic and Atmospheric Administration [NOAA] n.d.). Hydrodynamic approaches to predicting the motion of a body of rock subject to blast loading have been pioneered by researchers within the Russian scientific community (Hustrulid 1999). Most prominent among these are a series of papers by Neiman (1979, 1983, 1986). Hydrodynamics models use principles from fluid mechanics to develop velocity potential functions that describe the rock motion. They are advantageous in that the effects such as free face and additional blastholes can be accounted for, as exhibited in Figure 2.8.

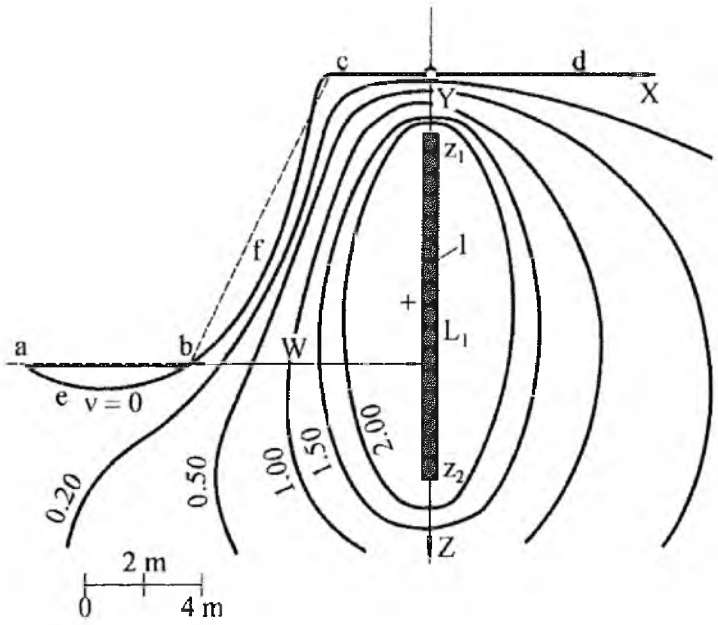

Figure 2.8 Hydrodynamic velocity potential contours for a blasthole (Source: Hustrulid 1999 [Figure 20.37, p. 936]. Reprinted with the permission of Taylor and Francis Publishing).

However, as Hustrulid and Lu (2002) pointed out, Neiman's models assume that all of the explosive energy is converted to kinetic motion in the rock mass, resulting in higher velocity contours near the blasthole than are realistic.

2.1.5 Empirical approaches

Empirical approaches have long been present in the field of blasting, including backbreak prediction. The defining line between empirical methods and other approaches in the context of blast-induced damage is not necessarily distinct. As was discussed at the beginning of this section, many of the prediction approaches developed make simplifying assumptions, some to the point that the hypothetical scenario being analyzed may seem entirely different than the real-world scenario. The question might be asked: when does the inclusion or omission of particular conditions or variables cross the line between

maintaining a reasonable level of theoretical soundness and becoming an empirical method? That question is not answered here, but merely presented as food for thought.

The formula for scaled distance presented in Equation 2.5 is, for all intents and purposes, an empirical approach. Thus, it might be said that any method based on the scaled distance concept is inherently empirical. However, a number of models with certain levels of theoretical rigorousness have been developed in conjunction with scaled distance.

A number of simplistic empirical approaches (i.e., "rules of thumb") have been proposed, some with specialized applications in mind. LeBlanc et al. (1996) gave a list of several of these. A frequent characteristic is that only one or two variables are needed in the formulation; hence, they are labeled as simplistic. As an example, Ouchterlony et al. (2001) discussed recommendations made by the Swedish National Road Administration for cautious blasting. The equations to generate blasting tables use only one variable: the charge weight. Ouchterlony et al. (2001) discussed the need for incorporating other factors such as water, coupling, rock properties, and so forth. Clearly, an approach that could incorporate such factors yet remain accessible to the nonmathematically inclined user would require an empirical approach.

2.1.6 Statistics, fuzzy logic, and artificial neural networks

In recent years, blasting technologies have begun incorporating tools such as fuzzy logic and artificial neural networks (ANN). Fuzzy logic is a mathematical reasoning tool that does not evaluate in terms of absolute values, such as true and false, but rather in "partial truths" defined by membership functions. Fuzzy logic has applications where possibilities lie in more than one state, or when linguistic terms are

incorporated (Monjezi et al. 2009). ANN are essentially pattern recognition algorithms that can be programmed so a machine or computer can "learn." ANN architecture has been employed within the mining industry in expert control systems for monitoring processes that require the system to analyze feedback and adapt to changes. These approaches have been tested in backbreak prediction with increasing degrees of success over traditional statistical tools. Some examples are provided below.

Singh et al. (2008) compared prediction abilities between traditional multivariate regression analysis (MVRA) and a neuro-fuzzy interface system to estimate both PPV and frequency content in blast vibrations. The neuro-fuzzy interface significantly outperformed MVRA. Two studies comparing MVRA with ANN produced similar results, with the ANN predicting blast vibration outcomes with much greater accuracy (Álvarez-Vigil et al. 2012; Khandelwai and Singh 2009). In a third study by Rathore et al. (2013) comparing MVRA and ANN in vibration amplitude and frequency prediction, the results were similar. However, their ANN model achieved higher R^2 correlation coefficients of 0.999 and 0.994 in predicting PPV and frequency, respectively, compared to 0.981 and 0.940 for the regression model. Dehghani and Ataee-pour (2011) conducted a study comparing ANN against various scaled distance formulations for vibration prediction. The correlation coefficient of the ANN vibration predictions was higher than any of the other methods.

Backbreak prediction has been performed using both fuzzy logic and MVRA. Monjezi et al. (2009) used both fuzzy theory and MVRA to predict backbreak limits at a mine. The fuzzy approach gave an R^2 correlation coefficient of 0.95, versus 0.34 for MVRA. Mohammadnejad et al. (2013) applied MVRA using a support vector machine

(SVM) learning algorithm for predicting backbreak. Over a study of 193 data sets, the SVM algorithm achieved an R^2 correlation coefficient of 0.94.

2.1.7 Fractal geometry

Fractal geometry is a subset of chaos theory in mathematics in which seemingly random patterns have the property of being self-similar, meaning that they appear the same regardless of scale (Stewart 2002). Fractal geometry has been gaining presence in a number of scientific fields of study including rock mechanics and geological investigations. The literature on applications of fractal geometry to the field of blasting is scant, but slowly gaining a presence. A couple of fractal damage models have already been presented (Yang and Wang 1996; Qian and Hiu 1997). Lu and Latham (1999) presented a rock blastability criterion using the fractal dimension of in situ block sizes. It is the author's opinion that the application of fractal geometry to backbreak prediction presents an interesting study with significant potential. Fractal geometry has the potential to better describe the random progression of crack growth in rock than other methods employed in fracture mechanics.

2.1.8 Numerical methods

Numerical methods for analyzing physical processes have become increasingly popular over the past few decades. In addition to being able to perform simulations of phenomenon beyond the abilities of analytical and empirical approaches, numerical methods provide detailed insight into physical quantities not easily measurable in laboratory and field tests. The most common numerical modeling formulations are finite difference methods (FDM), finite element methods (FEM), boundary element methods

(BEM), and discrete element methods (DEM). In addition to these exist a large number of other numerical approaches, as well as coupled or hybrid methods. Each method has its advantages and disadvantages in terms of complexity, computational requirements, robustness in adapting to different scenarios, modeling setup considerations, and so forth. Several companies such as ANSYS, COMSOL, SIMULIA, and Itasca make a wide variety of commercial modeling software packages. In addition, a number of free programs are available for limited or specialized modeling applications.

The literature on numerical modeling of blasting with regard to damage is quite extensive. Only a couple of the more prominent studies will be covered here.

A coupled numerical modeling tool currently under development at the writing of this thesis is the Hybrid Stress Blasting Model (HSBM) (Furtney et al. 2010; Hustrulid et al. 2009; Onederra et al. 2010; Onederra et al. 2013a, 2013b). The HSBM employs a detonation model and a rock breakage engine comprised of three parts: (1) a continuum model for near-field rock response, (2) a brittle discrete element model that can fracture into "pieces" and move, and (3) a gas product model that can simulate burden movement under acceleration from high-pressure gas expansion (Onederra et al. 2013b). The Mohr–Coulomb failure model is used in both the continuum and DEM components (Onederra et al. 2013a). The near-field continuum mesh uses Itasca's FLAC® finite difference code. The DEM model uses a simplified version of Itasca's PFC3D® DEM code that accounts only for translation of particles and neglects rotation. Laboratory-scale tests have been conducted comparing HSBM predictions to measured damage in instrumented concrete blocks, as shown in Figure 2.9 (Onederra et al. 2010; Onederra et al. 2013a, 2013b).

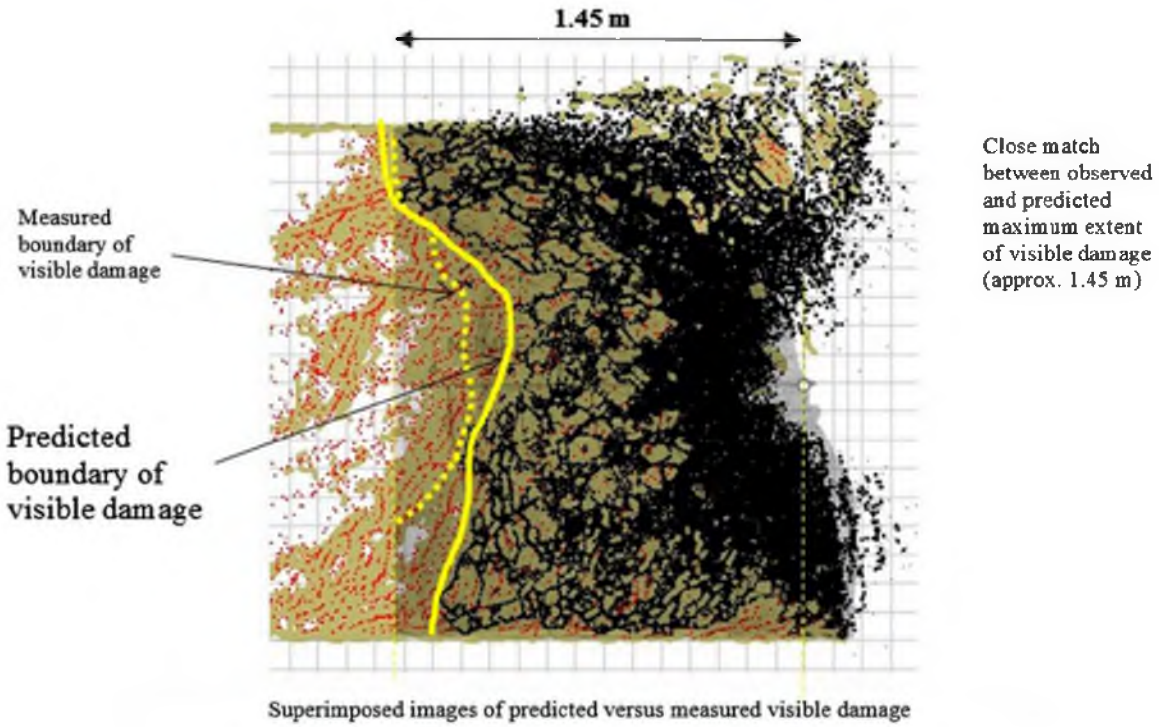

Figure 2.9 HSBM simulation of a blasthole in a concrete block
(Source: Onederra et al. 2013b. Reprinted with the permission of Elsevier).

Another numerical modeling tool that has made a large presence in modeling blasting phenomenon is Autodyn™, formerly developed by Century Dynamics but now under ANSYS. Autodyn™ is essentially a nonlinear hydrocode simulator that utilizes different types of solvers including dynamic FEM with both Eulerian and Lagrangian formulations, arbitrary Eulerian-Lagrangian formulation, smooth particle hydrodynamics, finite volume modeling for computational fluid dynamics, and the ability to couple between different types of models. Autodyn™ incorporates a large database of equations-of-state, constitutive relationships, and failure models for modeling a wide range of materials.

Examples of studies using Autodyn™ include damage prediction (Katsabanis 2001; Preece and Chung 2003; Preece and Lownds 2008; Sun 2013; Zhu et al. 2008),

crack prediction (Banadaki 2010; Zhu et al. 2007), cratering (ISEE 2011), air decking (Katsabanis 2005), and vibration studies (Park and Jeon 2010). Figure 2.10 shows an example model by Preece and Lownds (2008) showing pressure contours and a tensile damage region as two adjacent blastholes detonate at different instances. Simulations and laboratory or field observations have been compared in some studies with satisfactory results (ISEE 2011; Sun 2013).

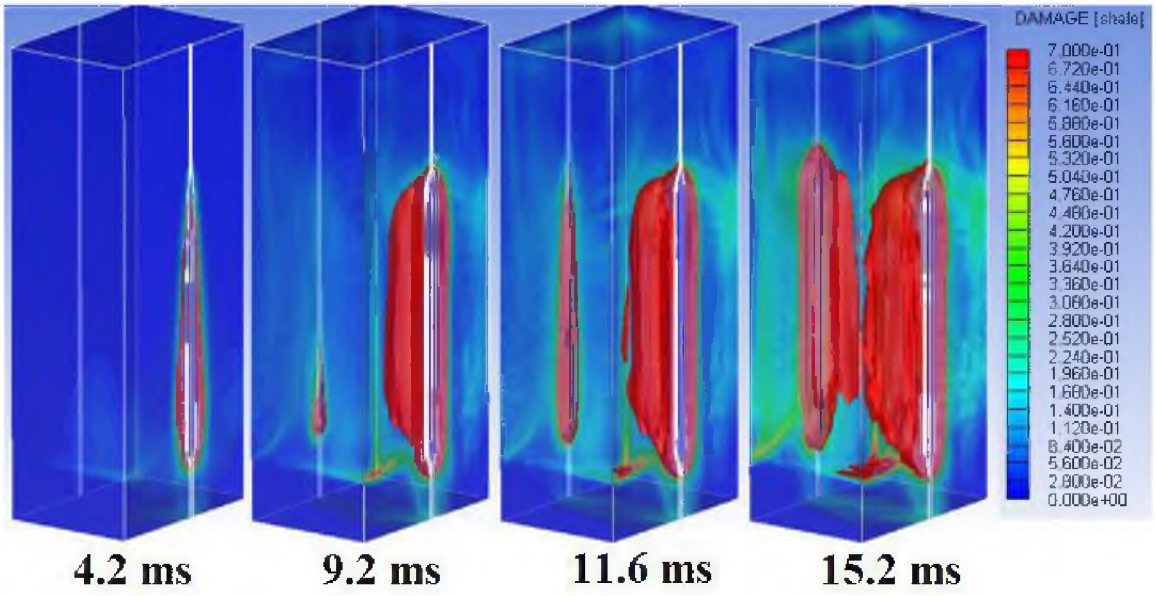

Figure 2.10 Autodyn™ simulation of damage region (red) between adjacent blastholes (Source: Preece and Lownds 2008. Reprinted with the permission of the International Society of Explosives Engineers).

3. EXPERIMENTAL PROCEDURE

To obtain experimental data on near-field blast damage, a field test was conducted at a surface mine located in Western Utah. A rhyolite outcrop was selected as the test site. The top of the outcrop was level with the ground surface. A single, confined blasthole, loaded with ammonium-nitrate fuel oil (ANFO) blasting agent detonated. Instrumentation was positioned in nearby drillholes and on the surface to record the vibrations and observe the blast damage. Observation of the drill and drilling rates for the blasthole and monitoring holes indicated the test area was fairly uniform throughout the depth of the test. The equipment, field experiment setup, and results are presented as follows.

3.1 Equipment summary

Three forms of instrumentation were chosen for measuring the effects of the explosive charge in rock:

- Vibration transducers,
- Borescope, and
- Time-domain reflectometer (TDR).

Vibration transducers, clear acrylic tubing, and thin, two-conductor twisted wires were grouted downhole using quick-setting Hydro-Stone® cement. The vibration transducers were selected to record the ground motion. Data collection was accomplished using two oscilloscopes. Additional seismographs were placed on the surface using bolts drilled into to rock outcrops and bonded with epoxy. A borescope was used in

conjunction with clear acrylic tubing to view cracks that formed in the cement grout. Thin two-conductor wires positioned downhole were analyzed with the TDR meter to detect stretching or breaking.

3.1.1 Vibration transducers

Four uniaxial vibration transducers were selected for downhole vibration records. In addition, 3 triaxial seismographs were secured on the surface. All of the transducers were geophones, with the exception of one accelerometer.

3.1.1.1 Geophones

Geospace GS-20DM geophones were selected for use in obtaining near-field vibration histories. Two different natural frequencies—28 Hz and 40 Hz—were picked so a comparison between the two could be made. Both can operate at a 90° tilt angle and remain within tolerance. The GS-20DM are designed to be 50% smaller than traditional geophones and thus employ a smaller moving mass and stronger magnets (Geospace Technologies 2012). It was anticipated that a smaller moving mass would allow the geophone to withstand higher shock. Spurious frequencies can occur beyond 600 Hz for the 28-Hz geophone and 850 Hz for the 40-Hz geophone. Tables 3.1 and 3.2 list selected properties for each of the geophones used. Figures 3.1 and 3.2 display the manufacturer's frequency response curves for each geophone with different shunt resistances applied.

A comparison of the damping effects of different shunt resistors was conducted on both geophone models. Using the procedure described in Section C.1.1.2 and Equation C.7, damping coefficients (denoted as β) were calculated and compared with the manufacturer's values and Equation C.8. The results are presented in Table 3.3. In most

Table 3.1 Selected properties of the Geospace GS-20DM 28-Hz geophone

At 25° C	Metric units	Imperial units	Tolerance
Natural frequency	28 Hz		10.0%
Spurious frequency	>600 Hz		
Max tilt angle	90 °		
Open circuit damping	0.60		10.0%
Circuit damping with 182 Ω shunt	0.90 *		
Intrinsic voltage sensitivity (±7%)	0.151 V/cm/sec	0.384 V/in/sec	
Sensitivity with 182 Ω shunt	0.061 V/cm/sec*	0.154 V/in/sec*	
DC resistance	270 Ω		5.0%
Moving Mass	5.6 g	0.20 oz	5.0%
Height (less stud)	2.64 cm	1.04 in	
Diameter	2.22 cm	0.875 in	
Weight	43 g	1.5 oz	

* Estimated

Source: Geospace Technologies (personal communication)

Table 3.2 Selected properties of the Geospace GS-20DM 40-Hz geophone

At 25° C	Metric units	Imperial units	Tolerance
Natural frequency	40 Hz		7.5%
Spurious frequency	>850 Hz		
Max tilt angle	90 °		
Open circuit damping	0.42		15.0%
Circuit damping with 182 Ω shunt	0.60		
Intrinsic voltage sensitivity (±7%)	0.151 V/cm/sec	0.384 V/in/sec	
Sensitivity with 182 Ω shunt	0.061 V/cm/sec*	0.155 V/in/sec*	
DC resistance	270 Ω		5.0%
Moving Mass	5.6 g	0.20 oz	5.0%
Height (less stud)	2.64 cm	1.04 in	
Diameter	2.22 cm	0.875 in	
Weight	43 g	1.5 oz	

* Estimated

Source: Geospace Technologies (personal communication)

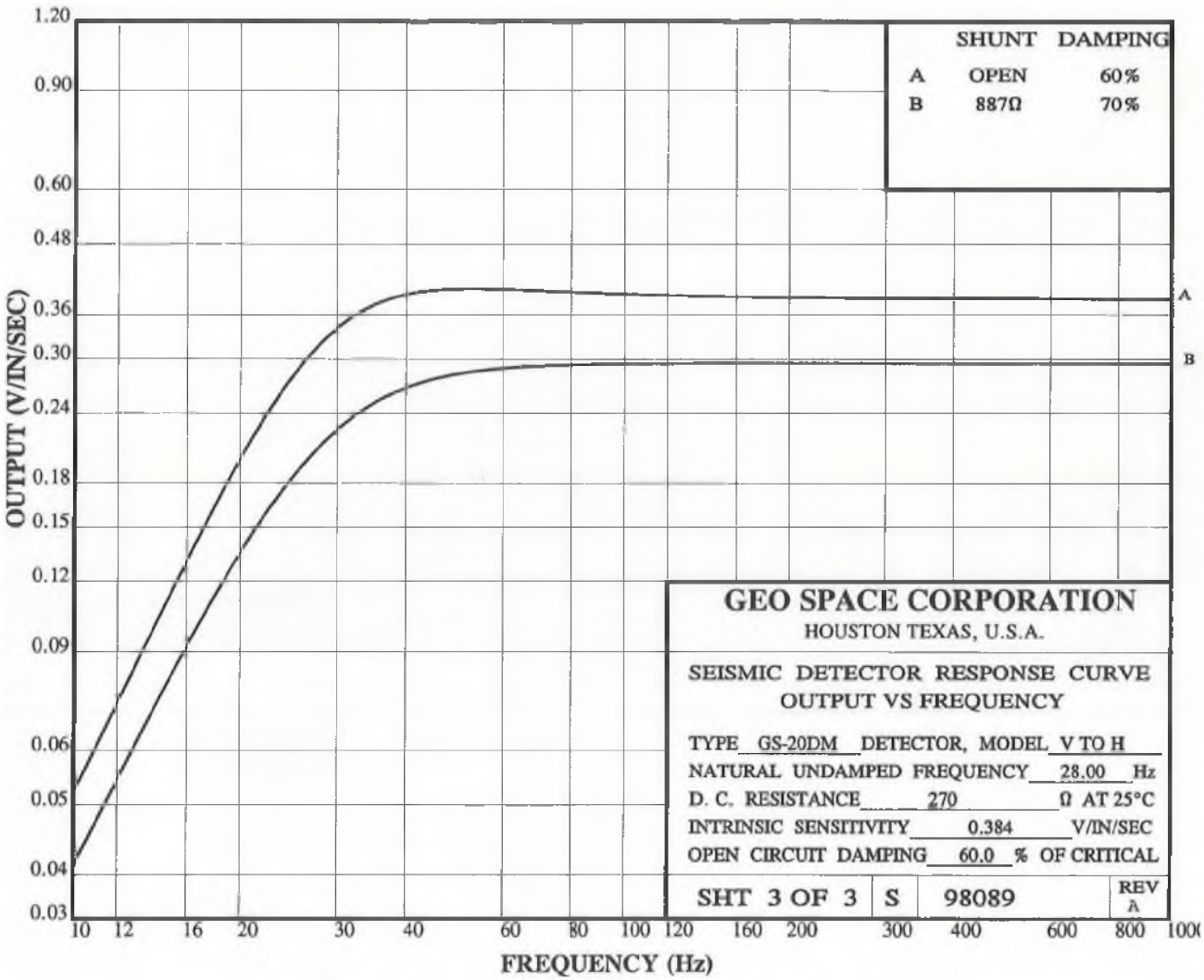

Figure 3.1 Frequency response curve for GS-20DM geophone, 28-Hz model
(Source: Geospace Technologies, personal communication. Reprinted with permission of Geospace Technologies).

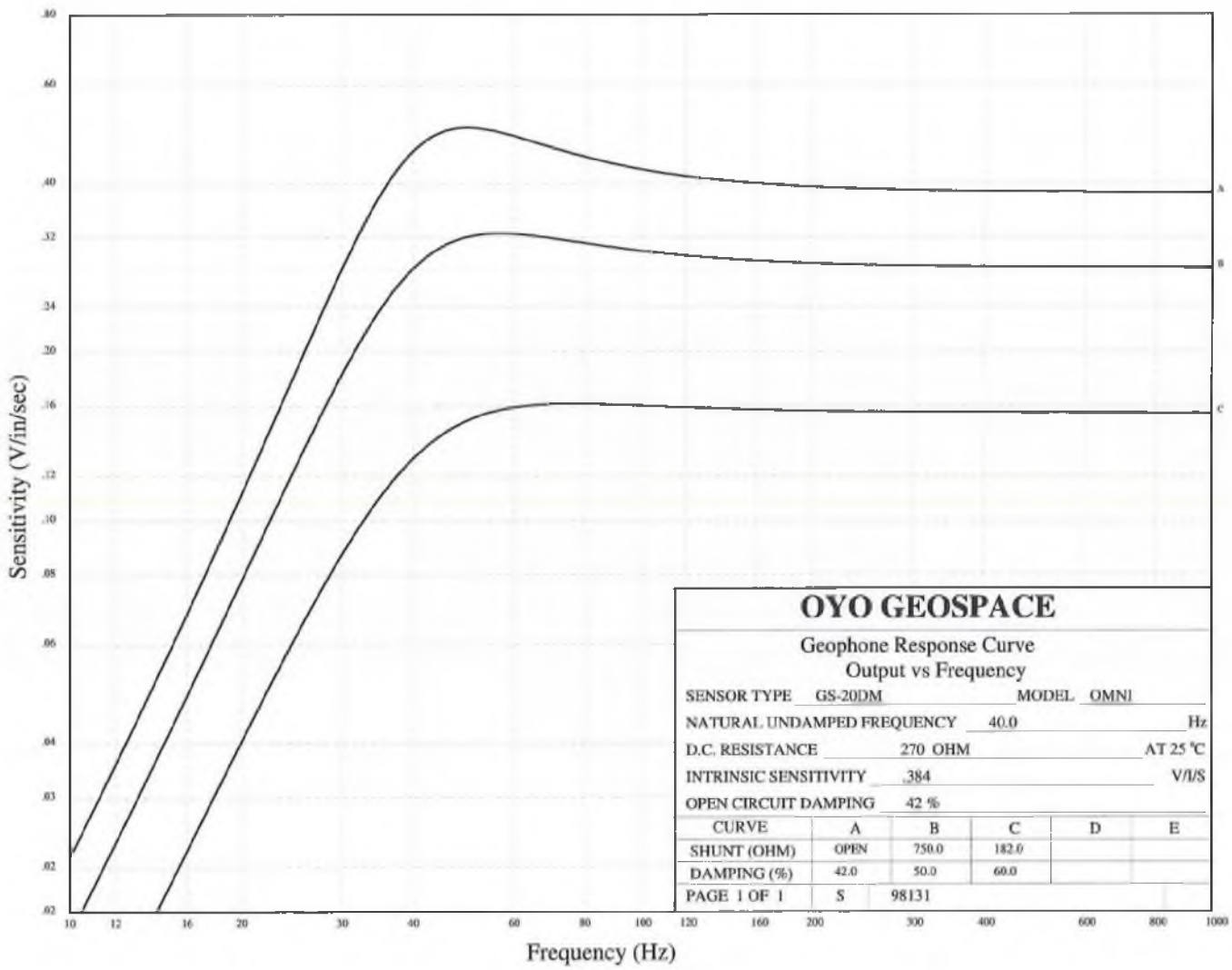

Figure 3.2 Frequency response curve for GS-20DM geophone, 40-Hz model
(Source: Geospace Technologies, personal communication. Reprinted with permission of Geospace Technologies).

Table 3.3 Comparison between measured and calculated damping coefficients

Sensor frequency (Hz)	Shunt (Ω)	Damping coefficient		
		Manufacturer	Measured	Calculated*
28	Inf	0.60	0.60	
28	887	0.70	0.70	0.80
28	182	NA	**0.90	1.11
40	Inf	0.42	0.45	
40	768	0.50	0.53	0.64
40	182	0.60	0.65	0.93

* Using Equation C.8 as presented by Hofmann (2003)

** Estimated

cases, measured β coefficients compared closely with the manufacturer's values, while calculated β coefficients were significantly overestimated, particularly with smaller shunt resistances. In some cases, β coefficients for certain resistances were not available from the manufacturer's frequency response charts. As was mentioned in Section C.1.1.2, Equation C.7 is only applicable for β coefficients below 0.7. For the 28-Hz geophone, a damping coefficient of 0.90 for a shunt resistance of 182 Ω was estimated visually by examining Figure 3.3. Notice that as the geophone's internal mass initially rebounds, it slightly overshoots the baseline. A critically-damped mass (β = 1) would not overshoot, but come to rest as quickly as possible. Therefore, a β of 0.90 was considered reasonable.

Shunt resistors of 182 Ω were selected for each geophone. This shunt value was chosen so that sufficient restraint would be applied to each geophone's mass without overdamping. The resistors were soldered across the terminals of each geophone and then waterproofed with silicone sealant. For both geophone models, a 182 Ω shunt reduced the sensitivity by about 60%. For the 28-Hz and 40-Hz geophone models, this shunt resistance resulted in damping coefficients of 0.9 and 0.6, respectively.

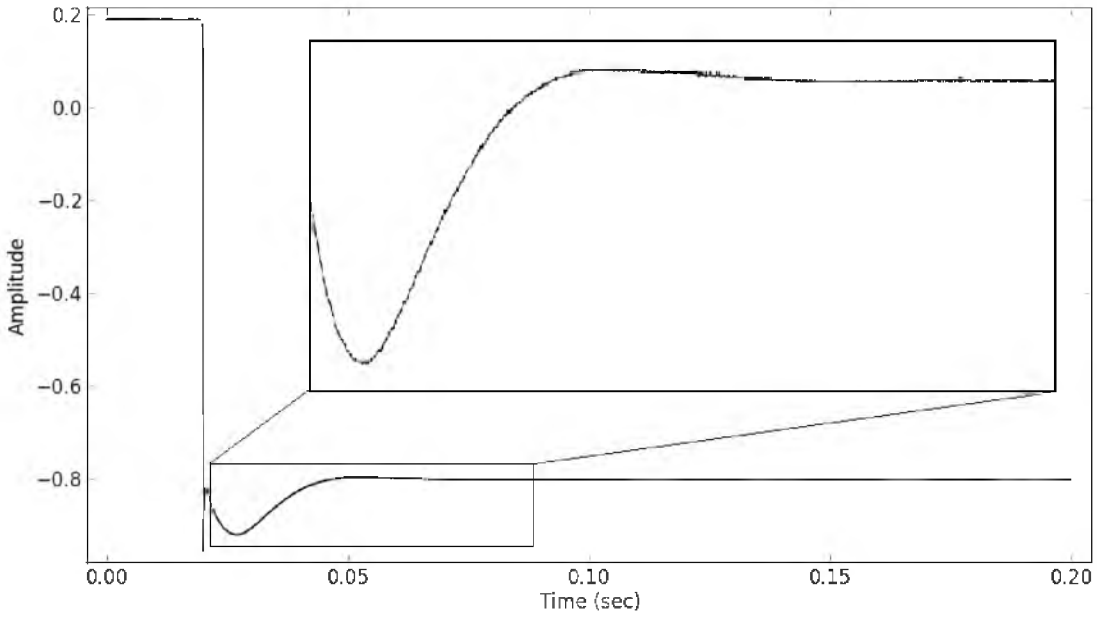

Figure 3.3 Damping coefficient estimation for 28-Hz geophone with 128-Ω shunt

To verify the accuracy of the geophones, simple impulse and steady-state vibration tests were conducted in which the response was compared between these geophones and an Instantel Minimate Plus^{TM} seismograph. An ideal testing apparatus would be a shaker table, but one was not available at the time. For testing impulse response, the geophones and seismograph were secured to a table and/or each other with two-sided tape and vibration events were created by thumping the table. The data collected exhibited a fair amount of scatter. There are three likely reasons for this. First, the method of coupling the geophones and seismograph to the table was crude, and thus it is possible that some motion in the records is the result of movement relative to the table. The second reason is the difference in frequency and response between the geophones and seismograph. High frequencies that showed in vibration histories of the GS-20DM geophone models were sometimes absent in the Instantel seismograph, which has a flat response frequency range of 2 to 250 Hz. Many of the vibration histories also showed

different oscillation patterns after the initial impulse event, particularly between the geophones and the seismograph, indicating that different oscillatory behaviors of the internal masses were occurring. The third reason could be a difference in phase response. The direction of each impulse event (up or down) was recorded. Tests showed that the Instantel seismograph did not autocorrect for phase, and since its lowest flat response frequency is 2 Hz, its measurements could appear dissimilar at frequencies below the natural frequencies of the 28-Hz and 40-Hz geophones.

Steady-state vibrations were conducted by mounting the seismograph and geophones to the apparatus pictured in Figure 3.4. A DC shunt-wound motor was mounted on one side of a base, in this case a steel beam. A stiff aluminum cantilever was secured on the other end. The free end of the cantilever rested on top of an offset cam secured to the shaft of the motor. A spring connected the free end of the cantilever to the steel beam and the tension could be adjusted by a screw with a wing nut. Three different

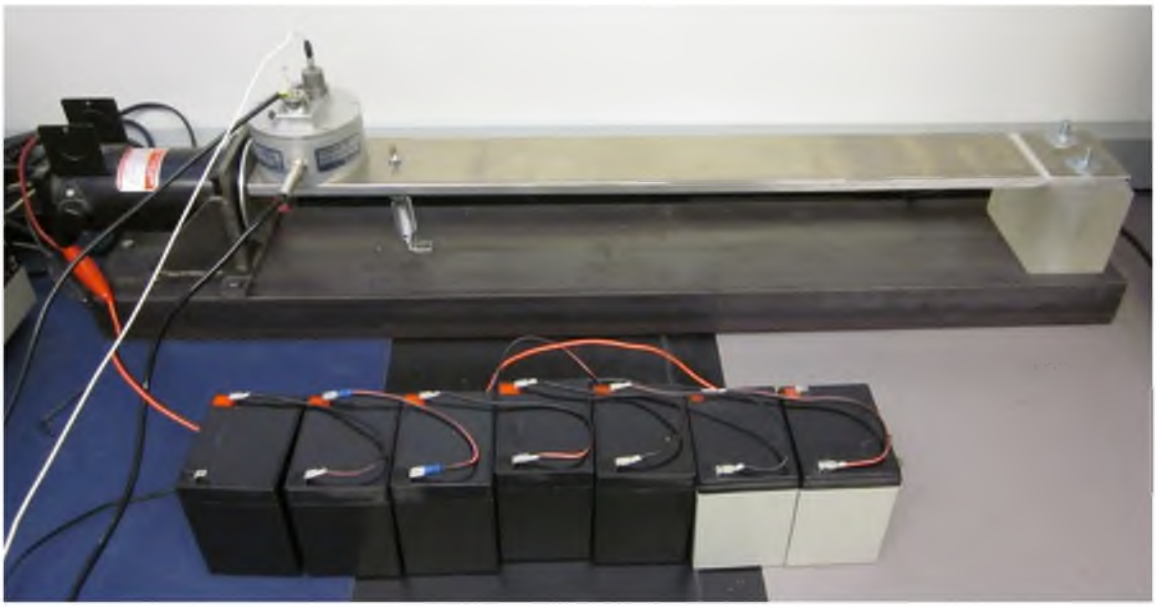

Figure 3.4 Apparatus for testing vibration transducers

offset cams were used: 0.152 mm (0.006 in.), 0.610 mm (0.024 in.), and 1.270 mm (0.050 in.), as shown in Figure 3.5. Ball bearings were fitted over the cams and a rubber band was placed around the bearings to prevent rattling between the offset cam and the cantilever, as seen in Figure 3.6. A mount was made to clamp the geophones in place. This and the Instantel seismograph were bolted to the cantilever directly above the motor shaft. Speed was controlled via 12 V batteries connected in series, from 12 to 84 V.

While this apparatus proved somewhat useful in testing the vibration transducers, it had a several limitations. First, the maximum speed of the DC motor was 2160 RPM, limiting the frequency ranges that could be tested to a maximum of 36 Hz. Thus only frequencies up to the natural frequency of the 28-Hz geophone and below that of the 40-Hz geophone could be tested. Higher frequencies could be achieved by incorporating a gear box or pulley, but this was not attempted. However, low frequencies could be tested, in which the range the transfer function presented in Equation C.4 is especially critical.

Figure 3.5 Offset cams 6.096 mm (0.024 in.) (left) and 12.70 mm (0.050 in.) (right)

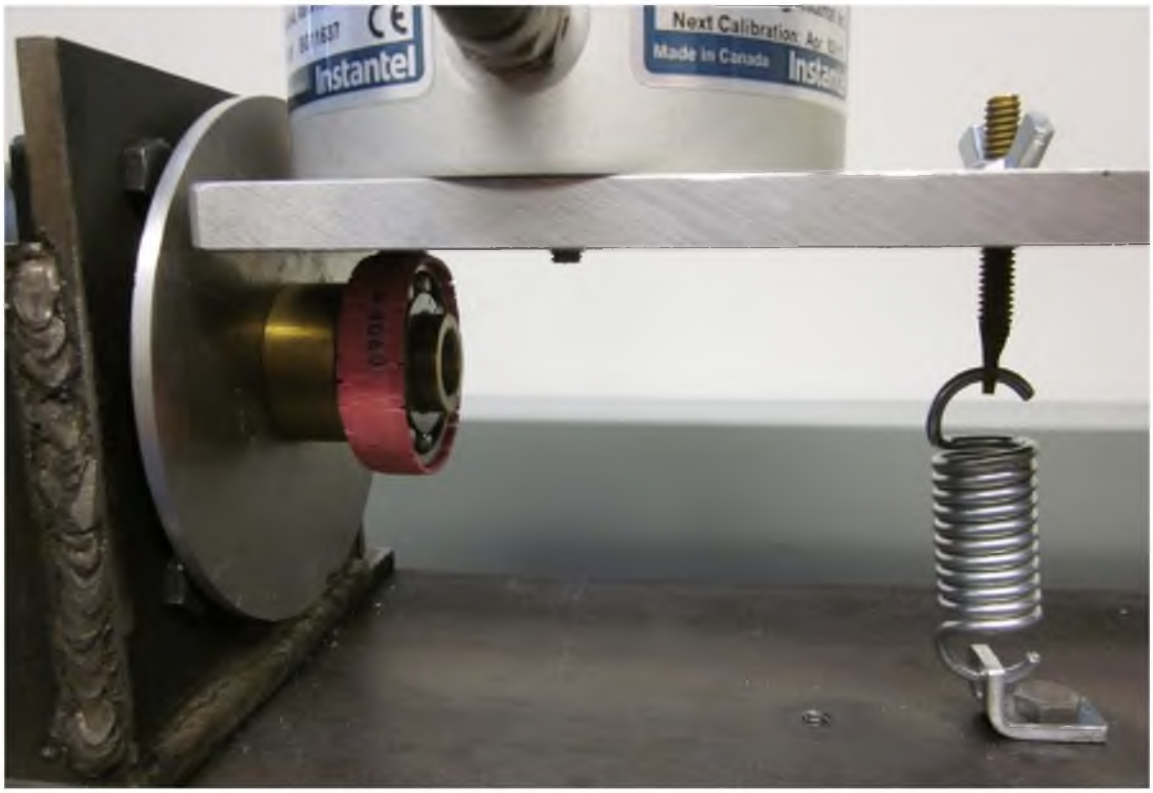

Figure 3.6 Offset cam on shaft, seismograph mounted on cantilever, and tension spring

Figures 3.7 and 3.8 show plots comparing scaling constants as calculated by the transfer function for the 28-Hz and 40-Hz geophone and from experimental data. The data show some scatter, but overall the trend is comparable.

The second limitation concerned the presence of noise in the vibration records. This was likely due to several sources such as minor rattling in the bearings, vibrations from different components as induced by the oscillations, and electrical noise in the equipment. Fairly consistent 120-Hz and 240-Hz noises were also present—possibly harmonics from nearby AC electrical sources. Applying a flat-line filter for frequencies in the vibration records above 50 Hz mitigated some of the noise but not all. This created some subjectivity in selecting the peak particle velocities.

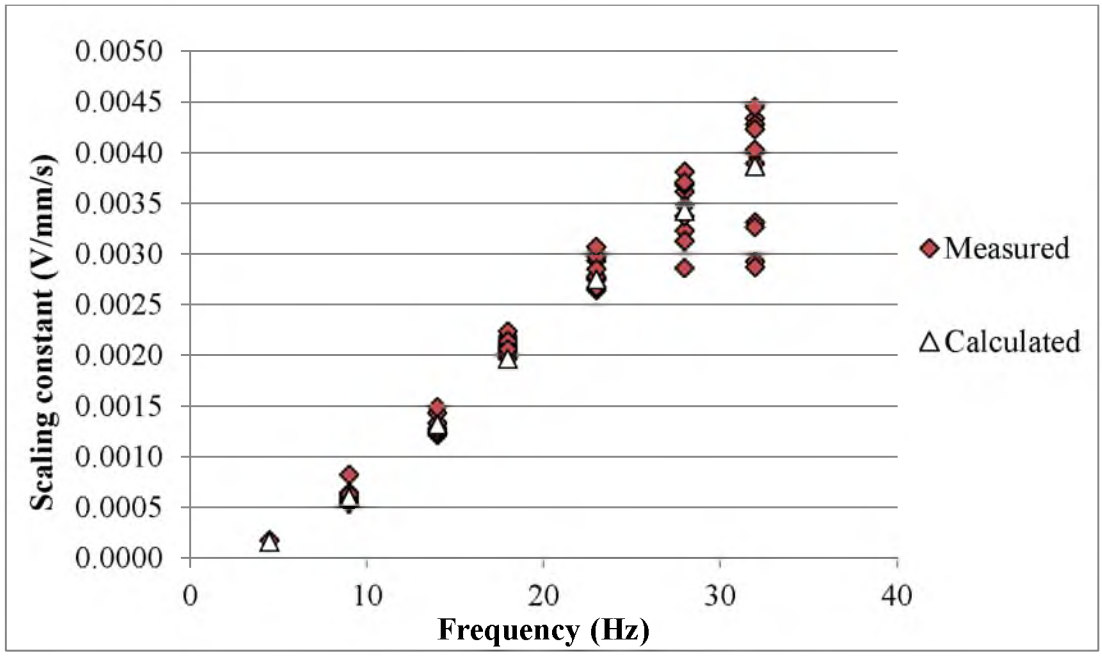

Figure 3.7 Geophone scaling constant for the 28-Hz geophone with a 182-Ω shunt

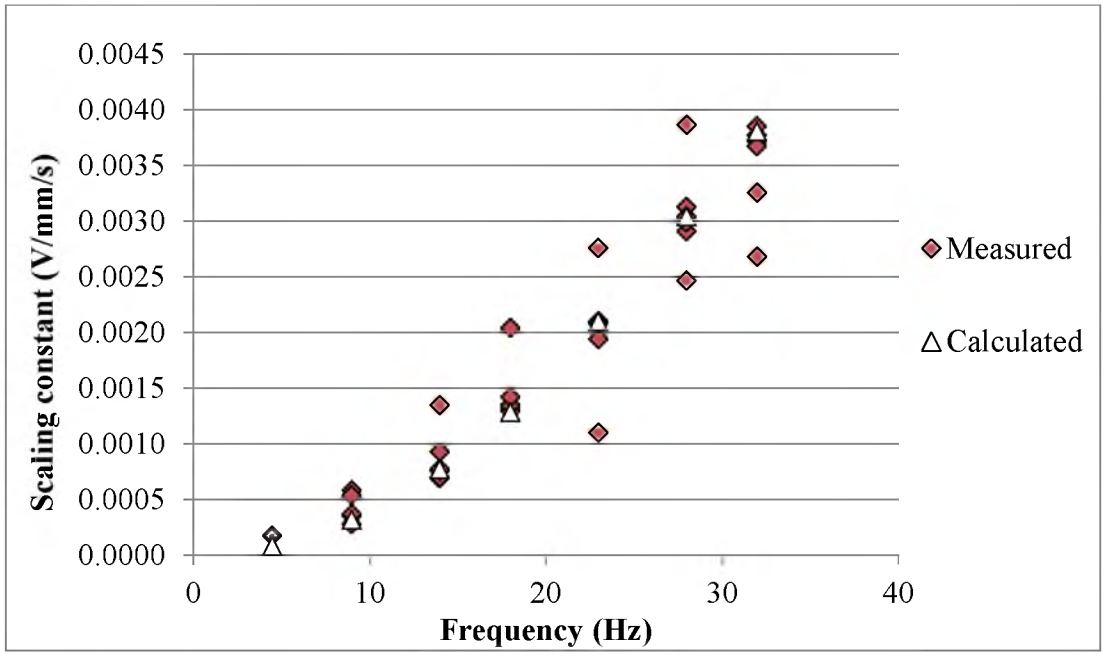

Figure 3.8 Geophone scaling constant for the 40-Hz geophone with a 182-Ω shunt

The third limitation concerned the regularity of the offset cam rotation. The cam offset 1.270 mm (0.050 in.) demonstrated irregular motion at higher frequencies with greater amplitudes. Because of the force applied by the cantilever and tension spring on the cam, the motor would begin to raise the cantilever more slowly and then drop it faster. This distorted the usual sinusoidal vibration. A solution to this problem would be to install a flywheel, but this was not thought necessary.

Vibration amplitudes up to 180 mm/s (7.0 in./s) were obtained through steady-state oscillations of the vibration transducers. The correlation of vibration levels between the shunted geophones and the Instantel seismograph appeared to be satisfactory at low frequencies. Although the testing program was not as rigorous nor as precise as using a shaking table calibration, the results were considered adequate for the purposes of the field test to be performed.

3.1.1.2 Accelerometers

A PCB Piezotronics 353B32 ICP® shear quartz accelerometer was available for measuring near-field vibrations for the field test. The ICP® label indicates an integrated circuit accelerometer. A PCB Piezotronics 480E09 battery-powered signal conditioner was used in conjunction with the accelerometer. The sensitivity of the accelerometer was 50 mV/*g*, or 5.10 mV/m/s^2 (1.55 mV/in./s^2). The frequency range (±3 dB) was from 0.35 Hz to 15 kHz, with a resonance frequency of 28 kHz. The linear range of acceleration was ±100 *g* with an overload limit of ±10,000 *g*. This was considered adequate for the test being performed, although a higher shock limit would have been preferable. As noted by Yang et al. (1993), blast vibrations within a couple meters of a blasthole can exceed frequencies of 50 kHz and shock loads of 50,000 *g*. Table 3.4 lists selected specifications

Table 3.4 Selected specifications of the PCB Piezotronics 353B32 accelerometer

	Metric units	Imperial units	Tolerance
Sensitivity	5.10 mV/m/s^2	1.55 mV/ft/s^2	5%
Measurement range	±981 m/s^2	±3217 ft/s^2	
Overload limit	±90866 m/s^2	±321742 ft/s^2	
Frequency ranges	–5000 Hz		5%
	0.7–8000 Hz		10%
	0.35–15000 Hz		±3 dB
Resonance frequency	≥28000 Hz		
Nonlinearity	≤1%		
Transverse sensitivity	≤5%		
Excitation voltage	18–30 V-DC		
Discharge time constant	0.5–2 s		
Height	29.9 mm	1.18 in.	
Weight	20 g	0.71 oz	
Sensing element	Quartz		
Sensing geometry	Shear		
Housing material	Titanium		

Source: PCB Piezotronics (2002)

of the accelerometer. Each PCB accelerometer is calibrated by the manufacturer; thus no verification of the accelerometer's performance was deemed necessary.

3.1.2 Data acquisition

Two oscilloscopes, a Nicolet Model 3901 and a Nicolet Model 310, were used for data acquisition from the vibration transducers. Each oscilloscope was equipped with two channels, and communication with the sensors was established via BNC cables. The voltage scale could be varied from 100 mV to 40 V. The smallest sampling interval was 1 μs for each channel. Each oscilloscope could record 4,000 points per channel. The oscilloscopes required a 110-V AC power supply to run.

Downloading data from the Nicolet 3901 required the use of a 25-pin crossover serial cable and computer or laptop equipped with either a 25-pin serial port or a 9-pin serial port and a 25-pin to 9-pin serial adapter. The download was accomplished using Waveform Basic™ software. The Nicolet 310 possessed a dual-bay 3 ½-in. floppy reader that used double-density disks. Downloaded data entailed saving the data onto a disk and using an executable program on a computer to extract each record.

3.1.3 Time domain reflectometry

An AEMC CA7026 time domain reflectometer (TDR) was obtained to evaluate stretching or breaks in the two-conductor wires secured downhole, pictured in Figure 3.9. This TDR has a graphical display that allows the user to visually analyze the impedance

Figure 3.9 AEMC CA7026 graphical TDR

profile of the wire. Cable attachment could be made by either a BNC connector or alligator clips. The resolution of the instrument, however, is limited. The graphical display did not possess a zoom feature and thus measurements made by the cursor could only be made within ±2–3 ft. Another limitation of the instrument was the occurrence of an initial pulse at the beginning of the impedance profile. This effectively limited the closest obtainable reading to at least 15 m (50 ft). An extra length of wire was required to extend the two-conductor downhole wires so that measurements could be made. Table 3.5 lists selected properties of the TDR.

The two-conductor wires that were cemented downhole were made from 24- and 28-AWG copper magnet wire. Each set of wires was made by taking a length of wire, securing the midway point of the wire around an immobile object (i.e., a chair leg), clamping the two ends of the wire in a drill bit chuck, and twisting the wires together. Figure 3.10 shows the twisted magnet wire. Two-conductor, insulated 21-AWG shot wire was soldered onto the ends of each twisted magnet wire to extend the length so TDR readings could be taken.

Table 3.5 AEMC CA7026 TDR specifications

	Metric units	Imperial units
Ranges @ V_p=70%	100–3500 m	330–11700 ft
Resolution	1% of range	
Accuracy	±1% of range	
Minimum cable length	15 m	50 ft
V_p range	0–99%	
Selectable cable impedance	50, 75, 100 Ω	
Display resolution - LCD	128x64 pixels	

Source: AEMC Instruments (2011b)

Figure 3.10 Twisted magnet wire. A pen is shown for size comparison.

3.1.4 Borescope

A Dianichi Nippon Diaguide borescope with an integrated light source was used for visually inspecting downhole fracturing of the rock mass. The borescope required a power supply for running the light source. The viewing lens was equipped with an attachment onto which a camera could be mounted. Unfortunately, a suitable camera that could focus on the image through the viewing lens was not available. Figure 3.11 shows a picture of the borescope.

3.1.5 Quick-setting grout

Hydro-Stone® cement, manufactured by U.S. Gypsum, was selected for securing equipment downhole. This particular grout was chosen for its rapid set time and light color, which aided in viewing cracks through the borescope. Table 3.6 lists selected properties.

3.2 Field experiment setup

For the field experiment, a single blasthole was drilled to a depth of 6.7 m (22 ft) with a top hammer percussive drill rig. Three colinear observation holes were located at

Figure 3.11 Borescope; viewing apperture inset

Table 3.6 Hydro-Stone® cement properties

	Metric units	Imperial units
Mixing proportions by weight (cement : water)	100 : 32	
1 hr. compressive strength	27.6 MPa	4000 psi
Dry compressive strength	69.0 MPa	10000 psi
Max setting expansion	0.24%	
Density - wet	1.91 g/cm^3	119 lb/ft^3
Density - dry	1.73 g/cm^3	108 lb/ft^3
Set time (machine mix)	17–20 min	

Source: U.S. Gypsum Corporation (1999)

distances of 1.1 m (3.5 ft), 2.1 m (6.9 ft), and 3.8 m (12.4 ft) to the south of the blasthole. Each was drilled to a depth of 4.9 m (16 ft). The bit diameter used to drill the holes was 114.3 mm (4.5 in.); thus, a drillhole diameter of 120.7 mm (4.75 in.) was assumed. The accelerometer and three shunted geophones were positioned down the two observation holes furthest from the blasthole. Two Instantel DS-200 seismographs were positioned in between the observation holes on the surface. An Instantel Minimate Plus seismograph was positioned beyond the third observation hole. Diagrams of the setup are shown in Figures 3.12 and 3.13. Table 3.7 gives a list of the vibration transducers in the diagrams.

To aid in securing the vibration transducers downhole, the accelerometer and geophones were precast in Hydo-Stone^{TM} as shown in Figure 3.14. A short length of PVC pipe was placed in the top of the cast. Cardboard molds and wires were used to secure the instruments, but during the casting process two of the geohones shifted positions slightly. The amount of shifting was determined to be inconsequential. To position the instrument casts downhole, additional lengths of PVC pipe were coupled to each cast. Each cast was lowered downhole so that the axes of the vibration sensors were aligned in the direction of the blasthole.

Two pairs of the two-conductor twisted wires for TDR measurements were placed down each instrument hole. Each hole had one TDR wire configuration with 28-AWG and one with 24-AWG magnet wire so a comparison could be made. Each TDR wire configuration consisted of a 5.5-m (18-ft) length of twisted magnet wire downhole, which was soldered to an 18.3-m (60-ft) length of shot wire. The only exception was the length of 28-AWG wire down instrument hole 1. The wire was accidentally broken in

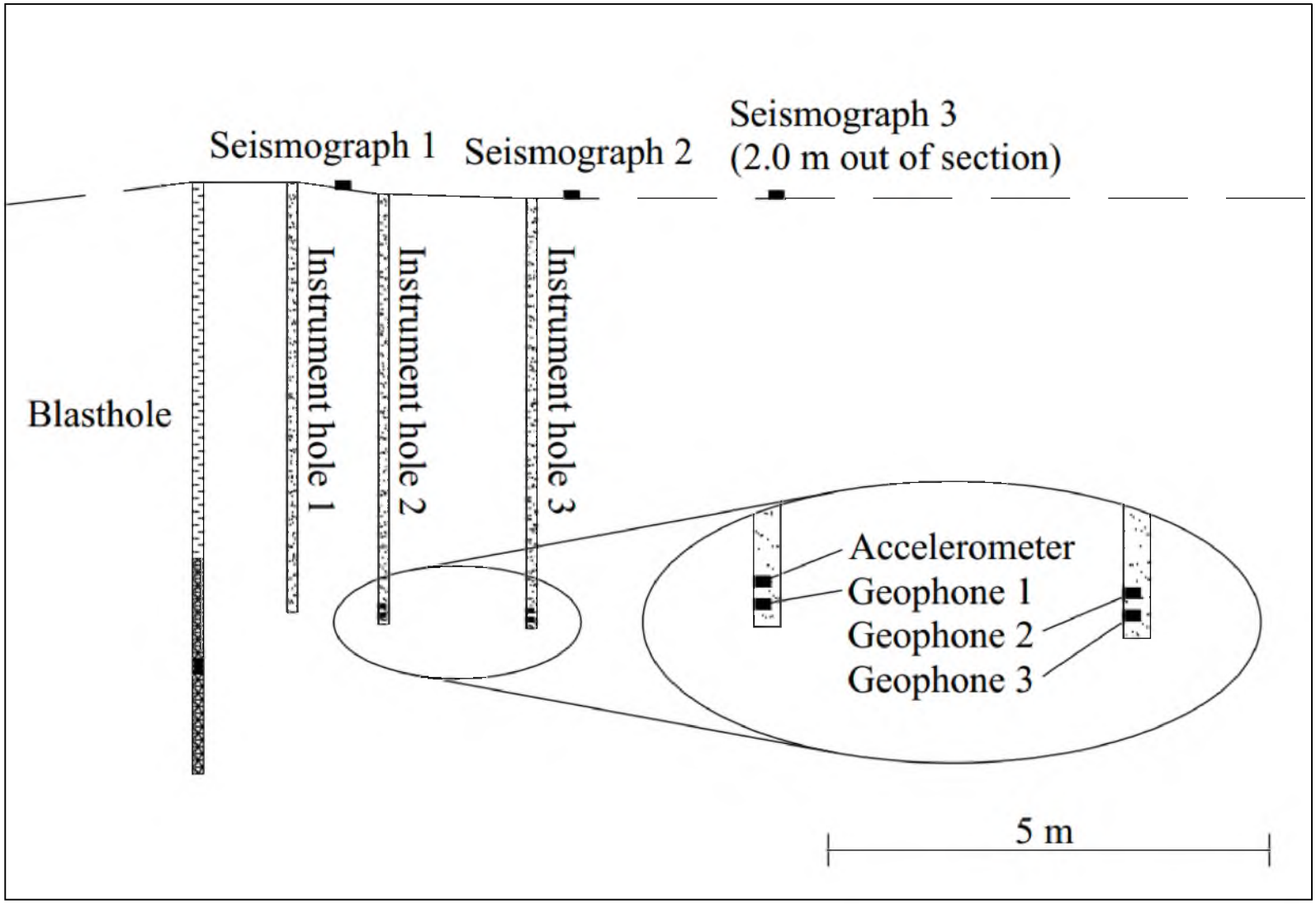

Figure 3.12 Section view layout of blasthole, observation holes, and seismographs

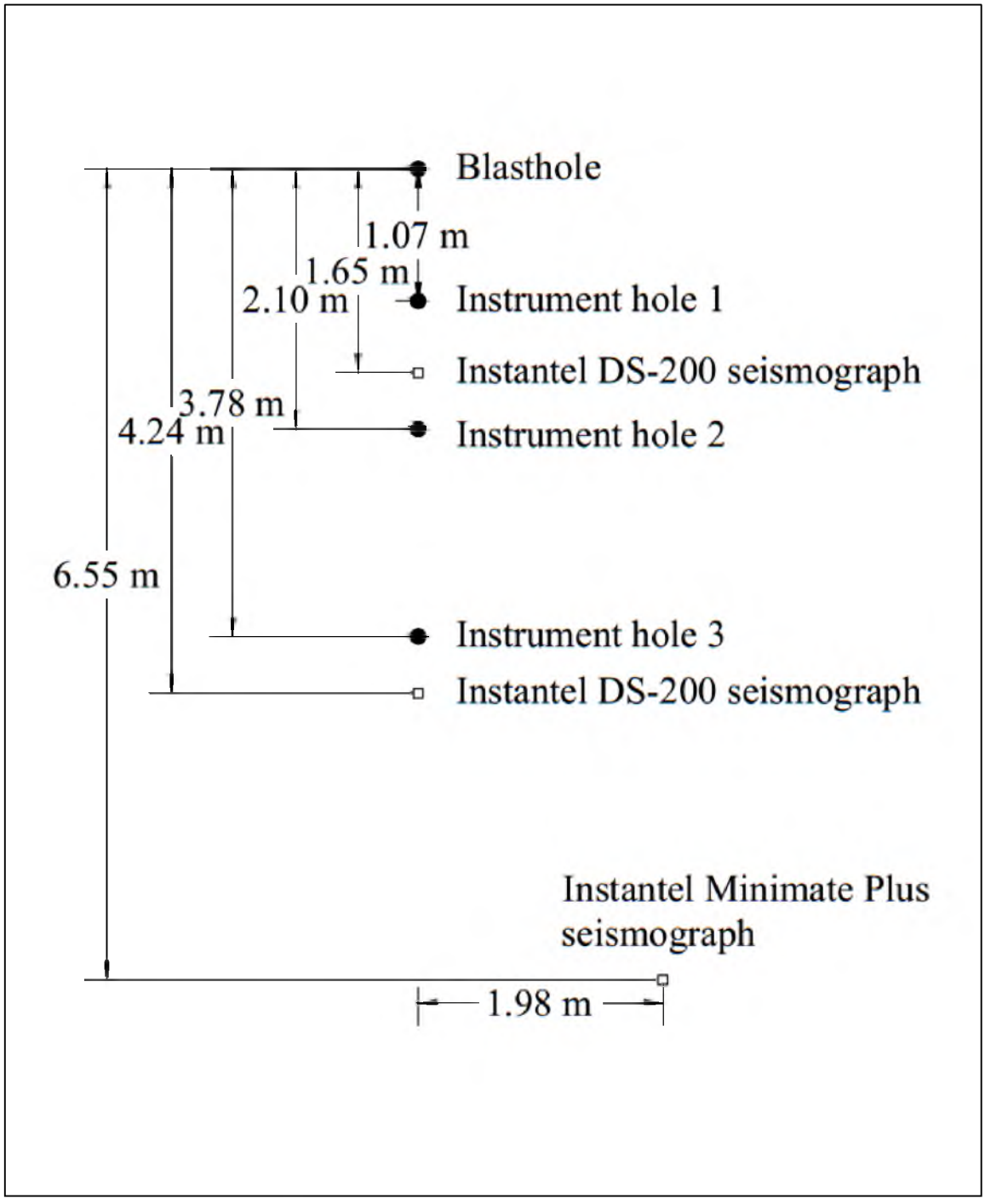

Figure 3.13 Plan view layout of drilhole and seismograph positions

Table 3.7 Vibration transducer labels

Label	Vibration sensor
Accelerometer	PCB 353B32
Geophone 1	Geospace GS-20DM, 28–Hz, 182–Ω shunt
Geophone 2	Geospace GS-20DM, 28–Hz, 182–Ω shunt
Geophone 3	Geospace GS-20DM, 40–Hz, 182–Ω shunt
Seismograph 1	Instantel DS-200
Seismograph 2	Instantel DS-200
Seismograph 3	Instantel Minimate Plus

Figure 3.14 Vibration transducers precast in Hydro-Stone™

half during the setup phase of the experiment, resulting in a length of 2.9 m (9.5 ft) instead of the original 5.5 m (18 ft). Insulating tape was wrapped around the ends of each twisted wire pair and at the solder joint between the magnet wire and shot wire to ensure that no short circuiting occurred.

Clear acrylic tubes with inner and outer diameters of 12.7 mm (0.500 in.) and 15.9 mm (0.625 in.), respectively, were coupled together and positioned downhole. For the two holes with the vibration instruments, the acrylic tube and TDR twisted wires were taped to the PVC casts before being lowered downhole. For the hole closest to the blasthole, only the clear acrylic tube and twisted wires were placed downhole.

After positioning the instruments, pipes, and wires downhole, the Hydro-Stone™ cement was mixed using a power drill and mixing paddle and poured down the instrument holes until filled to the top. Figure 3.15 shows a photograph of the test site. Figure 3.16 displays a diagram of the instrument holes.

Coaxial cable was used to connect the vibration transducers with the oscilloscopes. An infrared phototransistor was used as an external trigger for the oscilloscopes. Nonelectric initiation line was fed through the transistor housing, which would respond to the bright flash by producing a voltage spike. A sampling interval of 10 μs was selected, which is equivalent to a sampling rate of 100 kHz. The length of a record at this rate is 40 ms, which is sufficient to measure the initial shock wave and the high-amplitude vibrations that would follow. A pretrigger period of 2 ms was selected. For the geophones, a voltage setting of 20 V was selected.

For the accelerometer, the in-line signal conditioner was set to a gain of unity and the voltage scale on the oscilloscope was set to 10 V. The oscilloscopes were powered by

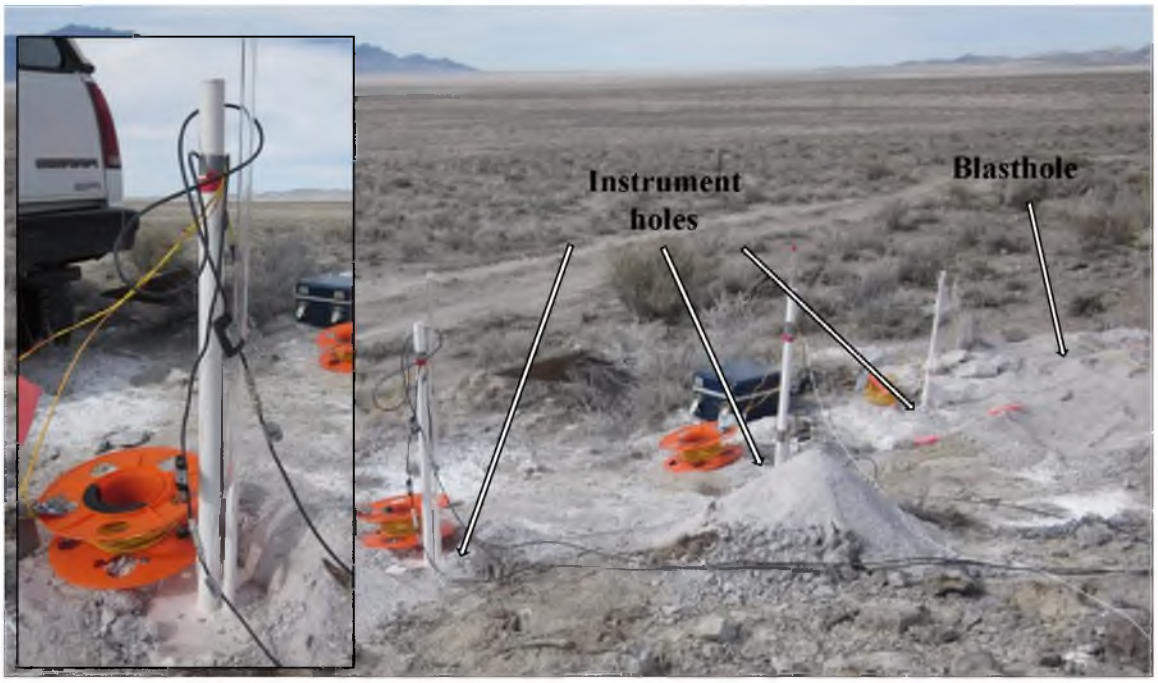

Figure 3.15 Layout of instrument and blastholes; inset shows the top of instrument hole 3.

a deep-cycle battery with an inverter. The oscilloscopes were placed inside protective covers (as shown in Figure 3.17) to protect them from possible flyrock.

The Instantel DS-200 and Minimate Plus seismographs were both set at their maximum sampling rates. The DS-200s can sample at a frequency up to 512 Hz and the Minimate Plus up to 4,096 Hz. All seismographs have a peak amplitude limit of 254 mm/s (10.0 in./s) that can be recorded.

The bottom 2.4 m (8 ft) of the blasthole was loaded with ANFO and center-primed, which amounts to about 23.7 kg (52.2 lb) of blasting agent. Drill cuttings were used to stem the remaining 4.3 m (16 ft) of the blasthole to the collar, creating a heavily-confined explosive charge. The charge was initiated via a nonelectric downline to the detonator and booster. A length of detonation cord secured to the booster ran out of the

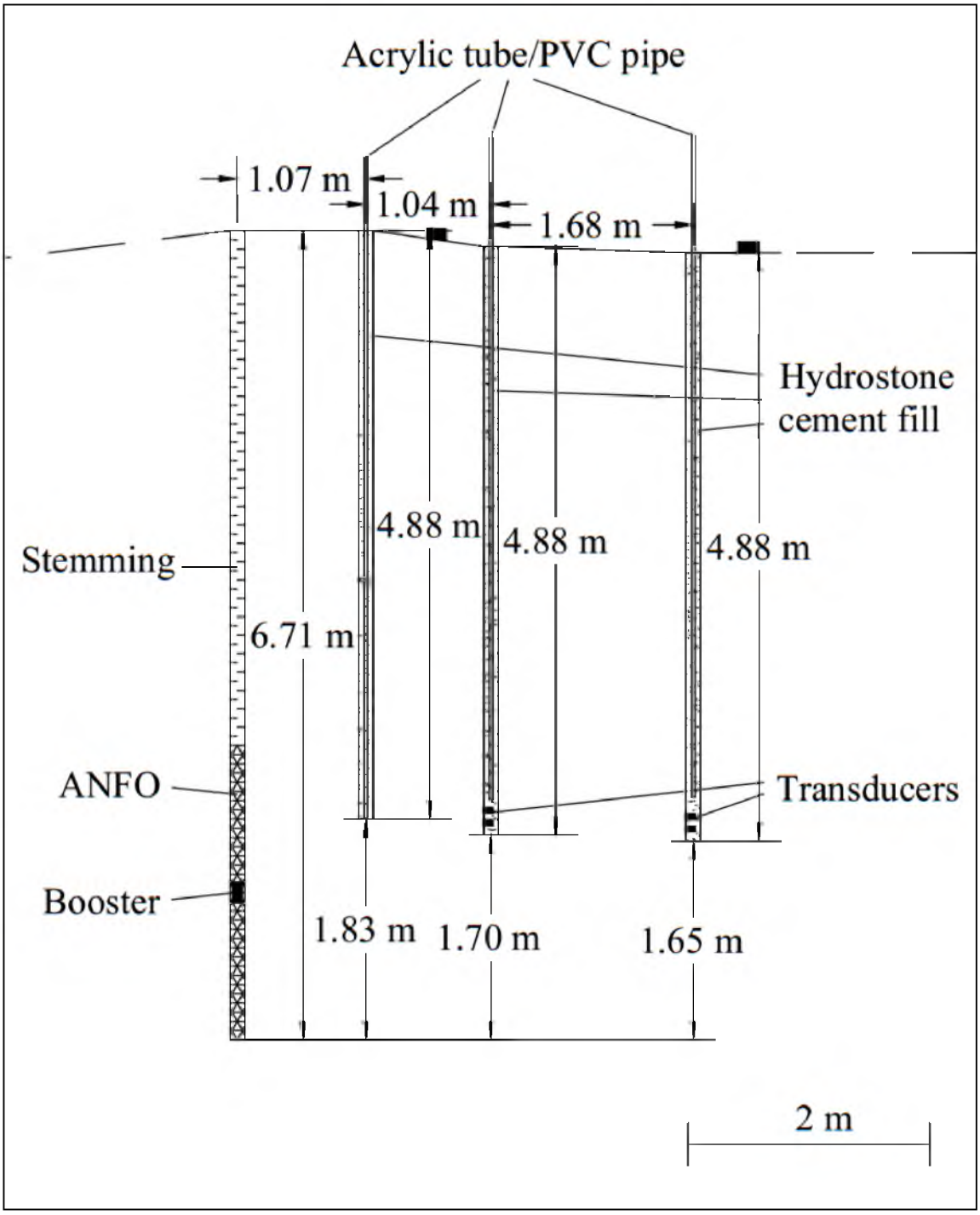

Figure 3.16 Section view layout of the blasthole and instrumented holes

Figure 3.17 Oscilliscopes in their protective covers, powered by a deep-cycle battery

hole collar and joined with another length of nonelectric initiation tube, which was connected to the external trigger for the oscilloscopes.

3.3 Results

3.3.1 Vibration records

The raw vibration records are shown in Figures 3.18, 3.19, 3.20, and 3.21. The 20-V scale on the oscilloscope proved adequate for the geophones. However, the 10-V scale, which is equivalent to 200 *g* of acceleration, was too low for the accelerometer. The initial pressure peak and a secondary peak were clipped as the acceleration limit was exceeded. Extrapolation of these first two peaks was performed, as is shown in Figure 3.22. The estimated shock experienced by the accelerometer is at least 450 *g*. This is lower than the near-field accelerations expected by Yang et al. (1993). Since the linear acceleration range of this particular accelerometer was exceeded (±200 *g*), the extrapolation is only a rough estimate.

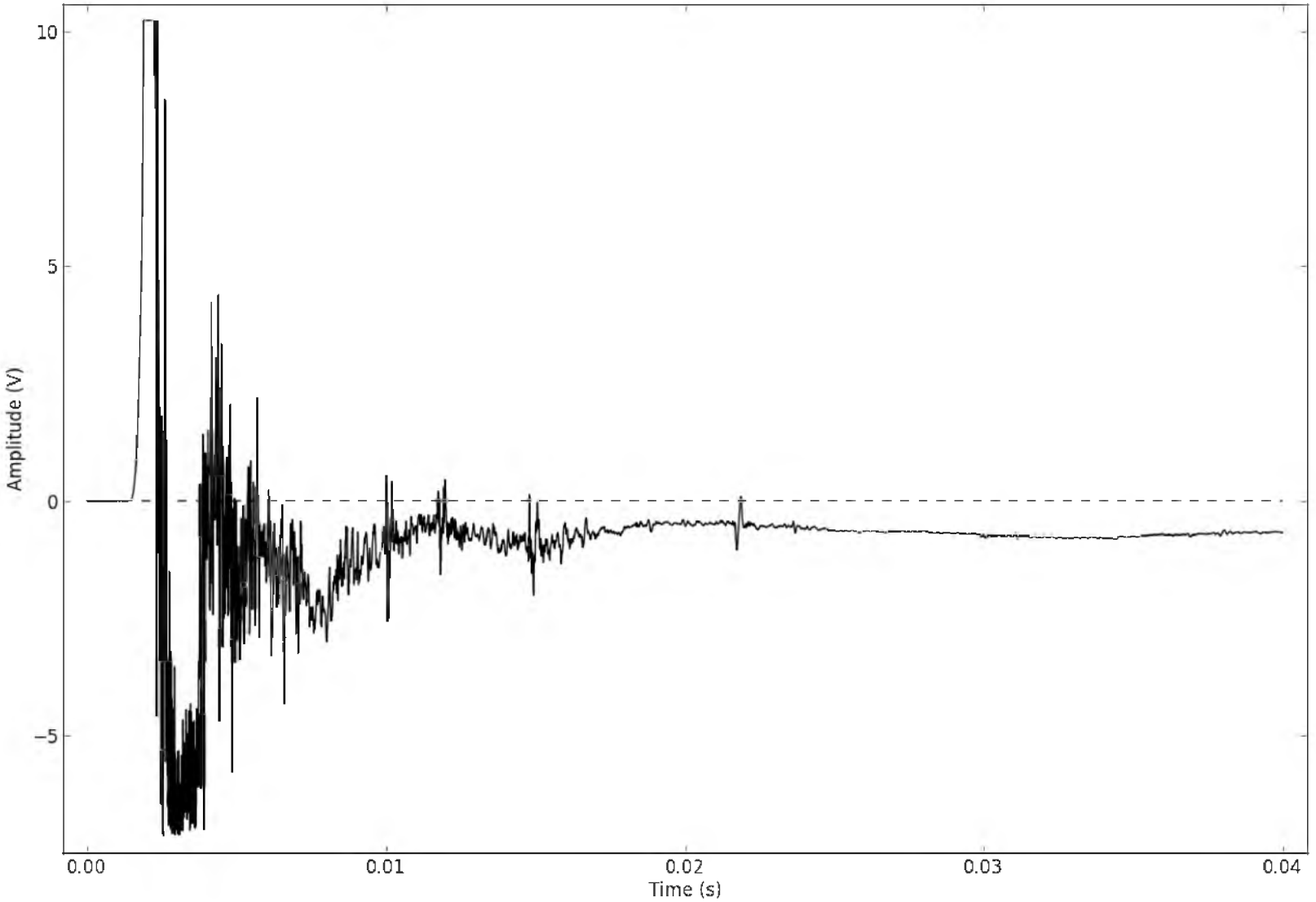

Figure 3.18 Accelerometer record (raw)

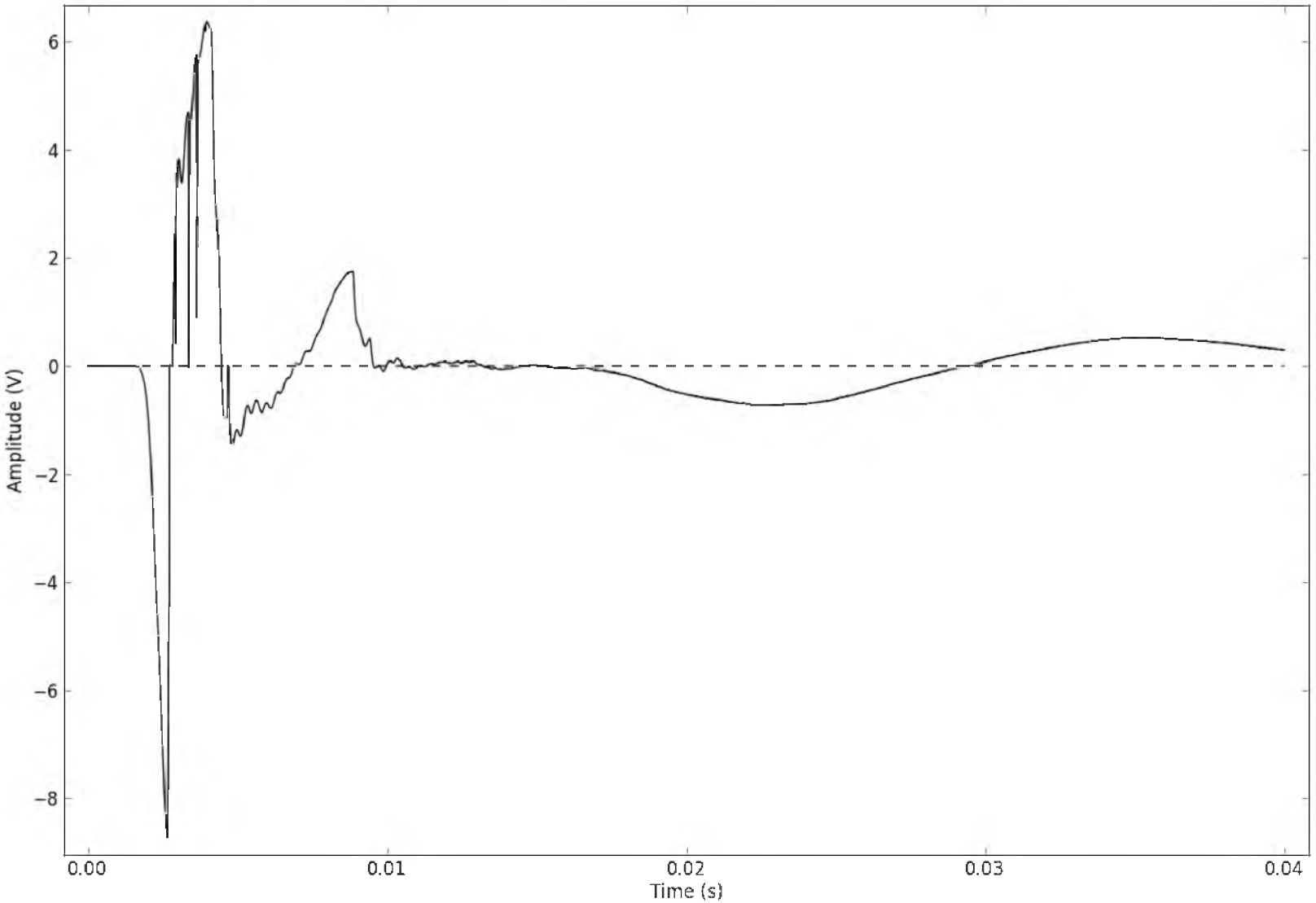

Figure 3.19 Geophone 1 record (raw)

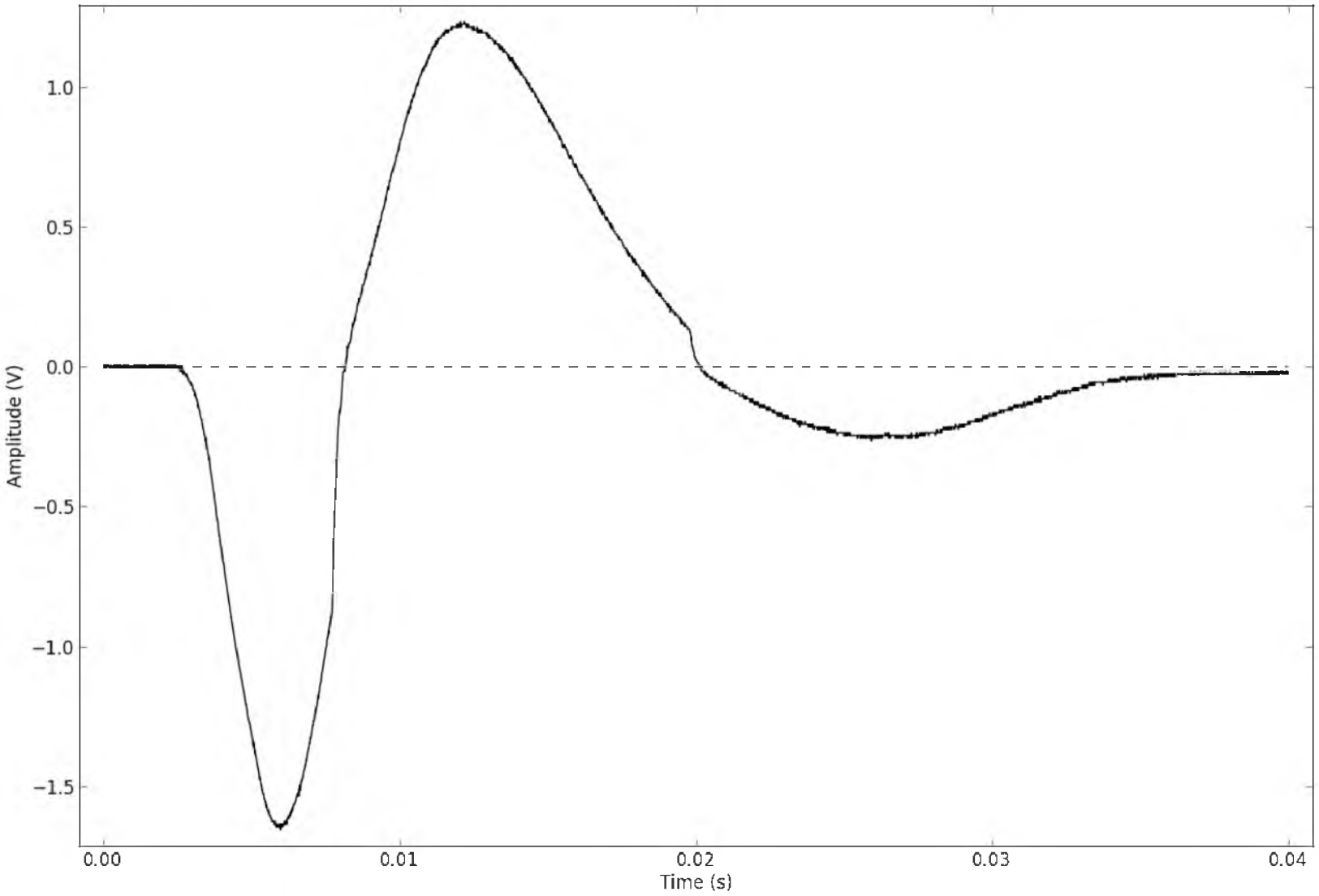

Figure 3.20 Geophone 2 record (raw)

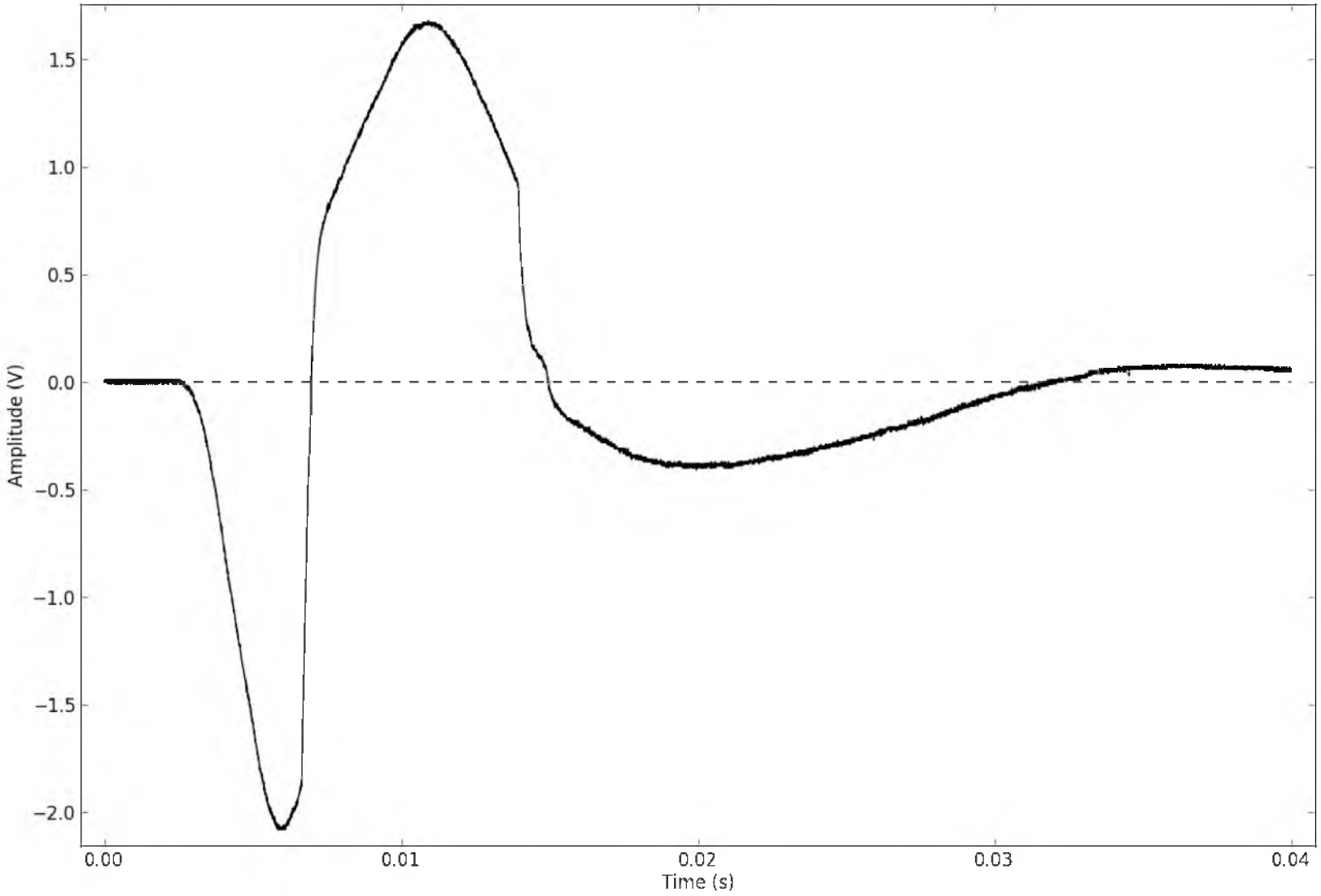

Figure 3.21 Geophone 3 record (raw)

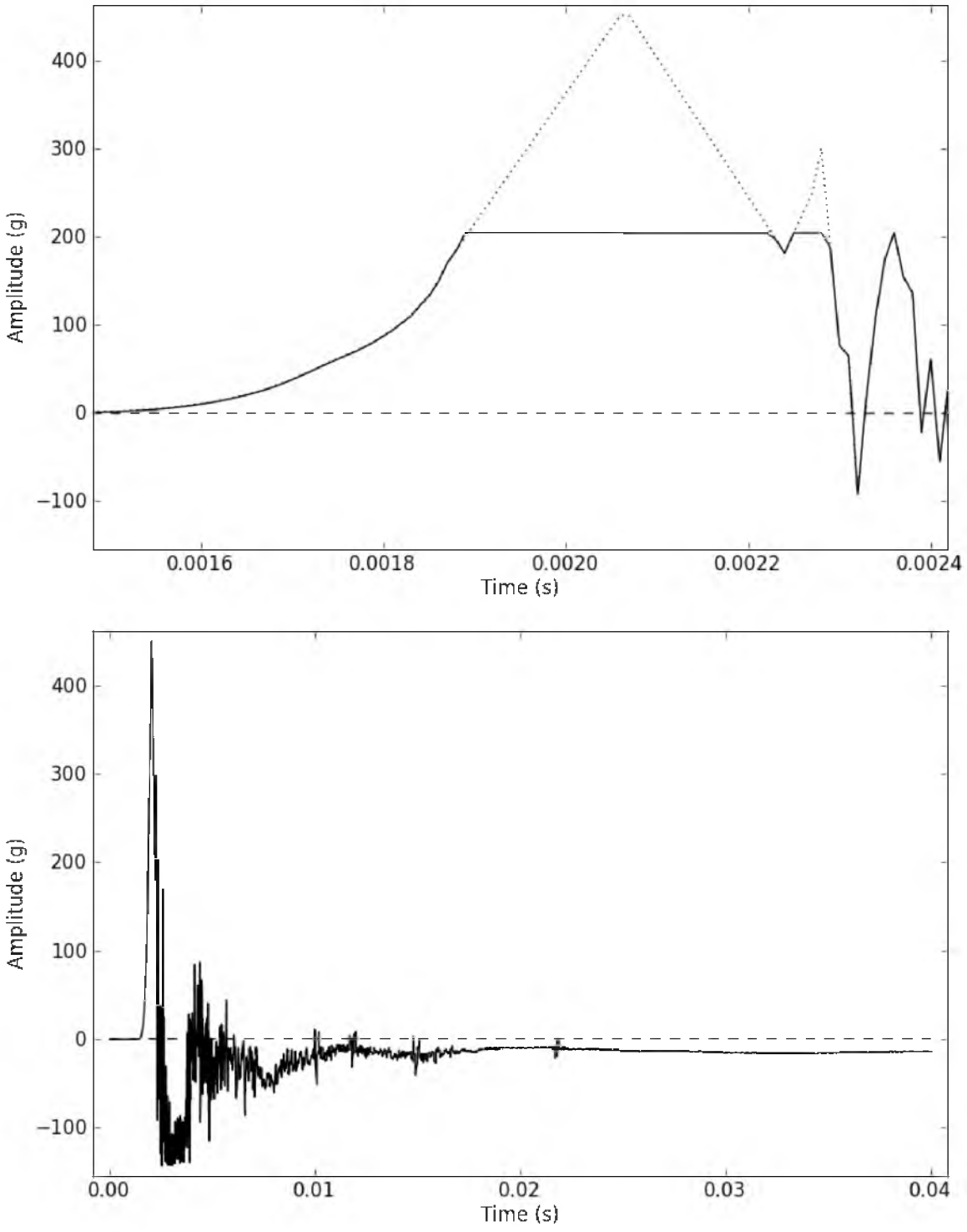

Figure 3.22 Adjusted accelerometer record. Top – peak extrapolation, bottom – adjusted record.

The scaled vibration records are shown in Figures 3.23, 3.24, 3.25, and 3.26. The accelerometer record was integrated and the baseline manually adjusted for drift. An attempt was made to correct the geophone records for both frequency-dependent amplitude and phase. Distortion of the records occurred during signal processing, likely originating from low-frequency components. Observation of the frequency spectra for each record indicated that the dominate frequencies were above the resonance frequency for each geophone. It was decided that simply scaling each record by its transduction constant and shunt resistance and reversing phase by 180° would suffice. Peak particle velocities (PPV), however, were manually estimated. Table 3.8 lists the measured PPV and the corresponding frequencies.

The record for geophone 1 contains a rather sharp peak, followed by a large overshoot superimposed with high-frequency, saw-tooth vibrations. This suggests that the geophone's internal mass hit the limit of its motion and rebounded back. Confirmation comes from the dominate frequency for the geophone's peak velocity being almost three times that of the integrated record of the accelerometer. Thus, the PPV of the geophone may not be the true PPV of the ground motion. The PPV obtained from the integrated accelerometer is also suspect due to linear extrapolation of the clipped acceleration peak. However, the PPVs for geophone 1 and the integrated accelerometer record are only 7% different, which is a relatively minor difference. Given this small difference, and that no additional means were available to independently verify the accurary of the vibration measurements, the PPVs obtained for both vibration sensors were used as presented.

Figure 3.27 shows the frequency spectra for the downhole vibration transducers from 0 to 1,000 Hz. Because of the high sampling rate, the resolution in this range is poor

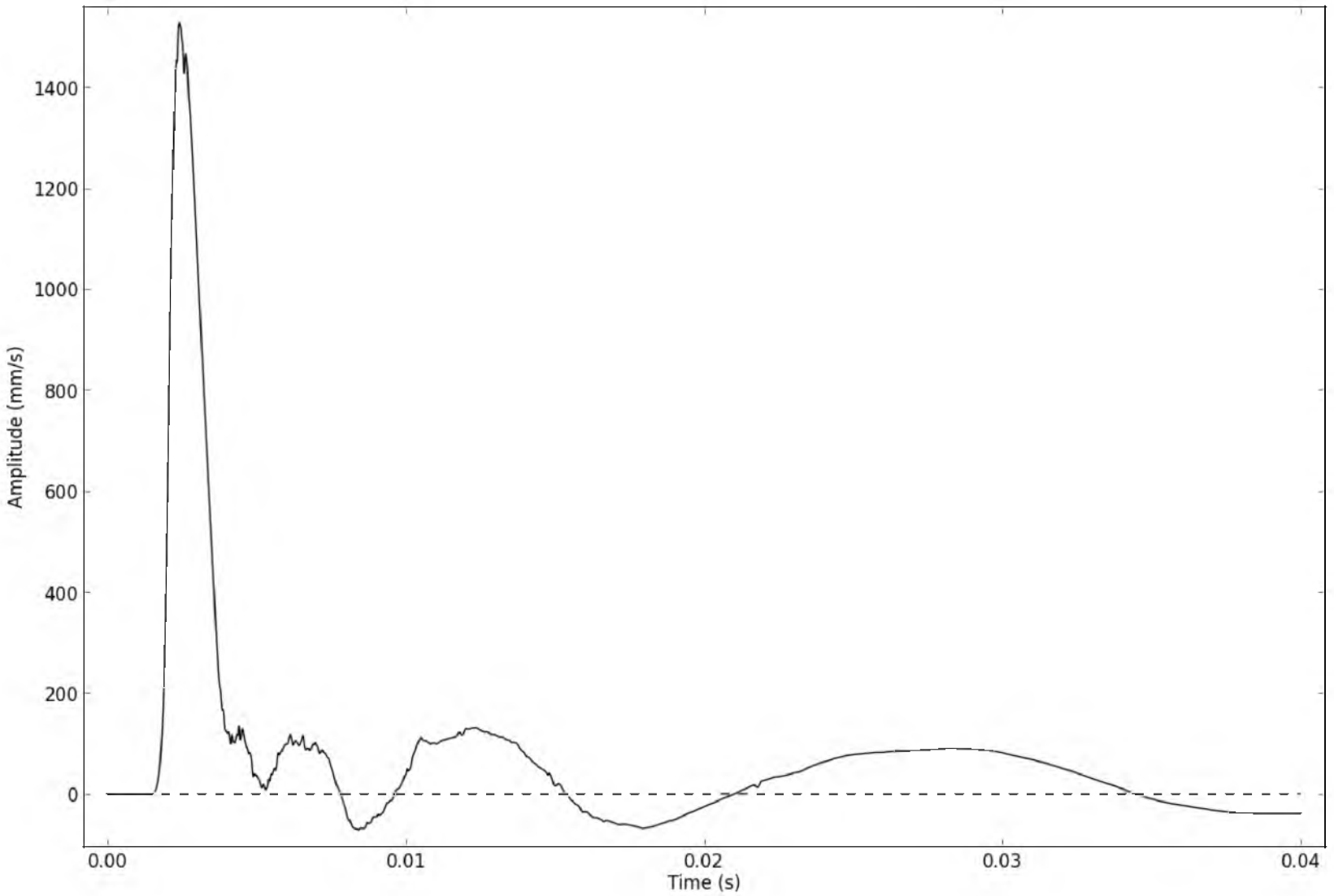

Figure 3.23 Accelerometer record – integrated and baseline adjusted

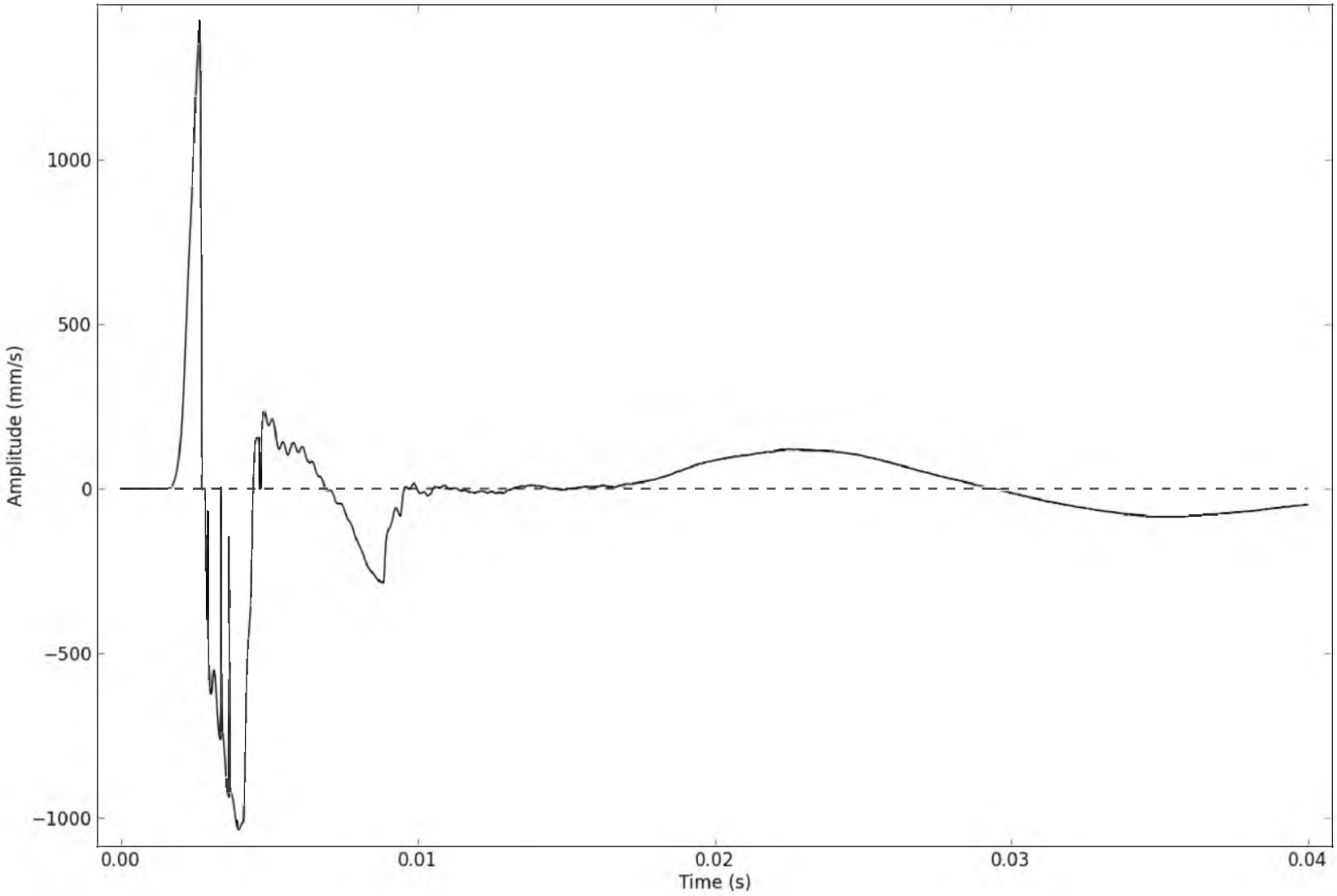

Figure 3.24 Geophone 1 record (adjusted)

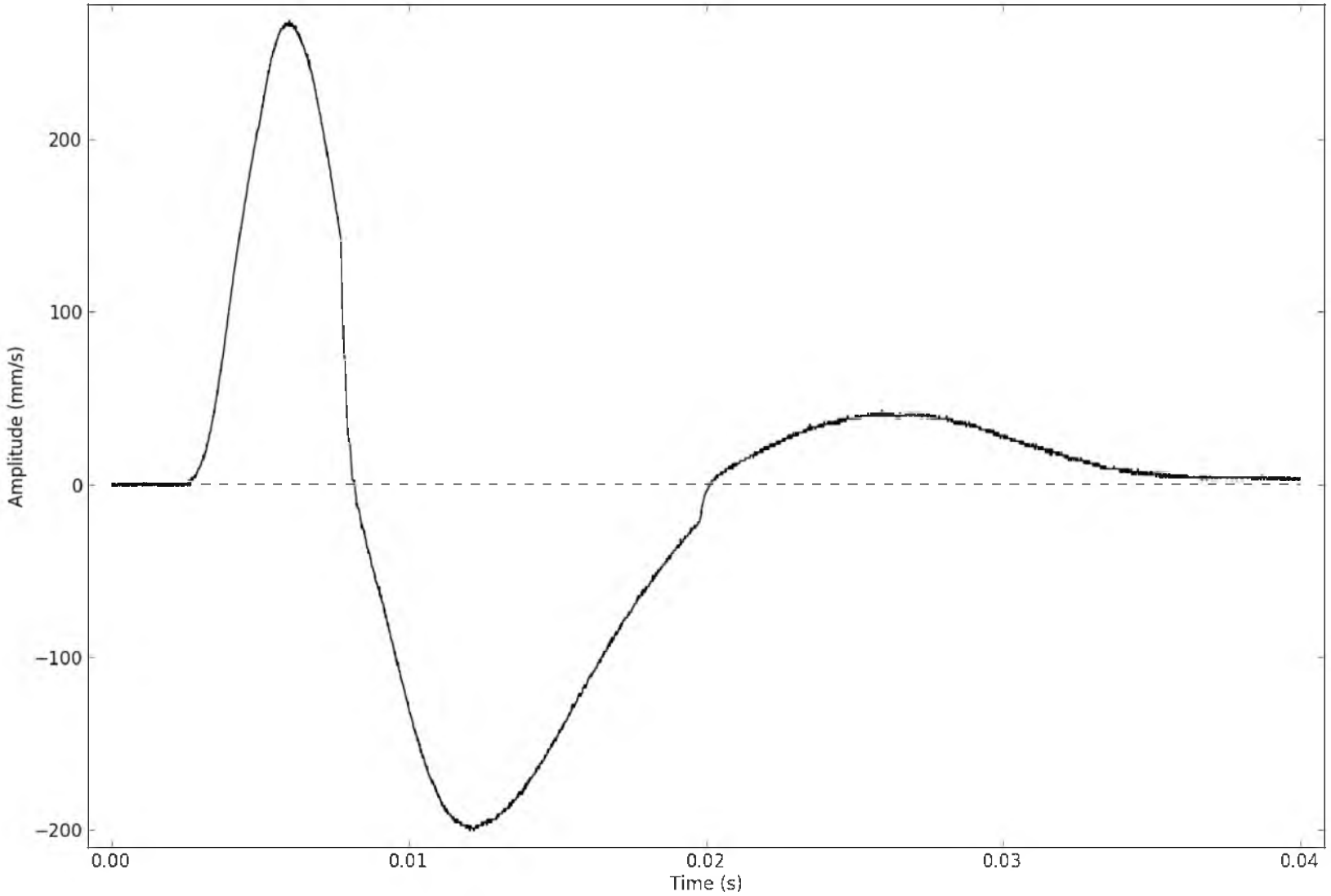

Figure 3.25 Geophone 2 record (adjusted)

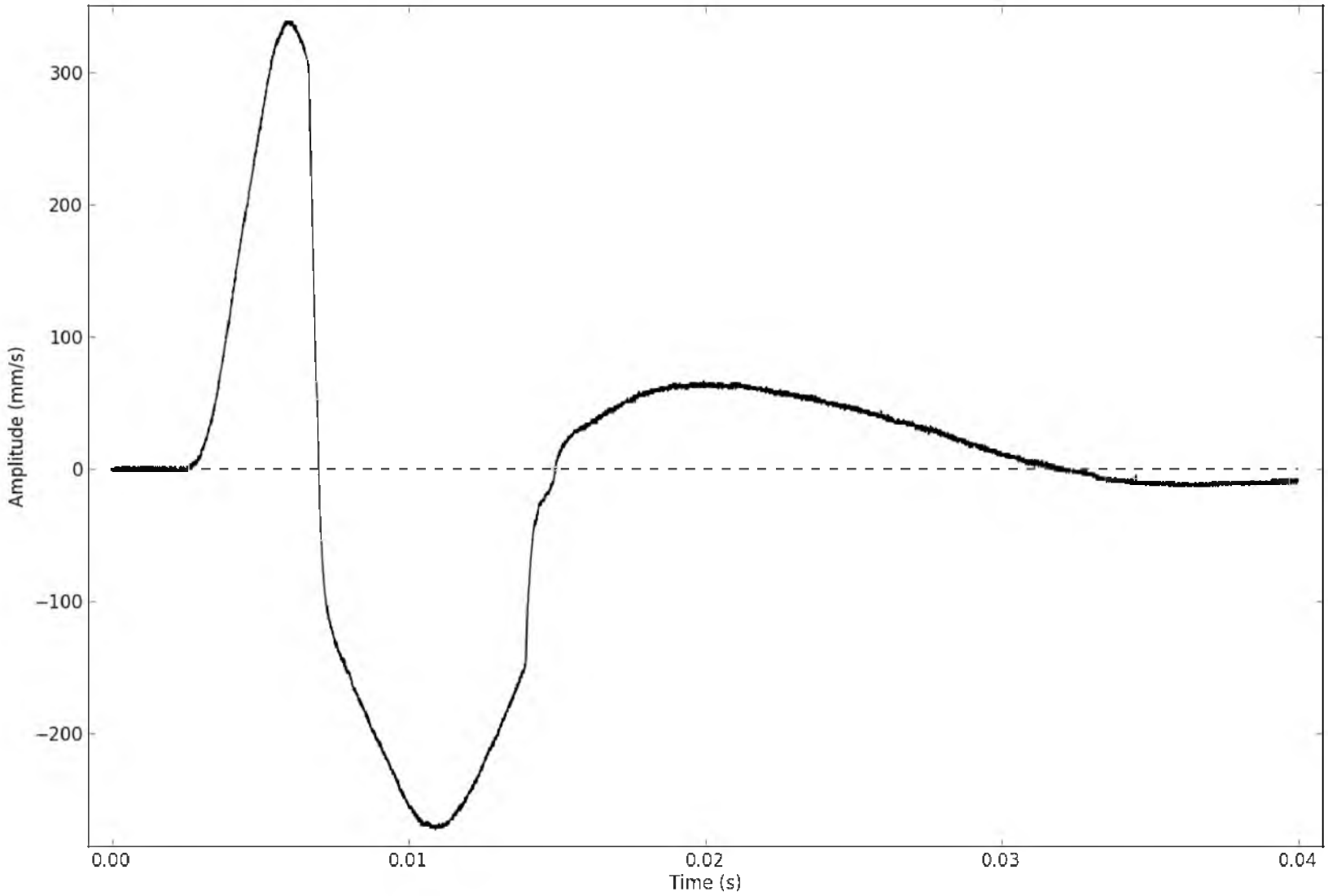

Figure 3.26 Geophone 3 record (adjusted)

Table 3.8 Measured peak particle velocities and their approximate frequencies

Transducer	PPV (mm/s)	PPV (in./s)	Approximate peak frequency (Hz)
Accelerometer	NA	NA	700
Accelerometer (integrated)*	1527	60.1	220
Geophone 1*	1438	56.6	650
Geophone 2	287	11.3	100
Geophone 3	333	13.1	125

* Magnitude and frequency suspect as explained

but nonetheless provides the best estimate for the frequency content of each vibration record. As expected, a greater proportion of high frequencies are present in the instruments closer to the blasthole than those farther away.

Since a sampling rate of 100 kHz was used, sampling theory suggests that the highest detectable frequency is 50 kHz. This is well beyond the ranges of the geophones and beyond the resonance frequency of the accelerometer. The frequency spectra of the accelerometer and geophone 1 are plotted over this range in Figure 3.28 to demonstrate the limitation of using geophones for near-field blast vibrations. The accelerometer shows vibrations at frequencies up to about 14 kHz, which is within the linear range of the accelerometer's frequency response. Vibrations at frequencies around 45 kHz are also present, although this is well above the resonance frequency of the accelerometer. In contrast, amplitudes of frequencies beyond 5 kHz for the geophone are negligible. As discussed by Yang et al. (1993), higher frequencies are indicative of failure in the rock. Caution is recommended in directly comparing geophone and accelerometer records, however, as the former measures acceleration while the latter velocity.

The vibration histories recorded by both Instantel DS-200s were severely clipped, and thus did not provide useful information for determining the PPV at their locations.

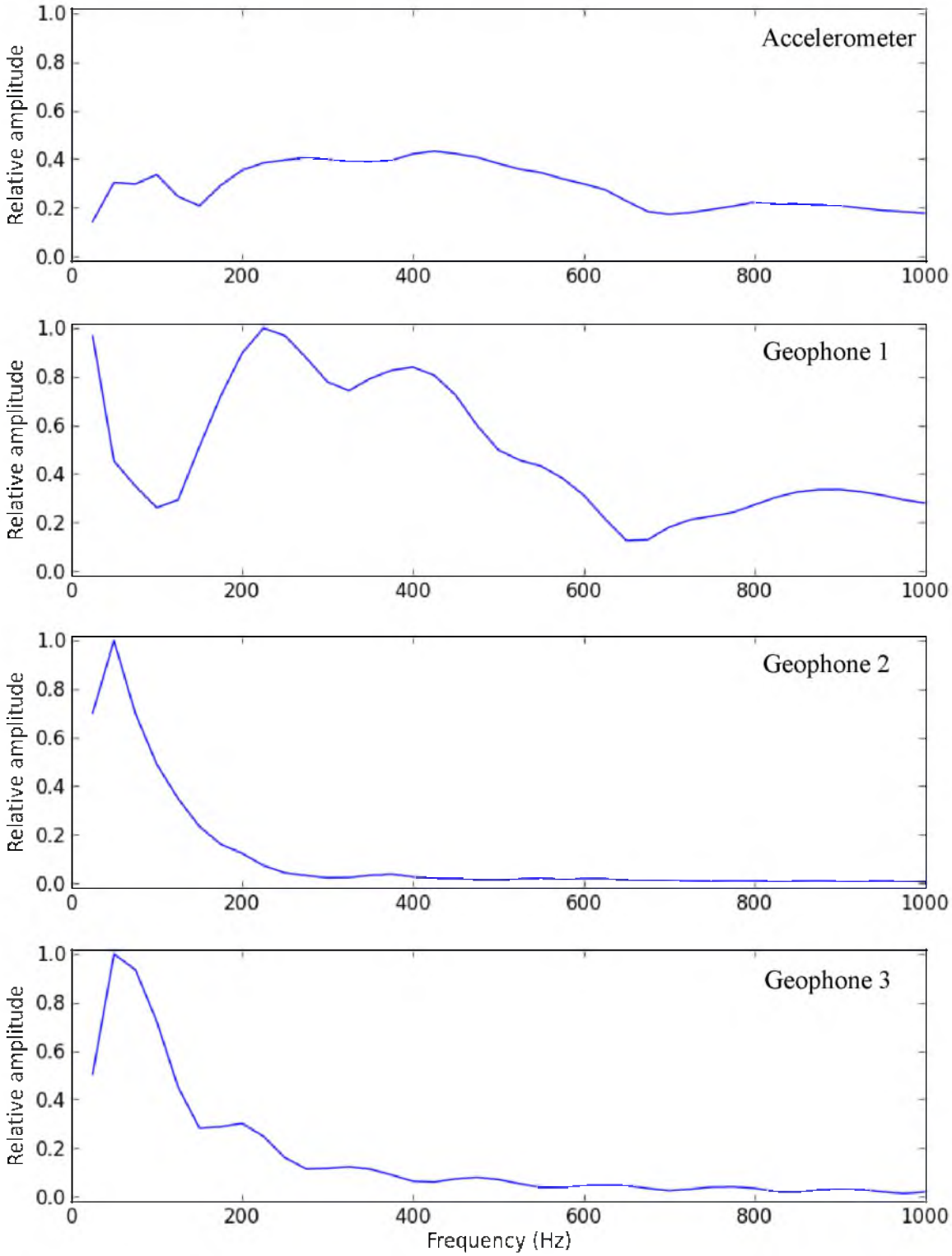

Figure 3.27 Frequency spectrum for downhole vibration transducers

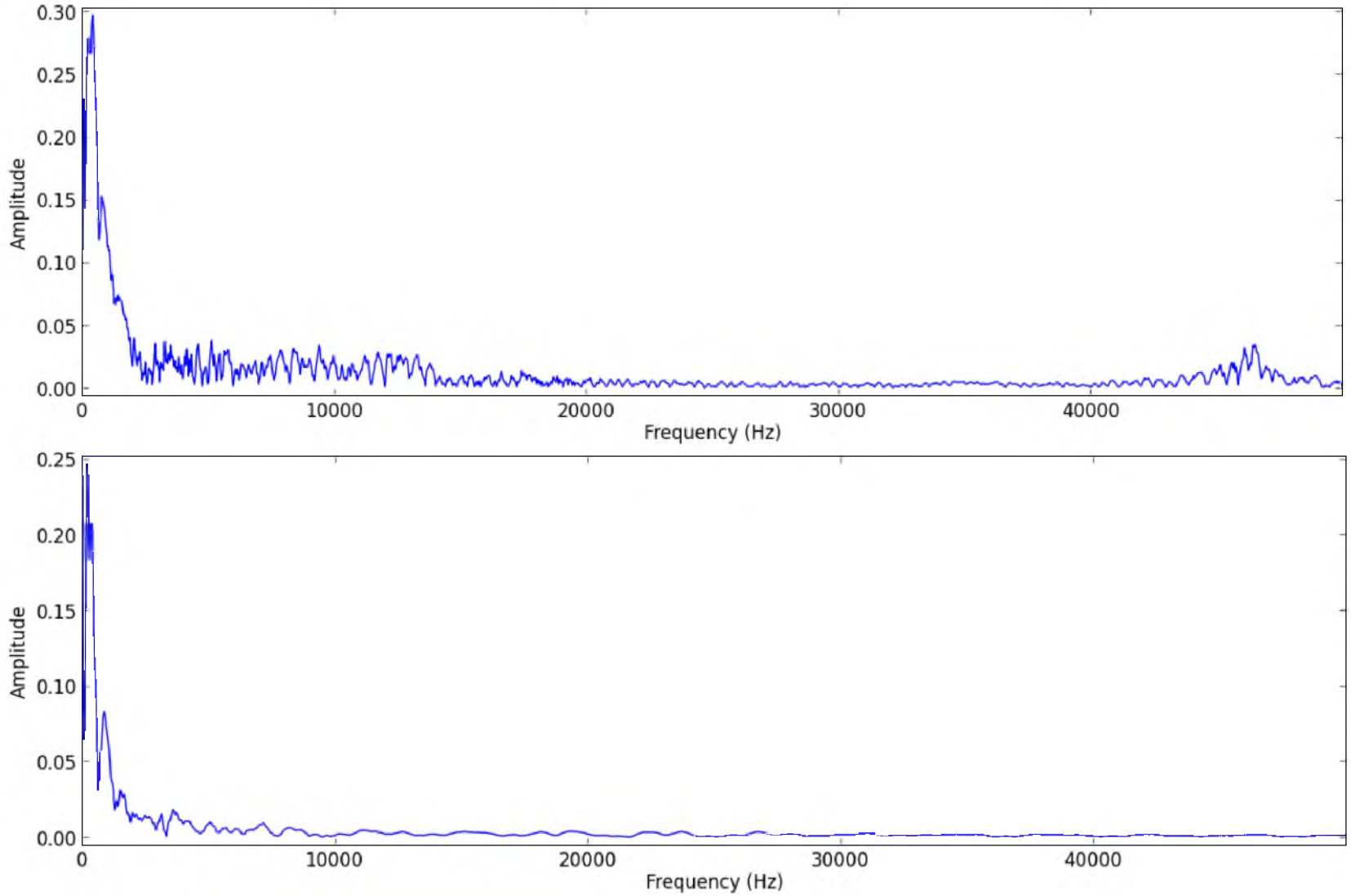

Figure 3.28 Frequency spectra for accelerometer (top) and geophone 1 (bottom)

The vibration history recorded by the Instantel Minimate Plus barely clipped on the longitudinal axis of motion, and thus the PPV at its location was measured to be 254 mm/s (10.0 in./s). For completeness, the initial portions of the vibration records for all three seismographs are displayed below in Figures 3.29, 3.30, and 3.31.

3.3.2 TDR results

TDR measurements of the downhole twisted wire pairs were able to detect movement of the rock around the blasthole. The thinner 28-AWG magnet wire proved to be more sensitive and was considered more useful than the 24-AWG wire. Because of the poor resolution of the TDR, it was difficult to ascertain the exact depth for each event detected. The best that could be determined was whether the damage occurred in the top, middle, or bottom third of the blasthole. Only one wire, the 28-AWG wire in instrument hole 1 closest to the blast, sheared completely near the top of the hole. The 24-AWG wire in the same hole appeared stretched along the length of the hole, indicating damage along the entire length of the hole. In instrument hole 2, the 28-AWG wire detected shifting of the rock in the top and middle sections of the blasthole. The 24-AWG wire in the same hole did not change. In instrument hole 3, virtually no permanent rock displacement was measured. Table 3.9 lists the TDR-measured lengths of each wire before and after the blast using a V_p value of 73%. Figure 3.32 shows digitized versions of the impedance signals measured with the TDR. The precision of the TDR readings obtained by the screen cursor with the stated V_p was ±0.9 m (3 ft).

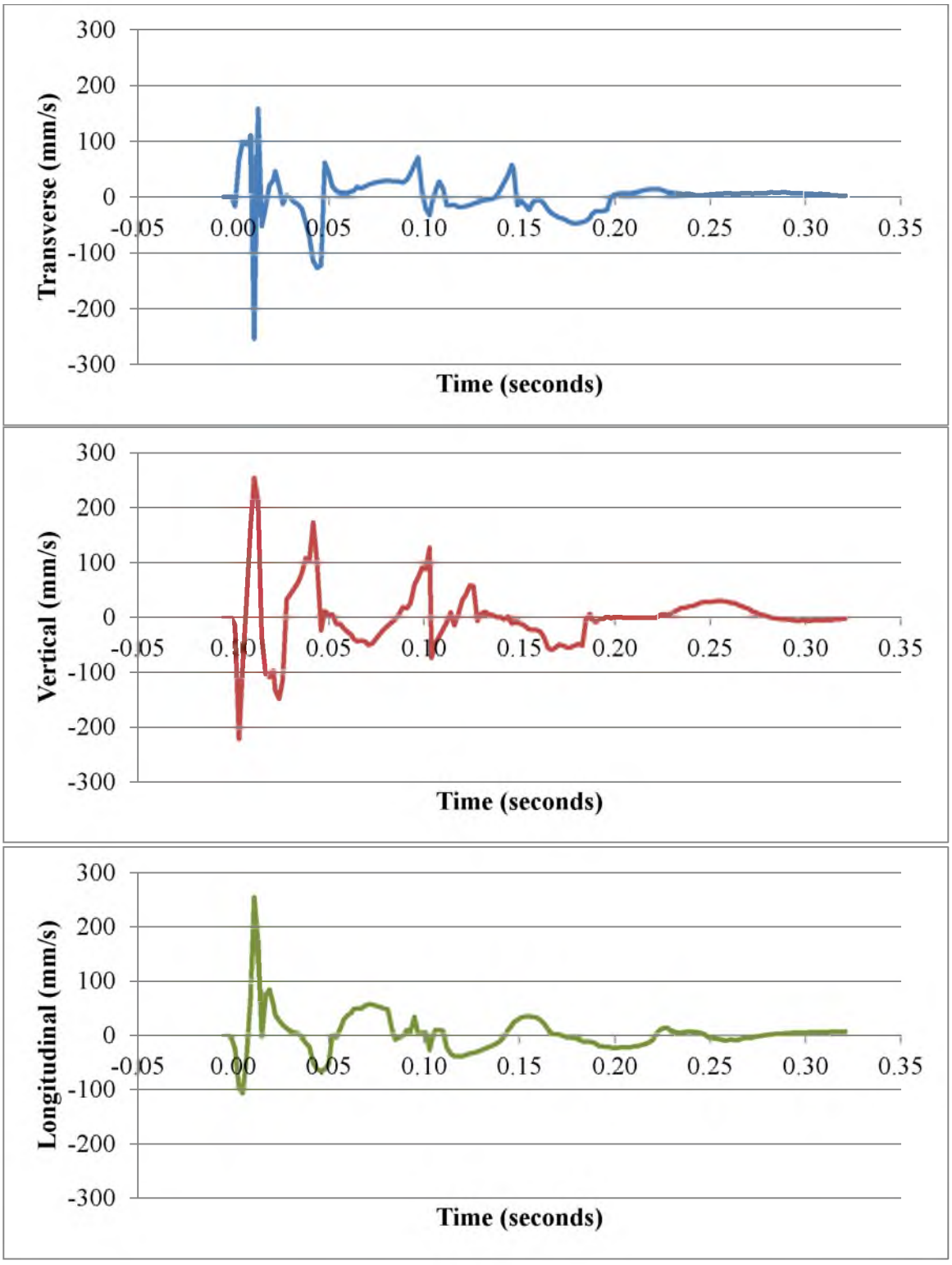

Figure 3.29 Vibration record for seismograph 1 – Instantel DS-200 closest to blasthole

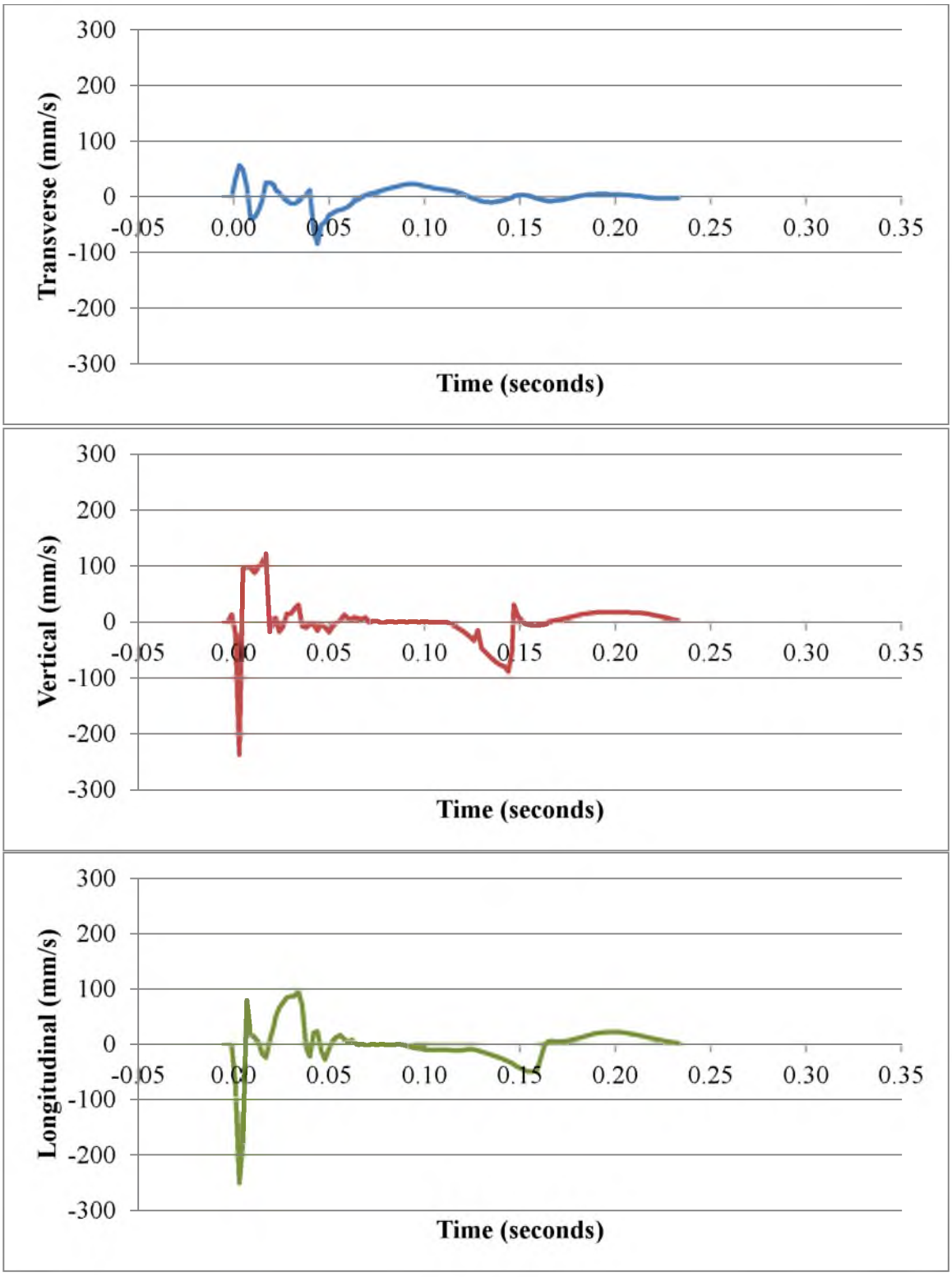

Figure 3.30 Vibration record for seismograph 2 – Instantel DS-200 near instrument hole 3

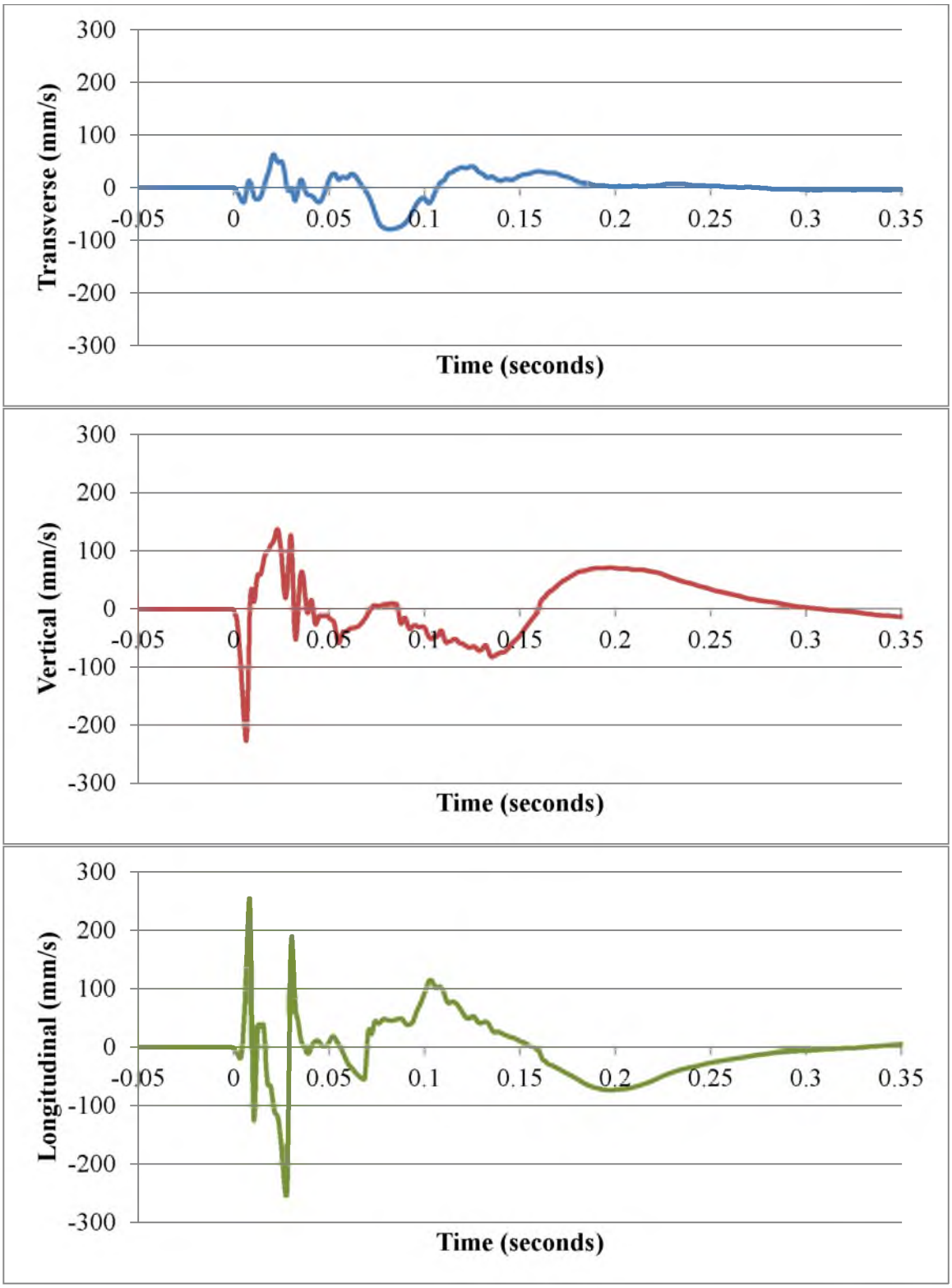

Figure 3.31 Vibration record for seismograph 3 – Instantel Minimate Plus

Table 3.9 TDR measurements before and after the blast

Hole	SW length		MW length		MW AWG	TDR interpretation
	m	ft	m	ft		
1	18.3	60.0	5.5	18.0	24	Stretching; possible break near bottom of hole
1	18.3	60.0	2.9	9.5	28	Break near top of hole
2	18.3	60.0	5.5	18.0	24	No change
2	18.3	60.0	5.5	18.0	28	Stretching; possible break near middle of hole
3	18.3	60.0	5.5	18.0	24	No change
3	18.3	60.0	5.5	18.0	28	No change

SW – Two-conductor shot wire; MW – Twisted magnet wire

3.3.3 Borescope observations

The light color of the grout made the fractures easy to see with the borescope. Even hairline cracks were discernible. An obstruction was present at a depth of about 1.13 m (3.7 ft) in instrument hole 1 that prevented further observations. The likely reason is that the acrylic tube sheared, a conclusion supported by TDR readings for that hole. Fractures were observed the entire length of instrument hole 2. Instrument hole 3 only had a few small fractures.

Unfortunately, a suitable camera was not available for photographing the image through the borescope eyepiece. A diagram of the fracture distribution is available in Figure 3.33. A subjective scale was used to rate the cracks according to thickness ranging from the largest at around 6 mm (1/4 in.) to hairline. Table 3.10 lists the field observations used in Figure 3.33.

A few notes concerning this method of observing blast damage are made here. First of all, no preblast survey was conducted because of time constraints. The possibility does exist that small volumetric changes in the cement as it cured could induce

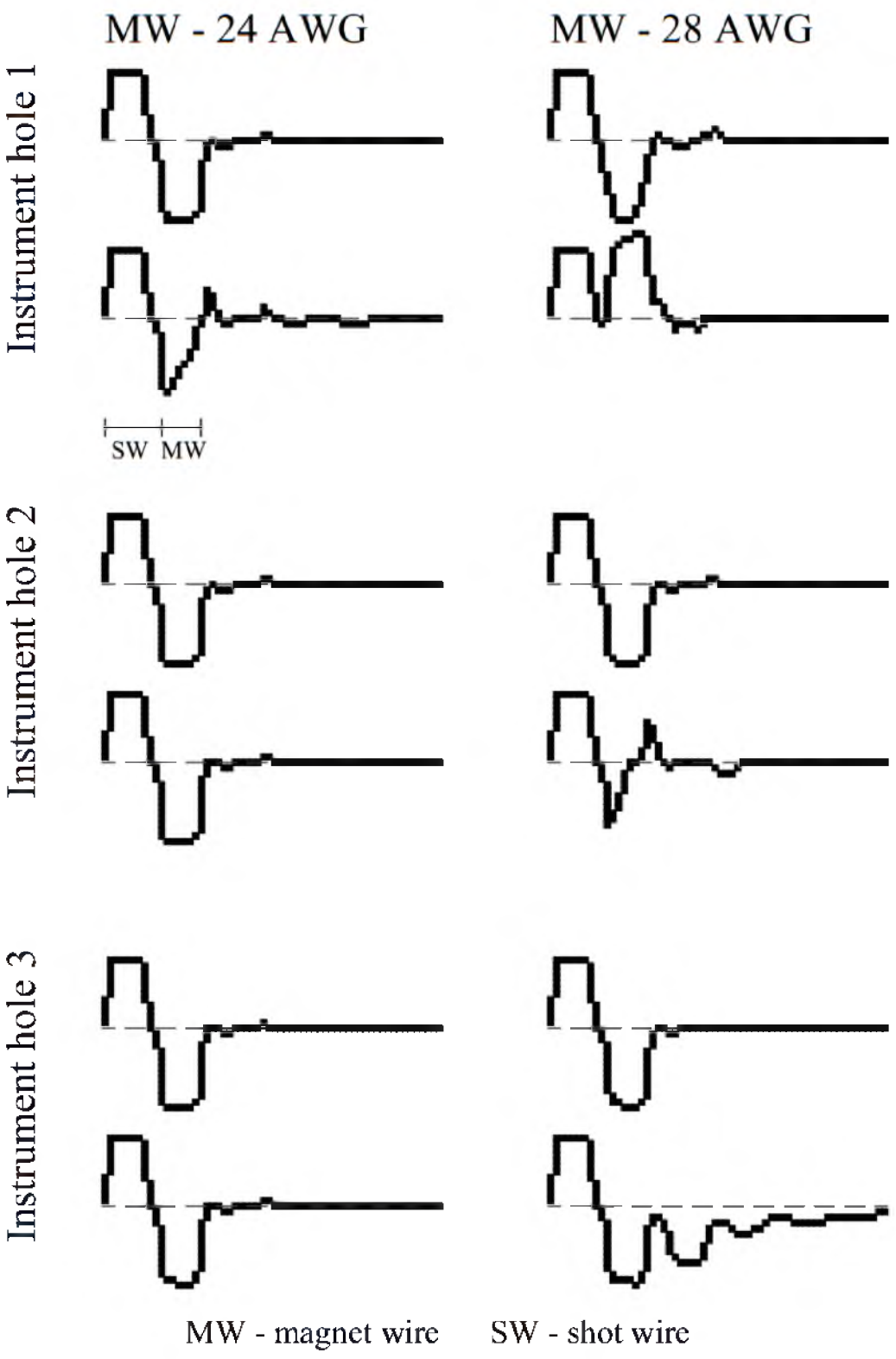

Figure 3.32 Digitized TDR signatures

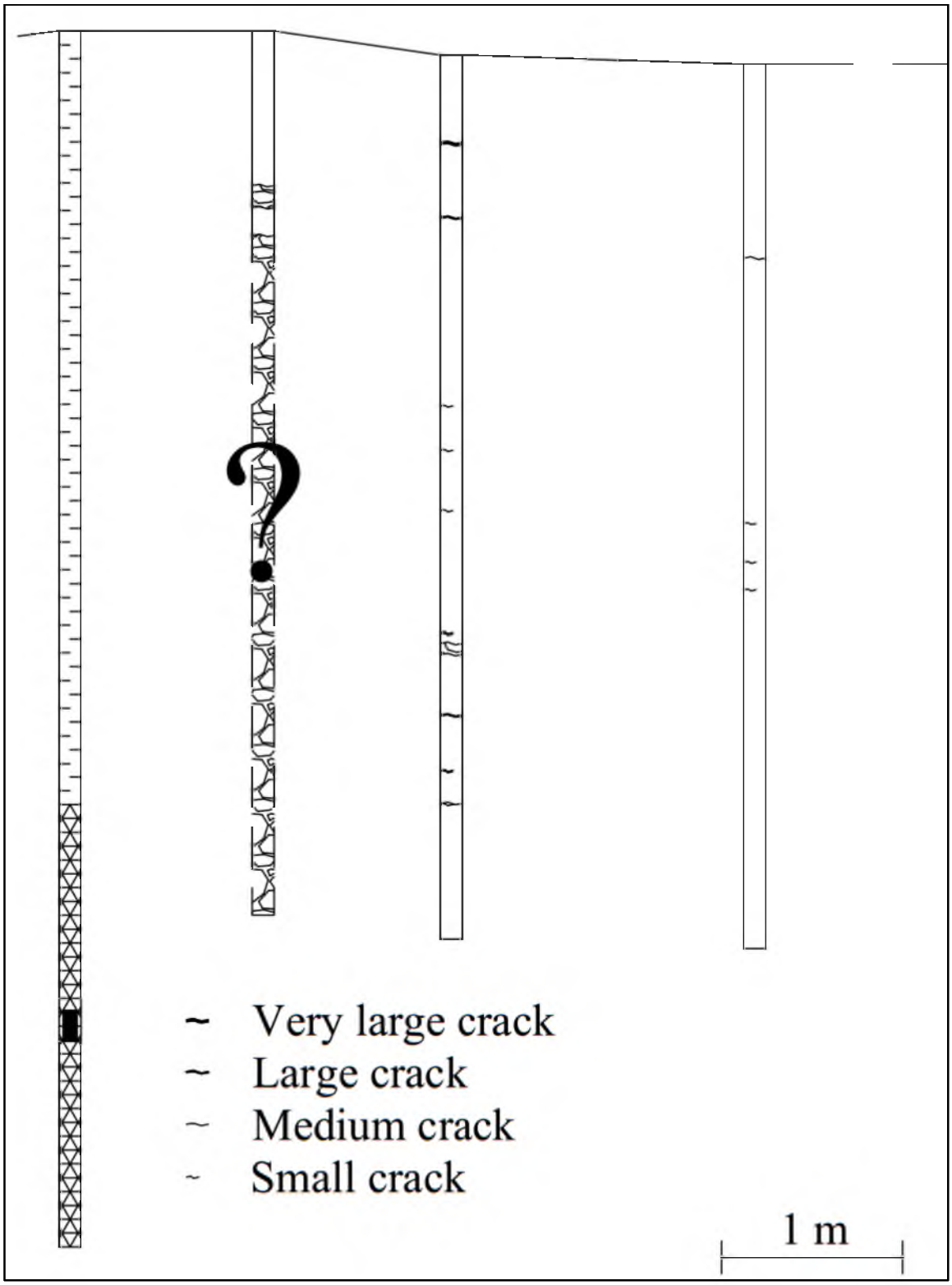

Figure 3.33 Fracture distribution observed with borescope

Table 3.10 Field notes of crack observations

Hole	Depth below collar		Notes
	Meters	Feet	
1	0.85	2.20	Start of fracture zone
1	0.98	2.80	End of fracture zone
1	1.13	3.20	Shearing of tube
2	0.61	3.70	Very large crack
2	1.02	2.00	Large crack
2	2.06	3.35	Small crack
2	2.30	6.75	Small crack
2	2.64	7.55	Small crack
2	3.31	8.65	Two small cracks
2	3.37	10.85	Start of fracture zone/large cracks
2	3.43	11.05	End of fracture zone/large cracks
2	3.76	11.25	Large crack
2	4.07	12.35	Two small cracks
2	4.13	13.35	Medium crack + small crack
2	4.16	13.55	Small crack
3	0.89	13.65	Medium crack
3	1.07	2.91	Small crack
3	2.53	3.51	Small crack
3	2.75	8.31	Very small crack

cracking. However, Hydro-Stone™ has a maximum setting expansion of only 0.24%. The pattern of fractures observed does not suggest any cracking in the grout from volumetric changes. Thus the likelihood of cracking during the setting phase is unlikely.

It is possible that the stress wave may have induced fractures in the cement itself. The HydroStone™ datasheet did not list material properties other than compressive strength. However, the HydroStone™ does not appear as brittle or stiff as the rhyolite and as such would be less prone to tensile fracture. The movement of joint sets or preexisting fractures at the test site could also cause cracking in the cement, possibly even at a

distance beyond the limit of tensile fracturing in the rhyolite. No data was available, though, on joint set distribution, so this possibility could not be verified.

Yang et al. (1993) pointed out that observation holes in the near field filled with grout could cause impedance mismatches for wave propagation if the rock and cement possess different properties. This consideration was not made for the field experiment, so its potential effect on the data collected are not known. An interesting exercise would be to conduct a numerical simulation of this problem and analyze the results. That is beyond the scope of this work, however.

3.3.4 Visual observations

Cracks appeared in the ground surface opposite the instrument holes. The ground was sloped downwards on this particular side, possibly making it a more favorable pathway for high-pressure gases to escape in addition to reflection of surface waves. Figure 3.34 is a photo taken of the cracks.

3.3.5 Summary of results

The borescope provided the best means by which to determine damage in the rock surrounding the explosive charge. Fracturing of the rock was observed up to 3.78 m (12.4 ft) from the blasthole. Significant fracturing was observed within 2.10 m (6.9 ft) of the blasthole. The necessary setup to employ this method is relatively inexpensive and easy to apply in the field. The only expensive component is the borescope itself, which must be equipped with a built-in light source.

Measurements taken using time-domain reflectometry seem to corroborate observations with the borescope. However, the TDR measurements in themselves lack

Figure 3.34 Surface cracks after the blast

precision and can be difficult to correctly interpret. Calibration of the TDR settings to the thin wire seems to be preferable for greater sensitivity. The necessary setup to employ time-domain reflectometry is the most inexpensive method used and is also easy to apply in the field. A graphical TDR meter can be obtained starting at $750.

Correlation of the PPV with TDR measurements and fracture observation using a borescope indicate that vibration amplitudes of around 1,490 mm/s (58.5 in./s) can cause moderate to extensive damage in rhyolite (a fairly sound rock) with some preexisting structures and joint sets. Minor fracturing was present at approximately 310 mm/s (12.2 in./s), although the cracks observed were at least a couple of meters above the vibration transducers in instrument hole 3. These may be the effect of wave reflection from the free face, or dilation of joints and/or preexisting structures rather than tensile failure of the rock itself.

The extent of damage in the rock mass was between 2.10 m (6.9 ft) and 3.78 m (12.4 ft), with PPV in the region attenuating from 1,490 mm/s (58.5 in./s) to 310 mm/s (12.2 in./s) in-line with the elevation of the explosive column. The measured PPV is based on dilatational wave motion. Measurement of shear wave motion would require triaxial vibration transducers to record transverse and vertical movement in addition to longitudinal.

4. DAMAGE PREDICTION

Three methods were chosen for predicting the extent of damage from the blasthole in the previous section. The purpose was two-fold: (1) to compare the prediction models against each other and (2) to evaluate how well each model compares to the field data. The three approaches selected were

- A modified Holmberg–Persson approach developed by Smith (2003),
- The shock wave transfer (SWT) model developed by Sun (2013), and
- Numerical simulation using ANSYS Autodyn™.

4.1 Rhyolite properties

In order to employ predictive models, mechanical properties of the rhyolite rock were needed. A suite of rock mechanics tests were conducted on a sample of rhyolite obtained from the test site. Table 4.1 lists the results of the testing program. Details of the tests are provided in Appendix E.

4.2 Modified Holmberg–Persson approach

Smith (2003) took the least squares method (LSM) approach presented in Section B.4.3 for the scaled distance method and adapted it for the Holmberg–Persson (HP) model. The goal is to minimize the sum of the residuals squared SRS between measured and predicted vibrations. Mathematically, this is expressed as

Table 4.1 Properties of rhyolite from the field test site

Property	Metric	Imperial
Density	2.56 g/cm^3	160 lb/ft^3
Unconfined uniaxial compressive strength	222.3 MPa	32236 psi
Tensile strength	11.3 MPa	1638 psi
Shear strength*	47.7 MPa	6916 psi
Young's modulus	36.6 GPa	5311 ksi
Dynamic Young's modulus*	47.1 GPa	6836 ksi
Poisson's ratio	0.27	
Dynamic Poisson's ratio*	0.23	
Moh–-Coulomb friction angle*	65 °	
Confined Mohr–Coulomb friction angle	53 °	
Mohr–Coulomb cohesion*	25.1 MPa	3634 psi
Confined Mohr–Coulomb cohesion	36.6 MPa	5315 psi
P-wave velocity	4606 m/s	15111 ft/s
S-wave velocity	2739 m/s	8988 ft/s
Porosity	0.0238	
Dynamic unconfined compressive strength	301.6 MPa	43740 psi
- Dynamic increase factor	1.4	
- Average load strain rate	285 s^{-1}	
Dynamic tensile strength	40.6 MPa	5894 psi
- Dynamic increase factor	3.6	
- Average load strain rate	349 s^{-1}	

* Calculated from other parameters

$$SRS_{j,f} = \sum_{i=0}^{i=n} [PPVactual_i - PPVpredict_i]^2 \quad (4.1)$$

where

$SRS_{j,f}$ is the sum of the residuals squared for the k_j term in the HP formulation,

k_j ranges from k_{min} to k_{max},

$PPVactual_i$ is the measured PPV at position i,

$PPVpredict_i$ is the PPV at position i as predicted by the Holmberg–Persson formulation, and

f is an index ranging from α_{min} to α_{max} used to calculate $PPVpredict_i$.

The Holmberg–Persson formulation is given as

$$PPVpredict_i = k_j \sum_{T}^{H} \left(\frac{qdZ}{[r_0^2 + (z - z_0)^2]^{\beta_f/2\alpha_f}} \right)^{\alpha} = k_j(Summation\ Term) \quad (4.2)$$

where

q is the loading density of the explosive per unit length,

H is the depth to the bottom of the explosive column,

T is the depth to the top of the explosive column,

dZ is an incremental charge length, evaluated from T to H,

(r_0, z_0) are the coordinates of the point in space under consideration, and

k, β, and α are the site specific constants as given in Equation B.32 in Appendix B.

A scaling law for α/β needs to be defined; thus, β_f automatically adjusts based on α_f.

Differentiating Equation 4.1 with respect to k_j and setting $dSRS/dk$ equal to zero, the same derivation presented in Equations B.35 and B.36 can be performed. The end result is that an optimum k_j can be found for each α_f using the formula

$$k_j = \frac{PPVactual_1 + PPVactual_2 + \cdots}{(Summation\ Term)_1 + (Summation\ Term)_2 + \cdots} \tag{4.3}$$

The incremental charge length dZ is determined using a "just-touching" sphere model, originally developed by Hustrulid (1999) and incorporated by Smith (2003) into the modified HP approach. As displayed in Figure 4.1, a cylindrical segment of the column can be replaced by a sphere of equal volume so that the ends of the spheres are barely touching. The effects of each sphere are then numerically summed in the HP model. Since the HP model is a radial vibration model that does not distinguish between dilatational and shear wave motion, approximating the individual energy sources as spheres is a reasonable assumption. For a cylindrical column segment with diameter d, the necessary height $dZ$for both the cylinder and sphere is

$$\frac{4}{3}\pi\left(\frac{dZ}{2}\right)^3 = \pi b\left(\frac{d}{2}\right)^2 \tag{4.4}$$

$$dZ = \sqrt{3/2}d = 1.2247d \tag{4.5}$$

A script was written in Python to calculate the least squares fit to a set of vibration data and plot results from the modified HP model. The code is available in Appendix F. Data from the field test as listed in Table 4.2 were entered into the program. Constants for two of the most widely-used scaling laws were compared: α/β = 1/2 and α/β = 1/3. The

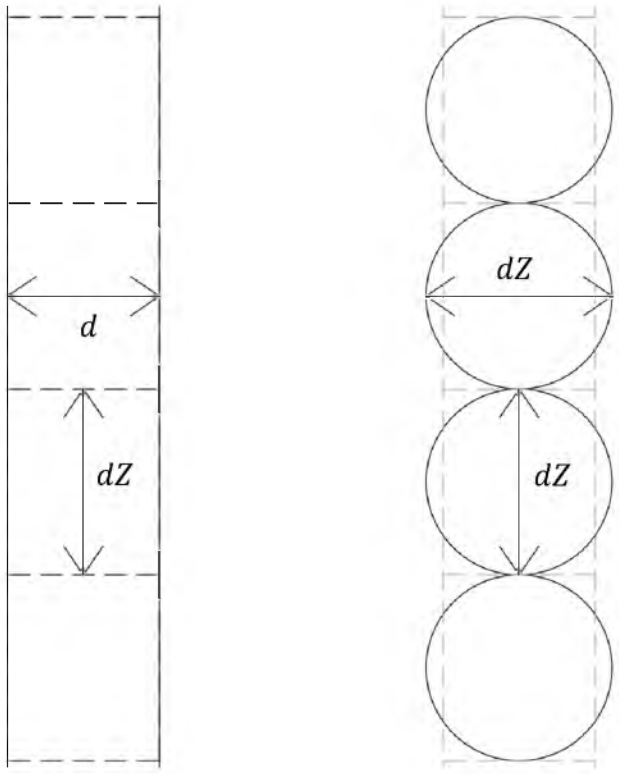

Figure 4.1 Just-touching sphere model for dividing the explosive column into increments

Table 4.2 PPV data used in the modified HP model

Sensor	R (m)	Z (m)	PPV (mm/s)
Accelerometer	2.41	4.85	1527
Geophone 1	2.41	4.94	1438
Geophone 2	4.08	4.91	287
Geophone 3	4.08	4.97	333
Instantel MinimatePlus	6.86	0.00	254

constants and SRS for each approach are presented in Table 4.3. For the given data set, the SRS from each scaling law are virtually identical (slight differences are discernible only beyond 0.1 mm^2/s^2). Cubed root scaled distance was used for the remainder of this analysis, since it is considered to be a better estimator of PPV at closer distances.

Vibration limits for tensile damage were determined by rearranging Equation 2.3 as presented in Section 2.1.1.1 into Equation 4.6:

$$PPV = \frac{\sigma_t c_P}{E} \tag{4.6}$$

where σ_t, c_P and E are the tensile strength, Young's modulus, and P-wave velocity of the rhyolite as given in Table 4.1. Depending on whether static or dynamic properties are used, the damage limits are 1,421 mm/s (55.9 in./s) and 3,971 mm/s (156.4 in./s). Figures 4.2 and 4.3 show vibration contours and damage limits generated by the HP model using both static and dynamic material properties. The maximum radial extent for each damage zone is 2.5 m (8.2 ft) and 1.7 m (5.6 ft) for the static and dynamic cases, respectively.

Measured and predicted PPV using the HP approach are compared in Table 4.4. Since both the square root and cubed root scaling laws returned identical results, only the set of values for cubed root scaling are shown. Figure 4.4 displays the data in Table 4.4,

Table 4.3 HP scaled distance constants from field data

Constant	Scaling law			
	α/β=1/2		α/β=1/3	
	mm/s	in./s	mm/s	in./s
α	1.387	1.387	0.924	0.924
k	746.93	264.79	870.88	445.06
SRS	64006	99.21	64006	99.21

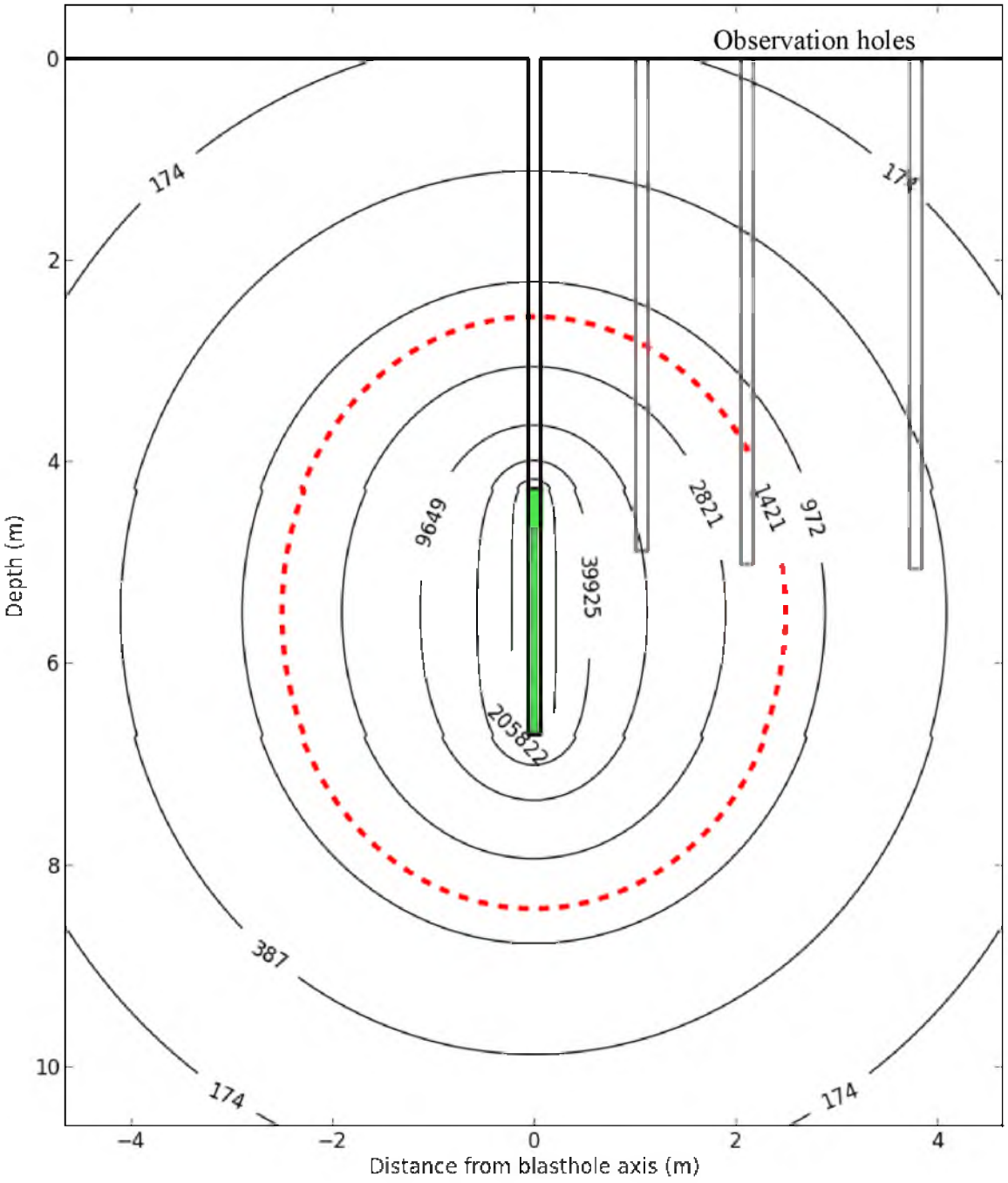

Figure 4.2 HP vibration contours (mm/s) and damage limit using static properties

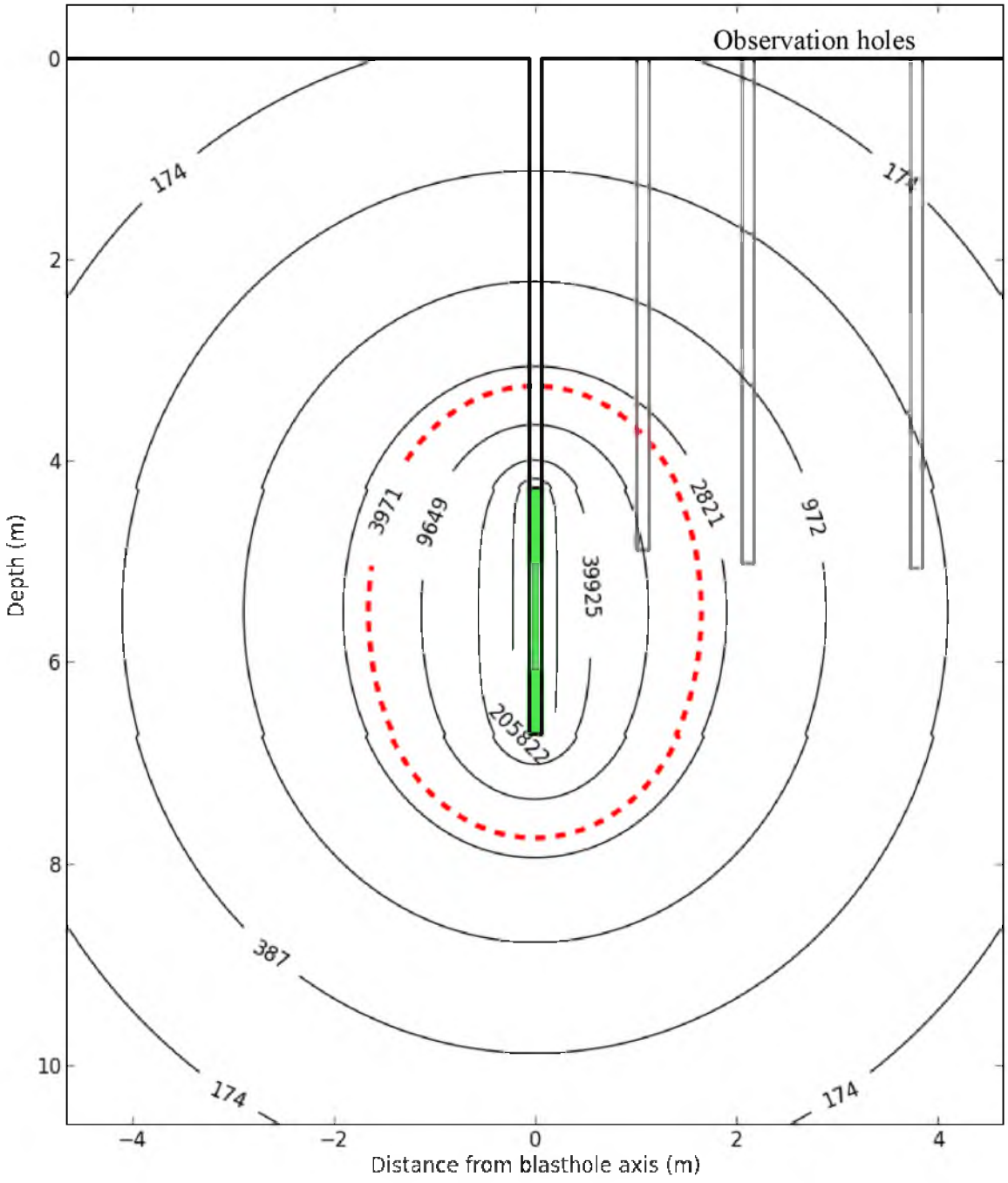

Figure 4.3 HP vibration contours (mm/s) and damage limit using dynamic properties

Table 4.4 Measured and predicted PPV using HP approach

Sensor	Measured PPV		Predicted PPV		Residuals	
	mm/s	in./s	mm/s	in./s	mm/s	in./s
Accelerometer	1527	60.1	1488	58.6	39	1.5
Geophone 1	1438	56.6	1530	60.2	-92	-3.6
Geophone 2	287	11.3	384	15.1	-97	-3.8
Geophone 3	333	13.1	386	15.2	-53	-2.1
Instantel MinimatePlus	254	10.0	50	2.0	204	8.0

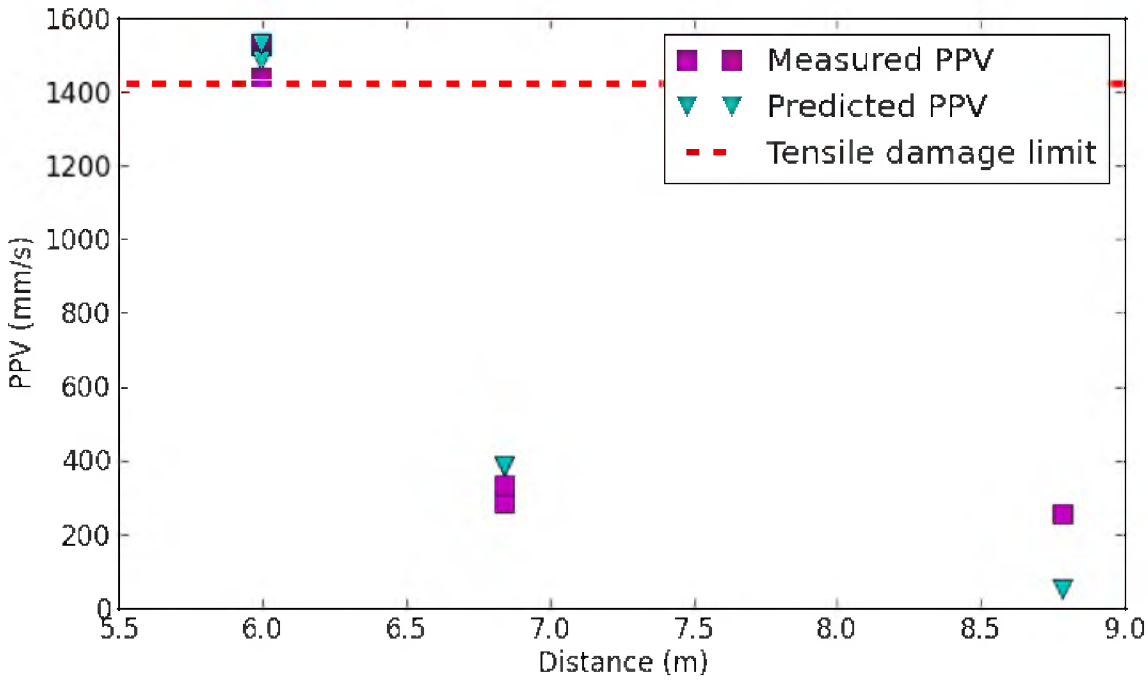

Figure 4.4 Plot of PPV versus distance; tensile damage limit based on static properties.

along with a tensile damage limit. Note that while measured and predicted PPV for the downhole vibration transducers are relatively close to each other, the predicted PPV for the Instantel Minimate Plus seismograph is only $1/5^{th}$ that of the measured PPV. Given that the Instantel was mounted on the surface, the discrepancy likely results from the HP model's inability to account for interaction of the stress wave with the surface.

4.3 Shock wave transfer model

The shock wave transfer (SWT) model developed by Sun (2013) was used to estimate the damage region around the blasthole from the field experiment. The SWT model incorporates shockwave mechanics to determine the transfer of shock from the explosive charge to the borehole wall. An assumption similar to the "just touching" sphere model employed in the modified HP prediction approach was incorporated into the SWT model for estimating the radial damage from a cylindrical charge column. The mathematical background of the model is rather lengthy and will not be presented here. An executable file was written by Sun in Visual Basic to perform the calculations.

The SWT program accepts both static and dynamic compressive and tensile rock strengths. If only static strength properties are entered, the program estimates their dynamic counterparts. Explosive properties used were obtained from a Dyno Nobel data sheet for DYNOMIX (Dyno Nobel n.d.). Figure 4.5 shows the data input and results output for the dynamic case. The damage limit for tensile failure is 2.6 m (8.4 ft) with only static strength properties entered and 1.9 m (6.3 ft) with dynamic strength properties included.

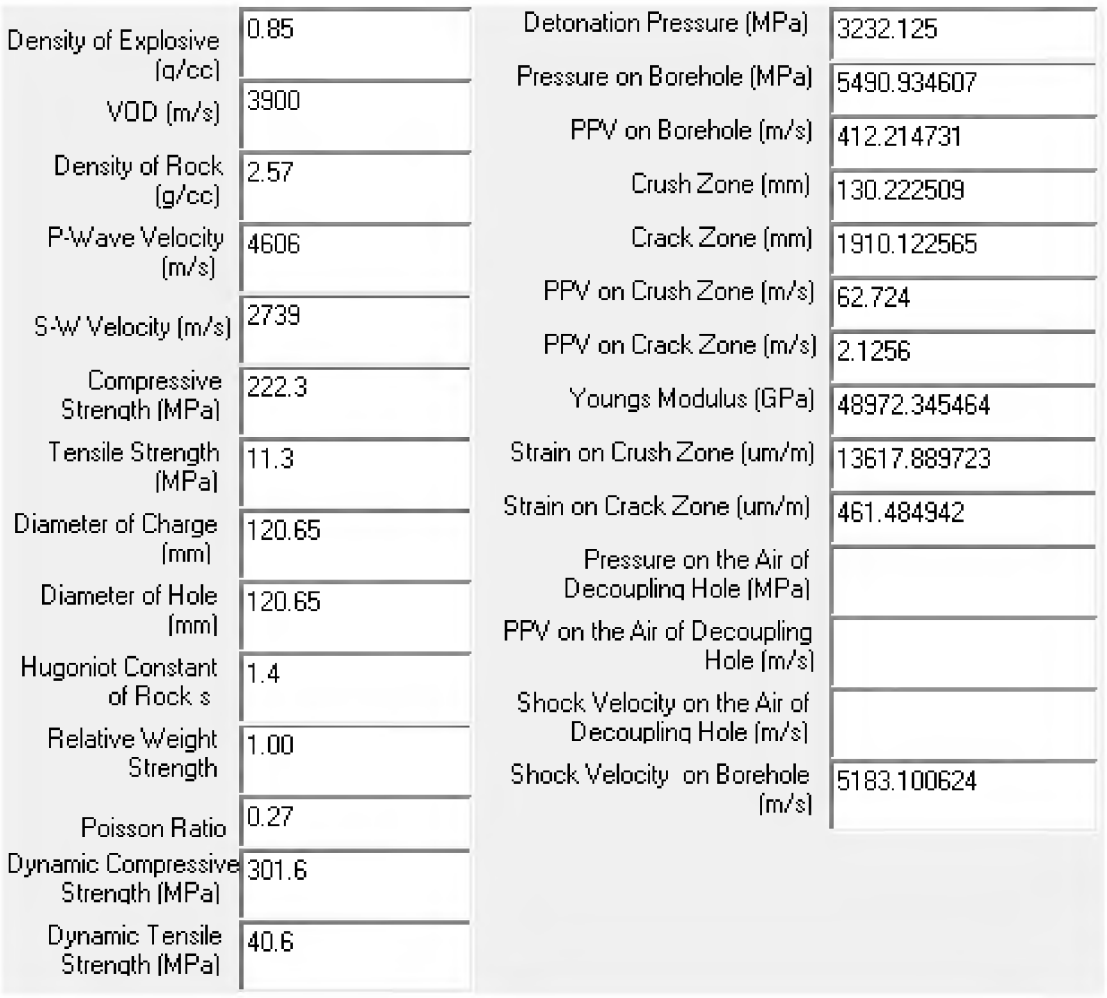

Figure 4.5 SWT program with input (left) and output (right)

4.4 Finite element modeling with Autodyn™

Autodyn™ v6.1, a dynamic finite element modeling and hydrocode software program, was used to model the extent of blast-induced damage. Autodyn™ is currently owned by ANSYS, but the version used was developed under Century Dynamics. The RHT constitutive model was employed for modeling the behavior of the rhyolite. The RHT model was developed by Riedel et al. (1999) for modeling failure in concrete. It employs the P-α equation of state developed by Herrmann (1969) to model compaction in porous materials. Failure can occur in either compression or tension, and accounts for

phenomenon such as strain hardening, damage accumulation, strain softening from damage, and porous collapse. Several published numerical investigations on rock blasting have employed the RHT model in Autodyn™ such as Katsabanis (2005), Park and Jeon (2010), Preece and Chung (2003), and Preece and Lownds (2008).

A two-dimensional axisymmetric model was created in Autodyn™ to simulate the blasthole employed in the field test, shown in Figure 4.6. The axis of symmetry runs through the center of blasthole. Two meshes with uniform element sizes were used: a Lagrangian mesh for the rhyolite and an Eulerian mesh for the ANFO, air, and stemming. The Lagrangian mesh was set at 12.80 m (42.0 ft) with 1,008 elements in the x-direction and 6.03 m (19.8 ft) with 500 elements in the y-direction. The Eulerian mesh was set at 14.33 m (47.0 ft) with 1,128 elements in the x-direction and 6.03 m (19.8 ft) with 500 elements in the y-direction. The additional 1.52 m (5.0 ft) above the surface was added to allow the gases and stemming to vent out of the blasthole. A total of 504,000 elements were contained in the Lagrangian mesh and 564,000 cells in the Eulerian mesh. The

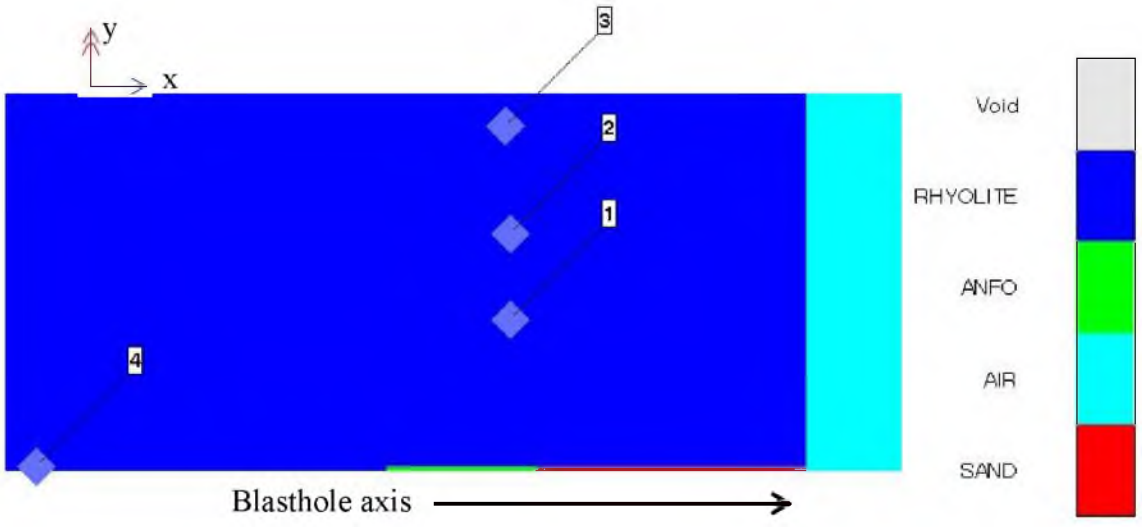

Figure 4.6 Autodyn model with gauge points displayed

individual element dimensions were 1.27 cm in the x-direction and 1.2065 cm in the y-direction. The dimension in the x-direction was selected to be a whole multiple of a foot and to avoid poor element shape factors in the conjunction with the y-dimension. The dimension in the y-direction was selected so that five elements would span the radius of the blasthole, a recommendation made by D.S. Preece (personal communication). The default units were set at cm, ms, and g.

For stemming, sand was selected to simulate drill cuttings. Void space was defined in the region outside the blasthole and beneath the surface. Interaction between the Lagrangian and Eulerian meshes was enabled. A transmitting boundary was defined at the sides and base of both meshes, and at the top of the Eulerian mesh. The point of detonation was specified at the midpoint of the ANFO column. Gauge points 1 and 2 were placed at the two locations where the downhole vibration transducers were secured in the field test. Gauge points 3 and 4 were placed at the edges of the model to check for any reflections from the transmitting boundaries.

4.4.1 Material properties

Autodyn™ possesses a library with properties, equations of state, constitutive models, and failure criteria for a wide variety of materials. For rhyolite, a concrete material labeled CONC140MPA was selected. Certain material parameters were modified to reflect the rhyolite properties measured during the rock mechanics testing program, as listed in Table 4.5. Shear modulus G was calculated from Young's modulus E and Poisson's ratio ν using the formula

Table 4.5 Modified RHT properties for rhyolite

Property	Value
Reference density	2.57000E+00 (g/cm3)
Porous density	2.56000E+00 (g/cm3)
Shear Modulus	1.44200E+05 (bar)
Compressive Strength (fc)	2.22300E+02 (bar)
Tensile Strength (ft/fc)	5.10000E-02 (none)
Shear Strength (fs/fc)	2.15000E-01 (none)

$$G = \frac{E}{2(1+\nu)} \tag{4.7}$$

Initially the experimentally-obtained compressive and tensile strengths were used. However, the damage zone generated around the blasthole was unrealistically small. Problems with the prediction of certain phenomenon of the RHT model have been encountered in the past (Tawardrous et al. 2013). Tawardrous et al. (2013) investigated some of the issues and developed workable solutions. However, these fixes were not available for the current modeling task. At the recommendation of D.S. Preece (personal communication), the compressive strength was reduced by a factor of 10. Since tensile and shear strengths are determined from the compressive strength, these values also decreased by a factor of 10.

For the P-α compaction model, no parameter adjustments were made. Efforts to change the bulk modulus and porous soundspeed to values calculated from measured rock properties resulted in error warnings from Autodyn™. The erosion strain, which is a variable that removes heavily-distorted elements and transfers their properties to adjacent elements, was set at 50%.

ANFO was selected from the Autodyn™ material library. The JWL equation of state, developed by Lee et al. (1968), was employed. The density was changed to 0.85 g/cm^3, and the density cut-off was set to a value of 1E-4 to avoid small timesteps as the gaseous products vented from the blasthole.

Sand was selected from the Autodyn™ material library. A porous compaction model was employed, in which the properties of sand are specified for a set of pressures. The erosion strain was set to 100%.

Air was modeled as an ideal gas using the Autodyn™ material library reference. When filling a region of the model with air, Autodyn requires that the internal energy be specified. The specific internal energy of air u_{air} was determined to be 2.163E+03 erg/g using the thermodynamic relationship $u_{air} = c_v T$, where c_v = 0.721 kJ/kg is the constant volume specific heat capacity of air, and the temperature T was chosen as 300 K (27° F).

For all of the materials, the maximum soundspeed cutoff was lowered to avoid small timesteps. The internal energy transport option was selected for Euler grid calculations to avoid Euler cell errors that occurred using total energy transport. Detailed material properties can be found in Appendix G.

4.4.2 Simulation results

The model took about six days for a 3.0 GHz 32-bit desktop to calculate the first 20 ms of simulation time. Since an older version of Autodyn™ was used, parallel processing capability was not supported. The progression of damage around the blasthole is shown in Figure 4.7. The RHT model employs a cumulative damage scale that ranges between 0.0 for intact rock and 1.0 for rock that has undergone total failure. Small regions of mild damage were observed at the boundaries below and to the sides of the

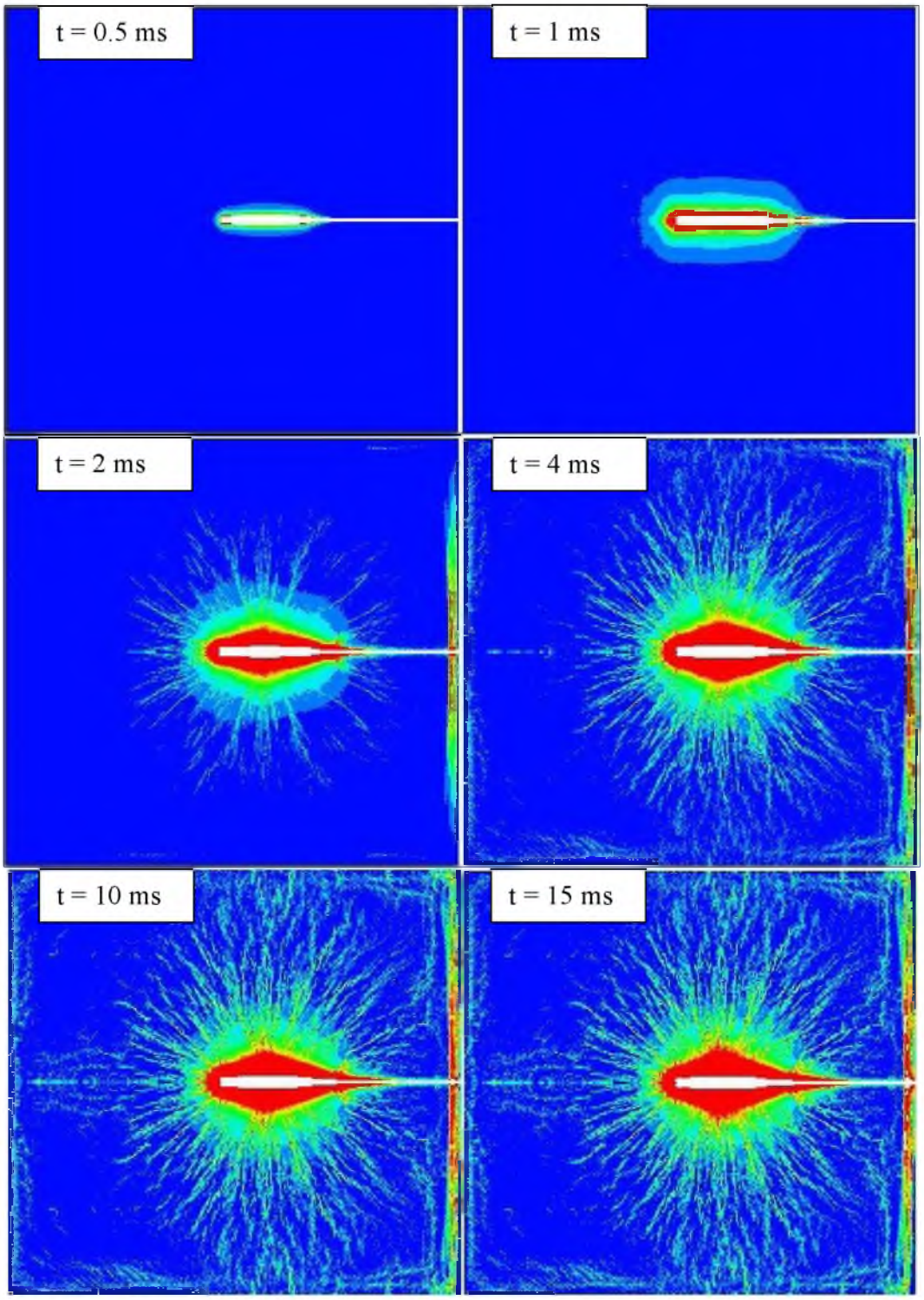

Figure 4.7 Progression of damage region; damage scale from blue = 0.0 to red = 1.0

blasthole. This is likely a boundary effect and is not representative of a realistic solution. Figure 4.8 displays the damage profile at 20 ms when the simulation was terminated and Figure 4.9 shows the material locations.

From the results of the Autodyn™ simulation, the regions of crushing and tensile fracturing are clearly visible. Also noticeable is the rupturing of ground at the surface as the stress waves reflect off the free face. This is comparable to the visible cracking observed next to the blasthole in the field experiments. The damage region appears to be well developed after only a few milliseconds. Additional damage afterwards is relatively minor.

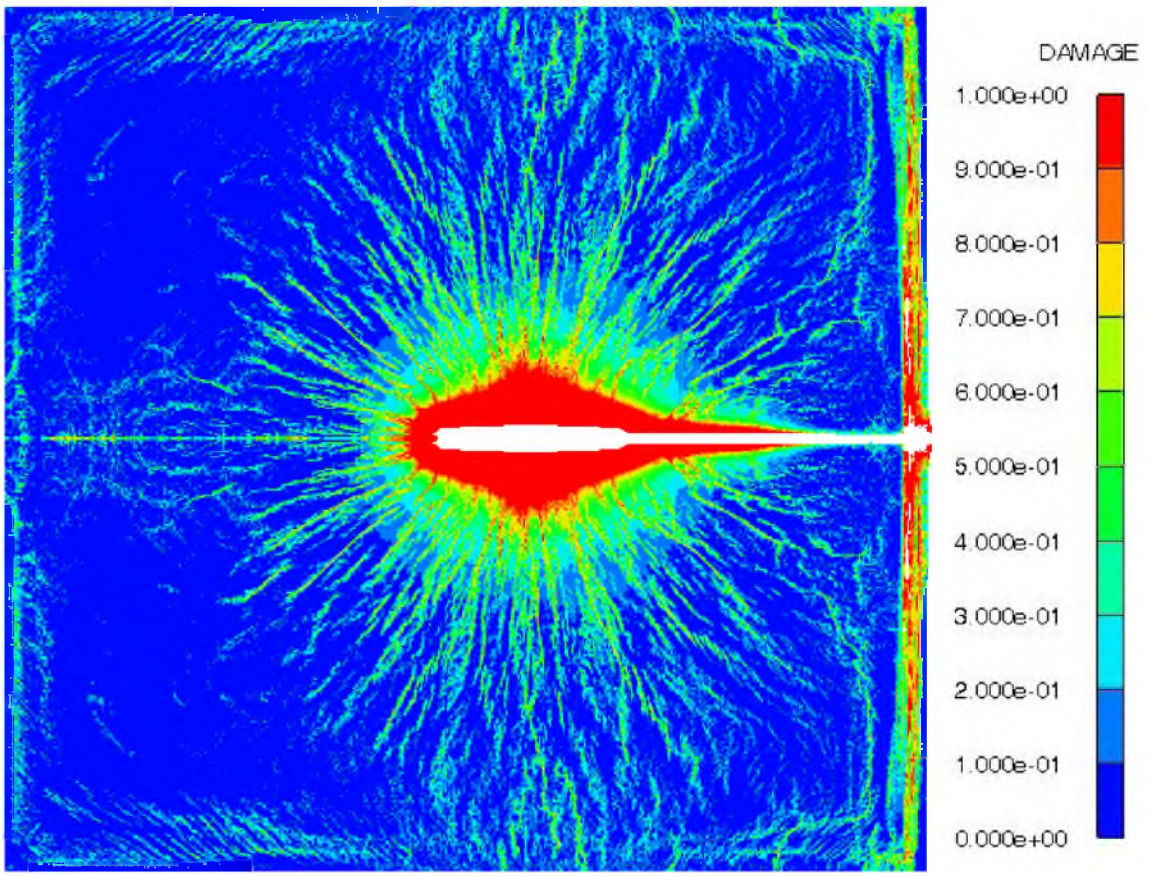

Figure 4.8 Damage profile at 20 ms

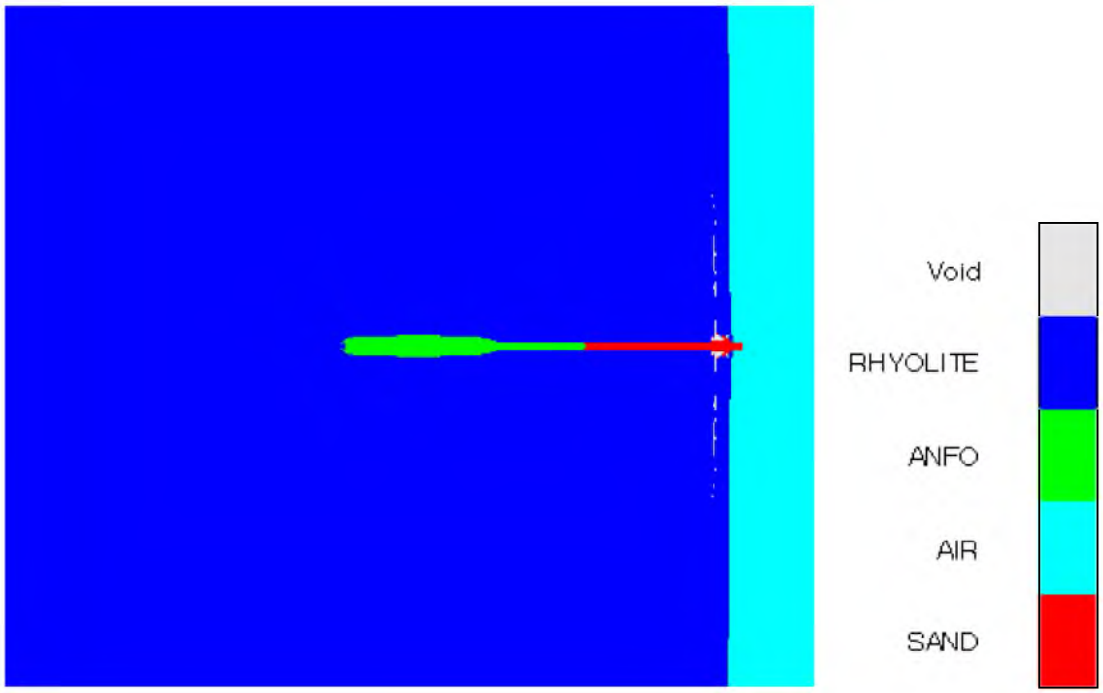

Figure 4.9 Material locations at 20 ms

The maximum extent of the red damage region in a radial direction, which is interpreted to indicate failure in compression, is 0.94 m (3.1 ft) in radius. The maximum extent of damage exceeding a value of 0.2, which was interpreted as radial cracking from failure in tension, is 5.2 m (17 ft) in diameter.

The vibration histories recorded at the gauge points show both dilatational and shear wave motion. This supports observations made by several individuals such as Heelan (1953) and Blair and Minchinton (1996) that shear waves are of primary origin from an explosive charge detonating in a solid medium. As an example, the simulation's x- and y-direction vibration histories for gauge 1 are shown in Figures 4.10 and 4.11, corresponding to the vertical and longitudinal components of motion, respectively.

A comparison was made between the PPV recorded from the field test, the original Autodyn^{TM} model that used the measured rock strengths, and the model that

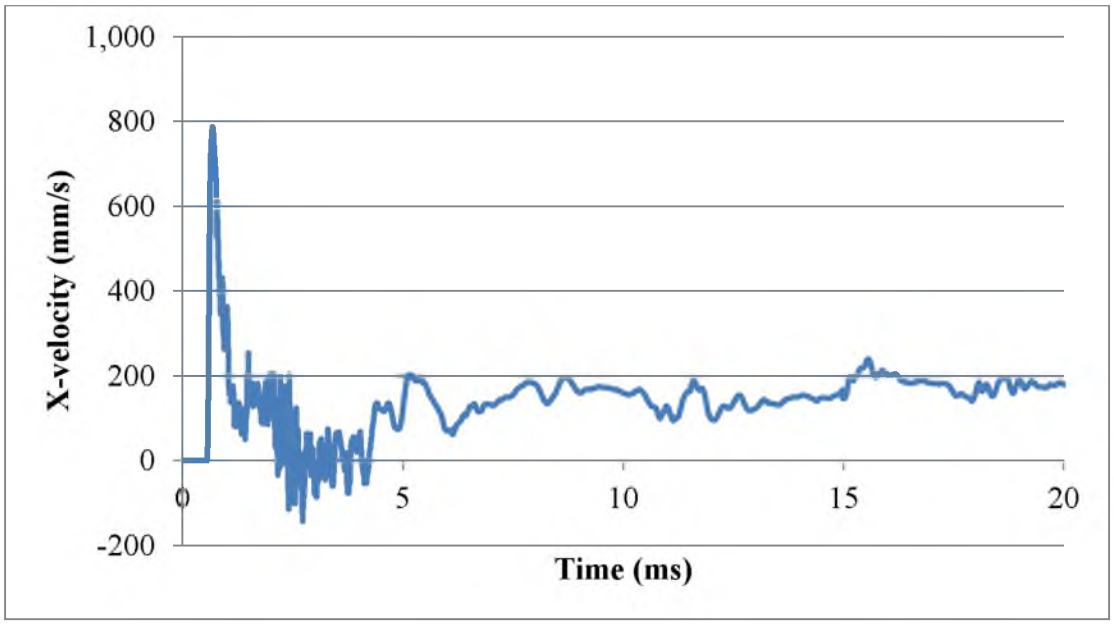

Figure 4.10 Vertical vibration history at gauge 1

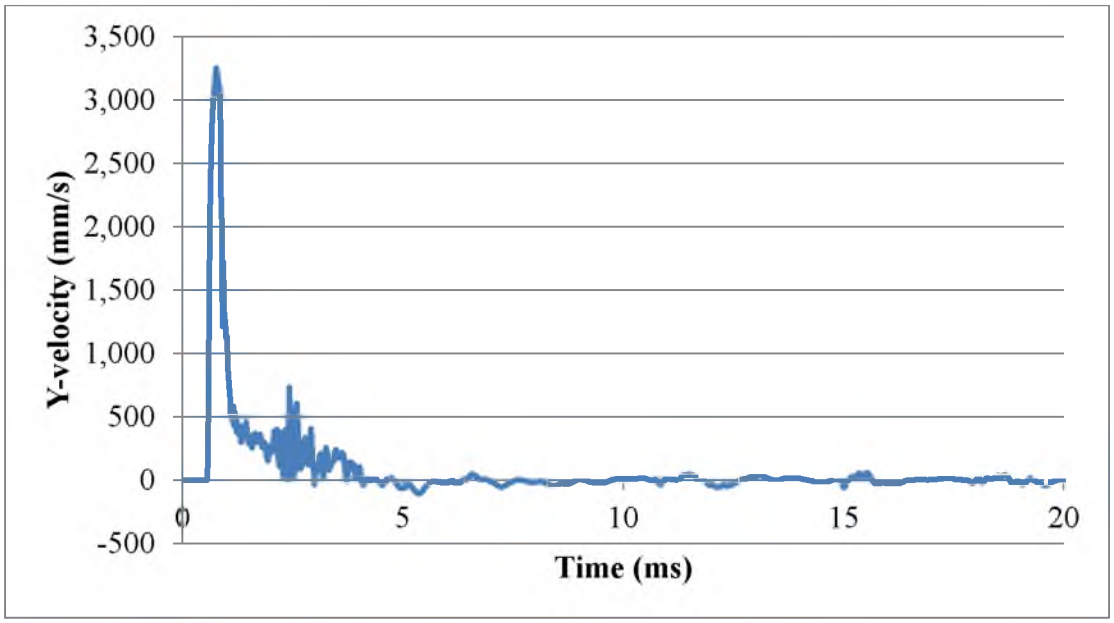

Figure 4.11 Longitudinal vibration history at gauge 1

scaled the rock strengths by a factor of 10. The results are presented in Tables 4.6 and 4.7. While reducing the strength properties seem to give a reasonable damage zone, the measured and simulated PPV differ significantly. Both Autodyn™ simulations significantly overestimate PPV. It appears that Autodyn's implementation of the RHT model cannot accurately account for near-field attenuation of ground vibrations.

4.5 Modeling summary

Table 4.8 compares the damage zone around the blasthole measured in the field with three prediction approaches. In this case, the damage zone is defined as the furthest point at which tensile failure in the rock can visibly occur. There is a significant amount of variability between results. Part of this stems from determining the appropriate material properties to use. Static and dynamic tensile strengths can give very different results.

The HP model reasonably predicts the tensile failure limit using static tensile strength, but underpredicts with dynamic tensile strength. The SWT model gives results that are for the most part within the vicinity of the field observations. The version of the SWT model that estimates dynamic rock properties from static properties provided the most accurate results. Reducing rock strengths in Autodyn™ by a factor of 10 may have been excessive. The finite element simulation predicted an area of cracking noticeably larger than was observed in the experiments. Some of this may be due to ambiguity in determining what threshold on the RHT model's damage scale constitutes tensile failure.

A refined model with rock strength properties reduced by a factor of 5–8 instead of 10 would probably give more realistic results. Refinement of the Autodyn™ model

Table 4.6 Measured and simulated longitudinal vibrations at the gauge 1 position

Source	Y-velocity	
	mm/s	in./s
Field experiment - Accelerometer	1527	60.1
Field experiment - Geophone 1	1438	56.6
Simulation with nominal rock strengths	2752	108.4
Simulation with rock strengths reduced to 1/10th	3250	128.0

Table 4.7 Measured and simulated longitudinal vibrations at the gauge 2 position

Source	Y-velocity	
	mm/s	in./s
Field experiment - Geophone 2	287	11.3
Field experiment - Geophone 3	333	13.1
Simulation with nominal rock strengths	1687	66.4
Simulation with rock strengths reduced to 1/10th	1867	73.5

Table 4.8 Comparison of damage zone estimates from field data and prediction models

Method	Radial extend of fracture zone			
	m		ft	
Material properties - static (S) or dynamic (D)	S	D	S	D
Field experiment	2.1–3.8		6.9–12.4	
Modified Holmberg–Persson model	2.5	1.7	8.2	5.6
Shock wave transfer model	2.6	1.9	8.4	6.3
Autodyn™ finite element model	5.2		17	

beyond the results shown here was considered outside the scope of this thesis and was therefore not undertaken.

5. CONCLUSIONS AND RECOMMENDATIONS

5.1 Conclusions

A field experiment was performed to determine the extent of damage surrounding a blasthole. A confined, cylindrical explosive charge was detonated in a body of competent rhyolite rock. Measurements were conducted using three types of instrumentation secured in nearby monitoring holes with grout. Near-field vibrations were measured with unidirectional vibration transducers. Fractures were observed with a borescope, lowered downhole through clear acrylic tubes that had previously been grouted in place. Thin, two-conductor, twisted wires were grouted downhole to detect shearing in the rock, and their continuity was measured with a time domain reflectometer (TDR).

Three methods were used to predict the extent of the damage zone around the blasthole: a modified Holmberg–Persson (HP) method developed by Smith (2003), a shock wave transfer (SWT) model developed by Sun (2013), and a dynamic finite element simulation using the commercial software program ANSYS Autodyn^{TM}. A comparison was made between each approach and the field data, with damage defined as the limit of tensile failure in the rock.

The following results and conclusions were found:

- Fracturing was observed downhole at radial distances up to 3.78 m (12.4 ft) from the blasthole. Moderate fracturing was observed 2.10 m (6.9 ft)

from the blasthole. Cracks were also visible on the ground surface adjacent to the blasthole.

- Vibration measurements show significant fracturing occurring in the rock mass at peak particle velocities (PPV) of 1,490 mm/s (58.5 in./s), but no cracks at PPV of 310 mm/s (12.2 in./s). The limit of radial cracking for the rhyolite lies between these two values. A tensile failure limit was estimated to be 1,421 mm/s (55.9 in./s) from the relationship $PPV = \sigma_t c_P / E$, where σ_t is the tensile strength (in this case the static tensile strength), c_P is the P-wave velocity, and E is Young's modulus of the rhyolite. This vibration level possibly occurred only a short distance beyond the monitoring hole 2.10 m (6.9 ft) from the blasthole.
- Cracks present in the grout surrounding the clear acrylic tubing were easily observed with the borescope. Even hairline cracks were distinguishable. A light-colored grout aided visibility.
- Rock displacement and shearing was detectable using a TDR and thin, two-conductor, twisted wires. Of the two wire gauges used (24- and 28-AWG), the 28-AWG wire was more sensitive to changes in the status of the grout and thus more useful as a damage indicator. Impedance profiles for each length of wire were difficult to interpret, however. Corroboration with fracture observations was needed to better interpret results. Limits in the resolution of the TDR instrument reduced the precision with which events could be located. The TDR appears capable of detecting moderate to significant damage, but not mild damage such as small fractures.

- The extent of the tensile failure damage limits estimated by each prediction method employed were within the general vicinity of the field observations, but varied widely. The modified HP model reasonably predicted the damage limit using static material properties, but underpredicted with dynamic material properties. The SWT method predicted a reasonable damage limit using dynamic strength properties estimated by the program from static strength properties. Entering dynamic strength properties of the rock directly into the SWT program slightly underpredicted the damage zone. The Autodyn™ finite element model overestimated the extent of the radial fracturing region. Strength properties in the model were reduced by a factor of 10, however, to obtain reasonable results with the RHT constitutive failure model. Calibration of the model would likely result in a better estimate of the damage limit.
- Of all the methods that have been developed for predicting backbreak, it is the author's opinion that numerical methods hold the greatest potential. Numerical models attempt to simulate the physics of the real world and thus can account for factors that most others cannot, such as as free faces, confinenment, and crack growth. Of the three damage prediction approaches included in this thesis, only the Autodyn™ simulation could simulate interaction between the stress wave and the ground surface. The HP and SWT models could not. The disadvantages in using numerical methods is that they are complex and require a software package to

implement. Good modeling practice and model calibration is necessary to obtain reasonable results.

5.2 Recommendations for further sturdy

Numerous field investigations have been conducted to determine the extent of blast-induced damage, including single-hole blasts (for instance, see Smith [2003] and Yang et al. [1993]). The field work conducted in this thesis provides a unique study of damage around a blasthole using three forms of measurements: near-field vibrations, a borehole fracture survey, and continuity testing with a TDR. To the author's knowledge, all three have never been used in conjunction with each other in the same experiment. In addition, a new method to visually observe blast-induced fractures was developed. The method can be easily implemented in the field at a low cost, although a borescope itself is an expensive instrument. Several methods for estimating the size of the damage zone around a blasthole were also applied and evaluated against the field measurements.

The research presented in this thesis brings to light several areas for additional study and investigation. The following list presents a set of recommendations for future research.

- To fully measure the motion of a rock body subject to blast loading, triaxial vibration transducers should be employed. Knowing all three components of vibrations can provide a better understanding of the modes of vibration and the relative energies of each wave type. Uniaxial vibration sensors were utilized in this study due to budgetary limitations. An interesting study would be to compare vibration-based damage prediction methods using a peak vector sum (PVS) of the three components of

motion. The author did not come across any near-field vibrations studies that explicitly used a PVS; peak particle velocity tends to be the common metric. A study using the PVS would require triaxial recording capability.

- Fracture surveying by grouting clear acrylic tubing down a monitoring hole and observing cracking in the grout with a borescope proved to be very successful. Ease of installation, relatively low cost, and clarity with which fractures can be distinguished makes this survey method an attractive and effective means to directly observe blast-induced damage. Future studies of backbreak, both research and operations-oriented, could employ this technique with a likely degree of success.
- The presence of a grout-filled hole adjacent to a blasthole could potentially cause coupling problems or an impedance mismatch between the grout and the surrounding rock. If so, the accuracy of measurements taken by instruments secured in the grout might suffer. Cracking could also occur in the grout itself but not in the adjacent rock. An area of investigation would be to study the effects of the high-frequency shockwave on a grout-filled hole in the vicinity of the explosive charge. Numerical simulations and laboratory tests would be ideal, since the testing conditions can be more easily controlled.
- No preblast fracture, fault, and joint-set mapping was performed for the the experiment in this thesis. While not deemed critical due to the competency of the rock outcrop at the test site, the possibility does exist that some cracks observed in the grout may have been caused by shifting

along discontinuities in the rock rather than tensile failure. Mapping such structures to correlate with postblast fracturing would require either a preblast fracture survey with a downhole-camera or drilling and retrieving core samples adjacent to the monitoring holes. Even then, attempts to find a plausible correlation between blast-induced fracturing in the grouted monitoring hole and shifting of the rock mass along preexisting structures may not yield much useful information. Nonetheless, an in-depth study to determine this particular aspect of the rock mass behavior on the grout may be worthwhile. A field experiment similar to the one performed in this thesis, instead conducted at a highly-fractured test site, may produce observable cracking well beyond the limit of tensile failure in the rock.

- Time domain reflectometry using thin, two-conductor wires as employed in this thesis may not be very informative nor useful for scientific research, but its ease of installation and low cost make it a candidate for incorporating into wall control studies at an active mining operation. Moderate to significant damage can be detected behind a blast pattern. Measurements with a TDR require little to no postprocessing, making it useable by the average mine worker.
- Most publications on methods for predicting the extent of blast damage include validation against field data. However, very little literature reviewed by the author presents direct comparisons of mulitiple prediction approaches against each other and field tests. This thesis used three different prediction methods to estimate the zone of radial fracturing and

evaluated them against results from the experiment. A more extensive study comparing, say, five to ten different prediction methods against field results would provide a better understanding of the accuracy of each method. Even a comparative analysis of several damage prediction models against each other, without evaluation against a field test, might yield valuable insight.

- The field experiment was conducted using a blasthole with much more confinenment than is normally employed in practice. The goal of this experiment was to obtain a worst-case scenario of backbreak. The geometry of the test was expected to increase radial fracturing in comparison with a normal blasthole. Future studies could focus on the damage region from a typical production hole, which uses some stemming, or a trim hole, which uses no stemming. The presence of a free face on one side of the blasthole would be preferable. This would simulate conditions from a normal shot where prior rows have already been fired, leaving a free face adjacent to the last row.

APPENDIX A

THEORY OF ROCK BREAKAGE BY EXPLOSIVES

An important requirement in studying any kind of physical process lies in understanding the underlying theory. Blasting entails the interaction of complex physical processes—processes, however, that are governed by fundamental principles. While much research continues to be directed towards a more precise knowledge of these processes, the general behavior of explosive-rock interaction during blasting is well known.

The mechanisms by which explosives induce rock breakage are many and include (Atlas Powder Company 1987) the following:

- Compressional and tensile shock wave and strain wave energy,
- Wave reflections at free faces and boundaries within the rock mass,
- High pressure gases acting on the surrounding rock mass,
- Flexural rupture,
- Shear waves,
- Release-of-load,
- Nucleation of cracks at preexisting flaws and discontinuities, and
- In-flight collisions.

There are four different stages in the blasting process (Atlas Powder Company 1987; Floyd 2008):

- Detonation of the explosive column,
- Shock and stress wave propagation,
- High pressure gas expansion, and
- Displacement of fragmented rock.

While each stage is distinct from the others, they are not necessarily sequential in order of occurrence. They overlap and interact with each other to produce the final product: fragmented and displaced rock.

A.1 Detonation of the explosive column

The first stage in the fragmentation process is the detonation of the explosive charge to release its chemical energy. Detonation refers to a specific type of chemical reaction; namely, one that propagates via a highly-energetic shock wave (Meyer et al. 2002). This is distinct from a similar process called deflagration in which the reaction front propagates through thermal contact and radiation, such as occurs with burning gasoline or propellants. Very large temperature and pressure gradients are formed, which contribute to a very rapid rate of reaction. One-dimensional detonation theory dictates a stable detonation front called the Chapman–Jouguet (CJ) plane. Immediately behind exists the reaction zone, where the detonation pressure is generated. Figure A.1 shows an illustration of the CJ plane, reaction zones, and outgoing shockwave during the explosive detonation process.

Detonation velocities range on the order of 1,500–9,100 m/s (5,000–30,000 ft/s). At these velocities, a typical explosive column in a blasthole is consumed within several milliseconds. In addition to explosive properties, the velocity of detonation (VOD) is also dependent on degree of confinement and the diameter of the explosive charge (Atlas Powder Company 1987). Higher explosive VODs release gaseous products more quickly, resulting in higher pressures and are thus more suited for fragmenting hard rock. Lower explosive VODs release gaseous products over a longer duration and thus perform better in soft rock and applications that require greater heave of the blasted material.

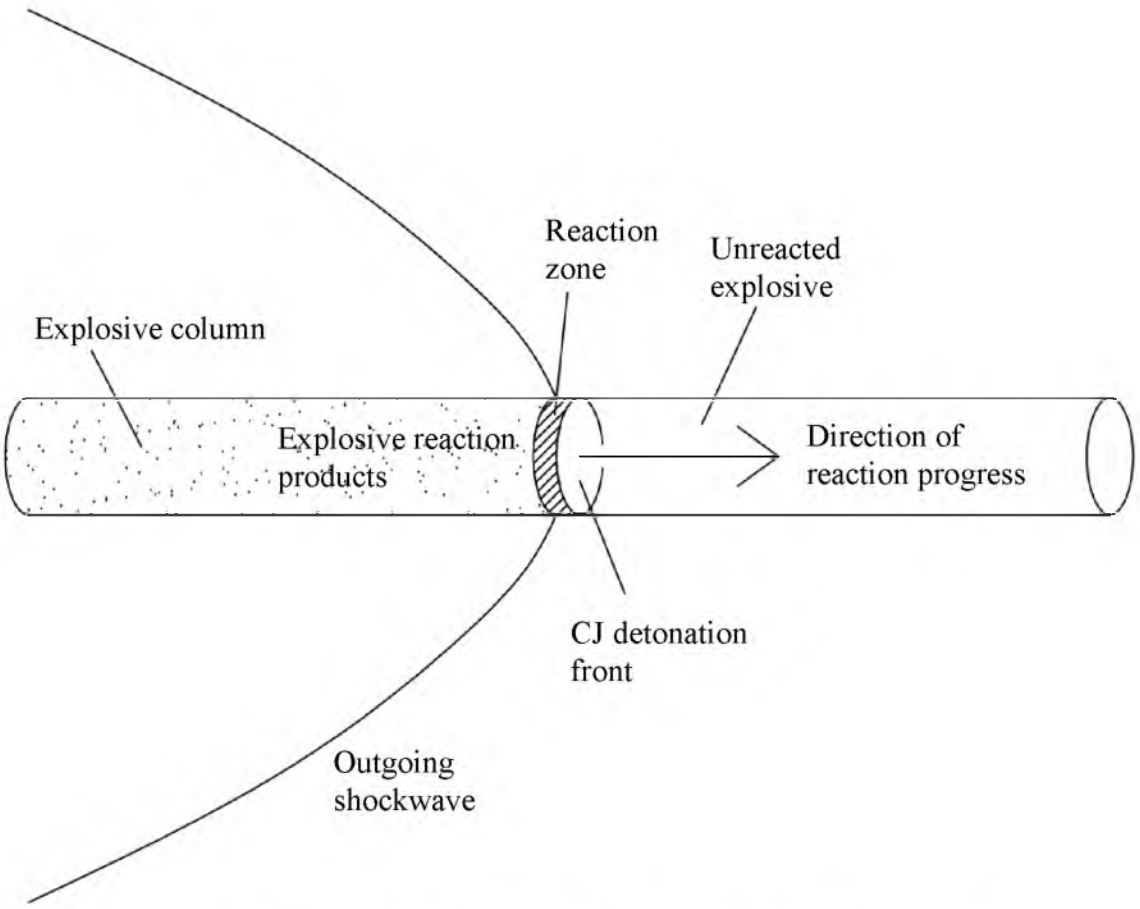

Figure A.1 Illustration of detonation process in an explosive column

For a well-confined explosive, the detonation pressure is given by

$$P_D = K\rho_{exp}(VOD)^2 \tag{A.1}$$

where P_D is the detonation pressure in kbar, K is a constant specific to the explosive, ρ_{exp} is the explosive density in g/cm^3, and VOD is in ft/s (Atlas Powder Company 1987). For ANFO, K = 2.375E-7. Detonation pressures range on the order of 9,000–27,500 MPa (9–275 kbar), with temperatures from 1,900–4,150 K (3,000–7,000 °F).

In transitioning to the next stage of rock breakage, the expansion of gaseous products from the reaction zone apply a pressure along the walls of the borehole. Absent

an equation of state, the borehole pressure P_B for a fully-coupled explosive is estimated to be equal to one-half of the detonation pressure (Persson et al. 1994; McKenzie 1999).

$$P_B = P_D/2 \tag{A.2}$$

Sun (2013) cautioned against using this simple approach, however, citing an analysis of the shock wave transfer from the explosive to the borehole walls.

For a decoupled explosive, the borehole pressure is significantly less. If the constant volume explosion pressures P_E is known, the borehole pressure can be estimated provided that the ratio γ of the specific heat values c_p and c_v is known ($\gamma = c_p/c_v$) (Persson et al. 1994). A typical value for γ is on the order of 1.5.

$$P_E v_E^{\gamma} = P_B v_B^{\gamma} \tag{A.3}$$

where v is the specific volume of the explosive at the indicated state. For a unit length of the blasthole, the specific volume only depends on the diameters of the borehole and charges d_B and d_C, respectively.

$$P_B = P_E \left(\frac{d_B}{d_C}\right)^{2\gamma} \approx P_E \left(\frac{d_B}{d_C}\right)^{3} \tag{A.4}$$

McKenzie (1999) gave a relationship similar to Equation A.1 for computing the borehole pressure but included a coupling factor f_c, which is the ratio of the volume of the explosive to the volume of the blasthole (minus the stemming column):

$$P_B = 0.12 f_c^n \rho_{exp} (VOD)^2 \tag{A.5}$$

Here, P_B is in Pa, ρ_{exp} is in kg/m^3, VOD is in m/sec, and n is a coupling factor, usually taken to be 1.2 to 1.3 for dry holes and 0.9 for saturated rock.

A.2 Shock and stress wave propagation

The second stage in fragmentation is the creation of a shock wave that propagates outward from the borehole wall into the surrounding rock mass. The rapid decomposition of the explosive into gaseous products generates extremely high pressures that are transmitted to the borehole wall (Atlas Powder Company 1987; Floyd 2008). Within two to three diameters of the blasthole, extensive crushing and/or plastic deformation of the rock occurs as the dynamic compressive strength of the rock is exceeded. After the pressure pulse applied by the explosive column peaks, it decays exponentially as the borehole cavity expands and the gases cool. Figure A.2 shows the radial and tangential stress decay at two different distances from the borehole. Field experiments by Brinkmann (1990) produced borehole expansions ranging from 36% to 67%, depending on the type of explosive used.

Beyond the pulverized zone of rock, the shock wave energy has diminished enough such that the rock material no longer fails in compression, but can still fail in shear and tension. The stress pulse traveling outwards compresses the rock and simultaneously induces a tangential or "hoop" stress. The tangential stress component induces tensile failure in the rock, which manifests itself in the form of cracks that extend radially outwards. Studies indicate that the creation of these radially-formed cracks occurs at a distance of about one blasthole diameter from the borehole wall (Persson et al. 1994). Initially, the density of radial fractures is high. Further out, the number of cracks rapidly decreases as stress relaxation from fracturing favors the continuing extension of

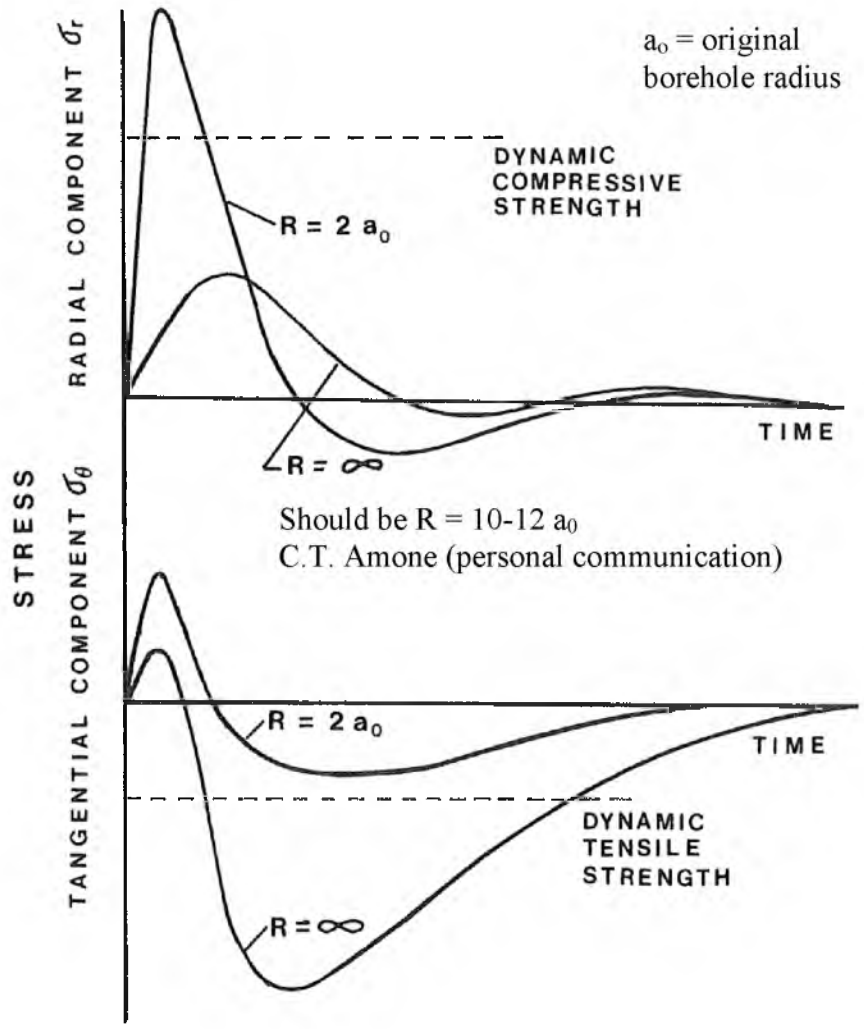

Figure A.2 Generalized stress histories for two different distances *R* from blasthole (Source: Dowding and Aimone 1992. Reprinted with the permission of the Society for Mining, Metallurgy, and Exploration; www.smenet.org).

only a few long cracks. Crack growth occurs until about 20–30 blasthole diameters from the borehole wall (Floyd 2008). According to Oriard (1982), the extent of radial cracking is controlled by

- Explosive energy,
- Rate of energy transmission to the adjacent rock, and
- Strength properties of the rock.

Numerical modeling of the shock wave and fracture process indicates that a significant time lag occurs between the shock wave front and the development of cracks and damage zones (ISEE 2011). The limiting factor appears to be the rate of crack growth.

Figure A.3 presents a visualization of the region of damage surrounding an explosive charge. Figure A.4 indicates regions where dynamic rock strengths are exceeded.

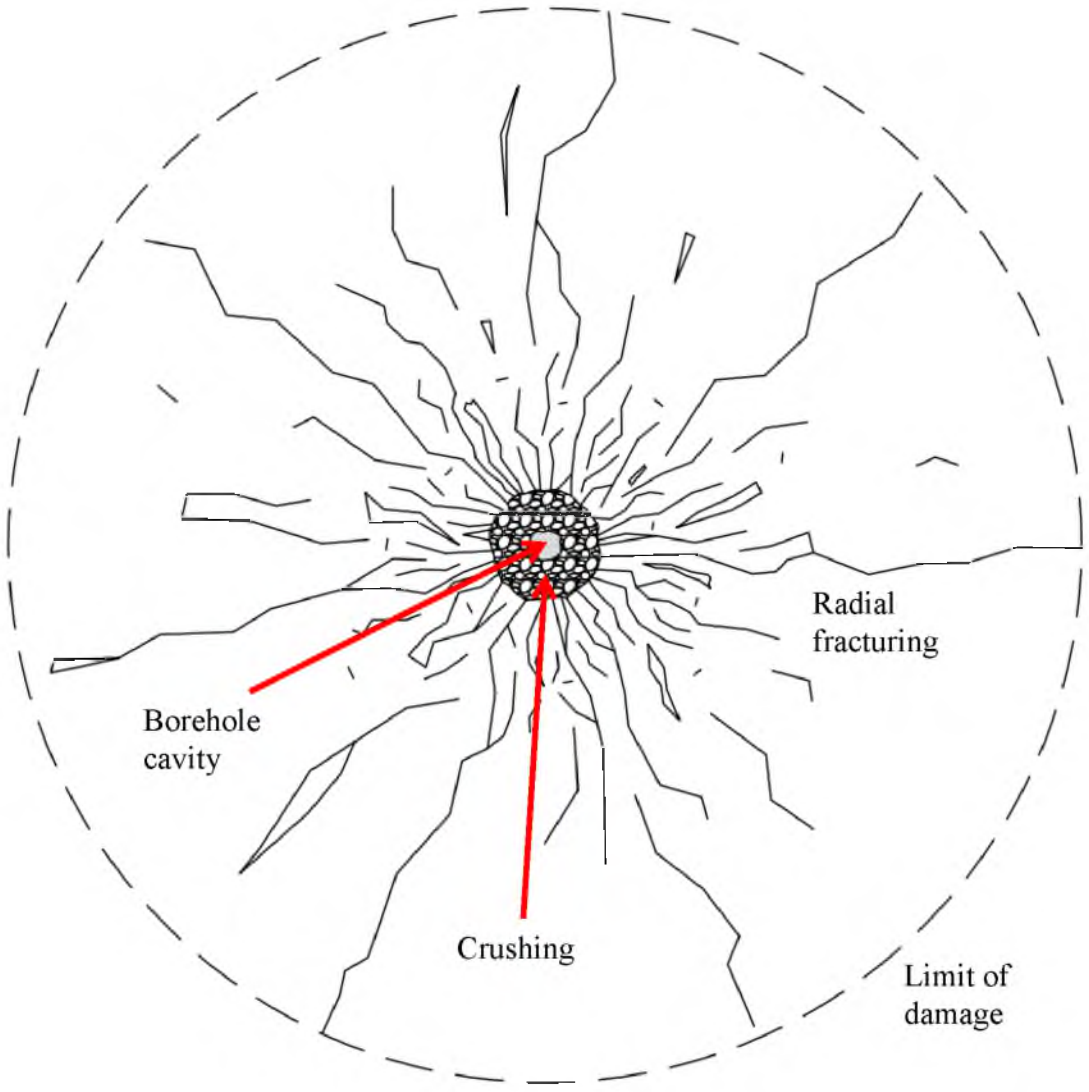

Figure A.3 Regions of damage surrounding an explosive charge

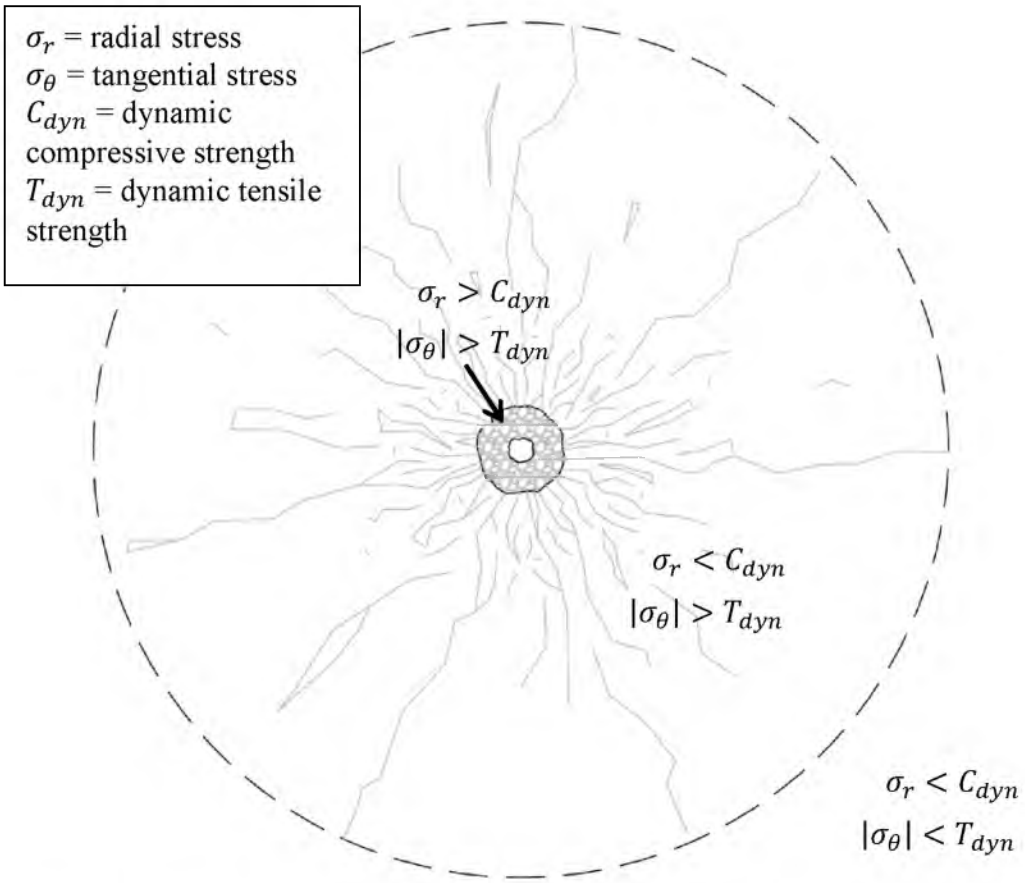

Figure A.4 Stress fields in the damage region in relation to dynamic rock strengths

In addition to the stress wave originating from the explosive charge, rock breakage and fracture growth is also aided and influenced by reflection and transmission of the wave across boundaries (Atlas Powder Company 1987; Floyd 2008; Hustrulid 1999). Reflection of a dilatational wave at free surface results in a phase change; thus, a compressional wave becomes a tensile wave and vice versa (Kolsky 1963). If the reflection occurs at an incident angle normal to the free surface, the magnitude of the reflected wave's stress is equal to that of the incoming wave. In the case of a wave with sufficient energy, the reflection of the wave as tensile can exceed the tensile strength of the rock and cause spalling and flexural rupture. Reflection of a wave across a

discontinuity in the rock can also achieve the same result, particularly if the ratio of acoustic impedance as the wave travels from material 1 to material 2 is less than one (Atlas Powder Company 1987).

As explained by Hustrulid (1999), reflection of a stress wave can preferentially impede or encourage the growth of cracks at specific orientations. When a stress wave emanates outwards from an explosive charge, it contains both a radially-oriented compressive component and a tangentially-oriented tensile component. After encountering a free face, the reflected wave contains a radially-oriented tensile component and a tangentially-oriented compressive component. When the stress wave encounters a crack, it will either assist or retard the crack's growth, depending on how the stress components are aligned with the tip of crack. Determining which will occur involves resolving where and when the stress wave and crack tip will meet through analyzing their respective trajectories and velocities. Figure A.5 shows two different

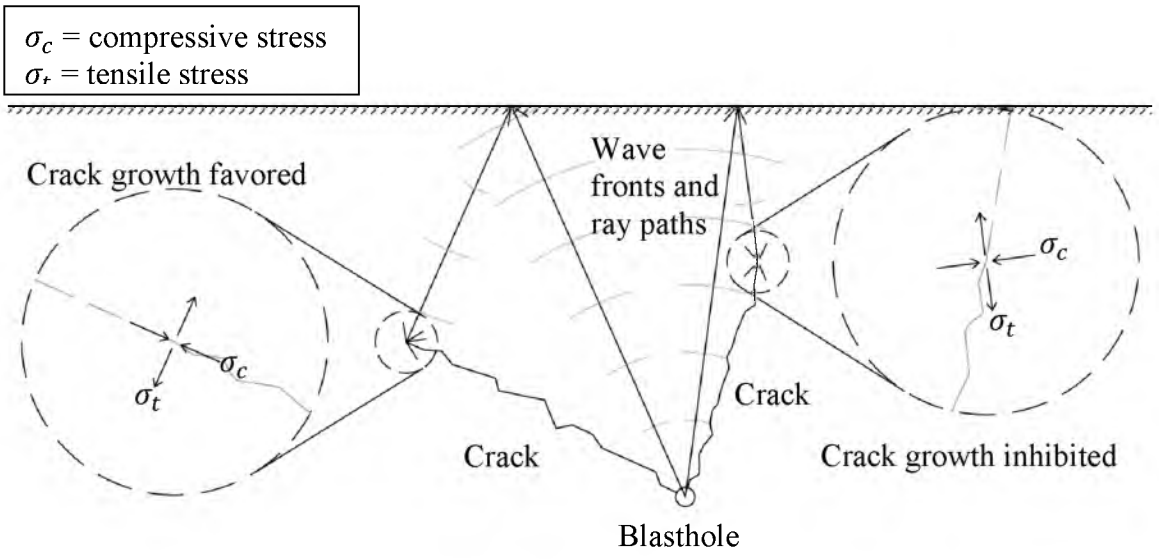

Figure A.5 Interaction between stress wave and crack growth. After Hustrulid (1999).

possibilities. The scenario on the left favors crack growth while the scenario on the right inhibits crack growth.

Initially the shock wave is travelling faster than the dilatational wave velocity c_P (ISEE 2011). The shock wave dissipates energy quickly and becomes a compressional wave travelling at the velocity c_P. The theoretical maximum crack tip velocity, on the other hand, is equal to $0.38c_P$, although experiments with concrete by Curbach and Eibl (1990) indicated actual peak velocities between $0.20c_P$ and $0.30c_P$.

Studies into the nature of crack growth have shown that preexisting flaws and discontinuities in a rock mass exert significant influence on the nature of the fracture network that is formed as the stress wave passes through (Atlas Powder Company 1987). Tests in unflawed material result in only a small number of dominant cracks that extend far out from the borehole. The dense fracturing, and consequently the zone of fragmentation, remains clustered near the blasthole. On the other hand, even a small flaw some distance out from the blasthole can alter the pattern of fractures developed in that the flaw may act as a nucleus for crack growth. Virtually all rock bodies are heterogeneous and contain a high concentration of fractures and flaws ranging from microscopic to macroscopic in size. Consequently, the size and shape of the fragmentation zone from a blast is highly dependent upon the rock structure.

Beyond the fracture zone, the stress wave energies have dissipated to the point where no further breakage occurs. These waves continue outward as elastic waves and cause vibrations that are measurable for large distances.

A.3 High pressure gas expansion

Immediately after the shock wave is transmitted to the rock mass, the high pressure gases in the expanding borehole cavity begin to force their way into the fracture network. The gases travel along paths that offer the least resistance, which include both the fracture network and preexisting discontinuities, cracks, faults, joints, and seams of weak material (Atlas Powder Company 1987). Where no path exists, gas pressures may be high enough to create new cracks or extend existing ones (Floyd 2008). The gases continue to work within the rock matrix until either they vent at a free face or the pressure magnitude drops to a certain threshold. Studies indicate this threshold to be around 100 MPa (14,500 psi) (McKenzie 1999). As the gas flows out of the rock mass, the pressure load is released (Atlas Powder Company 1987). Rebound of the rock material instigates high tensile stresses that contribute to the breakage process.

The exact degree to which the high pressure gases contribute to the fracturing and rupture of the rock mass has not been fully agreed upon (Atlas Powder Company 1987). Some claim that the fracture network is complete by the time the gases begin streaming into the rock surrounding the blasthole, while others say that a significant portion of the fracturing is directly attributed to gas action. In all reality, the most plausible scenario is that the shock wave and gas pressures work in conjunction with each other. One mechanism may dominate the other, but this likely is dependent upon the structure and properties of the in-situ rock and the properties of the explosive used. A series of experiments were conducted by Brinkmann (1990) in which steel liners were positioned along the blasthole walls to prevent the flow of explosive gases into the surrounding rock. A comparison made between the normal and lined blastholes indicated that (1) the shock

wave was primarily responsible for fragmentation, and (2) high-pressure gas expansion was responsible for burden breakout through flexural rupture. Numerical and experimental studies conducted by McHugh (1983) using steel liners in Plexiglas cylinders found that high pressure explosive gases are responsible for extending the lengths of tensile cracks by as much as a factor of five to ten.

Field studies of gas pressures behind blasts show that both positive and negative pressures occur (McKenzie 1999). Initially, the gases from the explosive reaction exert a very large positive pressure. As both the shock wave and the gases are emitted into the rock mass, fractures, joints, and other discontinuities dilate from severe vibrations and gas flow. Movement of the rock mass as a whole also occurs. As the gases vent, the combination of crack dilation, vertical swelling of the fragmented rock mass, and release of load are attributed to the creation of negative pressures, as seen in Figure A.6. Pressure calculations based on a polytropic gas law seem to confirm this (Ouchterlony et al. 1996).

Pressure histories show that gas pressures remain within the rock mass anywhere from a fraction of a second to several seconds (McKenzie 1999). Velocities of penetration, while highly variable and dependent upon rock mass permeability, have been measured to be around 200–300 m/s (660–980 ft/s), or 5–10% of the dilatational wave velocity. Gas penetration distances have been measured up to 21 m (70 ft). In a series of field tests performed by Brent and Smith (1996), an exponential relationship was found to satisfy pressure readings taken at variable distances, suggesting that pressures decay exponentially with distance from the explosive charge(s). Overall, the residence time of high pressures and distance of penetration are largely influenced by confinement (McKenzie 1999). If the gas pressure is relieved rapidly, gas penetration distances are

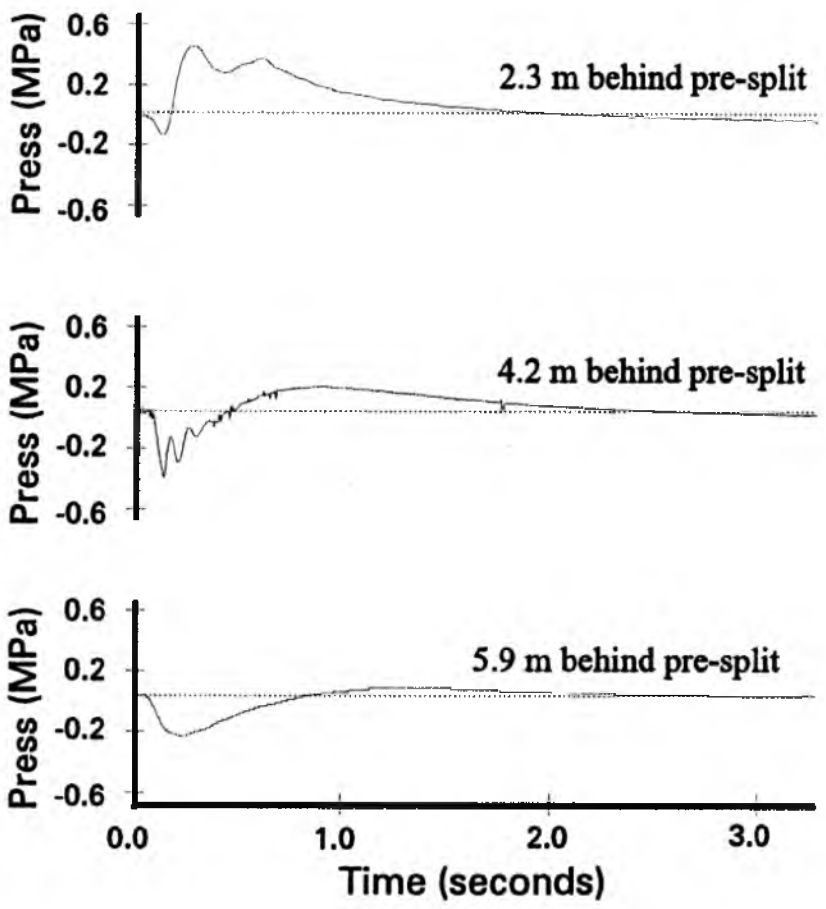

Figure A.6 Example pressure histories behind a bench blast
(Source: McKenzie 1999. Reprinted with the permission of The Australasian Institute of Mining and Metallurgy).

small. If an explosive charge is highly confined, peak pressures are higher, penetration distances increase, and the pressures themselves tend to remain positive. Confinement is controlled primarily by the effective burden between an explosive charge and free face, but is also influenced by stemming and rock permeability.

A.4 Displacement of fragmented rock

The last stage in the fragmentation process constitutes movement of the preconditioned rock. Both the shock/strain wave and gas pressures contribute to displacement of the broken rock, but it is primarily gas action that is responsible for the

heave (Floyd 2008). It is at this stage that having an adequate free face is essential. Stress relief is provided as the broken rock moves along the path of least resistance. Regions of rock that may not have been fully fragmented experience flexural rupture from the pressurized gas flow, provided that a free surface is present. In-air collisions of rock fragments also add to the breakage process in a minor role (Atlas Powder Company 1987; Floyd 2008).

A.5 Partitioning of explosive energy

Several studies have been conducted on explosive energy distribution among each of the breakage mechanisms previously discussed (Hinzen 1998; Ouchterlony et al. 2004; Sanchidrián et al. 2007; Spathis 1999). The results of one such study by Ouchterlony et al. (2004) are presented here. The following energy balance was used in partitioning the energy:

$$\eta E_0 = E_k + E_f + E_s + other\ losses \tag{A.6}$$

where

E_0 is the explosive weight strength,

E_k is the kinetic energy of throw,

E_f is the fragmentation energy (based on the creation of new surface area through fracturing),

E_s is seismic energy,

$\eta = E_G/E_0$ is the utilization ratio or relative work capacity of the explosive, where E_G is called the Gurney energy determined using the cylinder expansion tests, and

$other\ losses$ include a number of factors: heat transferred to the rock mass, shock wave losses such as crushing, friction losses, etc.

Losses included in the η term are residual heat from blast fumes, air shock waves, and sometimes an incomplete chemical reaction of the explosive. Usable work from the explosive is contained in the kinetic energy and fragmentation terms. The results of the study were as follows:

- Crushing and other losses in the rock mass 20–40%,
- Kinetic energy of throw 10–20%,
- Seismic energy 5–10%, and
- Fragmentation energy 0.1–2%.

These are only rough estimates. However, they give one an overall idea of the energy content of each breakage mechanism.

A.6 Fracture mechanics

The field of fracture mechanics is quite extensive and complex in nature. While little attention will be given in this thesis to a rigorous study of fractures, its strong presence in the fragmentation process requires that it at least be mentioned.

Cracks form in brittle materials as a result of failure either through compression, shear, or tension. Depending on the conditions of failure, the latter two tend to be more common as the stress magnitudes at failure in shear and tension are lower than in compression. As pointed out by Persson et al. (1994), the relative energies of deformation until fracture in uniaxial tension versus uniaxial compression are 1:100. Once a crack is formed, further brittle failure is directed in a manner that extends crack growth. This growth results from tensile stresses that concentrate at the tip of the crack.

The energy required for a crack to propagate can be described using a fundamental material constant called the fracture toughness G_{IC} (Persson et al 1994). It is related to the properties of a material and the stress intensity at the tip of the crack by the formula

$$G_{IC} = \frac{1-\nu^2}{E} K_{IC}^2 \tag{A.7}$$

where ν is Poisson's ratio, E is Young's modulus, and K_{IC} is the critical stress intensity factor at the tip of a crack when the crack just starts to propagate. Note that this formula only applies for a biaxial stress state, in which one of the three principal stresses is equal to zero.

One of the difficulties in fields concerning fracture mechanics is predicting the point of failure in a brittle material. Crack propagation progresses in a random fashion. Part of this is due to the fact that a preexisting flaw, even of microscopic proportions down to a grain boundary, will affect the local strength of the rock and consequently the most favorable orientation in which a crack will grow. Thus, cracks may extend in directions that are not always in the direction of the largest shear stresses (Persson et al. 1994). This adds a random component to predicting failure in brittle rock. Statistics can be used to normalize this behavior and obtain averages, but not in predicting failure planes, failure stresses, and fracture paths in a precise and exact fashion.

An extensive amount of effort has been put into researching and developing failure criterion for brittle materials. Numerous models exist, ranging from the simple Mohr–Coulomb model to advanced constitutive relationships such as the RHT model, developed by Reidel et al. (1999) and used for concrete-like materials. Models have even

been developed specifically for estimating blast damage, such as Yang et al. (1996) and Yang and Wang (1996). One of the more interesting theories on brittle failure was developed by Lundborg (1972). His theory uses a random microcrack model to formulate a statistical theory of brittle material strength. When simplified, however, this theory can be reduced down to the classical models of Mohr–Coulomb, von Mises, Tresca, and others (Persson et al. 1994).

A.7 Blasting to minimize damage

Blast-induced damage manifests itself in a number of forms during blasting operations. These may include the following (Floyd 2008):

- Compressional failure surrounding each blasthole;
- Tensile failure in the form of spalling and radial fractures;
- Shear failure and slippage, particularly along preexisting planes;
- Crack extension through both tensile failure and gas penetration;
- Block heaving and cratering behind a blast from high gas pressures; and
- Release of load fracturing from the rebounding rock mass.

Various field techniques have been developed for minimizing backbreak. These range from simple modifications on production blasts to specialized blast designs that require additional effort to implement. The five main types according to Floyd (2008) and Oriard (1972, 1982) are explained as follows.

A.7.1 Modified production or trim blast

In this type of blast, one or more design parameters are changed such as the number of rows, delay sequence, etc. (Floyd 2008). Often, the number of rows is limited,

providing a narrow pattern width in which effective burden control (i.e., adequate free face) can be assured. This type of blast is most easily implemented without hindering production operations.

A.7.2 Cushion or buffer blast

A cushion or buffer blast is similar to a trim blast, but the last row or two have smaller charge weights, reduced burden and spacing, and little or no stemming (Floyd 2008). Narrow blasts of three or four rows are conducted. Care is taken to ensure that adequate horizontal relief is provided as each row is detonated in succession.

A.7.3 Presplit or midsplit blasting

Presplitting involves drilling a row of closely-spaced holes at the pattern design limits and detonating them prior to the adjacent rows (Floyd 2008; Oriard 1982). The objective is to create a fracture line that will impede the penetration of high-pressure gases into the bench and limit crack growth. By using decoupled or light charges with no stemming, the shock wave applied by the borehole pressure is minimized (Oriard 1982). As the expanding gases apply a less damaging pressure pulse on the borehole walls, a quasistatic stress field is created that favors the formation of a tensile crack between presplit holes, as displayed in Figure A.7. If the fracture extends the entire distance between adjacent holes, a pathway is made for gases from blasting to vent out the surface instead of penetrating into the rock beyond the intended limit. In order for a presplit to be successful, though, adjacent holes must be detonated simultaneously to create the appropriate stresses. One caveat with presplitting is that additional, unintended damage may be induced (Oriard 1982). Drilling accuracy is also critical in creating an effective

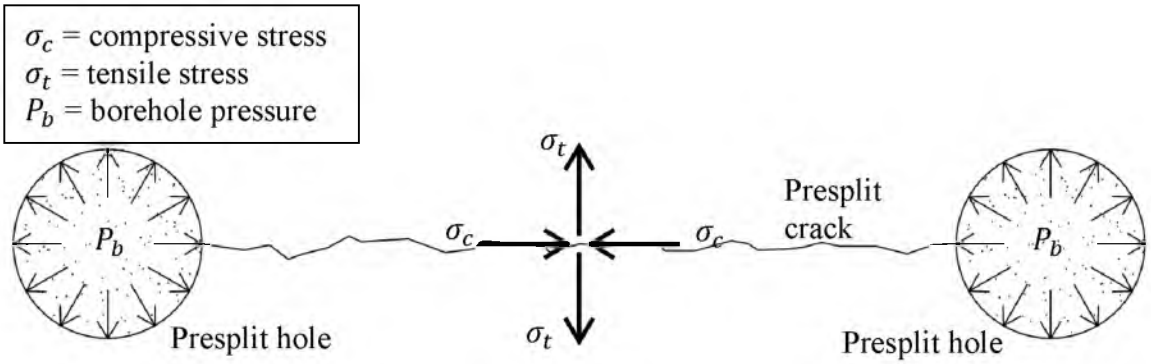

Figure A.7 Development of presplit crack. After Oriard (1982).

presplit; drillhole deviations of 150 mm (6 in.) can render the presplit plane poor (Tose 2006).

While presplitting can be successful in inhibiting gas flow, it is ineffective in stopping vibrations. The U.S. Bureau of Mines conducted a study in which vibrations levels were measured across a presplit fracture plane (Devine et al. 1965). They measured no significant attenuation of seismic vibrations while traversing across the presplit. In addition, they observed that forming the presplit itself sometimes created the largest vibration events. This can be attributed to the fracture plane closing as the material deforms under the stress wave, as is demonstrated by Hustrulid (1999) for the case of a planar wave in a bar.

A.7.4 Smooth wall blasting

Smooth wall blasting is similar to presplitting in most respects, except that the final row of closely spaced, lightly charged holes are initiated at the end of a blast (Oriard 1972). For agreeable results, smooth wall blasting requires a very small burden.

A.7.5 Line drilling

When a smooth wall with no out-of-plane fracturing or damage is essential, line drilling can be used. A line of holes spaced closely at 6- to 12-hole diameters apart is drilled along the final wall. No explosive is loaded in these holes. A buffer row is drilled adjacent to the line with reduced spacing and loaded with a light charge.

APPENDIX B

WAVE PROPAGATION AND SEISMIC VIBRATIONS

As discussed in Section A.5 in Appendix A, the detonation of an explosive charge in rock transmits a large amount of energy to its surroundings in a very short timeframe. Around 5–10% of this energy results in seismic disturbances (Ouchterlony et al. 2004). Although seemingly small, this portion of the energy released plays a significant role both in extending the outer fringes of the fracture zone and in affecting the stability of slopes, excavations, and structures at further distances.

Numerous studies have been conducted into studying blast-induced waves and how to minimize the vibrations they generate. Blast vibrations may be divided into near-field and far-field. The distinction lies in the types of waves that occur. Near-field vibrations concern close distances on the order of 15 m (50 ft), in which body waves are predominant. Far-field vibrations are dominated by surface waves and can be perceived for thousands of feet. Most vibration analyses focus on far-field effects, for these are a greater cause for concern among mining operations and construction activities. Rock damage, however, is influenced by near-field vibrations. Whatever the emphasis, a key component to studying blast-induced damage lies in understanding the fundamentals of seismic waves.

B.1 Fundamentals of seismic waves

In a basic sense, physical waves are the propagation of energy through a medium. Most waves can be approximated as elastic. This allows for the simplifications that permit development of the formal mathematical theory and provides a starting point for understanding nonelastic wave behavior. A propagating wave exhibits certain distinct characteristics. A wave propagates by transferring the energy disturbance from one element in the elastic continuum to the next through the action of forces (Bollinger 1971).

During this oscillation, however, no bulk movement or transport of matter occurs. These elements only undulate along limited-displacement paths that return to their origin after the wave has passed. The motion of a wave can be separated into two distinct components: wave velocity and particle velocity. Figure B.1 provides a visual aid. The wave velocity is the rate at which the disturbance travels through a medium. The particle velocity is the speed of oscillation of a single particle or element as the wave passes through it. The maximum displacement of this particle is a measure of both the amplitude and energy of the wave at that point (the energy of a wave is proportional to its amplitude squared, or $E_s \propto A^2$).

As mentioned earlier, seismic waves can be separated into body waves and surface waves. Body waves are comprised of P-waves and S-waves and are dominant within the interior of a solid. For P-waves, also referred to as dilatational or irrotational waves, the particle vibration is parallel to the direction of propagation, and displayed in Figures B.2 and B.3 (Bollinger 1971). Thus when a P-wave passes through a medium, the elements of the medium undergo volume change through compression and rarefaction. P-waves are also the fastest of all wave types.

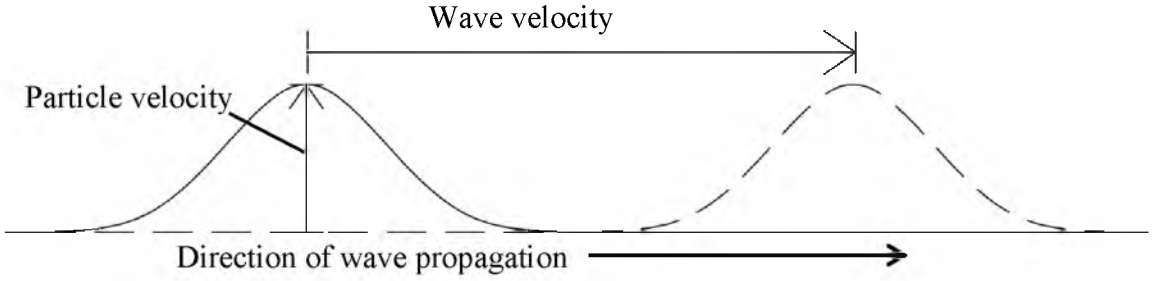

Figure B.1 Wave propagation velocity and particle velocity

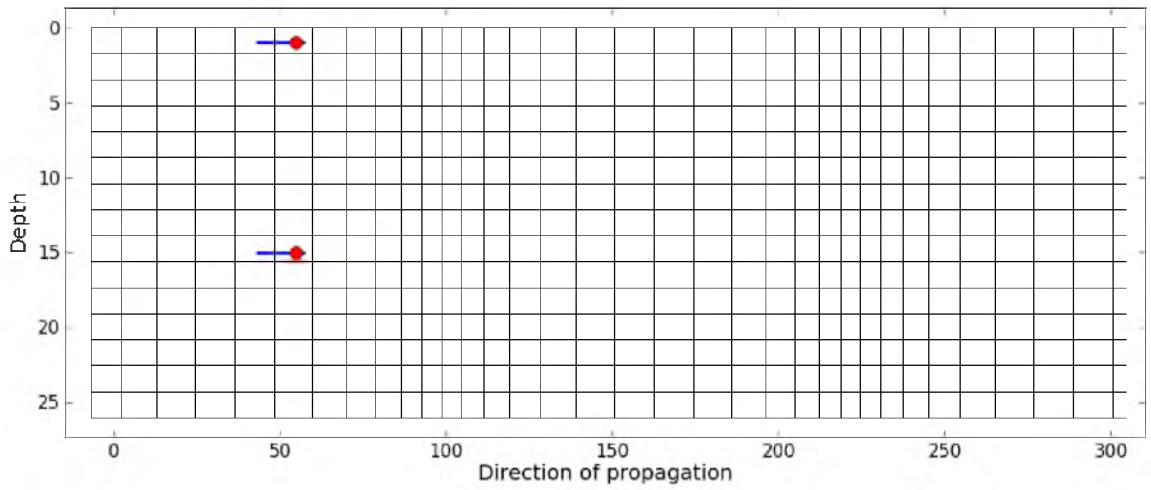

Figure B.2 Section view of a P-wave. Red points show particle motion.

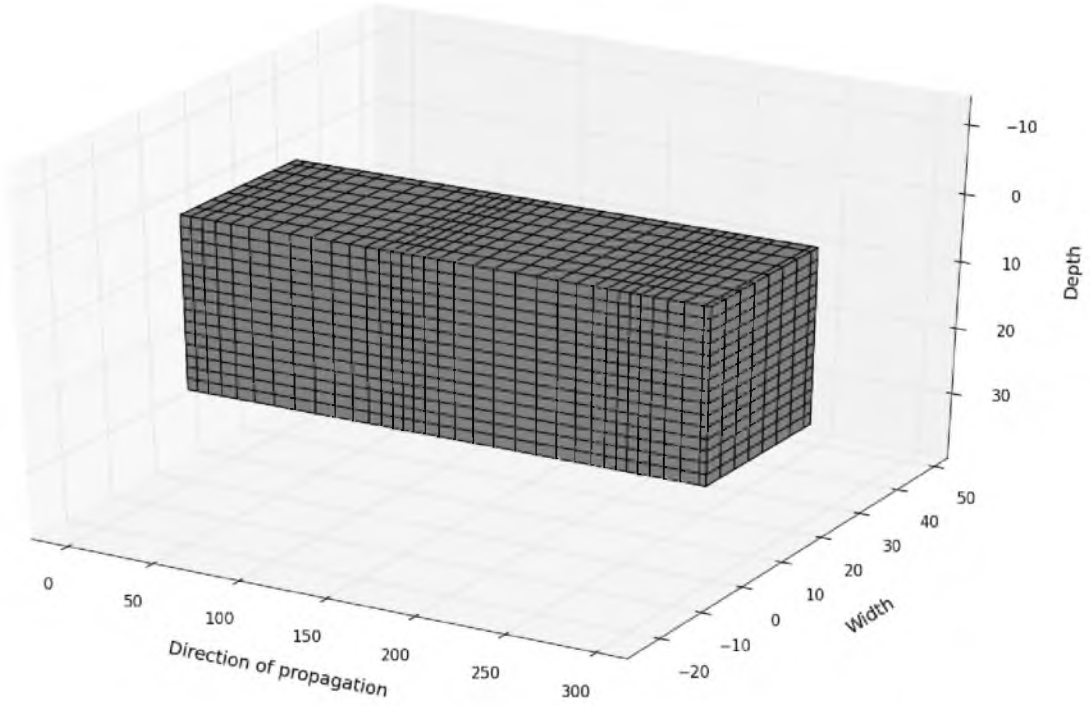

Figure B.3 Three-dimensional view of P-wave propagation

For S-waves, also referred to as shear or distortional waves, the particle vibration is perpendicular to the direction of propagation, as shown in Figure B.4. Elements through which an S-wave passes through will experience distortion and rotation in both the vertical and horizontal directions, but no volume change. S-waves can be broken down into vertical and horizontal polarizations, as displayed in Figures B.5 and B.6. S-waves are slower than P-waves.

Surface waves require the presence of a free boundary such as the surface of the earth and only exist near this boundary. Surface waves can appear either as Raleigh waves or Love waves. The amplitude of these waves is dependent upon depth below the surface (Bollinger 1971). For both wave types, the particle motion is perpendicular to the direction of propagation. With Raleigh waves, the particle oscillation is vertical, whereas with Love waves it is transverse. Particles through which a Raleigh wave passes move in an elliptical fashion, as shown in Figures B.7 and B.8. At a depth above $1/5^{th}$ of the wavelength, the motion is retrograde, and below it is prograde (Russel 2013). While

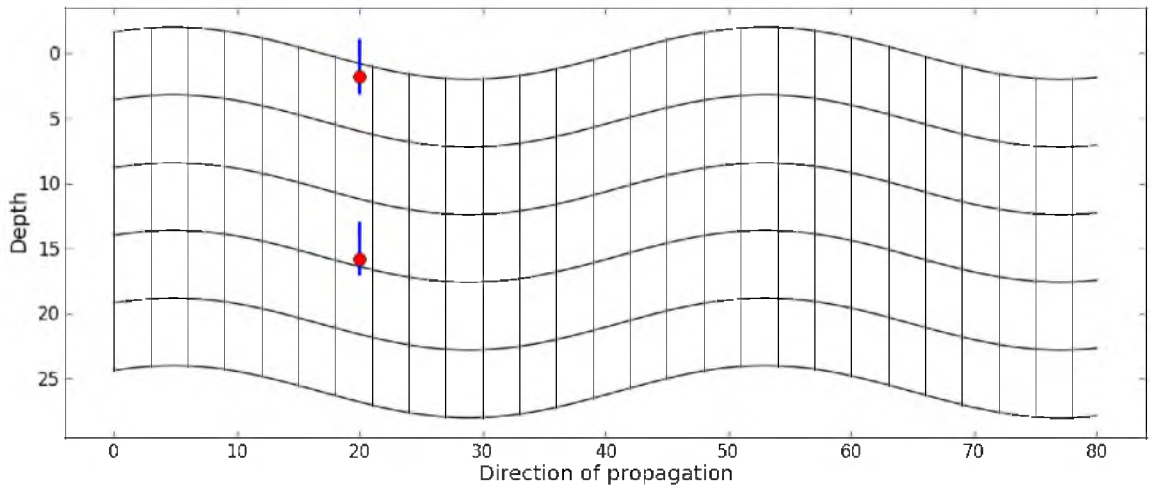

Figure B.4 Section view of an S-wave. Red points show particle motion.

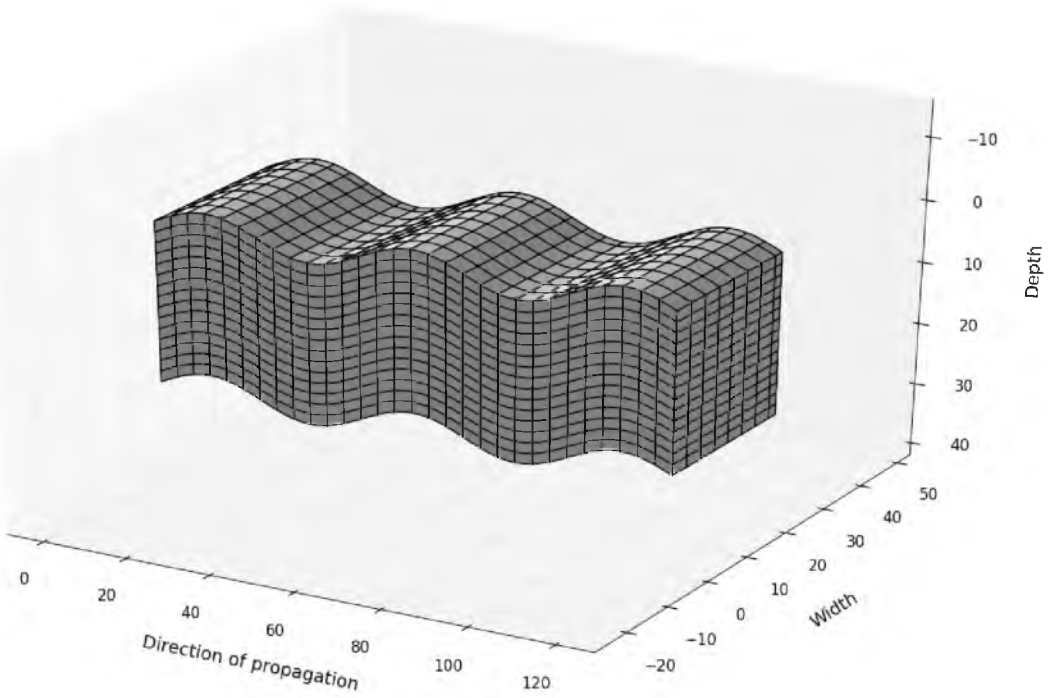

Figure B.5 Three-dimensional view of vertical S-wave propagation

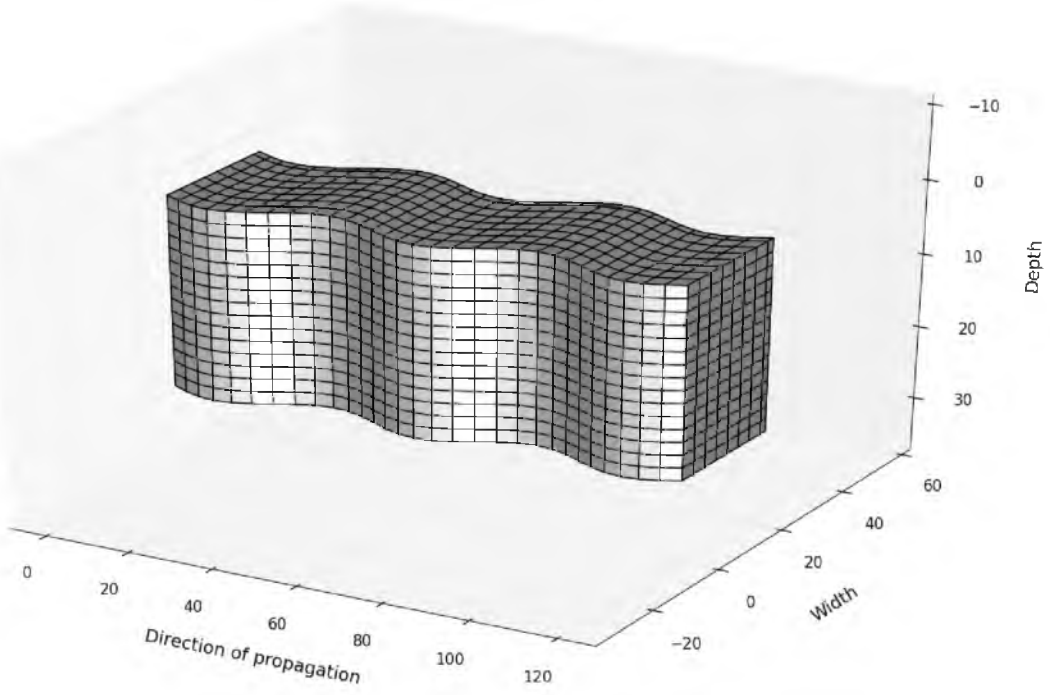

Figure B.6 Three-dimensional view of horizontal S-wave propagation

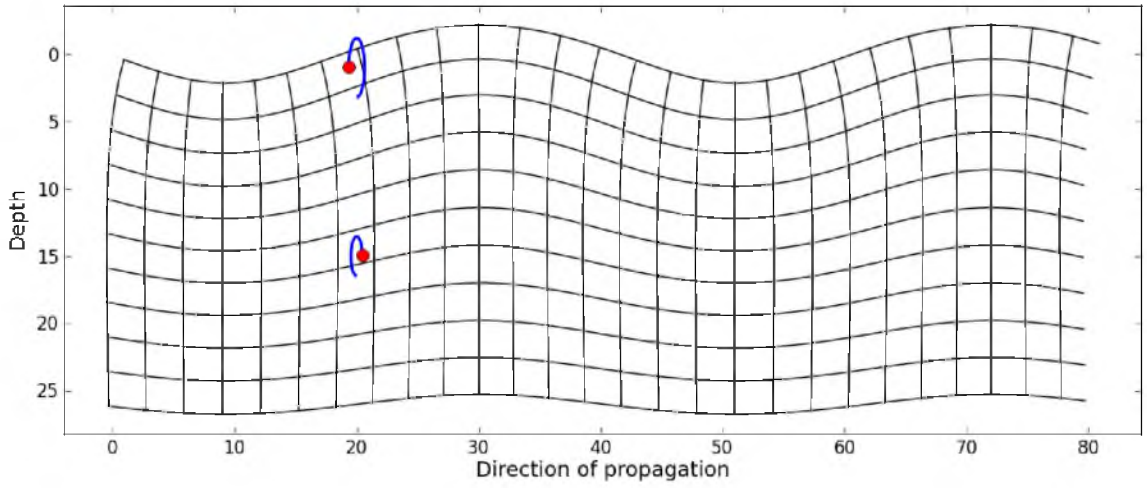

Figure B.7 Section view of a Raleigh-wave. Red points show particle motion.

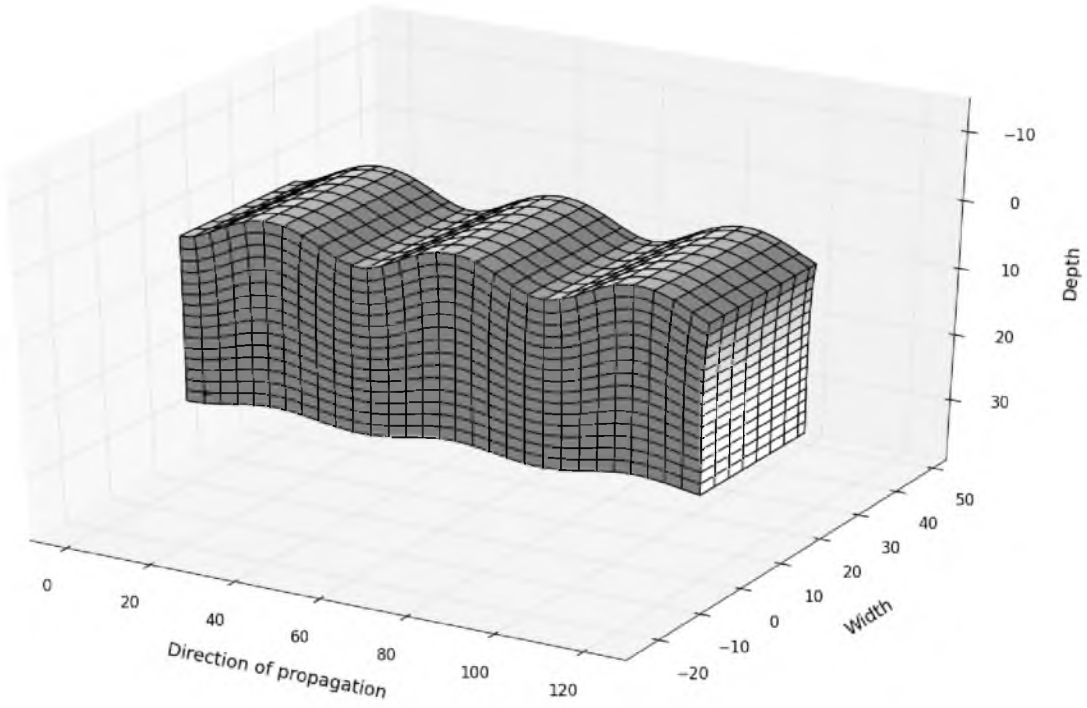

Figure B.8 Three-dimensional view of Raleigh-wave propagation

Raleigh waves only require a free boundary, Love waves additionally require a layer over a half-space to occur (Bollinger 1971). Raleigh waves are usually the surface wave of primary concern when considering far-field blast vibrations.

While the influence of shock waves is limited to short distances from an explosive energy source, they are nonetheless instrumental in the fracturing process. A shock wave is characterized by a transition zone in which its passage through a medium induces very rapid gradients in quantities such as pressure, density, stress, and velocity (Davidson 2008; Kolsky 1963). The result is a highly-compressive wave, similar to a P-wave, that travels faster than the acoustic velocity of the medium (ISEE 2011; Kolsky 1963). This occurs because as the density of the medium increases in the shock transition zone, the bulk modulus increases, resulting in a greater dilatational wave velocity (Kolsky 1963).

B.2 Wave propagation velocities from classical wave theory

Classical wave theory in an elastic continuum is developed using the concept of a stress differential on an infinitesimal element, as shown in Figure B.9 (Kolsky 1963). In a three-dimensional, unbounded medium, the state of stress at a point can be described in a tensor containing nine components, six of which are independent. The resulting strains comprise normal and shear deformation and rotation of the element.

If a stress differential is present (i.e., a net non-zero force is applied), then the variation in stress can be used to develop the equations of wave motion. Figure B.10 demonstrates this for stresses acting on the x-face of an infinitesimal element. Using force equilibrium, the relationship is as follows:

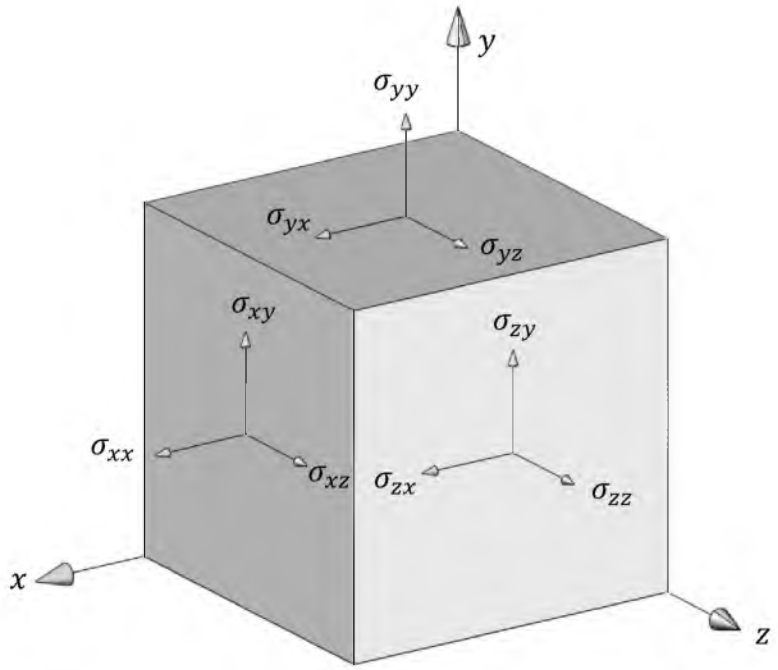

Figure B.9 Elemental stresses

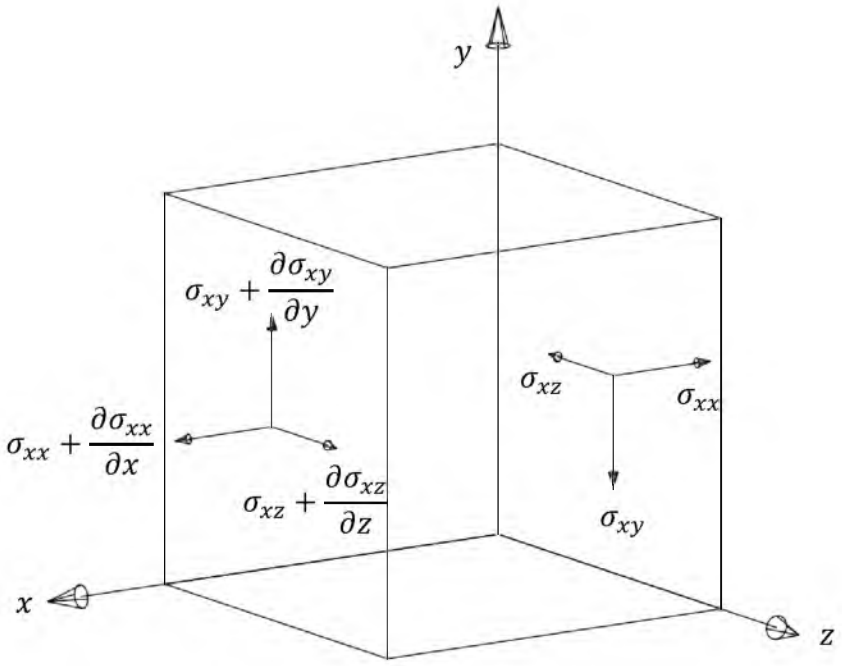

Figure B.10 Stress differential in the x-direction. After Kolsky (1963).

$$\left(\sigma_{xx}+\frac{\partial\sigma_{xx}}{\partial x}\delta x\right)\delta y\delta z-\sigma_{xx}\delta y\delta z+\left(\sigma_{xy}+\frac{\partial\sigma_{xy}}{\partial y}\delta y\right)\delta x\delta z-\sigma_{xy}\delta x\delta z$$

$$+\left(\sigma_{xz}+\frac{\partial\sigma_{xz}}{\partial z}\delta z\right)\delta x\delta y-\sigma_{xz}\delta x\delta y$$

$$=\left(\frac{\partial\sigma_{xx}}{\partial x}+\frac{\partial\sigma_{xy}}{\partial y}+\frac{\partial\sigma_{xz}}{\partial z}\right)\delta x\delta y\delta z \tag{B.1}$$

where

σ_{xx} is the stress normal to the x-face,

σ_{xy} and σ_{xz} are the shear stresses acting on the x-face in the y and z-directions, and

δx, δy, and δz are the dimensions of the infinitesimal element. The same relationship can be developed for the y and z-faces of the element.

Using valid relationships between stresses and strains in an isotropic, elastic medium, the full equations of wave motion in a three-dimensional unbounded medium with respect to both space and time t are derived as

$$\rho\frac{\partial^2 u}{\partial t^2}=(\lambda+G)\frac{\partial\Delta}{\partial x}+G\nabla^2 u \tag{B.2}$$

$$\rho\frac{\partial^2 v}{\partial t^2}=(\lambda+G)\frac{\partial\Delta}{\partial y}+G\nabla^2 v \tag{B.3}$$

$$\rho\frac{\partial^2 w}{\partial t^2}=(\lambda+G)\frac{\partial\Delta}{\partial z}+G\nabla^2 w \tag{B.4}$$

where

u, v, and w are the displacements in the x, y, and z-directions,

ρ is the density of the medium,

λ is Lamè's constant and G is the modulus of rigidity (shear modulus), and

Δ is the fractional change in volume, or dilatation, and is equal to the sum of the normal strains acting on an element; $\Delta = \epsilon_{xx} + \epsilon_{yy} + \epsilon_{zz}$.

The symbol ∇^2 is the partial differential operator

$$\nabla^2 = \left(\frac{\partial^2}{\partial x^2} + \frac{\partial^2}{\partial y^2} + \frac{\partial^2}{\partial z^2}\right) \tag{B.5}$$

Note that this formulation does not account for body forces such as gravity.

Differentiation of Equations B.2, B.3, and B.4 with respect to the appropriate dimension permits separation into dilatational and distortional components of wave motion. Dilatational, or P-wave, motion is described by

$$\rho \frac{\partial^2 u}{\partial t^2} = (\lambda + 2G)\nabla^2 u \tag{B.6}$$

and similarly for v and w. Distortional, or S-wave, motion is described by

$$\rho \frac{\partial^2 u}{\partial t^2} = G\nabla^2 u \tag{B.7}$$

and similarly for v and w. Note that both of these equations follow the standard format for the wave equation $\partial^2 u/\partial t^2 = c^2 \nabla^2 u$, where c is the wave propagation speed, and so the propagation speed for each type of wave can be determined using elastic constants. Thus the velocity of P-waves and S-waves are given by (Kolsky 1963; Persson et al. 1994)

$$c_P = \sqrt{\frac{\lambda + 2G}{\rho}} = \sqrt{\frac{E(1-\nu)}{\rho(1-2\nu)(1+\nu)}} \tag{B.8}$$

$$c_S = \sqrt{\frac{G}{\rho}} = \sqrt{\frac{E}{2\rho(1+\nu)}} \tag{B.9}$$

where E is Young's modulus and ν is Poisson's ratio.

Raleigh wave velocity can also be determined from classical wave theory. While the equations of motion for body waves are developed within a three-dimensional, unbounded medium, a surface wave requires the introduction of a two-dimensional free boundary. At this boundary, three of the nine stress components that describe the state of stress are zero. Analysis of the resulting equations of motion gives a wave speed equal to a fraction of the distortional wave velocity, or $c_R = \kappa c_S$. This fraction κ can be determined by solving the following cubic polynomial in κ^2 (Kolsky 1963)

$$\kappa^6 - 8\kappa^4 + (24 - 16\alpha^2)\kappa^2 + (16\alpha^2 - 16) = 0 \tag{B.10}$$

where $\alpha^2 = (1-2\nu)/(2-2\nu)$. Alternatively, Persson et al. (1994) gives an approximation of c_R as

$$c_R \approx c_S\left(\frac{0.86 + 1.14\nu}{1+\nu}\right) \tag{B.11}$$

To give the reader a relative comparison between the velocities of P-waves, S-waves, and Raleigh waves, a Poisson's ratio of 0.27 is assumed in Equations B.8, B.9, and B.10 and velocity ratios taken with respect to c_S. The result is c_P/c_S = 1.74 and c_R/c_S = 0.95.

B.3 Attenuation of wave energy

All seismic waves travelling through a medium, even ideal ones in which no energy is absorbed through friction losses, experience a decrease in amplitude as they progress. This is called attenuation. The only exception to this is an ideal plane wave travelling through a bar. Hustrulid (1999) identified four primary causes of attenuation:

- *Geometric spreading* – The decrease in amplitude that occurs as a wavefront encompasses an ever-increasing region. Energy is not lost, just spread over a larger region. The amplitude reduction can be calculated as

$$A = \frac{A_0}{R^n} \tag{B.12}$$

  where A is the amplitude of the wave at a distance R from its energy source, A_0 is the original amplitude, and n is a constant equal to 0 for plane waves, 1/2 for cylindrical waves, and 1 for spherical waves (Hustrulid 1999).

- *Dispersion* – Dispersion refers to the broadening of a wave pulse as its constitutive frequency components travel at different rates. In a perfectly-elastic, isotropic medium, a wave will not disperse. However, a number of factors such as variations in a material's elastic properties, discontinuities and boundaries, internal friction, anisotropy, etc., will cause the velocities of the components of a wave to become frequency dependent (Bollinger 1971; Hustrulid 1999; Kolsky 1963). Usually, the high frequency components travel at slower speeds than the low frequency components (Hustrulid 1999). As different frequency-velocity groups separate, the

result is a "spreading" of a wave and a reduction in amplitude and thus energy.

- *Reflection at acoustic boundaries* – When a wave meets an internal boundary, a portion of it is reflected, and thus energy is retained in the system that would have originally continued onwards. As can be imagined, a typical body of rock contains numerous internal boundaries ranging from grain-sized to large discontinuities and thus, attenuation through internal reflections is present.
- *Damping* – Damping, also called inelastic attenuation, occurs as a result of internal friction losses when energy is absorbed from the wave by the medium.

Attenuation can be simplistically modeled using two different approaches: an exponential law and a power law (Hustrulid 1999). They are

$$A = A_0 e^{-\alpha R} \tag{B.13}$$

$$A = \frac{A_0}{R^{\beta}} \tag{B.14}$$

where α and β are attenuation factors that incorporate the four sources of attenuation as previously discussed. Both approaches have been used in technical studies with success. Hustrulid (1999) makes the claim that the exponential law appears to be the most technically apt formulation for studying attenuation. He does note, though, that the power law has provided a stronger statistical correlation with experimental data in some studies.

One widely used approach to estimating seismic attenuation is through the use of the seismic quality factor Q, first pioneered by Born (1941). Studies of wave attenuation in rock samples of varying quality have shown that over a large range of frequencies, the energy losses of a wave can be described using a factor specific to the rock quality. The underlying relationship is

$$\frac{\Delta E_i}{E_i} = \frac{2\pi}{Q} \tag{B.15}$$

where E_i is the energy contained in a wave at cycle i, ΔE_i is the wave energy lost per cycle i, and Q is the seismic quality factor specific to the rock type (Hustrulid 1999). Over n cycles, the energy content is given by

$$E_n = E_0\left(1 - \frac{2\pi}{Q}\right)^n \tag{B.16}$$

where E_0 is the energy initially contained in the wave and E_n is the energy available in the wave after n cycles. When using the exponential law presented in Equation B.13 and noting that for a wave $E \propto A^2$, the Q factor can by incorporated as

$$A = A_0 e^{-\alpha R} = A_0 e^{\frac{\pi R}{Q\lambda}} \tag{B.17}$$

where λ is the wavelength of a specific frequency component of a seismic wave.

Since higher frequency wave components oscillate much more rapidly within a given travel distance than low frequency wave components, the end result is that high frequencies within a wave will attenuate much more rapidly. As noted by Born (1941), the ground acts as a low-pass filter. In the context of rock blasting, the implication is that

blast-induced seismic vibrations will increasingly shift towards containing low dominant frequencies as they travel farther away from the explosive energy source. Kjartansson (1979) developed a transfer function for Q-based attenuation that can easily be applied in the frequency domain. Several individuals have used Kjartansson's work to incorporate the Q factor into blast vibration attenuation models (Blair and Spathis 1982; Yang and Scovira 2010).

It is worth noting that while the Q factor seems to work quite well, there are instances where it can be inadequate (Hustrulid 1999). Also, conservation of momentum is not preserved using Q-based attenuation. As the radius of the wave front increases, the net momentum of the wave decreases. This is the result of assuming a constant wave propagation velocity.

B.4 Blasting vibrations

A significant amount of time and effort has been dedicated in the mining industry to understanding and controlling blast-induced ground vibrations. Most studies have focused on the effects of far-field surface vibrations and their effects on structures, with some of the most extensive ones being conducted by the U.S. Bureau of Mines. As mentioned at the beginning of the chapter, blast vibrations can be categorized into two types: near-field and far-field. The delineator lies in the types of waves encountered at different distances from the energy source. Within the immediate region of the explosive charge, the majority of seismic motion occurs as body waves emanating from the blast. Further out, a portion of these become surface waves as they encounter the surface of the ground. Since surface waves are confined to the plane of the earth's surface, their energy does not spread as rapidly as body waves. Thus, body waves are predominant in the near-

field, while surface waves constitute the bulk of the ground motion encountered in the far-field. In addition to direct body waves and surface waves, body waves can also be reflected and/or refracted dependent upon the structural geology and rock heterogeny in general. Near-field vibration characteristics are mostly governed by the explosive properties and blast design, whereas with far-field vibrations, the transmitting medium exerts the most influence (Siskind et al. 1980). Figure B.11 provides an illustration of the different paths that can be traveled by seismic waves.

B.4.1 Vibration measurements and criteria

Field measurements of blast vibrations are usually obtained using a seismograph equipped with vibration transducers such that motion is measured along three orthogonal axes, as shown in Figure B.12. These axes are oriented so that transverse, vertical, and longitudinal vibrations are independently recorded. Since velocity is a vector quantity, the three orthogonal motions can be treated as vectors that when combined fully specify the movement of a particle in three-dimensional space.

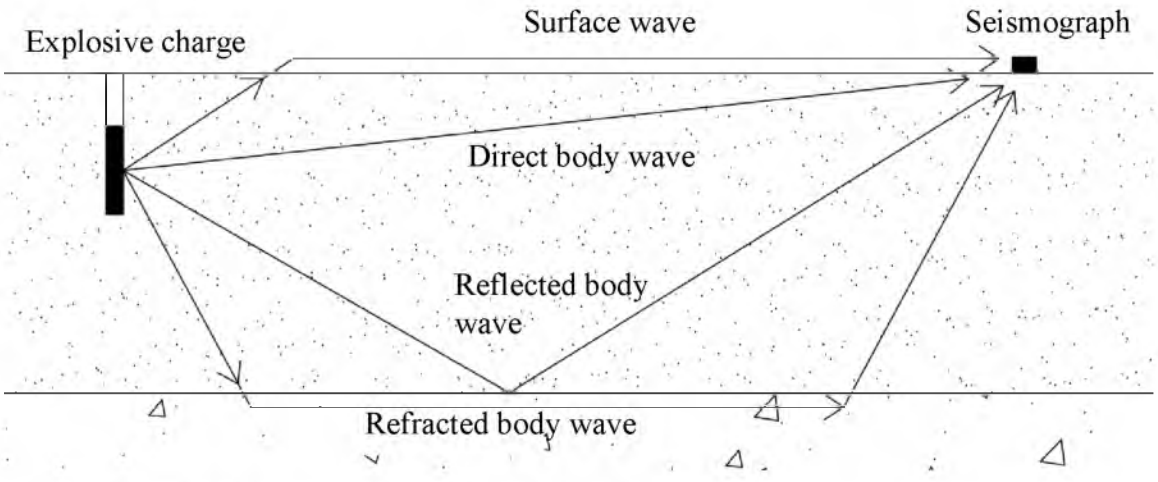

Figure B.11 Ray paths for various types of waves from an explosive charge

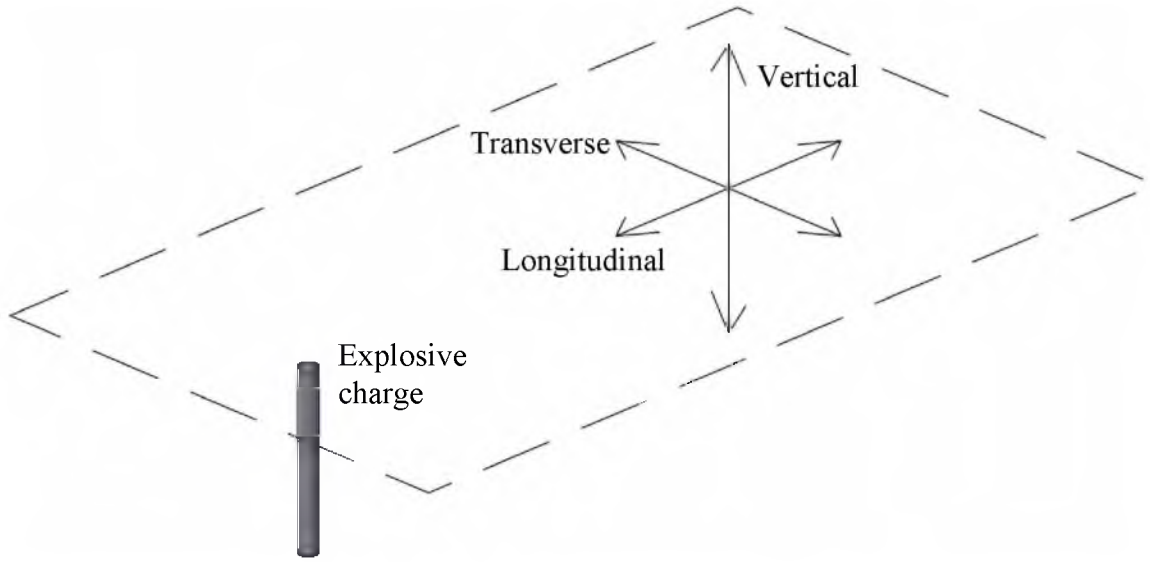

Figure B.12 Orthogonal ground motion axes

Particle vibrations can be characterized using displacement, velocity, or acceleration. Which one is employed in a particular scenario is mainly based on (1) the capabilities of instruments used in measuring vibrations and (2) the characterization's usefulness when applying a specific criterion. Given the wide variety of means available to measure vibrations, all three are used. Among the more popular tools at one's disposal are strain gauges, geophones, and accelerometers, which can measure displacement, velocity, and acceleration, respectively.

Often a conversion from one form to another may be necessary. There are two approaches that can be used. If the vibration history is available, numerical integration or differentiation may be performed according to the following relationships.

$$u = \int v\,dt = \iint a\,dt \tag{B.18}$$

$$v = \frac{du}{dt} = \int a\,dt \tag{B.19}$$

$$a = \frac{d^2u}{dt^2} = \frac{dv}{dt} \tag{B.20}$$

where u is displacement, v is velocity, a is acceleration, and t is time. However, these approaches may not always be practical if the vibration history is unavailable or computing resources are insufficient. Vibration characteristics can sometimes be approximated as simple sinusoids (Dowding 1985). In this case, the peak amplitude relationships between displacement, velocity, and acceleration can be expressed as (Dowding 1985; Siskind et al. 1980)

$$u_{max} = \frac{v_{max}}{2\pi f} = \frac{a_{max}}{4\pi^2 f^2} \tag{B.21}$$

$$v_{max} = 2\pi f u_{max} = \frac{a_{max}}{2\pi f} \tag{B.22}$$

$$a_{max} = 4\pi^2 f^2 u_{max} = 2\pi f v_{max} \tag{B.23}$$

where f is the frequency of the sinusoid.

Care must be taken when using either method. When using numerical methods, the inherent accuracy of either differentiation or integration must be considered (Dowding 1985). Numerical differentiation of a waveform's time history is highly sensitive to small changes in slope between discrete points. It is the author's observation that differentiating experimental time histories has a tendency to greatly amplify the effects of noise and produce significant spiking in the record. Tools such as smoothing,

low-pass filters and derivative formulas specifically for handling noisy data can be applied with varying degrees of success. Numerical integration, on the other hand, often produces an erroneous shift in the baseline of a record away from the origin. Methods to correct this shifting include hi-pass filters and baseline correction using an empirical function (Grazier 1979; Wang et al. 2011). The author has also observed that numerical integrated records tend to appear "smoothed" out, so that higher frequencies are not apparent.

Conversion between displacement, velocity, and acceleration using the sinusoidal approximation method has its limitations as well. A study conducted by the U.S. Bureau of Mines compared peak displacements calculated from velocities by the simple harmonic motion assumption versus numerically integrated velocity records and peak particle velocities calculated using the simple harmonic motion assumption versus measured velocities (Nicholls et al. 1971). As can be observed in Figures B.13 and B.14, their results show that assuming simple harmonic motion in approximating vibration amplitudes tends to underestimate peak values. Most blast vibrations are aperiodic and transient in behavior and thus, a simple sinusoid approximation will only provide a crude level of accuracy. Complex vibration histories cannot be approximated by simple harmonic motion and thus, transforming waveform data to a different metric requires numerical integration or differentiation (Siskind et al. 1980).

Of the three kinematic descriptors for vibration-induced particle motion—displacement, velocity, and acceleration—velocity has become the standard for blast vibrations. Reasons cited for this choice include the extensive body of scientific research correlating particle velocities with structural damage and the usability of velocity as a

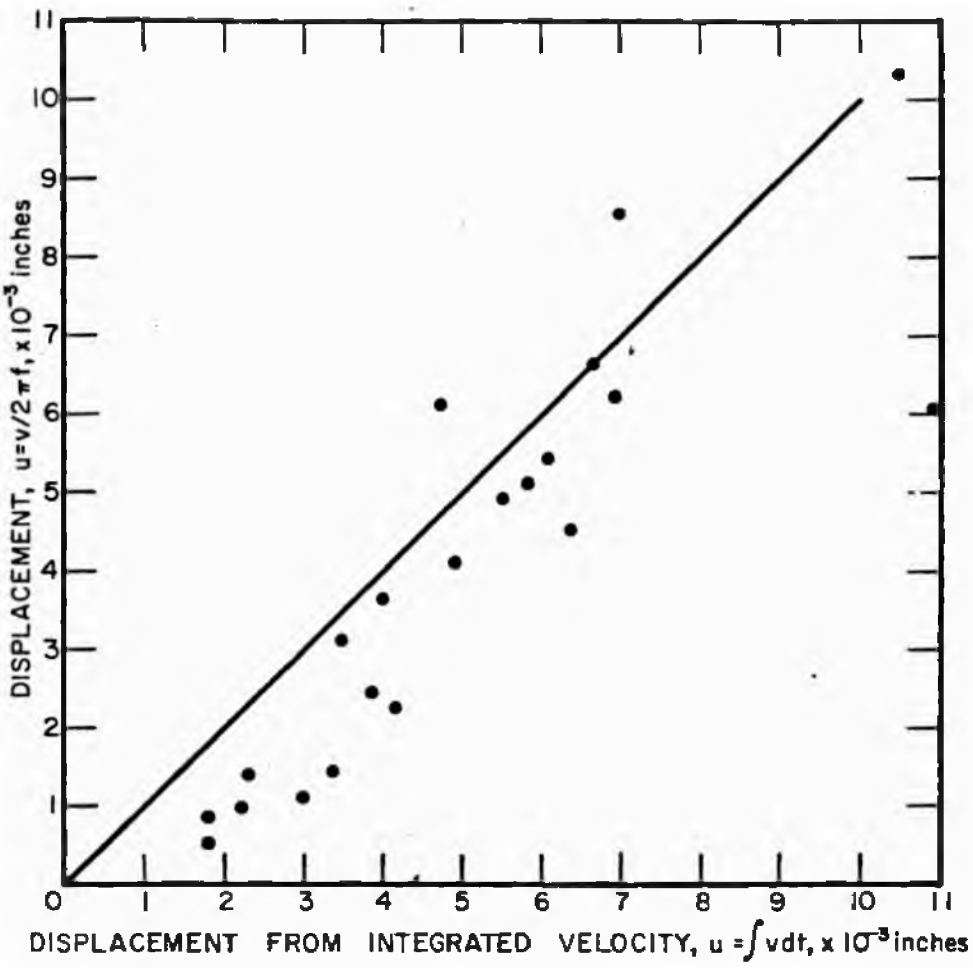

Figure B.13 Comparison of approximated and integrated displacements from velocities (Source: Nicholls et al. 1971. Courtesy of the U.S. Bureau of Mines).

damage predictor (Dowding 1985; Rosenthal and Morlock 1987). Peak particle velocities (PPV) can be reported either as the maximum velocity on one of the three vector components of motion or as the peak vector sum (Dowding 1985). The vector sum v_T, which represents the magnitude of particle motion, is calculated from the three vector components (transverse, vertical, and longitudinal) as

$$v(t)_T = \sqrt{v(t)^2_{trans} + v(t)^2_{vert} + v(t)^2_{long}} \tag{B.24}$$

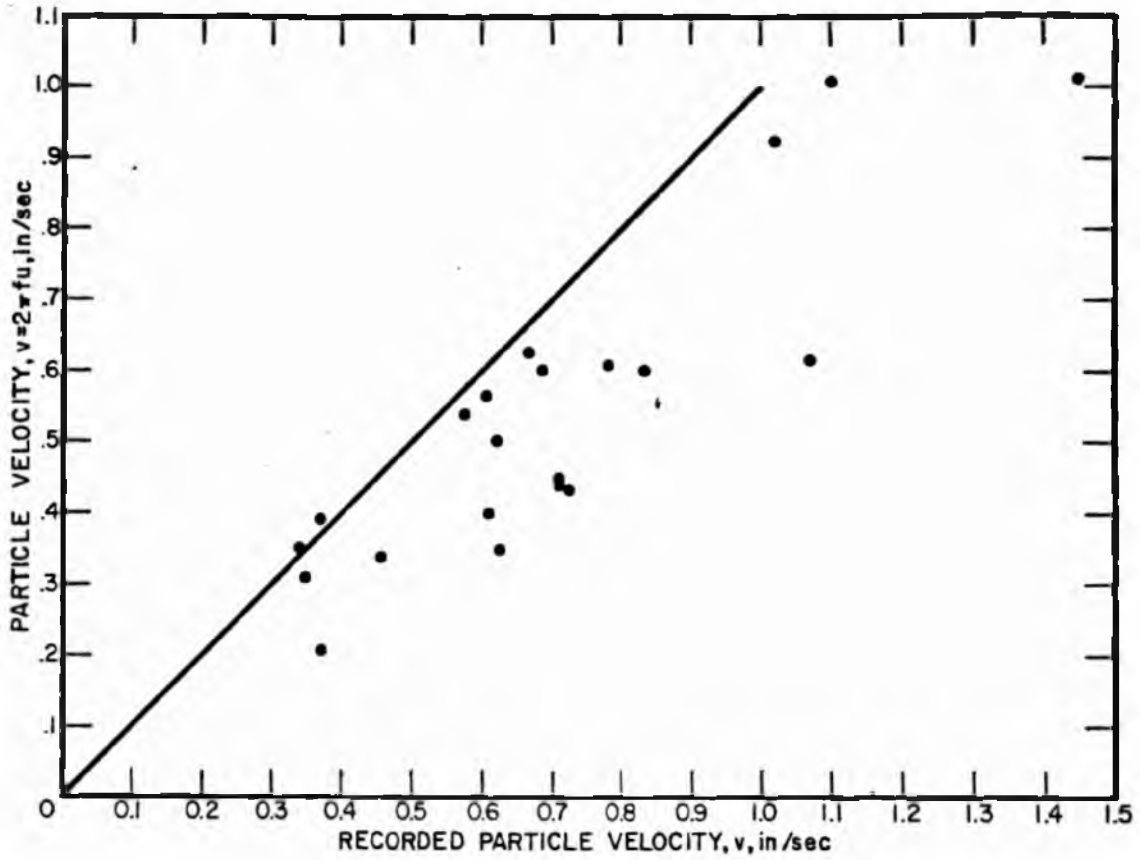

Figure B.14 Comparison of approximated and measured velocities (Source: Nicholls et al. 1971. Courtesy of the U.S. Bureau of Mines).

Particle velocity can also be related to strain using the relationship

$$\varepsilon = \frac{PPV}{c} \tag{B.25}$$

where ε is the strain and c is the wave propagation velocity (Dowding 1985).

Peak particle velocity alone is insufficient to determine damage thresholds, whether the concern is with structures or backbreak. Frequency content, and to a lesser extent duration, of a seismic vibration are also critical factors. Low frequencies have greater potential for causing damage in structures, especially when these frequencies approach resonance (Siskind et al. 1980). Conversely, high frequencies have greater

damage potential in rock due to higher strain gradients (Yang et al. 1993; Yang and Ray 2013). To better understand why, consider the following analysis using simple harmonic motion in one dimension.

Assume a particle vibration history can be represented as

$$v(t) = A_m \sin(kx + \omega t) \tag{B.26}$$

where

A_m is the magnitude of the vibration,

k is the wavenumber,

x is the spatial position of the particle,

ω is the angular frequency of the vibration, and

t is time.

Now this vibration is acting upon an infinitesimal element of cross-sectional area dA and mass dm. Differentiating $v(t)$ with respect to t, the acceleration is

$$a(t) = A_m \omega \cos(kx + \omega t) \tag{B.27}$$

with a maximum acceleration of $a_{max} = A_m \omega$. From Newton's 2nd law of motion, the maximum force applied dF_{max} on the element is

$$dF_{max} = a_{max}\, dm = A_m \omega dm \tag{B.28}$$

The maximum applied normal stress σ_{max} is

$$\sigma_{max} = \frac{dF_{max}}{dA} = \frac{A_m \omega dm}{dA} \tag{B.29}$$

Assuming linear elastic behavior, the maximum induced normal strain ε_{max} is

$$\varepsilon_{max} = \frac{\sigma_{max}}{E} = \frac{A_m \omega dm}{EdA} \tag{B.30}$$

Consider two different possible frequencies acting on the element: ω and 2ω. With frequency ω, the maximum strain is $\varepsilon_{max} = A_m \omega dm/EdA$, whereas with frequency 2ω, the maximum strain exerted is $\varepsilon_{max} = 2A_m \omega dm/EdA$. Even though the peak velocity amplitudes are the same, the strain doubles as the frequency doubles. Thus, the contribution of frequency to blast-induced damage is quite significant.

B.4.2 Scaled distance concept

To compare and correlate vibrations from different blasts and at different distances, a technique for normalizing the measured data must be applied. The scaled distance concept is the most widely used means to conduct this comparison. At distances far-field (and, to some extent, near-field), peak particle vibrations are related to the charge weight W and radial distance R from measurement according to the equation

$$PPV = k\frac{W^{\alpha}}{R^{\beta}} \tag{B.31}$$

where k, α, and β are site-specific constants (Persson et al. 1994). For blast patterns in which multiple holes are initiated at different instances, W is taken to be the effective charge weight within a given interval, usually 8 ms (Dowding 1985).

A scaling law is often assigned such that α/β is equal to a constant. Square root scaling ($\alpha/\beta = 1/2$) and cube root scaling ($\alpha/\beta = 1/3$) are common, with the former being more popular (Dowding 1985; Dowding and Aimone 1992). This leads to the

normalization of both distance and charge into what is termed "scaled distance," as shown in Equation B.32.

$$PPV = k\left(\frac{R}{W^{\frac{\alpha}{\beta}}}\right)^{-\beta} = k(SD)^{-\beta} \tag{B.32}$$

The differences in using square root versus cube root scaling lie in their origins. In both, the vibration amplitude attenuation is assumed to be related to the ratio of the distance from the explosive charge over the charge's radius, or R/r_e. With square root scaling, the explosive charge is assumed to be a long cylinder (i.e., a blasthole). Since the radius of the blasthole is proportional to the square root of the charge weight, $R/r_e = R/W^{1/2}$. With cube root scaling, the explosive is assumed to be a spherical or point charge. Thus, since the radius of the charge is proportional to the cube root of the charge weight, $R/r_e = R/W^{1/3}$.

There are advantages and disadvantages to both scaling laws. Only brief mention of them is given here; for more complete discussions, see Oriard (1982) or Dowding (1985). Square root scaling has become the prevailing tool (Dowding and Aimone 1992). Reasons for this convention include prevalence in studies by the U.S. Bureau of Mines and greater accuracy when predicting at farther distances (Oriard 1982). Cube root scaling tends to be more accurate at close distances. Cube root scaling also enjoys a theoretical backing with regards to energy considerations and is dimensionally consistent according to the Buckingham Pi Theorem (Dowding 1985; Oriard 1982). At medium distances, neither scaling law holds a distinct advantage.

As stated by Oriard (1982), what is important to bear in mind is that the scaled distance concept is a means by which comparisons of vibrations generated by different explosive charge sizes measured at different distances can be made for an expected range of data. It is not meant to give highly-accurate predictions nor facilitate theoretical correctness in predicting vibration attenuation. The scaled distance approach tends to fit rather poorly over large ranges. Its efficacy at close and medium distances has also been questioned (Blair 1987). Attempts to overcome this have been developed, ranging from using different best fit equations for specific domains to incorporating additional complexity.

B.4.3 Fitting a scaled distance model to field data

To determine the constants in Equation B.32, a data set with a reasonable amount of variability is needed. Once such a set is available, the common approach to fitting a curve is with the least squares linear regression technique. Linearization of Equation B.32 gives rise an equation of the form

$$\ln PPV = -\beta \ln SD + \ln k \tag{B.33}$$

This is identical to the equation of a line $y = mx + b$. Using the least squares approach as outlined in any statistics textbook, the best fit line is determined through minimizing the sum of the squares of the error (see Montgomery and Runger 2007). However, as noted by Smith (2003), applying such an approach to the scaled distance transformation in Equation B.33 minimizes the sum of the squares of the logarithm of the error, not the error itself. The logarithmic function inherently reduces large numbers proportionally more than small numbers, and small numbers (<1) can very rapidly have large negative

values. Thus, a best fit line using the simple linear regression approach will not necessarily produce an optimum fit, particularly when the range of the data set is large. Smith (2003) developed the following methodology for finding a true optimum.

Given a particular scaling law, the sum of the residuals squared can be iteratively calculated for a specified range of k and β and the minimum value selected,

$$SRS_{j,f} = \sum_{i=1}^{N} \left[PPV_i - k_j (SD_i)^{-\beta_f}\right]^2 \tag{B.34}$$

where

$SRS_{j,f}$ is an array of the sum of the residuals squared

PPV_i is the peak particle velocity for measurement i,

k_j is one of m values ranging incrementally from k_{min} to k_{max},

β_f is one of n values ranging incrementally from β_{min} to β_{max}, and

SD_i is the scaled distance for measurement i as calculated using Equation B.32.

Equation B.34 can be easily implemented using a computer programming language. Using a contour plotting feature, the array SRS can be visualized as a three-dimensional surface with the plotting axes given by the vectors k_j and β_f. The topographic minimum corresponds to the minimum sum of the residuals squared and is thus the optimal solution. Figure B.15 shows an example contour projection from a sample data set. This approach is limited, however, by the minimum and maximum constraints imposed for k_j and β_f. Care must be taken to ensure that the true minimum occurs within these constraints. Even a small change in the scaling law can drastically change the value of a constant and potentially exceed the assigned range.

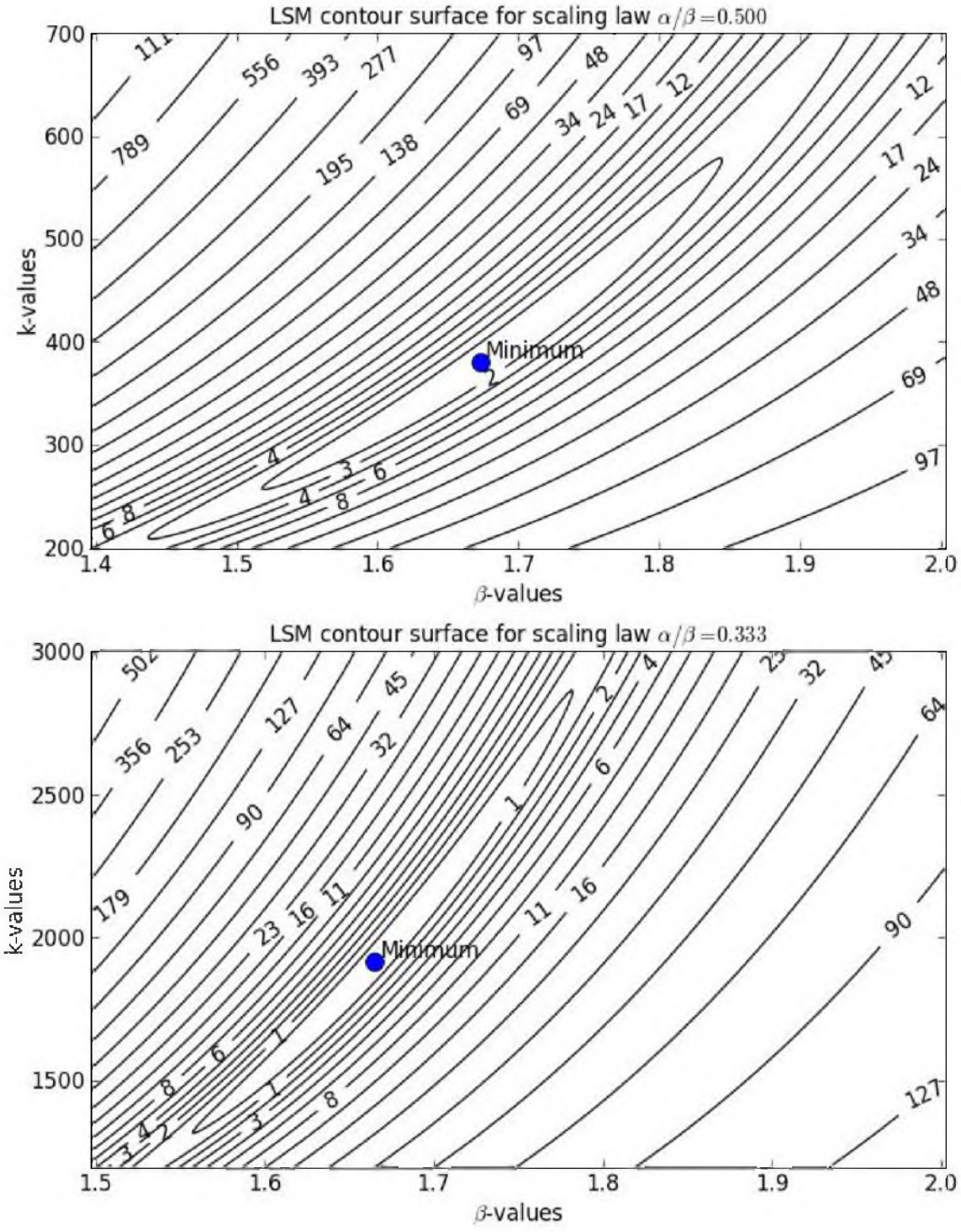

Figure B.15 Two-dimensional contour projection of *SRS* array

An alternative formulation for Equation B.34 is presented by Smith (2003) for reducing the iterative search for a minimum sum of the residuals squared from two to one dimensions (here after referred to as the least squares minimization, or LSM, method). By taking the derivative of the SRS array with respect to k or β and setting it equal to zero, a formula may be prescribed for one constant in terms of the other. Smith chose to derive the formulation in terms of $dSRS/dk$, which is simpler to differentiate. For a given β_f, the value of k_j with the minimum sum of residuals squared may be found as follows.

$$\frac{dSRS_j}{dk_j} = 0 - 2(PPV_1)(SD_1)^{-\beta_f} + 2k_j\left[(SD_1)^{-\beta_f}\right]^2 0 - 2(PPV_2)(SD_2)^{-\beta_f} + 2k_j\left[(SD_2)^{-\beta_f}\right]^2 + \cdots \tag{B.35}$$

$$k_j = \frac{PPV_1(SD_1)^{-\beta_f} + PPV_2(SD_2)^{-\beta_f} + \cdots}{(SD_1)^{-2\beta_f} + (SD_2)^{-2\beta_f} + \cdots}\dagger \tag{B.36}$$

An example comparison from a randomly-generated data set is given in Table B.1 for both the square and cube root scaling laws. In this case, the sum of the residuals squared for the LSM method is moderately less than for the linear regression approach, but the k constants are significantly different. For data with a wider range of scaled distances, the difference can be greater. Figure B.16 shows a graphical comparison of the

† The original formulation given by Smith (2003) for Equation B.36 is

$$k_j = \frac{PPV_2 + PPV_2 + \cdots}{(SD_1)^{-\beta_f} + (SD_2)^{-\beta_f} + \cdots}$$

However, an analysis of Equation B.35 demonstrates this formula to be incorrect.

Table B.1 Comparison of results between linear regression and LSM method

Scaling law	Parameter	Method	
		Logarithmic	Iterative LSM
$\alpha/\beta = 1/2$	β	1.409	1.502
	k	225.63	295.16
	SRS	16.693	14.870
$\alpha/\beta = 1/3$	β	1.461	1.691
	k	1146.35	2739.45
	SRS	21.346	15.45

data used in Table B.1. The code used to perform the calculations and draw Figures B.15 and B.16 was written using Python. The scripts are included in Appendix H.

For conservative estimates of expected peak vibration levels, a 95% upper-bound confidence interval is usually employed. Figure B.17 shows a large set of vibration data with upper confidence bounds at 84% and 95%. The methodology for computing this upper bound (and sometimes the associated terminology) appears somewhat ambiguous, as multiple methods exist. Dowding (1985) makes the observation that when plotting measured peak particle velocities against frequency of occurrence for a given scaled distance range, the distribution follows log-normal behavior. Dowding asserts that the upper-bound intervals must be computed using log-normal statistics. This involves finding the standard error of the least squares regression, raising 10 to this power plus a factor, and multiplying by the median value of the data set. The ISEE Blaster's Handbook (ISEE 2011) set forth a procedure in which the constant k in Equation B.32 is multiplied by the standard error of the least squares linear regression twice to obtain the 95% upper confidence bound, although no statistical explanation is given. A 95% confidence

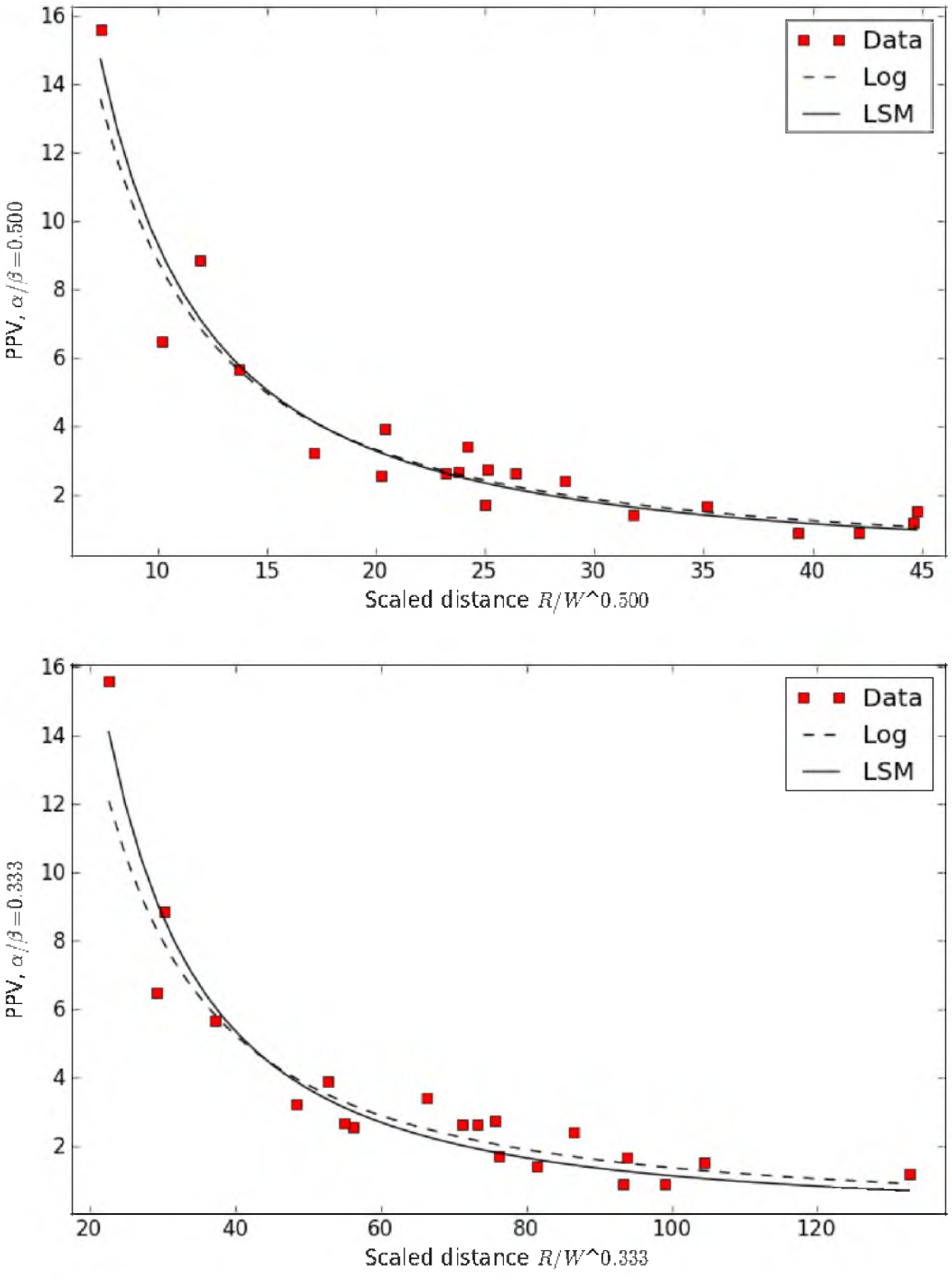

Figure B.16 Visual comparison of logarithm linear regression and LSM methods

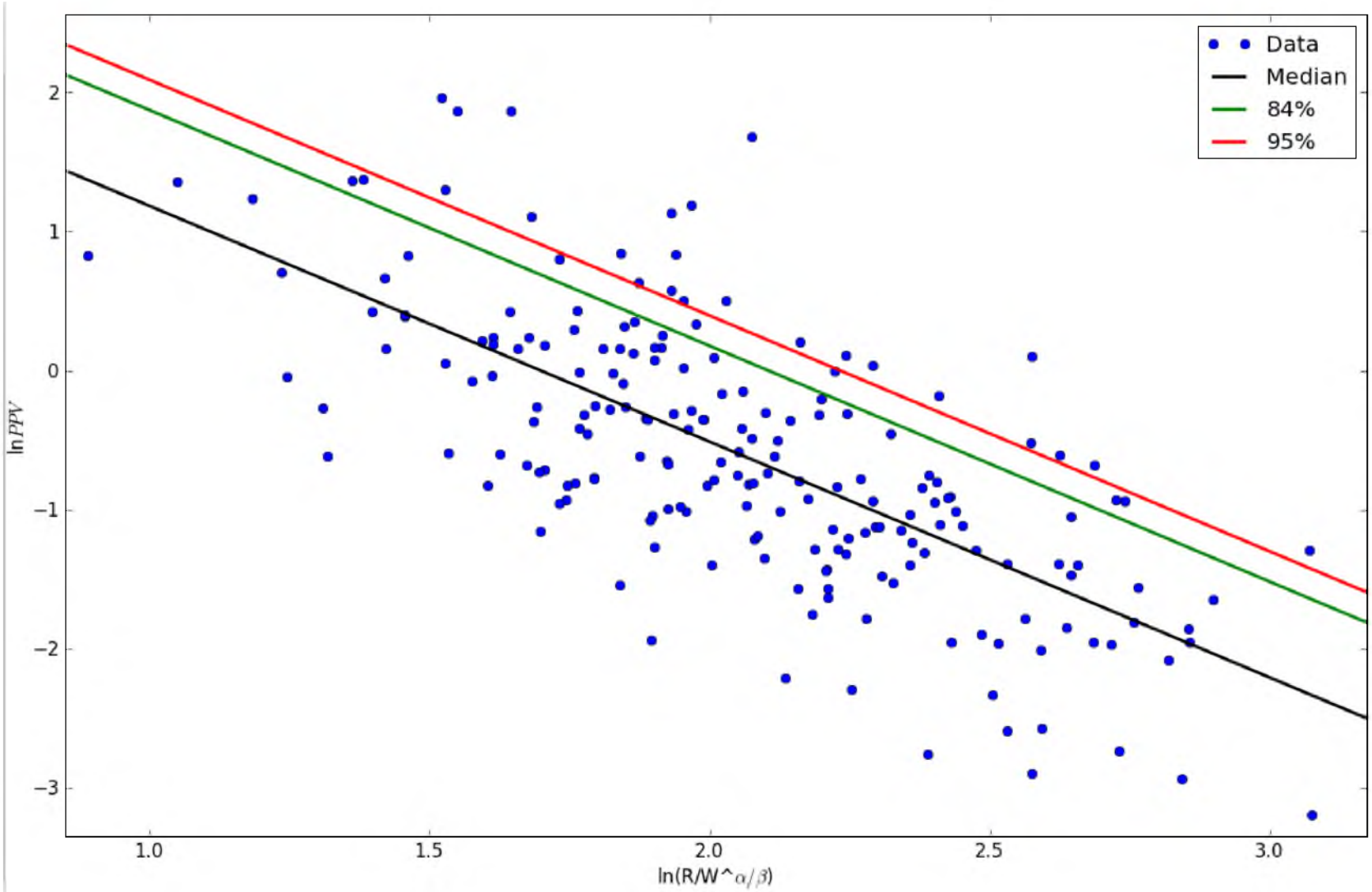

Figure B.17 Sample data set with best fit line and upper confidence bounds of 84% and 95%

interval could also be determined for the intercept of Equation B.33 using normal distribution statistics based on the t-distribution (Montgomery and Runger 2007).

B.4.4 Frequency and response spectra

As was shown at the end of Section B.1, the frequency content of a seismic vibration has a significant effect on its damage potential. A complete analysis of any vibration waveform will include an examination of its frequency spectrum, or at least the frequencies pertinent to the feature of interest. There are several ways to go about this.

B.4.4.1. Manual determination of peak frequency

A particular cycle in a vibration history can be manually examined to ascertain its frequency. This is a crude approach, but sufficient in some cases. To demonstrate, take the vibration signal shown in Figure B.18. The frequency f of the first peak can be estimated by measuring its width, equal to one-half of its period T:

$$f = \frac{1}{2\left(\frac{T}{2}\right)} = \frac{1}{T} \tag{B.37}$$

B.4.4.2. Fast Fourier Transform

One of the most common ways to obtain the frequency spectrum of a vibration history is to employ the Fast Fourier Transform (FFT). This algorithm can be used to transform a vibration history from the time domain to the frequency domain, providing its frequency content.

The theory of Fourier series states that any arbitrary function can be represented over a finite period by a series of sine and cosine terms. This theory can be applied to

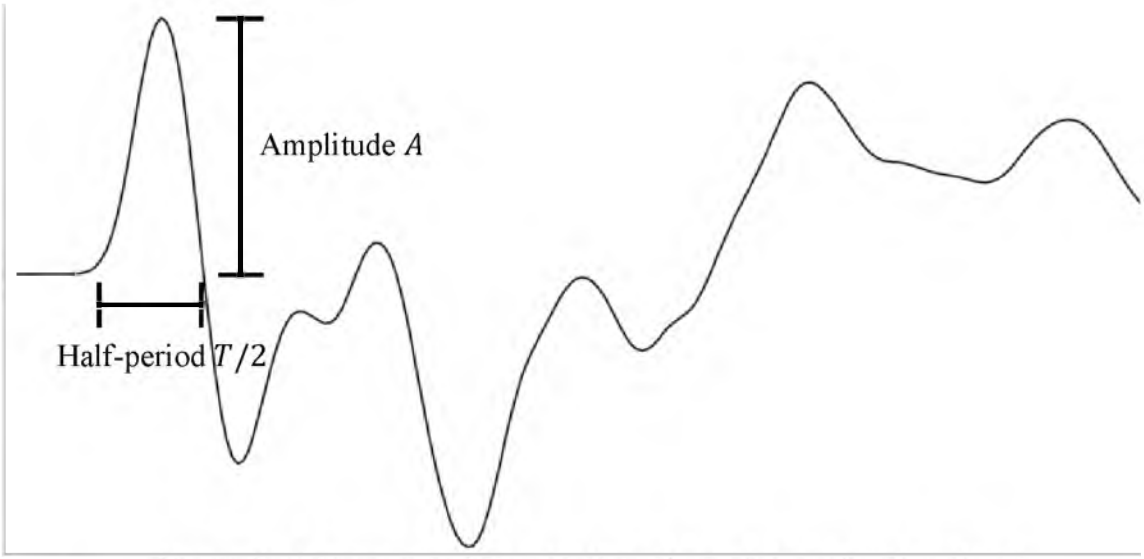

Figure B.18 Frequency determination of a peak in a vibration signal

digital data using the discrete Fourier transform (DFT). For a discrete data set $x[n]$ with N values, the Fourier transform $X[k]$ and inverse Fourier transform $x[n]$ can be represented as

$$X[k] = \frac{1}{N}\sum_{n=0}^{N-1} x[n]e^{-j2\pi k\frac{n}{N}} \tag{B.38}$$

$$x[n] = \sum_{k=0}^{N-1} X[k]e^{j2\pi k\frac{n}{N}} \tag{B.39}$$

where k and n are indices and j is an imaginary number and equal to $\sqrt{-1}$ (Cha and Molinder 2006). The term kn/N is the frequency at particular values of k and n. For a real-valued set $x[n]$, the transform output $X[k]$ is complex valued. The magnitude of $X[k]$ is the frequency amplitude spectrum of $x[n]$ when plotted against a specific range of frequencies. The phase spectrum of $x[n]$ can be calculated from the real and imaginary components of $X[k]$.

One drawback to using the DFT formulation in Equations B.38 and B.39 is that the number of operations to transform a data set of size N is on the order of N^2. This can lead to long calculation times for large data sets. The FFT is a computationally-efficient implementation of the DFT that reduces the number of calculations to, at best, on the order of $N \log_2 N$.

A sample vibration history and its frequency spectrum are shown in Figure B.19. Using this graph, the dominant frequencies present in the waveform can be observed at 23 Hz and 97 Hz. Although the FFT presents the frequency distribution within a vibration record, there is no direct relationship between amplitudes in the time and frequency domains. The amplitude scale of the frequency spectrum provides only a relative comparison of frequencies.

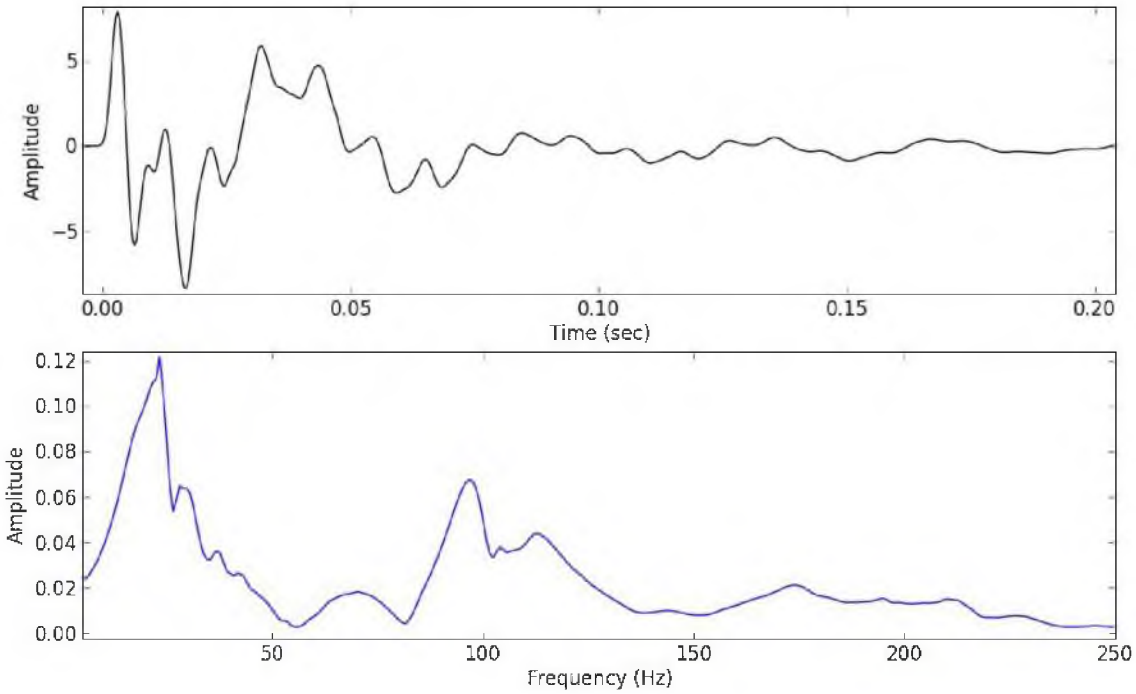

Figure B.19 Vibration history and associated frequency spectrum

A power spectrum may also be computed by taking the square of the frequency spectrum, or $P[k] = |X[k]|^2$. Since the energy of a wave is proportional to the square of its amplitude, the power spectrum can be used to compare the energy content of a wave as partitioned by frequency.

B.4.4.3. Response spectra

Response spectra can be used to evaluate the frequency content of a vibration history. A response spectra analysis is similar to Fourier spectrum analysis in that both show the distribution of frequencies. However, response spectra have the added advantage of being able to directly correlate ground motion amplitude with frequency. Response spectra analysis is more widely used in evaluating structural response, but can be applied to ground motion as well.

Response spectra analysis is based on a single-degree-of-freedom (SDF) mathematical system (Dowding 1985). The governing differential equation is that for a 2nd order mechanical oscillating system, as shown below.

$$m\ddot{x} + c\dot{\delta} + k\delta = 0 \tag{B.40}$$

where

$\ddot{x}$ is the acceleration of mass m,

c is the damping coefficient,

k is the spring constant,

$\delta = x - u$ is the relative displacement of mass m with respect to the ground,

$\dot{\delta}$ is the velocity of mass m with respect to the ground, and

u is the displacement of the ground.

Equation B.40 can be recast as

$$\ddot{\delta} + 2\beta p\dot{\delta} + p^2\delta = \ddot{u} \tag{B.41}$$

where

$\ddot{\delta}$ is the acceleration of mass m with respect to the ground,

$p = \sqrt{k/m}$ is the angular natural frequency of the undamped spring-mass system,

$\beta = \frac{c}{2\sqrt{km}}$ is the fraction of critical damping $2\sqrt{km}$, and

$\ddot{u}$ is the ground acceleration.

To determine the response spectrum of a particular velocity vibration history $\dot{u}(t)$, the following integral can be used, provided that δ and $\dot{\delta}$ are zero at the start time t_0 (Dowding 1985).

$$\delta(t) = -\int_0^t \dot{u}(\tau)e^{-\beta p(t-\tau)}\left[\cos[p_d(t-\tau)] - \frac{\beta}{\sqrt{1-\beta^2}}\sin[p_d(t-\tau)]\right]d\tau \tag{B.42}$$

where

t is the time interval,

τ is the dummy variable within the integral representing time, and

$p_d = p\sqrt{1-\beta^2}$ is the angular natural frequency of the damped spring-mass system.

Equation B.42 predicts the ground motion in terms of relative displacement, not absolute velocity (Dowding 1985). To estimate the particle velocity $\dot{\delta}(t)$, an approximation can be made in multiplying the maximum value of $\delta(t)$ by the angular natural frequency $p = 2\pi f$, where f is the natural frequency in Hz.

$$\dot{\delta}(t) \approx p\delta_{max} = 2\pi f \delta_{max} \tag{B.43}$$

This term $\dot{\delta}(t)$ is called the pseudovelocity or pseudospectral response velocity. It is an approximation based on simple sinusoidal motion, much like that discussed in Section B.1. Figure B.20 shows sample response spectra for two blast-generated vibration histories.

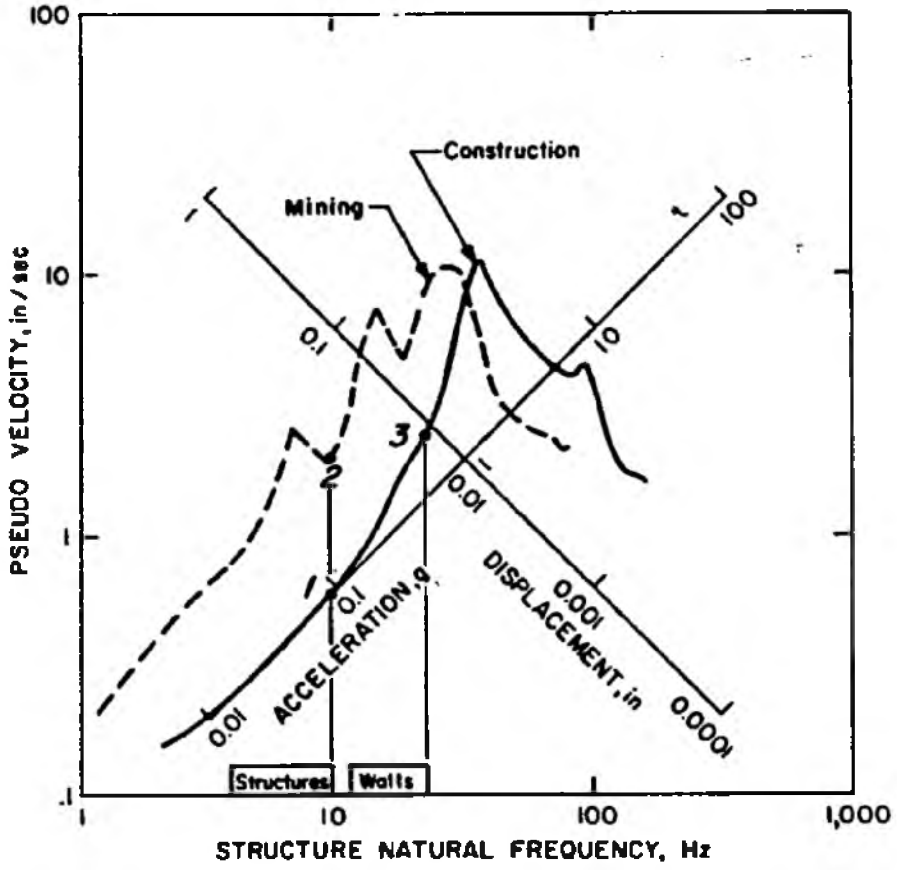

Figure B.20 Response spectra from two different blast vibration records (Source: Siskind et al. 1980. Courtesy of the U.S. Bureau of Mines).

APPENDIX C

MEASURING BLAST INDUCED DAMAGE

A wide variety of methods for measuring blast-induced damage in the field have been tried with varying degrees of accuracy and success. Measurement techniques can be divided into two categories: direct measurements and indirect measurements. For the purposes of this thesis, the distinction is defined as follows:

- *Direct measurements* involve direct observations of damage or of the blast event. Examples include vibration records, fracture observations, bench dilation, and so forth.
- *Indirect measurements* involve analyzing changes in rock properties resulting from the blast damage mechanism. These include methods to measure alterations in wave transmissions, strength, permeability, and geophysical properties.

When deciding on the types of measurements needed for conducting a blast damage study, a number of factors must be considered. Some methods can be easily employed during normal mining activities. Others are more labor intensive and/or expensive and are currently useful only for research purposes. The reliability of each method is important knowledge, both in terms of equipment and the nature of the measurements themselves. Equipment must be tested and, if appropriate, calibrated beforehand. Some methods may be highly sensitive to laboratory or field conditions such as temperature, weather, and durability, which must be taken into account. Because of the violent nature of blasting, instruments employed in near-field measurements can potentially be damaged or destroyed or otherwise unrecoverable.

Each method is tailored towards measuring a particular variable. No one technique can give a comprehensive assessment of blast damage. In any experimental

study of blast damage, an appropriate selection of variables or indicators to delineate between intact and damaged rock will need to be made.

C.1 Direct measurements

C.1.1 Vibration

One of the most common means of measuring blast damage, both near-field and far-field, is by vibration measurements. Studies in the mid- to late-1900s primarily focused on the effects of vibrations to structures. A more recent emphasis has been placed on near-field blast-induced damage in the scientific community, and with it vibration as a damage criterion continues to be widely-incorporated. While vibrations do not directly measure damage in the ground, they do provide a record of the ground motion. Through knowledge of the mechanical properties of the ground and the use of appropriate constitutive laws, these vibrations can be mathematically related to solid material behavior and thus failure models.

Two of the most common variables used to assess the possibility of failure are strain and strain rate. All solids eventually yield and/or fail when undergoing sufficient deformation. Rocks, being brittle, tend to fail at smaller strains than other solids such as metals. The magnitude of strain, and consequently stress, that a material can sustain is in part influenced by the strain rate. Studies on the behavior of solids under different loading rates show that the strengths of dynamically-loaded test specimens can be several times higher than for quasistatically loaded ones (Sun 2013). All three of the kinematic descriptors of vibration discussed in Section B.1 of Appendix B can be related to strain and/or strain rate.

As briefly mentioned in Section B.1, the most common instruments for use in measuring ground vibrations are strain gauges, geophones, and accelerometers. Each of these has advantages and disadvantages, including cost, ease of installation, response range and characteristics, and durability.

C.1.1.1. Strain gauges

A strain gauge is essentially a thin wire filament, constructed such that deformation in the plane occupied by the gauge will stretch or shorten the wire and alter its resistance. When a voltage is applied across the strain gauge, this change in wire length causes a change in current that can be measured. The relationship between resistance and strain is given by

$$\varepsilon = \left(\frac{1}{\lambda}\right)\left(\frac{\Delta R}{R}\right) \tag{C.1}$$

where ΔR is the change in resistance, R is the original resistance, and λ is called the gauge factor and is specific to the make of the strain gauge. Figure C.1 shows an example set of gauges.

Figure C.1 Two strain gauges, here mounted in perpendicular orientations

Strain gauges provide a direct measurement of strain. However, the strains that exist within a particular sample or body of rock can vary widely from several factors, especially if the rock is nonhomogeneous with respect to grain sizes. Thus, measured strains may be highly localized and thus representative of only a small region (Anderson et al. 2004). Strain gauges also require a strain balance, strong bonding to a surface, and calibration before each use. For mounting in nonhomogeneous materials such as rocks, larger strain gauges are preferable since they are less influenced by inhomogeneities such as grains that could produce inconsistent results (Micro-Measurements 2010).

C.1.1.2. Geophones

Geophones are instruments that measure vibrations in terms of velocity. While geophone designs vary, the basic construction is shown in Figure C.2. The working principle behind geophones is Faraday's law of induction, which states that a magnetic mass moving within a conductive wire coil generates a voltage proportional to the velocity of the mass.

Geophones can be modeled as a 2nd-order, mechanical oscillating system, which in terms of a differential equation can be expressed as (Bradley and Eller 1961)

$$m\frac{d^2\delta}{dt^2} + c\frac{d\delta}{dt} + k\delta = -m\frac{d^2u}{dt^2} \tag{C.2}$$

where

m is the magnetic mass,

c is the damping applied to th mass, here generated by friction and a counterelectromotive voltage,

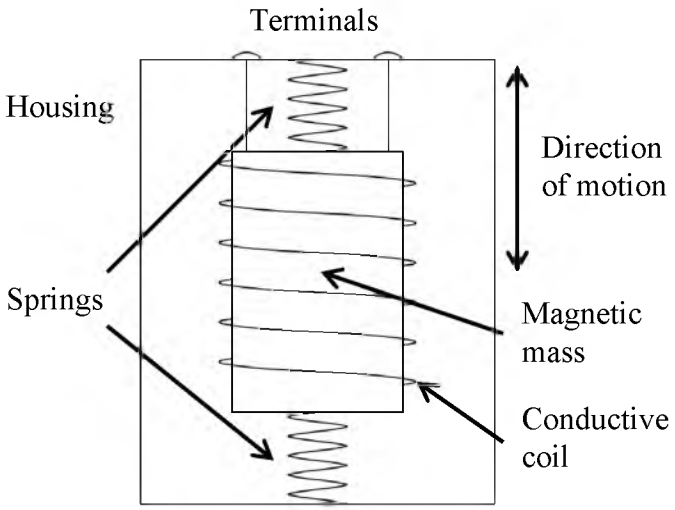

Figure C.2 Basic principles of a geophone

k is the spring constant,

δ is the displacement motion of the mass relative to the ground,

u is the displacement motion of the ground, and

t is time.

The solution to this equation for a vibration transducer involves assuming steady-state sinusoidal motion $u = u_0 \cos \omega t$ to satisfy the term $-m\, d^2u/dt^2$. This approach, however, ignores the transient terms that appear when solving Equation C.2 (Bollinger 1971). This fact warrants at least acknowledgement when monitoring blast vibrations, as blast vibrations are transient in nature. The frequency response of a geophone, given either as a ratio of displacements or velocities, is (Bradley and Eller 1961)

$$\frac{\delta}{u} = \frac{\dot{\delta}}{\dot{u}} = \frac{\left(\frac{\omega^2}{\omega_n^2}\right)}{\sqrt{\left(1 - \frac{\omega^2}{\omega_n^2}\right)^2 + \left(2\beta \frac{\omega^2}{\omega_n^2}\right)^2}} \tag{C.3}$$

where

$\dot{\delta}$ is the velocity motion of the mass relative to the ground,

$\dot{u}$ is the velocity motion of the ground,

ω is the particular frequency under consideration (can be either angular or conventional frequency f),

$\omega_n = \sqrt{k/m}$ is the undamped natural frequency of the geophone, and

$\beta = \frac{c}{2\sqrt{km}}$ is the fraction of critical damping $2\sqrt{km}$.

The transfer function for a geophone, which describes the dynamic response at different frequencies, is given by (Geospace Technologies, personnel communication)

$$E(\omega) = G\left(\frac{R}{r_c + R}\right)\left(\frac{\dot{\delta}}{\dot{u}}\right) = \frac{G\left(\frac{\omega^2}{\omega_n^2}\right)\left(\frac{R}{r_c + R}\right)}{\sqrt{\left(1 - \frac{\omega^2}{\omega_n^2}\right)^2 + \left(2\beta\frac{\omega^2}{\omega_n^2}\right)^2}} \qquad \text{(C.4)}$$

where

E is the excitation voltage output, and is a function of either δ/u or $\dot{\delta}/\dot{u}$,

G is the intrinsic voltage sensitivity of the geophone in units of V/mm/s (V/in./s),

r_c is the internal coil resistance of the geophone, and

R is the shunt resistance applied across the terminals. If no shunt is present, then $R \to \infty$, and so $\lim_{R\to\infty}[R/(r_c + R)] = 1$.

This function can be applied in the frequency domain to correct for low frequencies using the relationship (Cha and Molinder 2006)

$$Y(\omega) = Z(\omega)/E(\omega) \tag{C.5}$$

where

$Y(\omega)$ is the true ground motion, and

$Z(\omega)$ is the ground motion measured by the geophone.

In addition to dynamic response, geophones also have a phase lag in relation to ground motion. This lag ϕ is expressed as (Bradley and Eller 1961).

$$\phi = \tan^{-1} \frac{2\beta \frac{\omega}{\omega_n}}{1 - \left(\frac{\omega}{\omega_n}\right)^2} \tag{C.6}$$

As was discussed in Section B.1, knowing the frequency content of a blast-induced vibration is important information. Knowing the phase content can be useful too. For geophones, the phase difference between measured motion and true ground motion is close to 180° at frequencies above the natural frequency. If the actual polarity of ground motion is needed, consideration of the phase lag must be taken into account. When applying the transfer function in Equation C.4 to a record, correcting for both the amplitude and phase response will usually result in less error, as was demonstrated in a shaking table study conducted by Farnfield (1996). It is the author's observation that adjusting a vibration record from a geophone may also require a window and/or high-pass filtering. Low frequencies seem to have a tendency to cause severe distortions of transient or aperiodic vibration waveforms when correcting with the transfer function.

Figures C.3 and C.4 show the frequency response magnitude and phase, respectively, for a sample geophone. There are four things to note here. First, frequencies

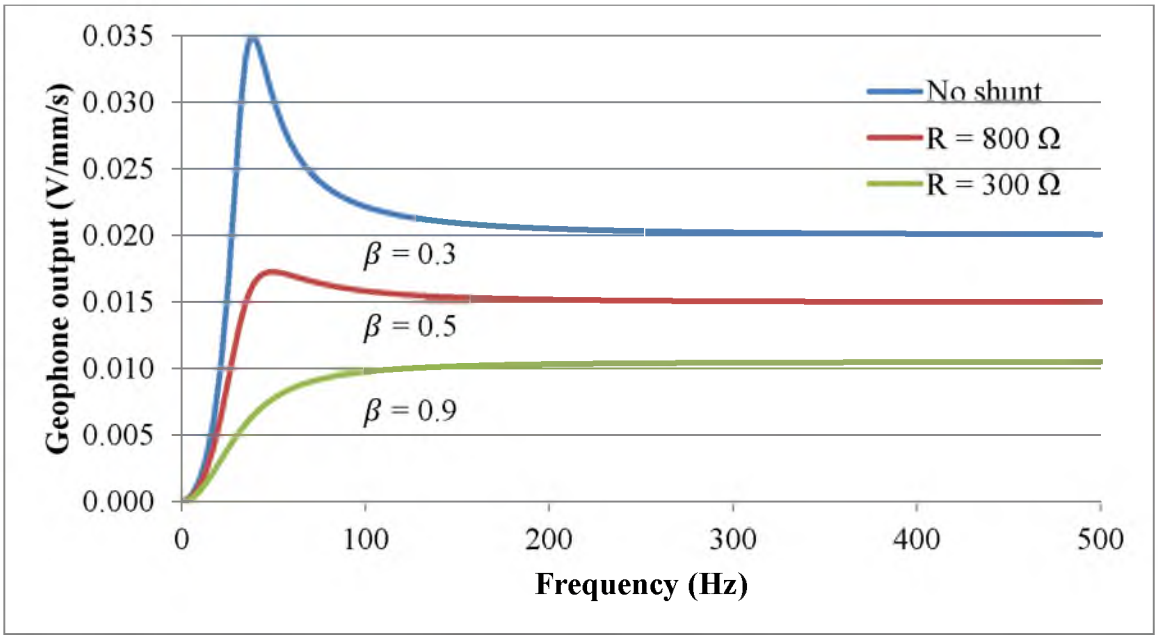

Figure C.3 Illustration of geophone frequency response

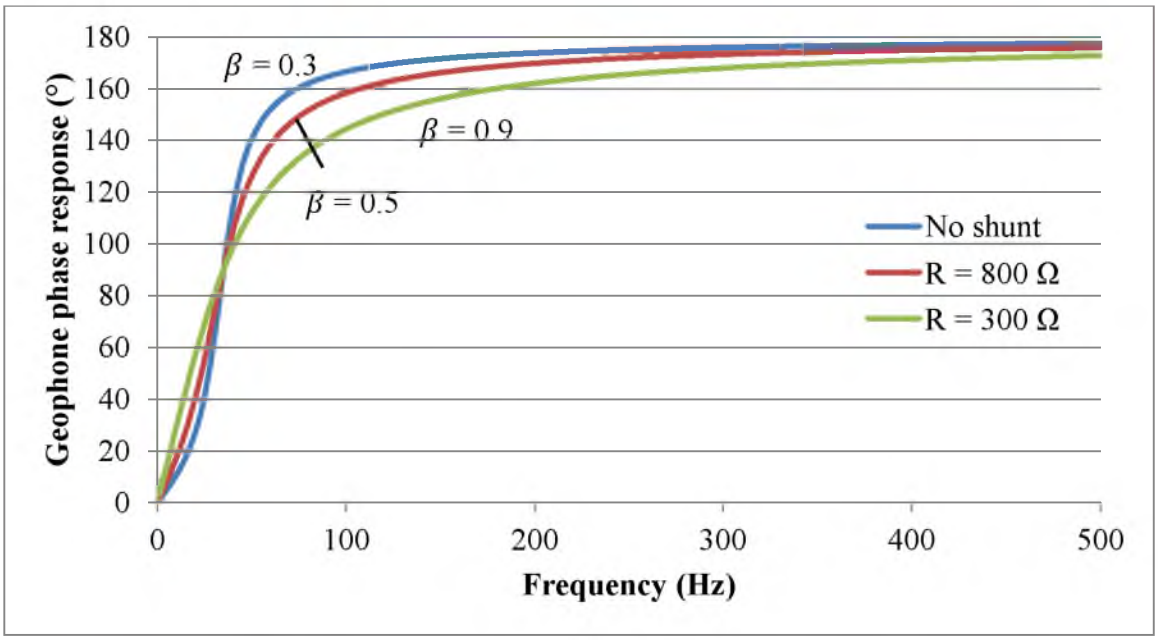

Figure C.4 Illustration of geophone phase response

near the natural frequency tend to distort when the fraction of critical damping is low. Second, although it may not be readily apparent, the damping and shunt resistance are related. The smaller the shunt resistance, the greater the damping. This relationship can be used to reduce the dynamic response of a geophone so that it can measure larger amplitudes such as near-field blast vibrations. Third, the response of the geophone flattens out at frequencies above its natural frequency. This is the preferred frequency range to employ a geophone. Fourth, at frequencies above the order of 800 Hz or so, an unwanted phenomenon called spurious frequencies can develop. This occurs from multiple causes. Sometimes, the internal mass of the geophone rattles transversely to its axis of motion in what is termed spurious resonance (Faber and Maxwell 1997). Other times, harmonics in the electrical signal may be amplified at high frequencies (Bradley and Eller 1961). The spurious frequency places an upper limit on the frequency range of a geophone.

The damping factor of a geophone may be estimated by using a battery with a small voltage (~1–2 V), a switch, and a data acquisition unit (Hagedoorn et al. 1988). The battery is connected across the terminals of the geophone and the switch is turned on, then off. This moves the internal mass away from its state of equilibrium then releases it, causing the internal mass to oscillate as it rebounds. The voltage history as recorded by the data acquisition unit will look similar to Figure C.5. The fraction of critical damping is calculated as

$$\beta = \sin\left[\tan^{-1}\left(\frac{1}{\pi}\ln\frac{A_1}{A_2}\right)\right] \tag{C.7}$$

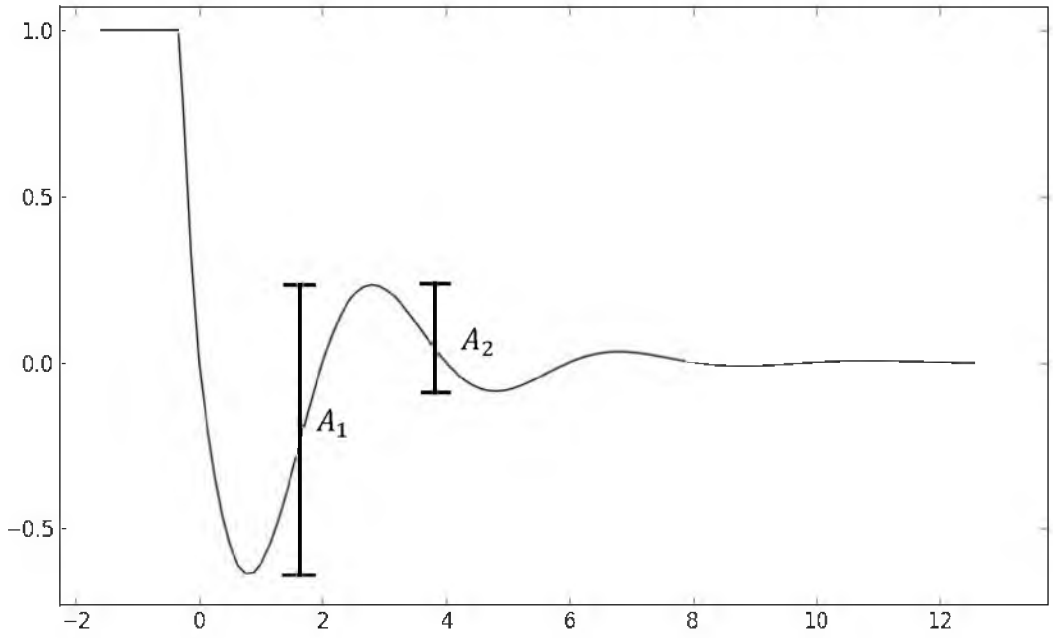

Figure C.5 Geophone damping factor estimation After Hagedoorn et al. (1988).

This technique is limited, though, for values of β less than 0.7 (Hagedoorn et al. 1988). Determining higher values of β requires the use a complex phase response method.

Another way to estimate critical damping is with the following formula given by Hoffman (2003):

$$\beta = \beta_{open} + \frac{G^2}{r_c + R} \tag{C.8}$$

where β_{open} is the open-circuit fraction of critical damping for the geophone and G, r_c, and R are the same as before. However, it is the author's observation that this formula has a tendency to overestimate β at higher values when compared to manufacturer's specifications for geophones.

Depending on the sensitivity of the measurements to be performed, there are a number of tests that may need to be performed on a geophone. Hagedoorn et al. (1988)

provided the following comprehensive list:

- Conformity to manufacturer's specifications:
  - Resistance,
  - Polarity,
  - Frequency,
  - Damping,
  - Sensitivity, and
  - Distortion.
- Upper frequency limit as dictated by spurious responses;
- Infiltration of unwanted noise through leakage;
- Stability in maintaining tolerances, even after events such as a shock;
- Sticking coil;
- Dirt, meaning that a something such as small fiber is touching the coil and thus affecting the geophone's threshold;
- Sensitivity to temperature variations; and
- Durability with repeated use and adverse field conditions.

Field application of geophones requires several considerations in addition to calibrating and testing the geophone. Most important among these is the quality of coupling between the instrument and the ground. Three practices often employed in the field are burying the instrument in the ground, driving a spike into the ground with the instrument mounted on the spike, and simply setting the instrument on the ground (Wheeler 2004). Poor or inadequate coupling will increase error present in vibration readings, as has been demonstrated through studies such as Segarra et al. (2013) and

Wheeler (2004). For near-field blast vibrations, which have large amplitudes, a solid means of anchoring is required. Options include bolting into a rock outcrop on the surface, securing downhole using a "foot" that can wedge itself between the borehole walls, or positioning downhole and the pouring in a grout mixture. In addition to coupling, the dynamic range of the geophone and the intrinsic noise levels must also be considered (Badger et al. 1990). Vibrations that exceed the range capability of the geophone or are below the noise threshold will result in poor measurements.

The response of many geophones is also sensitive to the orientation of the transducer. Some geophones are unidirection and must be vertical, some can operate at angles up to 90° from vertical, and some are omnidirectional and can be positioned at any angle.

C.1.1.3. Accelerometers

Accelerometers measure vibration in terms of acceleration. Their basic construction consists of a mass mounted on a piezoelectric element, usually made of quartz or certain kinds of ceramics (PCB Piezotronics 2013a). Vibrations experienced by the accelerometer cause the mass to apply a load to the piezoelectric element, which responds by producing a charge directly proportional to the acceleration. As shown in Figure C.6, there are three basic configurations in which the piezoelectric element can deform: compression, shear, and flexure.

Accelerometers cannot be connected to a normal data acquisition system without first routing the signal through a signal conditioner. The type of signal conditioner that can be used depends on the electronics included in the accelerometer. There are two main designs that dictate how the accelerometer operates: charge mode or integrated circuit

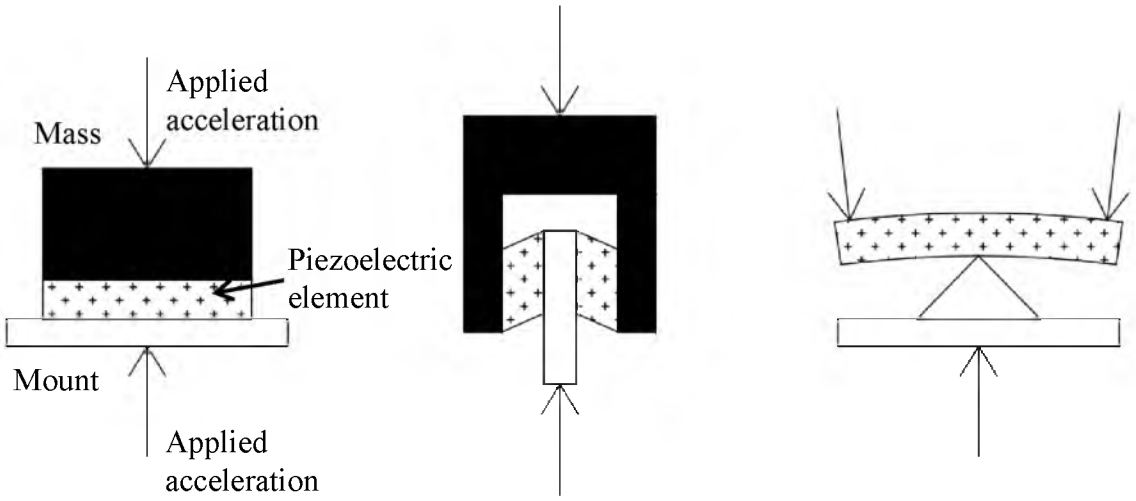

Figure C.6 Accelerometer designs: left – compressive, middle – shear, right – flexural
After PCB Piezotronics (2013b).

(PCB Piezotronics 2013a). The more basic type is a charge mode accelerometer, which internally consists of only the piezoelectric element itself. The high-impedance, electrical charge signal that comes from a charge mode accelerometer is very sensitive to the environment and corrupts very quickly, even when traveling through a shielded cable. In-line signal conditioners are required near the location of the accelerometer to convert the signal to a low-impedance voltage that can then be carried large distances with little alteration. The main advantage of charge mode accelerometers is their durability in high temperature applications. Integrated circuit accelerometers contain internal electronics that automatically convert the high-impedance charge to a low-impedance voltage as well as perform other tasks such as filtering and gain adjustment. Integrated circuit accelerometers require a constant DC power source and a signal conditioner that can be inline or built into to the data acquisition unit. There are multiple proprietary brands of integrated circuit accelerometers.

Because of the stiff nature of the piezoelectric element, accelerometers can measure very high frequencies up to 100 kHz (Bradley and Eller 1961). The frequency response of an accelerometer, shown in Figure C.7, is determined from two different considerations. The first comes from a mathematical analysis very similar to that used in Equations C.2 and C.3, which implies that the resonance frequency limits the upper bound of an accelerometer's usable frequency range. The lower frequency bound is determined by the time constant of the circuitry of the piezoelectric transducer and any incorporated electronics. The amplitude response is fairly flat within a specific range specified by the manufacturer. The phase response within this range is usually close to 0°. Thus, typically only scaling of an accelerometer record is needed, as opposed to applying a transfer function for a geophone.

Calibration and testing of an accelerometer is usually done by the manufacturer, as accelerometers tend to be significantly more expensive than geophones. Field application of the accelerometer involves many of the same considerations as a

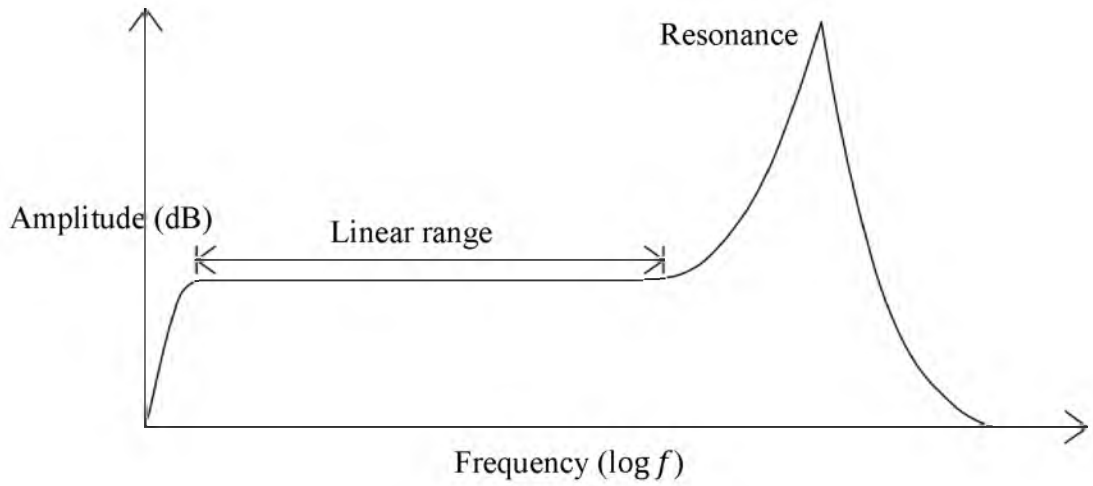

Figure C.7 General frequency response for an accelerometer

geophone, such as proper coupling, sensitivity to the environment and temperature, and so forth. However, accelerometers are more shock resistant than geophones and so have a higher dynamic range. Accelerometers are available in very small packages, unlike geophones, which are constrained by the size of the internal magnetic mass and conductive coil.

C.1.2 Visual assessment of damage

There are a number of ways to visually assess blast damage. Most are qualitative in nature, although they can still yield important information (Scoble et al. 1997). Some visual assessment techniques often require pre- and postblast application. Some are also highly subjective to the user's judgment.

C.1.2.1. Half-cast method

Controlled blasting techniques such as presplitting, smooth wall blasting, and line drilling will often leave one side of the perimeter holes intact. These are called half-casts, and have been used for blast damage assessment (Lizotte 1996; McKown 1986; Ouchterlony 1995; Scoble et al. 1997). Visual half-casts can be empirically quantified with a half-cast factor (HCF), equal to

$$HCF = 100\% \cdot \frac{total\ length\ of\ visible\ half-casts}{total\ length\ of\ perimeter\ holes\ drilled} \tag{C.9}$$

A high HCF corresponds with minimal backbreak; a low HCF indicates backbreak beyond design limits.

C.1.2.2. Fracture mapping

Fracture mapping is used to assess the stability characteristics of a slope or tunnel wall and identify potential weaknesses. Fracture mapping can be used to visually evaluate the effects of blast damage and draw comparisons between damaged and undamaged rock faces and between blast rounds. Methods of fracture mapping include line surveys and photogrammetry. Drawbacks to fracture mapping include limitations in assessing blast damage beyond the visible surface and challenges in differentiating fractures from naturally-occurring discontinuities (Scoble et al. 1997). On the laboratory scale, fracture patterns can be analyzed by using a wire saw to cut through a rock or concrete sample that has been blasted (Iverson et al. 2010). Drill core inspection can also be performed.

C.1.2.3. Borehole surveys

Surveys of blast-induced fracturing can be conducted downhole using borehole cameras (Brent and Smith 1996; McKenzie and Holley 2004; Scoble et al. 1997; Yang et al. 1993). Both pre- and postblast surveys are needed to evaluate newly-formed cracks. While borehole surveys allow direct observations of fractures otherwise unobservable, survey holes located close to a blasthole may collapse, rendering the hole inaccessible (Smith 2003). Borehole surveying also requires specialized equipment that is employable in the field and small enough to fit inside a drillhole.

C.1.2.4. Overbreak

Blast damage beyond design limits can be quantified as an overbreak percentage (Scoble et al. 1997; Singh and Lamond 1993). This can be accomplished by comparing design limits and postexcavation face profile surveys.

C.1.3 Rock mass classification methods

Rock mass classification methods are widely used in rock mechanics. Specialized classification schemes have been developed specifically for the use of assessing blast damage (Scoble et al. 1997; Paventi et al. 1996). Such methods, which incorporate visual inspections with other metrics, can be used to appraise the effects of a blast round.

C.1.4 Scaling time

Scaling time, both with mechanical equipment and manual means, has been studied as a production-friendly technique for assessing damage along a blasting perimeter (Scoble et al. 1997; Sutherland 1990). The reasoning behind this method is that the scaling time is a function of scaling area and blast quality (Scoble et al. 1997). Shorter scaling times should indicate better wall control.

C.1.5 Bench movement

Bench movement can be used as a sign of joint strength loss and block instability (McKenzie and Holley 2004). Movement can be measurement with extensometers or by placing movement markers and surveying displacement with a surveying instrument. McKenzie and Holley (2004) conducted a study in which movement markers were grouted in boreholes at varying distances and depths behind a series of blasts. Both dilation and settling of the bench, along with horizontal movement, were observed. Overall, movement decreased with distance and depth behind the blast in a somewhat linear fashion.

C.1.6 Pressure measurements

A number of studies have been conducted using pressure diaphragm transducers secured downhole in boreholes adjacent to a bench blast (Brent and Smith 1996; Menccaci and Farnfield 2003; Peterson 2001). These sensors can be used to measure gas pressures as the high pressure gases penetrate their way through the fragmented rock mass. Although not a direct measurement of damage within the rock itself, knowing the gas pressures within the zone adjacent to a blast can aid in understanding the combined effects of the shock wave and gas expansion on crack growth and in analyzing flexural rupture. Brent and Smith (1999) proposed a relationship between gas pressures and the increase in the volume of a monitoring hole within a fractured bench that could serve as an indicator of damage.

C.1.7 Time domain reflectometry

A time domain reflectometer (TDR) is an electronic tool used to detect faults, shorts, and other changes in a cable or conductive wire (AEMC Instruments 2004). It operates by sending a voltage pulse from one end of the cable and "listening" for echoes as part or all of the pulse reflects back when changes in impedance are encountered. Depending on the nature of the impedance change, the reflected signal will vary in shape and can be used to diagnose its source. Figure C.8 shows a sample set of events that can be detected. A TDR can also determine the approximate distance d to each event using the relationship

$$d = V_p c_0 \frac{t}{2} \tag{C.10}$$

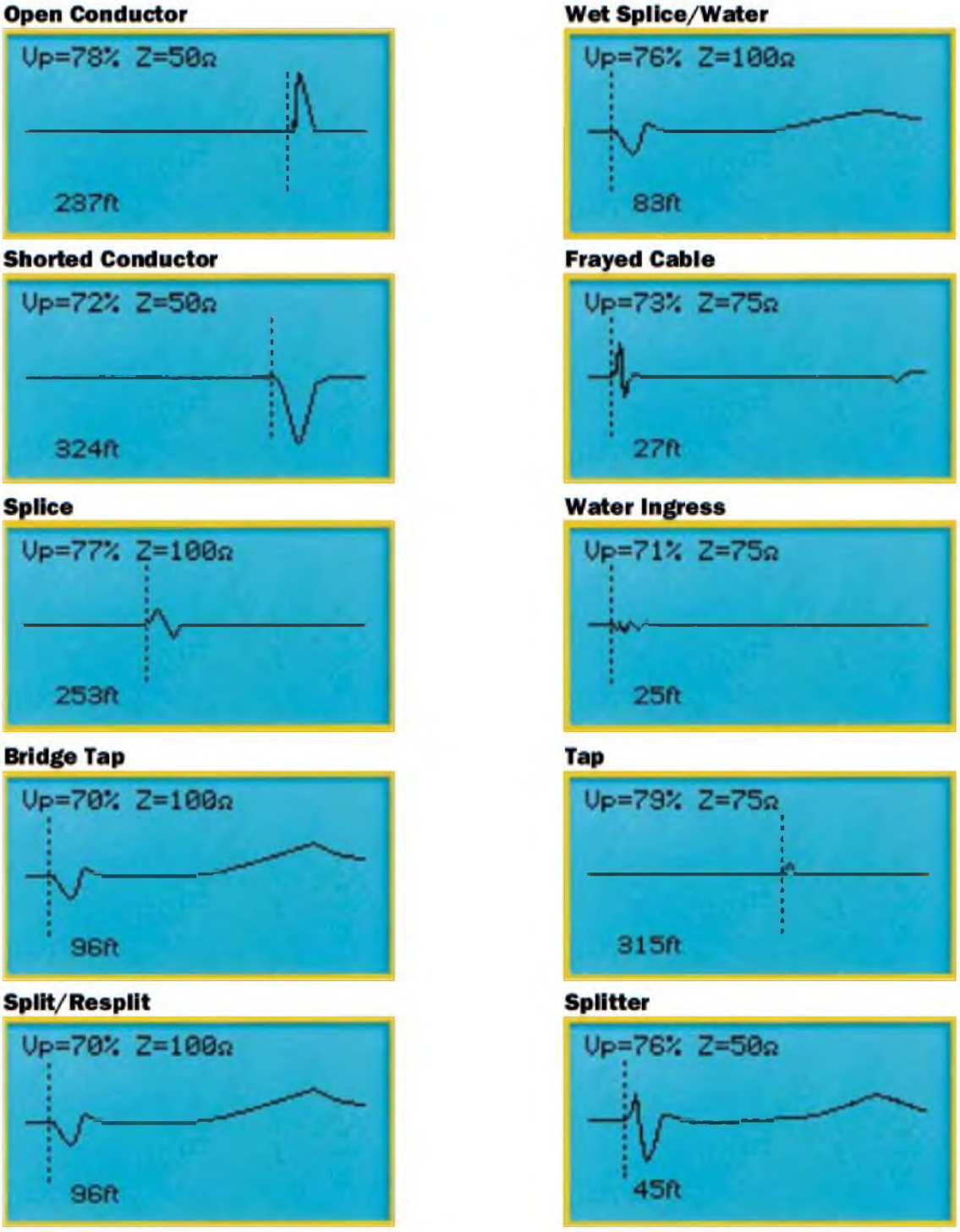

Figure C.8 Types of signals for a graphical TDR output
(Source: AEMC Instruments 2011a. Reprinted with the permission of Chauvin Arnoux Inc.).

where

V_p is a calibrated constant called the velocity of propagation and is expressed as a percent of the speed of light,

c_0 is the speed of light in a vacuum, and

t is the two-way travel time for the pulse from the TDR to the event and back.

In theory, the V_p value is a constant for each type of cable or wire and does not vary with length. For measurements in which multiple types of cables are connected in series, the following relationship can be derived for an average V_p:

$$V_{p-average} = \frac{d_1 + d_2 + d_3 + \cdots}{\frac{d_1}{V_{p1}} + \frac{d_2}{V_{p2}} + \frac{d_3}{V_{p3}} + \cdots} \tag{C.11}$$

where the V_p constant and distance d for each length of cable is denoted by 1, 2, 3, etc.

Time domain recflectometry has been utilized for assessing blast damage, though less commonly than most other methods (LeBlanc et al. 1996; Peterson 2001). TDR readings can give a qualitative indication of movement in the ground, but not exact displacements. The precision and accuracy of the measurements can be limited by the resolution of the TDR meter and field conditions such as temperature and the degree of coupling of the cable in the ground. Signal behavior can also be difficult to interpret at times. Nonetheless, whereas other methods that rely upon instrumentation positioned near the blasting are susceptible to damage, the TDR method relies upon such damage for obtaining measurements and thus can be positioned arbitrarily close without concern.

C.2 Indirect measurements

C.2.1 Seismic tomography

Seismic tomography methods can be used to quantify the increase of blast-induced fractures in a body of rock (Adamson and Scherpenisse 1998; Andrieux et al. 1994; LeBlanc et al. 1996; Singer et al. 2010; Spathis et al. 1987; Trivino and Mohanty 2013; Yang et al. 1993; Zhang and Chang 1999). Seismic tomography measures changes in the acoustic velocity of rock and the wave attenuation, usually with P-waves. A decrease in wave velocity often indicates an increase in crack density. Differences in attenuation rates pre- and postblast also can suggest deterioration of the rock mass from blasting. Both pre- and postblast surveys are required for this technique to be applicable. Cross-hole surveys are most commonly employed, in which the body of rock between two or more nearby holes is analyzed. Downhole-to-surface surveys can also be performed. Seismic tomography can detect changes from both micro- and macrofracturing. It is a relatively popular method as it can be used in the field with minimal setup, provided the appropriate equipment is available. It also produces a fairly complete picture of the damage zone if the observation holes are adequately located.

C.2.2 Ultrasonic P-wave velocity

Ultrasonic measurements of P-wave velocity in rock samples pre- and postblast have been used successfully for detecting shock-damaged rock (Hamdi et al. 2003; Iverson et al. 2010; Kilebrant et al. 2010; Kim and McCarter 1993). Similar to seismic tomography, the underlying principle is that P-wave velocity decreases as fracture density increases. However, this method requires that core samples be obtained from the test site, which requires additional labor and equipment.

C.2.3 Permeability

Permeability has been used to assess the zone of damage from blasting (Kelsall et al. 1984; Pusch and Stanfors 1996). Measurements are made in the field of the in situ hydraulic conductivity. Care must be taken to control field conditions; otherwise, results obtained may not reliable. Hydraulic conductivity is also affected by fracture and joint orientation.

C.2.4 Porosity

Porosity of rock samples pre- and postblast have been measured to indicate blast damage (Hamdi et al. 2003; Kilebrant et al. 2010). When rocks undergo intense blast-loading, the resulting fractures increase the rock's inherent porosity. Porosity measurements can be made in conjunction with ultrasonic velocity measurements since both rely on the same phenomenon.

C.2.5 Acoustic emissions

Acoustic emissions (AE) are a phenomenon that occurs during loading of a brittle rock sample (Seto et al. 1996). Under high stresses, localized failures of the rock as a microcrack forms or a pore collapses will emit a high-frequency elastic wave called an AE. If the rock sample is unloaded and then reloaded, AE will not occur until the rock is loaded past its previous maximum stress state. This is called the Kaiser effect. Given this behavior, AE can be used to give an accurate assessment of rock damage (Holcomb et al. 1990; Seto et al. 1996). However, this method requires rock sample preparation, a triaxial loading machine, and piezoelectric transducers that can measure very high frequencies in

the hundreds of kHz (Seto et al. 1996). This makes AE useful only for research investigations.

C.2.6 Ground penetrating radar

Ground penetrating radar can be used to gauge the depth of damage in rock. Adams et al. (1993) used ground penetrating radar to determine the effects of preconditioning ahead of a stope face. Ryu et al. (2013) performed a borehole radar reflection survey to determine the extension of fractures from blasting in a tunneling project. Ground penetrating radar requires both pre- and postblast surveys to measure increases in fracture density within the rock.

C.2.7 Electrical resistivity

Electrical resistivity (ER) has been used to gauge the depth of blast-induced rock damage (Ouchterlony et al. 1993; Scott et al. 1968). The theory is that greater fracture density will increase the resistivity of the rock. A study conducted by Ouchterlony et al. (1993) remarked that ER is sensitive enough to detect the presence of a single crack, and ER results correlated well with borehole fracture inspections. However, as noted by Scott et al. (1968), electrical resistivity methods are sensitive to the presence of water.

APPENDIX D

INTRODUCTION TO PYTHON

Since the reader may not be familiar with Python, a brief introduction is presented here. Python is a general-purpose, dynamic, high-level programming language that is also open-source, essentially free for both private and commercial use (Python Software Foundation 2013). It parses code via an interpreter writing in the C programming language. In addition to the built-in abilities of Python, there are numerous modules available to add a plethora of capabilities. Users can also write their own custom modules. One particular list of Python modules for Windows that the author found helpful is maintained online by Gohkle (n.d.).

Python 2.7 was used to meet the majority of programming requirements for this thesis. Python 3.2 was also available at the time, but certain modules desired by the author had not yet been updated to be compatible with the newer version of Python. For this thesis, the author heavily utilized the following modules and add-ons:

- Numpy – A numeric processing toolkit with higher-level math functions and built-in data types that allow for rapid computing, particularly large arrays and matrices.
- IPython – An interpreter based on the original Python interpreter, but with additional features and a more detailed output, particularly when debugging.
- Matplotlib – A plotting toolkit that in some respects emulates MATLAB®'s plotting environment, but with far more capabilities. Matplotlib functionality requires the Numpy module.
- SciPy – An advanced scientific computational toolkit with a wide variety of algorithms and mathematical tools for tasks involving optimization,

solvers, signal and image processing, interpolation, linear algebra, etc. SciPy functionality requires the Numpy module.

- Spyder – An interactive development environment (IDE) that may seem reminiscent of MATLAB®'s IDE, but with substantially different features.

The simplest way to obtain a complete and fully-functional scientific computing package is to obtain a compiled distribution called Python(x,y), available online at http://code.google.com/p/pythonxy/wiki/Welcome (Accessed May 2013). The author, however, did not use this package, for at the time it was only available in 32-bit, and 64-bit capability was desired.

Numerous resources are available on the Internet for learning and referencing the Python language, should the reader wish to understand the flow of the following scripts. Some details are briefly mentioned here to readily aid the uninitiated reader.

- Comments can be demarcated in three ways:
  - With three sets of double quotation marks on each side: """Comment 1""",
  - With three sets of single quotation marks on each side: '''Comment 2''',
  - With a number sign at the beginning of each line: # Comment 3.
- Appropriate indentation is enforced in Python, especially within function definitions and flow control statements such as for loops, while loops, and if statements.
- Python uses base-0 indexing in arrays, lists, and tuples.

APPENDIX E

ROCK MECHANICS TESTING PROGRAM

A rock mechanics testing program was conducted on a sample of rhyolite obtained from the test site. A total of 58 test specimens were obtained from the rhyolite sample. Measurements were taken of density, porosity, acoustic velocities, elastic moduli, and static and dynamic strengths.

E.1 Sample preparation

Test specimens were cored using NX and a custom 1 ¼ in.-sized diamond drill bits, then cut using a tile saw. Samples with a length-to-diameter ratio of L/D ≈ 2 were placed in a rotatory surface grinder and the ends ground parallel. Parallelism was checked using a dial indicator to an accuracy of 1/394 mm (1/10,000 in.). Dimensions of each sample were measured using calipers with a precision of 0.0025 mm (0.0001 in.). The samples were separated into four groups, based on dimensions:

- Group A – nominal diameter of 31.8 mm (1.25 in.), L/D ≈ 2,
- Group B – nominal diameter of 54.0 mm (2.125 in.), L/D ≈ 2,
- Group C – nominal diameter of 31.8 mm (1.25 in.), L/D ≈ 0.5, and
- Group D – nominal diameter of 54.0 mm (2.125 in.), L/D ≈ 0.5.

Table E.1 list the measured dimensions of each sample. In addition, weight was measured using an electronic scale. Groups A and B were prepared for compressive strength testing, and groups C and D for Brazilian tensile strength testing.

E.2 Porosity and density measurements

Porosity and density were measured for sample groups A and B. Each specimen was dried in an oven for 24 hours then weighed with an electronic scale. Each specimen was then soaked in deionized water for over 24 hours and again weighed. Group A

Table E.1 Measured dimensions of rhyolite test specimens

Sample ID	Diameter		Height		End parallelism		L/D ratio	Weight
	mm	in.	mm	in.	mm	in.		g
A01	31.483	1.2395	60.846	2.3955	0.051	0.0020	1.93	121.60
A02	31.496	1.2400	64.199	2.5275	0.005	0.0002	2.04	128.90
A03	31.496	1.2400	64.046	2.5215	0.005	0.0002	2.03	127.20
A04	31.483	1.2395	64.046	2.5215	0.010	0.0004	2.03	126.79
A05	31.483	1.2395	62.446	2.4585	0.015	0.0006	1.98	124.90
A06	31.483	1.2395	64.186	2.5270	0.013	0.0005	2.04	128.55
A07	31.483	1.2395	61.214	2.4100	0.010	0.0004	1.94	122.25
A08	31.483	1.2395	64.160	2.5260	0.023	0.0009	2.04	127.81
A09	31.509	1.2405	64.110	2.5240	0.023	0.0009	2.03	128.72
A10	31.483	1.2395	64.160	2.5260	0.018	0.0007	2.04	128.42
A11	31.483	1.2395	62.624	2.4655	0.015	0.0006	1.99	124.30
A12	31.483	1.2395	64.059	2.5220	0.015	0.0006	2.03	128.19
A13	31.496	1.2400	63.360	2.4945	0.018	0.0007	2.01	127.23
A14	31.483	1.2395	64.110	2.5240	0.023	0.0009	2.04	128.68
A15	31.483	1.2395	64.135	2.5250	0.020	0.0008	2.04	128.11
B01	53.289	2.0980	108.242	4.2615	0.010	0.0004	2.03	615.00
B02	53.315	2.0990	108.039	4.2535	0.008	0.0003	2.03	620.10
B03	53.391	2.1020	107.645	4.2380	0.005	0.0002	2.02	615.90
B04	53.454	2.1045	108.420	4.2685	0.015	0.0006	2.03	623.80
B05	53.454	2.1045	108.649	4.2775	0.018	0.0007	2.03	628.30
B06	53.353	2.1005	108.598	4.2755	0.008	0.0003	2.04	623.40
B07	53.505	2.1065	108.014	4.2525	0.015	0.0006	2.02	624.50
B08	53.454	2.1045	108.534	4.2730	0.010	0.0004	2.03	626.80
C01	31.509	1.2405	16.548	0.6515	NA	NA	0.53	32.75
C02	31.521	1.2410	16.497	0.6495	NA	NA	0.52	32.81
C03	31.521	1.2410	16.485	0.6490	NA	NA	0.52	32.75
C04	31.496	1.2400	16.231	0.6390	NA	NA	0.52	32.44
C05	31.496	1.2400	15.939	0.6275	NA	NA	0.51	31.58
C06	31.509	1.2405	16.205	0.6380	NA	NA	0.51	31.75
C07	31.483	1.2395	16.599	0.6535	NA	NA	0.53	32.90
C08	31.496	1.2400	16.231	0.6390	NA	NA	0.52	32.01
C09	31.496	1.2400	16.510	0.6500	NA	NA	0.52	32.83
C10	31.483	1.2395	15.799	0.6220	NA	NA	0.50	31.26
C11	31.483	1.2395	16.586	0.6530	NA	NA	0.53	33.13
C12	31.509	1.2405	16.523	0.6505	NA	NA	0.52	32.37

Table E.1 continued

Sample ID	Diameter		Height		End parallelism		L/D ratio	Weight
	mm	in.	mm	in.	mm	in.		g
C13	31.496	1.2400	16.104	0.6340	NA	NA	0.51	32.00
C14	31.509	1.2405	16.535	0.6510	NA	NA	0.52	32.85
C15	31.509	1.2405	16.599	0.6535	NA	NA	0.53	33.08
C16	31.496	1.2400	16.675	0.6565	NA	NA	0.53	33.39
C17	31.496	1.2400	16.535	0.6510	NA	NA	0.53	33.14
C18	31.483	1.2395	16.523	0.6505	NA	NA	0.52	33.07
C19	31.471	1.2390	16.688	0.6570	NA	NA	0.53	32.76
C20	31.483	1.2395	16.421	0.6465	NA	NA	0.52	32.66
C21	31.521	1.2410	16.269	0.6405	NA	NA	0.52	31.93
D01	53.086	2.0900	23.279	0.9165	NA	NA	0.44	129.80
D02	53.442	2.1040	23.889	0.9405	NA	NA	0.45	137.01
D03	53.556	2.1085	23.444	0.9230	NA	NA	0.44	135.78
D04	53.581	2.1095	23.470	0.9240	NA	NA	0.44	135.33
D05	53.581	2.1095	19.990	0.7870	NA	NA	0.37	128.25
D06	53.518	2.1070	24.130	0.9500	NA	NA	0.45	137.33
D07	53.238	2.0960	23.317	0.9180	NA	NA	0.44	132.70
D08	53.454	2.1045	23.355	0.9195	NA	NA	0.44	134.51
D09	53.531	2.1075	23.317	0.9180	NA	NA	0.44	135.12
D10	53.416	2.1030	23.254	0.9155	NA	NA	0.44	132.17
D11	53.556	2.1085	23.609	0.9295	NA	NA	0.44	135.79
D12	53.518	2.1070	23.800	0.9370	NA	NA	0.44	135.07
D13	53.518	2.1070	24.282	0.9560	NA	NA	0.45	137.08
D14	53.531	2.1075	22.974	0.9045	NA	NA	0.43	132.59

specimens were weighed to a precision of 0.01 g, and group B specimens to a precision of 0.1 g. Porosity (n) was calculated using the formula

$$n = \frac{V_V}{V_T} = \frac{(W_s - W_d)\rho_w}{V_T} \approx \frac{W_s - W_d}{V_T} \quad \text{(E.1)}$$

where

V_V and V_T are the volumes of void space and total volume of the sample, here in cm^3,

W_s and W_d are the saturated and dry sample weights in grams, and

ρ_w is the density of water, equal to 1.00 g/cm^3.

The average porosities for groups A and B were 0.0238 and 0.0164, respectively. It is likely that the B samples did not have sufficient time to soak, as they are larger than the A samples. Thus, for the purposes of this test, only the results from group A were used. The saturated, dry, and nominal densities for the rhyolite are 2.58 g/cm^3, 2.56 g/cm^3, and 2.57 g/cm^3, respectively. The results are shown in Tables E.2 and E.3. Note: samples A01 and A02 were not included in this set of measurements.

E.3 P-wave and S-wave velocities

P-wave and S-wave velocities were measured for samples from group A. An Olympus Panametrics-NDT Model 5072PR pulser-receiver with dual contact V103-RM transducers was used to create ultrasonic P-waves, and a Model 5073PR pulser-receiver with dual normal-incident shear wave V153-RM transducers was used to create ultrasonic S-waves. Both transducers operated at a frequency of 1 MHz. For each setup, an Agilent Model 54624A oscilloscope was used to display the ultrasonic wave and select the arrival times. The average P-wave velocity was 4,606 m/s (15,111 ft/s) and the

Table E.2 Porosity and density measurements – group A

Sample ID	Weight (g)		Density (g/cm^3)			Porosity
	Dry	Saturated	Dry	Saturated	Nominal	
A03	126.94	128.40	2.54	2.57	2.55	0.0293
A04	126.57	128.04	2.54	2.57	2.54	0.0295
A05	124.66	125.82	2.56	2.59	2.57	0.0239
A06	128.32	129.42	2.57	2.59	2.57	0.0220
A07	122.01	123.19	2.56	2.59	2.57	0.0248
A08	127.55	128.85	2.55	2.58	2.56	0.0260
A09	128.49	129.58	2.57	2.59	2.57	0.0218
A10	128.18	129.30	2.57	2.59	2.57	0.0224
A11	124.05	125.24	2.54	2.57	2.55	0.0244
A12	127.93	129.16	2.57	2.59	2.57	0.0247
A13	127.02	127.95	2.57	2.59	2.58	0.0188
A14	128.45	129.36	2.57	2.59	2.58	0.0182
A15	127.90	129.05	2.56	2.58	2.57	0.0230
Average			2.56	2.58	2.57	0.0238

Table E.3 Porosity and density measurements – group B

Sample ID	Weight (g)		Density (g/cm^3)			Porosity
	Dry	Saturated	Dry	Saturated	Nominal	
B01	613.70	617.90	2.54	2.56	2.55	0.0174
B02	618.80	623.00	2.57	2.58	2.57	0.0174
B03	614.50	618.90	2.55	2.57	2.56	0.0183
B04	622.40	626.90	2.56	2.58	2.56	0.0185
B05	627.10	630.90	2.57	2.59	2.58	0.0156
B06	622.50	626.50	2.56	2.58	2.57	0.0165
B07	623.70	627.00	2.57	2.58	2.57	0.0136
B08	625.90	629.30	2.57	2.58	2.57	0.0140
Average			2.56	2.58	2.57	0.0164

average S-wave velocity was 2,739 m/s (8,988 ft/s). Table E.4 lists the measurements for each sample. Specimens A07 through A15 were analyzed.

E.4 Static tensile strength

The Brazil method was used to determine the static tensile strength of the rhyolite. The sample group D was tested using a hollow plunger hydraulic cylinder and a hydraulic jack, displayed in Figure E.1. Each sample was placed inside the mounts shown in Figure E.2 and loaded until failure. The tensile strength T_0 is calculated using the relationship (Pariseau 2007a)

$$T_0 = \frac{2P}{\pi dh} \tag{E.2}$$

where P is the load at fracture and d and h are the diameter and thickness of the specimen, respectively. In theory, Brazil disks will split from the center outwards as seen

Table E.4 P- and S-wave acoustic velocities – group A

Sample ID	P-wave arrival	S-wave arrival	P-wave speed		S-wave speed	
	µs	µs	m/s	ft/s	m/s	ft/s
A07	13.5	22.6	4534	14877	2709	8886
A08	14.2	23.7	4518	14824	2707	8882
A09	14.0	23.4	4579	15024	2740	8989
A10	13.9	23.4	4616	15144	2742	8996
A11	13.7	23.2	4571	14997	2699	8856
A12	14.2	23.7	4511	14800	2703	8868
A13	13.4	22.7	4728	15513	2791	9157
A14	13.6	22.9	4714	15466	2800	9185
A15	13.7	23.2	4681	15359	2764	9070
Average			4606	15111	2739	8988

Figure E.1 Setup for conducting a Brazil test

with specimen D04 in Figure E.2. The average tensile strength was 11.30 MPa (1,638 psi). Table E.5 lists the results for the Brazil test.

E.5 Static compressive strength and elastic moduli

A set of tests were conducted using a triaxial compression machine to determine both unconfined and confined uniaxial compressive strengths, static Young's modulus, and Poisson's ratio. Three A samples and two B samples were loaded, unconfined, to failure. Two sets of three B samples each were confined in a Hoek cell at two different confining pressures and loaded until failure. Young's modulus was determined from the unconfined compression tests. Strain gauges were mounted on one of the test specimens to measure axial and transverse strains, which were used to estimate Poisson's ratio.

Figure E.2 Specimen after failure in Brazil test

Table E.5 Brazil tensile strength test – group D

Sample ID	Load at failure		Tensile strength		Load time
	kN	kip	MPa	psi	s
D01	19.9	4.48	10.27	1489	142
D02	24.2	5.45	12.09	1753	144
D03	25.1	5.65	12.74	1848	176
D04	21.7	4.88	10.99	1594	165
D05	20.8	4.68	12.37	1795	126
D06	27.4	6.17	13.53	1962	155
D07	22.0	4.95	11.29	1638	130
D08	20.6	4.63	10.50	1523	140
D09	17.9	4.02	9.12	1323	95
D10	16.7	3.75	8.55	1240	105
D11	22.9	5.15	11.53	1673	140
D12	24.7	5.55	12.34	1790	150
D13	21.3	4.78	10.42	1511	136
D14	23.9	5.38	12.39	1797	142
Average			11.30	1638	

Linear regression of the normal and shear strain plots was performed to determine constants for a Mohr–Coulomb failure criterion.

E.5.1 Uniaxial, unconfined compressive strength and Young's modulus

Three or four samples are recommended at each testing stage for unconfined and confined compressive strengths. Since only eight B samples were available for static compression testing, and two confining tests of three samples each were needed for the triaxial loading, the remaining two B samples were supplemented with three A samples for a total of five specimens for uniaxial, unconfined compression. The triaxial testing machine pictured in Figure E.3 was utilized. A loading rate of 1.33 kN/s (300 lb/s) was applied to each sample. The B samples were loaded to 111 kN (25,000 lb), unloaded to 4.45 kN (1,000 lb), and then loaded to failure. A load cell which provides a voltage

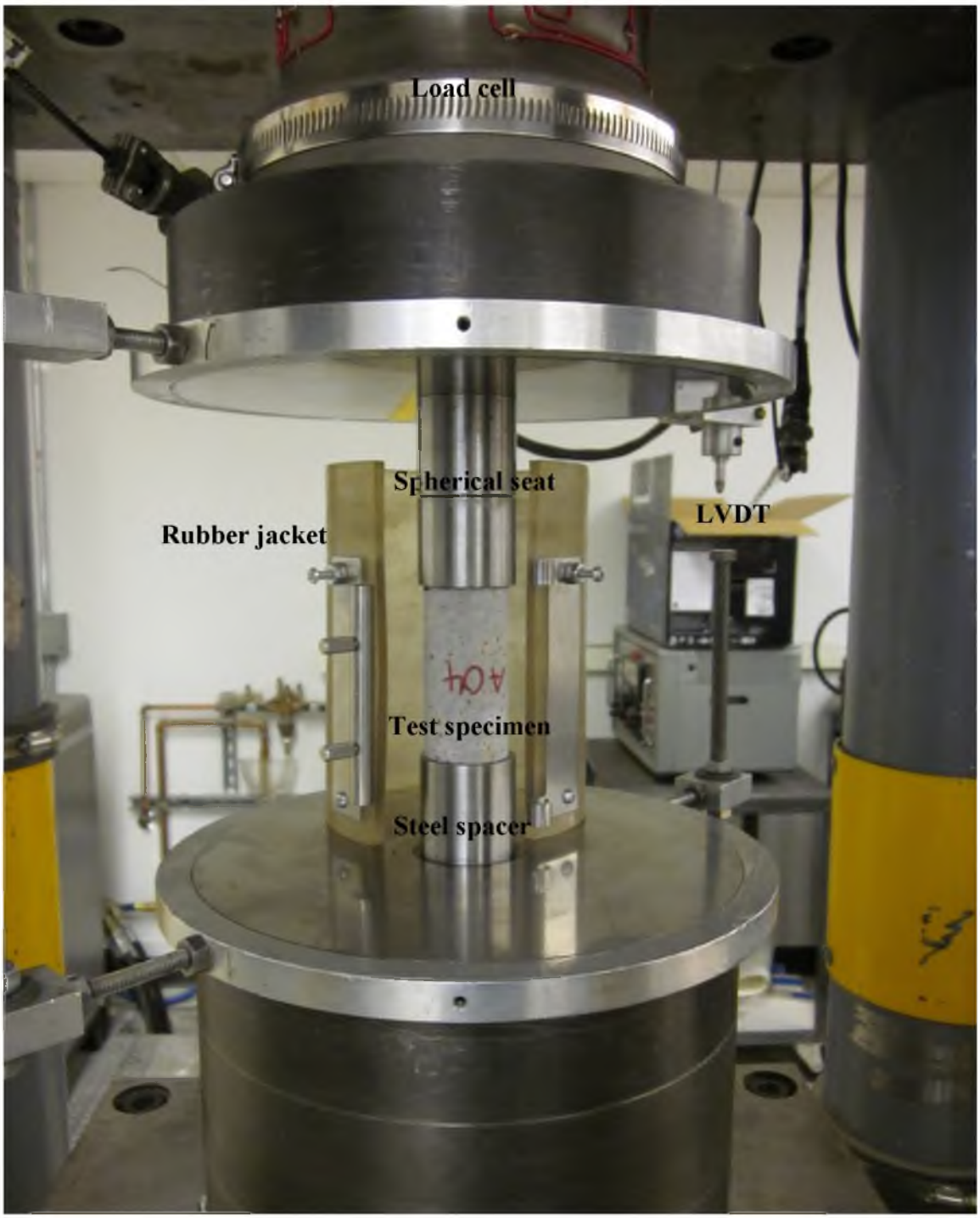

Figure E.3 Unconfined, uniaxial compression of a test specimen

proportional to the load was used to measure the applied normal load. Displacement was measured via both a displacement potentiometer, located beneath the sample loading area, and a pair of linearly variable differential transformers (LVDT) on either side of the sample. The LVDTs are much more precise and therefore were used in the calculations for Young's modulus. The average uniaxial, unconfined compressive strength of the rhyolite was determined to be 222.3 MPa (32,236 psi), indicating a very competent rock.

Young's modulus was calculated using loads from load cell data and displacements from the LVDTs (Pariseau 2007a). The LVDTs measure the combined displacement for the test specimen and the steel spherical seat and spacer. The total displacement U_T is equal to the sum of the displacements of the specimen U_r and the seat and spacer U_s, or $U_T = U_r + U_s$. Using the relationship between force F and displacement $F = KU$, where K is the stiffness, the following formula can be derived for the stiffness K_r of the sample.

$$\frac{1}{K_T} = \frac{1}{K_r} + \frac{1}{K_s} \tag{E.3}$$

$$K_r = \frac{1}{\frac{1}{K_T} - \frac{1}{K_s}} \tag{E.4}$$

When plotting force against displacement, the slope of the line is the stiffness.

The stiffness of the spherical seat and spacer can be determined from a separate loading cycle without a sample. Figures E.4 and E.5 show the stiffness plots for the NX and 1 ¼ in. sized samples. Knowing K_r, Young's modulus E can then be calculated as

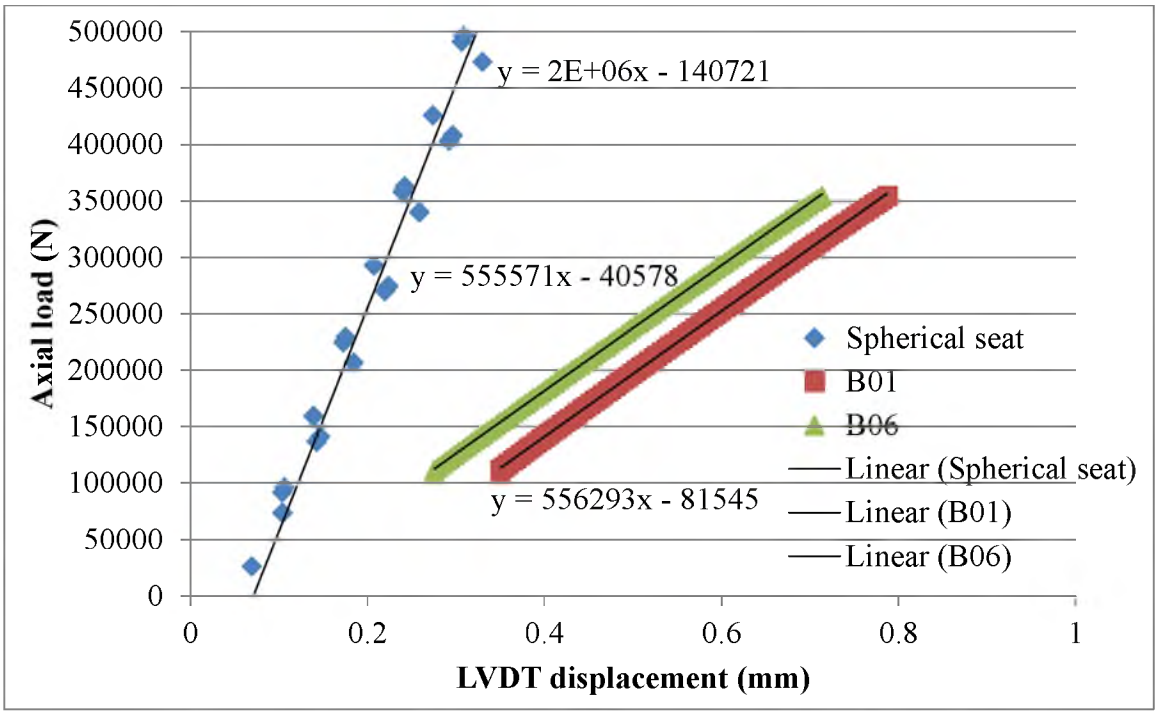

Figure E.4 Stiffness plots for samples B01 and B06

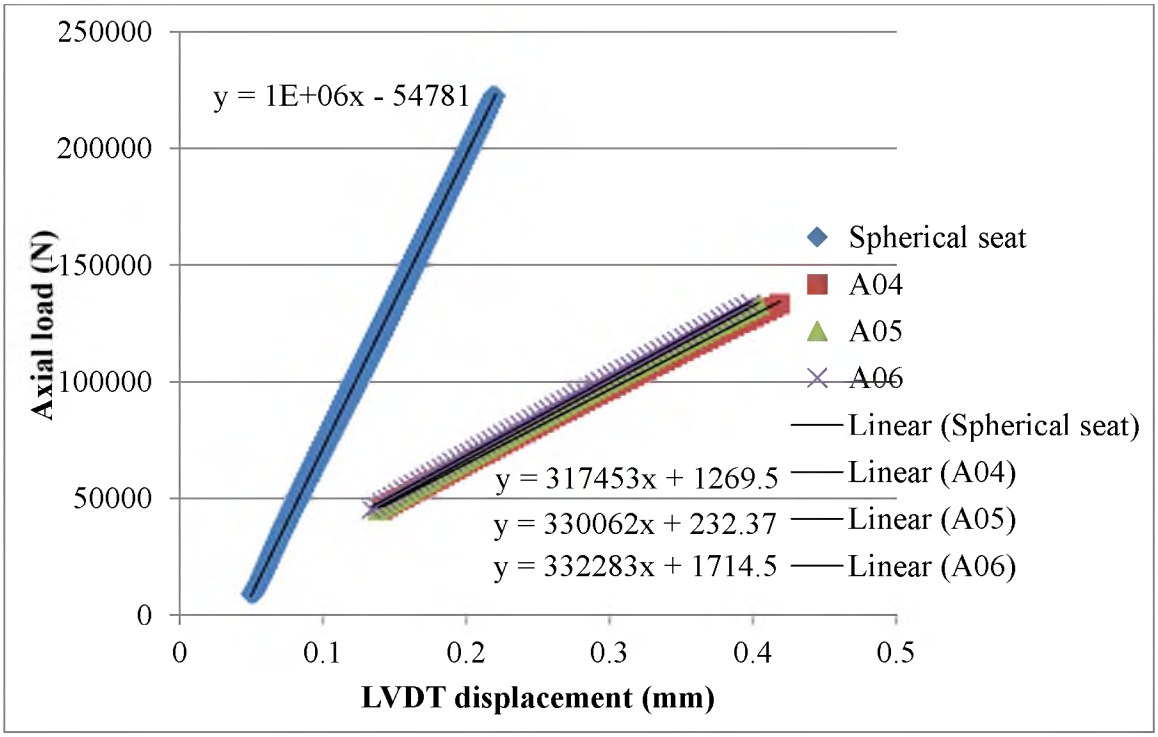

Figure E.5 Stiffness plots for samples A04, A05, and A06

$$E = K_r L/A \tag{E.5}$$

where A and L are the cross-sectional area and length, respectively, of the test specimen. The average Young's modulus was calculated to be 36.62 GPa (5,311 ksi). The individual results for each sample are listed in Table E.6.

E.5.2 Confined, triaxial compression

Compressive strength under confining pressure was tested using the same triaxial machine shown in Figure E.3. A Hoek cell, pictured in Figure E.6, was used to provide the confining pressure. Confining pressures of 20.7 MPa (3,000 psi) and 48.3 MPa (7,000 psi) were used, with three B samples per test. Confined compressive strengths of 414.1 MPa (60,055 psi) and 653.6 MPa (94,799 psi) were measured at confining pressures of20.7 MPa (3,000 psi) and 48.3 MPa (7,000 psi), respectively. Tables E.7 and E.8 list the individual confined compressive strengths for each test specimen.

E.5.3 Poisson's ratio

Four strain gauges (Micro-Measurements EA-06-375BG-120) were bonded to test specimen B01 to determine Poisson's ratio, as is shown in Figure E.7. Two were

Table E.6 Uniaxial, unconfined compressive strength and Young's modulus

Sample ID	**Load at failure**		**Compressive strength**		**Young's modulus**	
	N	**lb**	**MPa**	**psi**	**Gpa**	**ksi**
B01	474181	106600	212.6	30836	37.5	5445
B06	445938	100251	199.5	28930	37.5	5440
A04	161822	36379	207.9	30149	34.9	5066
A05	180837	40654	232.3	33691	35.9	5205
A06	201681	45340	259.1	37575	37.2	5399
Average			222.3	32236	36.6	5311

Figure E.6 Hoek cell for triaxial testing

Table E.7 Confined compressive strength at 20.7 MPa (3,000 psi)

Sample ID	**Load at failure**		**Compressive strength**	
	N	**lb**	**MPa**	**psi**
B02	1009890	227032	452.4	65610
B03	820952	184557	366.7	53183
B04	949581	213474	423.1	61370
Average			414.1	60055

Table E.8 Confined compressive strength at 48.3 MPa (7,000 psi)

Sample ID	Load at failure		Compressive strength	
	N	lb	MPa	psi
B05	1482552	333291	660.6	95816
B07	1477091	332063	645.8	93661
B08	1449219	325797	654.4	94919
Average			653.6	94799

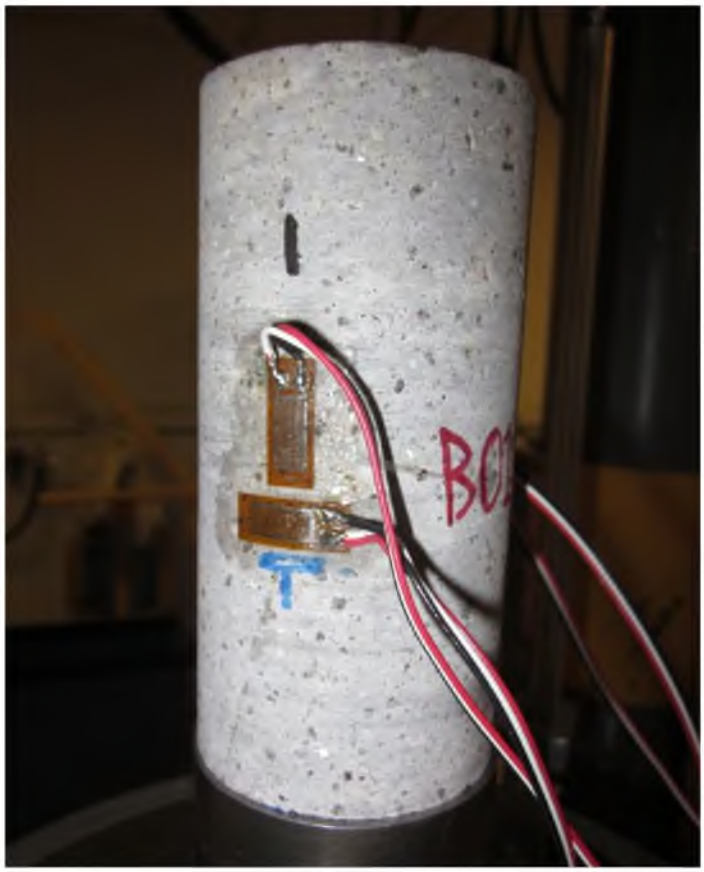

Figure E.7 Axial and transverse strain gauges

mounted in an axial orientation and the other two in a transverse orientation. Each strain gauge was wired in a quarter-bridge configuration, with an internal dummy resistance of 120 Ω. A strain gauge factor of 2.04 was used. Figure E.8 displays the individual strain gauge records, and Figure E.9 shows a plot of transverse over axial strain versus axial load. An interesting feature to note is the nonlinear increase in lateral strain around the middle section of the test specimen. According to W.G. Pariseau (personal communication), this is caused by microcracking in the rock that increases the volumetric strain beyond the elastic range.

Poisson's ratio was estimated to be 0.27 from the linear, reloading portion of the plot in Figure E.9. While only one measurement of Poisson's ratio was made, the value was in the expected range and thus, no further verification of this elastic constant was deemed necessary.

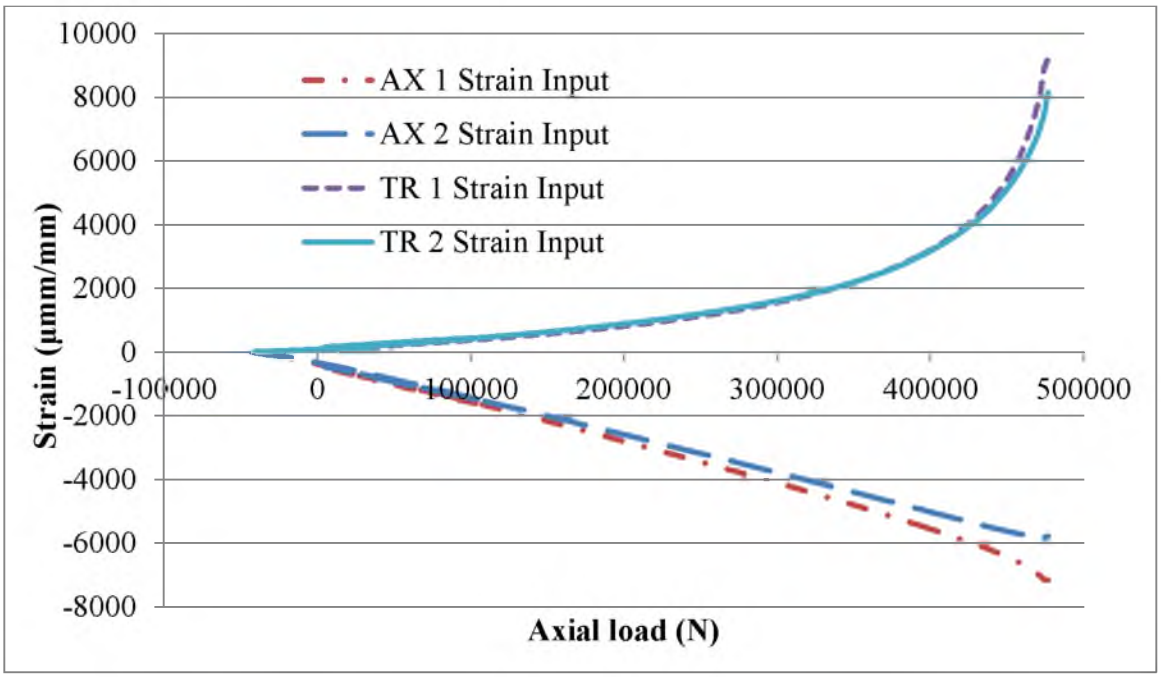

Figure E.8 Axial and transverse strain records

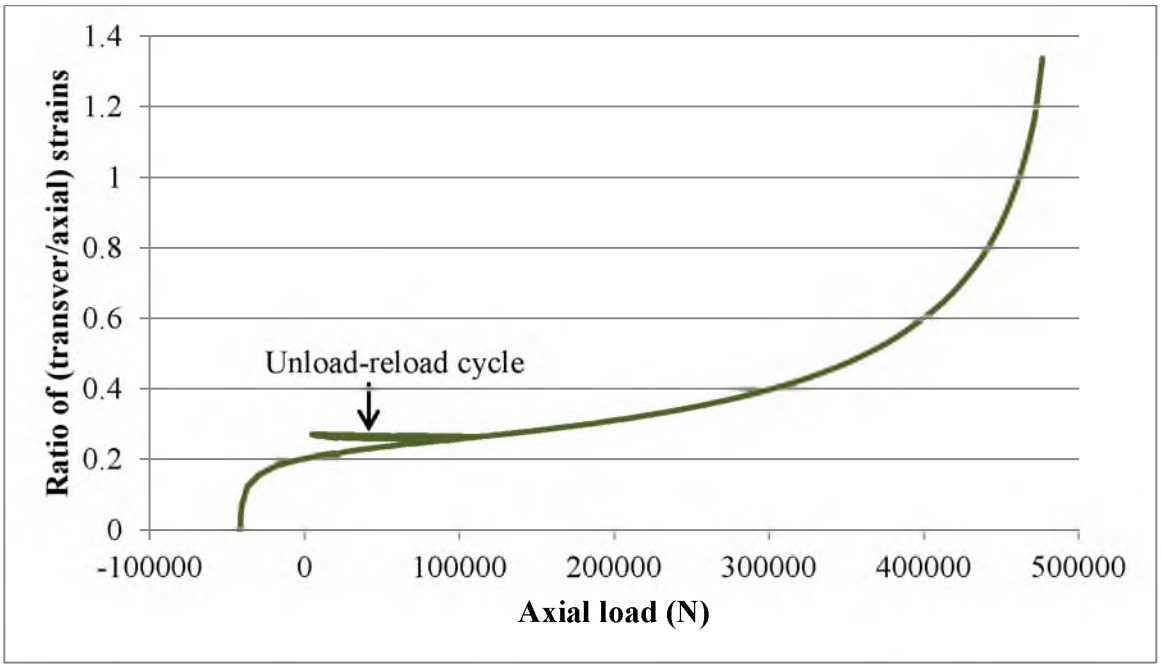

Figure E.9 Ratio and transverse over axial strains to estimate Poisson's ratio

E.5.4 Mohr–Coulomb constants

Constants for the Mohr–Coulomb (MC) failure criterion were determined from the experimental data. Only pertinent formulae and discussion are included; for a detailed overview of the theory, see Pariseau (2007a, 2007b).

One important note to make concerns the friction angle ϕ and cohesion c in the unconfined versus confined compressive stress ranges. As Pariseau (2007a) pointed out, an MC envelope fitted to the tensile and unconfined compressive strengths (T_0 and C_0) will overestimate confined compressive strengths C_p. Alternatively, an MC envelope that fits well with C_p and C_0 will overestimate T_0 and c. Friction angles also tend to be higher in the unconfined range than the confined range. Thus, for the purposes of this rock testing program, the two ranges were treated separately when analyzing the experimental data.

The MC failure envelope can by characterized by the equation (Pariseau 2007a, 2007b)

$$|\tau| = \sigma \tan \phi + c \tag{E.6}$$

where τ is the shear stress induced by the applied normal stress σ. When fitting a linear regression to the data, it is often easier to use the equation

$$\tau_m = \sigma_m \tan \psi + k \tag{E.7}$$

where

$\sigma_m = (\sigma_1 + \sigma_3)/2$ is the applied mean normal stress that is also the center of a Mohr circle when plotted in $\sigma - \tau$ stress space,

$\tau_m = (\sigma_1 - \sigma_3)/2$ is the deviatoric shear stress on the MC envelope directly above σ_m,

σ_1 and σ_3 are the major and minor principal stresses for the given stress state,

ψ is related to ϕ such that $\tan \psi = \sin \phi$, and

k is related to c such that $k = c \cos \phi$.

MC constants ϕ and c can be estimated for the unconfined compression range from T_0 and C_0 (Pariseau 2007a):

$$\sin \phi = \frac{C_0 - T_0}{C_0 + T_0} \tag{E.8}$$

$$c = \sqrt{C_0 T_0 / 4} \tag{E.9}$$

For the confined compression range, linear regression was used to determine $\tan \psi$ and k, which was then used to calculate ϕ and c. The MC parameters estimated from

experimental measurements are listed in Table E.9. Figure E.10 shows the experimental data plotted against both ranges for the MC envelopes using Equation E.7.

A visualization of the MC envelopes as compared to the test specimen Mohr-circles in $\sigma - \tau$ stress space is drawn in Figure E.11. Note how higher confined compressive strengths are significantly overestimated using ϕ and c as obtained from C_0 and T_0. However, T_0 and c are significantly overestimated when using ϕ and c as determined by a linear regression of all values for C_0 and C_p. The friction angles for both are different as well. It is the author's observation that a linear regression of all the experimental data will not provide a happy medium. Depending on the distribution of data, particularly the number of tensile strengths and confined compressive strengths used, a linear regression of all the data will produce either one of the undesirable scenarios above, or a portion of both. The range to select will depend on the engineering needs of a particular application.

E.6 Notes concerning dynamic strengths

Experimentally-obtained dynamic material strengths possess much greater variability than statically-determined strengths. Material strengths are dependent upon strain rate. At low strain rates encountered in quasistatic tests, the effects are not noticeable. As the strain rate increases, the strength of the rock increases. Dynamic compressive strengths for rock can be on the order of 2.5–4.6 times that of static compressive strengths at a strain rate on the order of 10^3 s^{-1}, disregarding the effects of confining pressure (Prasad 2000). Dynamic tensile strengths for rock can range from 2–12 times that of static tensile strengths at a strain rate of only 10^1 s^{-1} (Cho et al. 2003).

Table E.9 Mohr–Coulomb constants for unconfined and confined compression ranges

MC constant	Unconfined range				Confined range			
	Metric		Imperial		Metric		Imperial	
ψ	42	°			39	°		
ϕ	65	°			53	°		
k	10.75	MPa	1559	psi	21.88	MPa	3174	psi
c	25.05	MPa	3634	psi	36.65	MPa	5315	psi

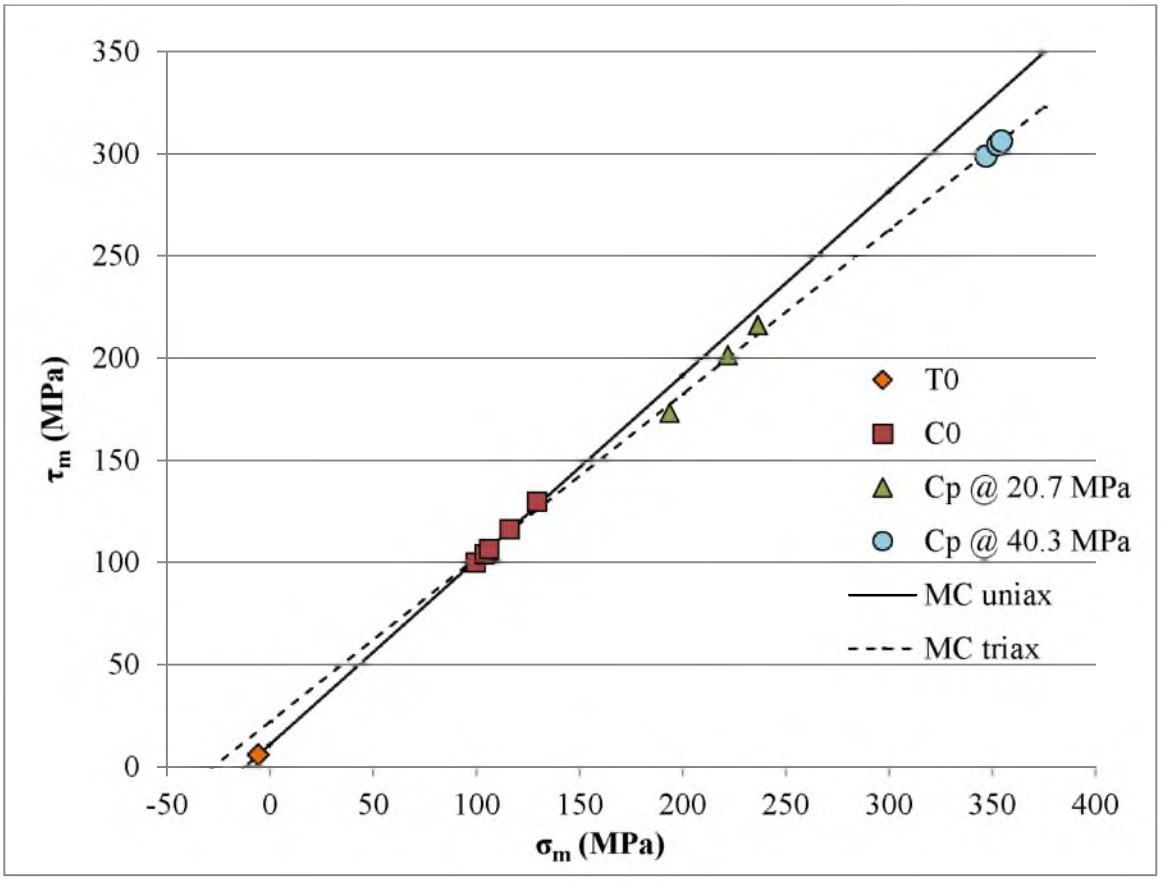

Figure E.10 Measured rock strengths with both MC envelopes shown

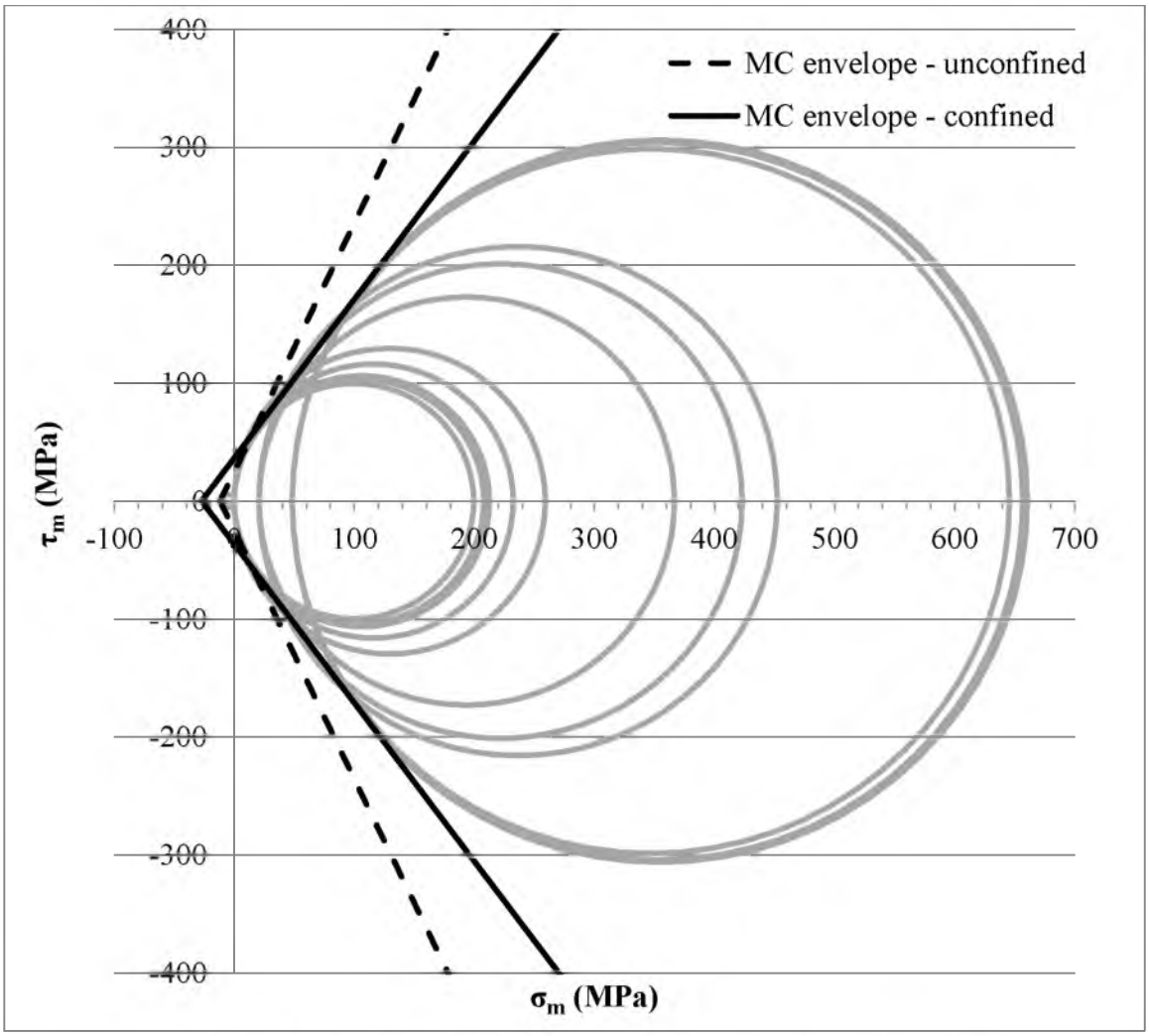

Figure E.11 MC envelopes compared to the test specimen Mohr circles

Sun (2013) reported that strain rates in the crushed zone around a blasthole are 10^2–10^3 s^{-1} and in the radial fracture zone are 10^0–10^1 s^{-1}.

E.7 Dynamic tensile strength

The dynamic tensile strength of the rhyolite was estimated using sample group C. A split Hopkinson pressure bar (SHPB) was used to perform the tests. The SHPB is presented in Figure E.12. Analysis of dynamic strengths from SHPB experiments rely on measuring strain pulses in the incident and transmitting bars. Equations have been

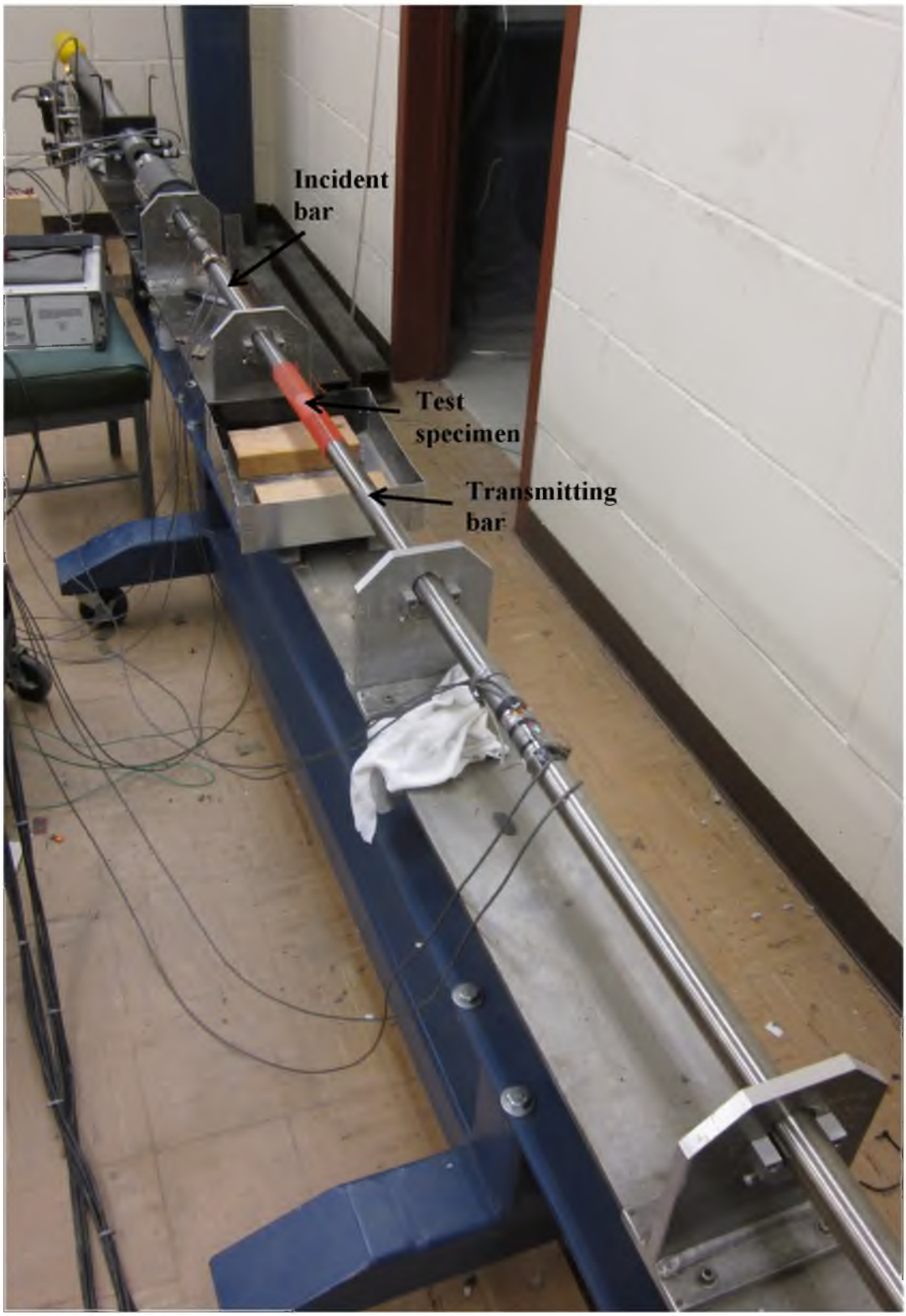

Figure E.12 Split Hopkinson pressure bar

derived to calculate dynamic strengths from strain records and measured properties of the bars. The theory and procedures in using SHPB are only briefly mentioned here; for further study, the author recommends Johnson (2010), Zhou et al. (2012), and Zhou and Zhoa (2011). In particular, the same data logger used in the SHPB tests was also used by Johnson (2010).

A Brazil test specimen is shown in Figure E.13. When a test specimen is loaded in the SHPB, three strain pulses are initially generated: the incident and reflected waves travelling within the incident bar and the transmitted strain wave that passes from the incident bar through the test specimen into the transmitting bar. Figure E.14 shows a typical strain signal measured during the tests. Strain gauges mounted on the incident and transmitting bar were used to measure these pulses. A Nicolet Odyssey data logger recorded the strain gauge readings at a sampling frequency of 10 MHz. Voltage readings from the strain gauges were converted to strain using the formula

$$\varepsilon = \frac{2V_m}{V_{ex}G\lambda} \tag{E.10}$$

Figure E.13 Brazil test specimen in SHPB

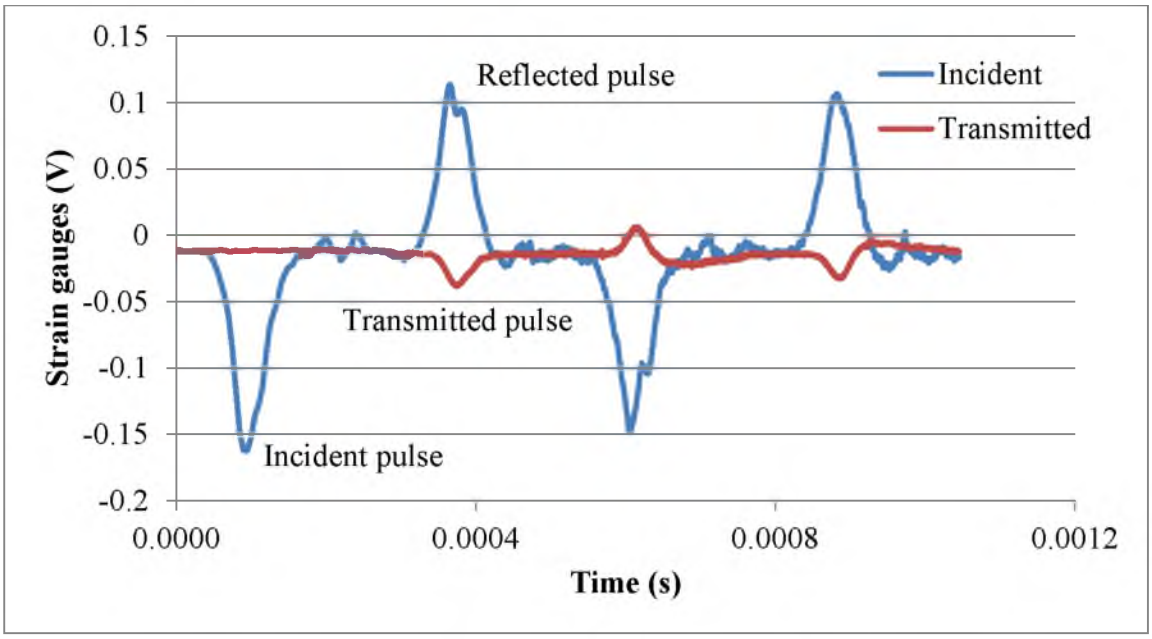

Figure E.14 Strain pulses in incident and transmitting bars

where

ε is the measured strain,

V_m is the measured voltage,

V_{ex} is the excitation voltage, here equal to 22 V,

G is the gain of the gauge signal amplifier, usually equal to 5 but verified beforehand, and

λ is the gauge factor of the strain gauges, here equal to 2.115.

For measuring the dynamic strength of the rhyolite, the Brazil test was applied with the SHPB. Equation E.2, which is used to calculate tensile strength under quasistatic loading conditions, is also applicable under dynamic loading conditions. The applied load P on a Brazil disk in the SHPB is calculated from the strain in the transmitted wave using the following equation (Xia et al. 2010):

$$P(t) = E_{bar} A_{bar} \varepsilon_t(t) \tag{E.11}$$

where E_{bar} and A_{bar} are Young's modulus and the cross-sectional area of the bar, respectively, and ε_t is the strain measured in the transmitting bar. Here, E_{bar} = 189.3 GPa and A_{bar} = 7.917 cm^2. The dynamic tensile strength is given by the peak load. Figure E.15 shows a plot of the stress load applied to a test specimen. Zhou and Zhoa (2011) cautioned, however, that this method may overestimate dynamic tensile strength by as much as 20%. Because of the high strain rates encountered using SHPB, fracture formation may begin well before the peak load is reached. To obtain the net strain rate applied in the test, the following relationship can be used (Zhou and Zhoa 2011). Keep in mind, however, that this does not provide the actual strain rate within the sample, as the cross-sectional area of a Brazil test specimen is not uniform in the direction of loading.

$$\dot{\varepsilon}(t) = \frac{c}{D}[\varepsilon_i(t) - \varepsilon_r(t) - \varepsilon_t(t)] \tag{E.12}$$

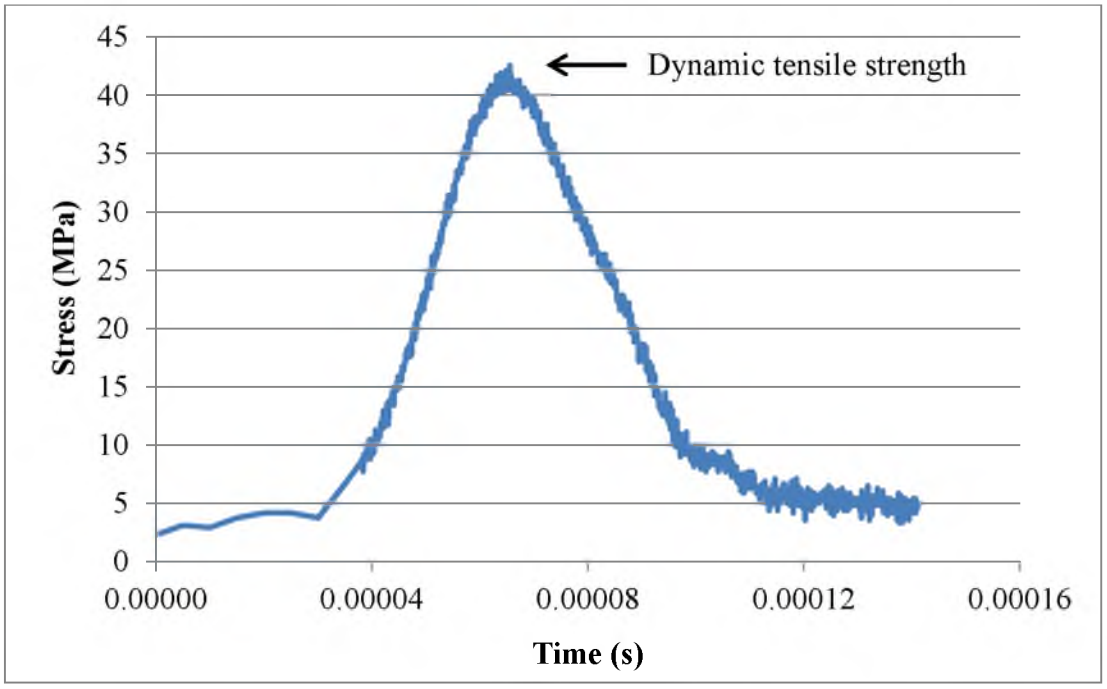

Figure E.15 Plot of stress load applied to Brazil test specimen

where

$\dot{\varepsilon}(t)$ is the net strain rate applied,

c is the longitudinal wave velocity in the bar, here equal to 4,992 m/s,

D is the diameter of the test specimen,

$\varepsilon_i(t)$ is the incident strain pulse,

$\varepsilon_r(t)$ is the reflected strain pulse, and

$\varepsilon_t(t)$ is the transmitted strain pulse.

Using Equation E.12 requires lining up the incident, reflected, and transmitted strain pulses so they occur at the same instance. Figure E.16 exhibits the strain records for sample C04 for the incident, reflected, and transmitted strain pulses used in Equation E.12. The sum of the incident and reflected pulses is also shown. In theory, the $\varepsilon_i + \varepsilon_r$ and ε_t signals should coincide closely, as the reaction forces at each end of the test

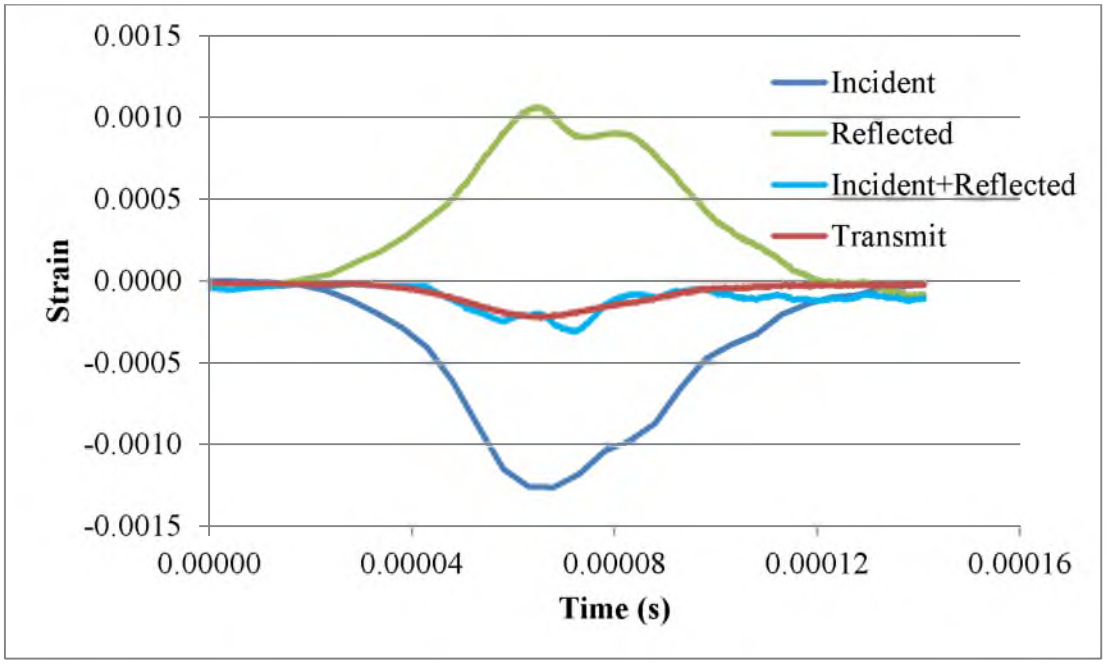

Figure E.16 Strain pulses shifted together for calculations for sample C04

specimen are approximately the same. The dynamic nature of the test, though, requires tailored pulse shaping with an appropriate striker bar for the $\varepsilon_i + \varepsilon_r$ and ε_t records to appear similar (Zhou and Zhoa 2011). Testing without a pulse-shaping striker will generate high frequency oscillations in the $\varepsilon_i + \varepsilon_r$ record, introducing an imbalance between the reaction forces at both ends of the sample.

Overall, the dynamic tensile strength of the rhyolite was determined to be 40.6 MPa (5,894 psi) at an average strain rate of 349 s^{-1}. This amounts to a dynamic increase factor of 3.6 over the static tensile strength. The results of the dynamic Brazil tension tests are listed in Table E.10. Tests were conducted both with and without pulse shapers.

E.8 Dynamic compressive strength

The SHPB setup used in Section E.7 was also used to test for dynamic compressive strength. A set of specimens from sample group A were tested using the SHPB employed for measuring dynamic tensile strength.

The strain rate in each test specimen can be calculated using Equation E.12, and the strain and stress in each sample are given by (Zhou and Zhoa 2011):

$$\varepsilon(t) = \frac{c}{D}\int_0^t [\varepsilon_i(t) - \varepsilon_r(t) - \varepsilon_t(t)]dt \tag{E.13}$$

$$\sigma(t) = \frac{A_{bar}}{2A_{sample}} E_{bar}[\varepsilon_i(t) - \varepsilon_r(t) - \varepsilon_t(t)] \tag{E.14}$$

where A_{sample} is the initial cross-sectional area of the sample. The compressive strength is the peak stress at failure. No pulse shaping was applied in testing, resulting in some

Table E.10 Dynamic tensile strengths – group C

Sample ID	Tensile strength		Dynamic increase factor	Peak strain rate
	MPa	psi		s^{-1}
C03	37.35	5417	3.3	351
C04	42.52	6168	3.8	334
C05	37.22	5398	3.3	358
C06	33.81	4903	3.0	358
C07	35.35	5128	3.1	325
C08	41.74	6054	3.7	320
C09	34.87	5057	3.1	290
C10	35.54	5155	3.1	324
C11	43.31	6282	3.8	363
C12	36.05	5228	3.2	280
C13	36.06	5230	3.2	279
C14	38.31	5557	3.4	292
C15	42.18	6117	3.7	289
C16	39.32	5703	3.5	289
C17	39.68	5755	3.5	378
C18*	45.93	6662	4.1	444
C19*	52.47	7609	4.6	445
C20*	50.83	7372	4.5	465
C21*	49.59	7192	4.4	439
Average	40.64	5894	3.6	349

* No pulse shaper used

unbalanced loading at both ends of the specimen and high-frequency strain components. Figure E.17 shows the superimposed strain records for one of the samples.

The results of the tests are listed in Table E.11. The average dynamic compressive strength of the rhyolite was determined to be 301.6 MPa (43,740 psi), which gives a dynamic increase factor of 1.4 times greater than the static compressive strength. The average strain rate for these tests was 285 s^{-1}. Samples that failed from tensile spalling were not included in the final results, but are listed in Table E.11.

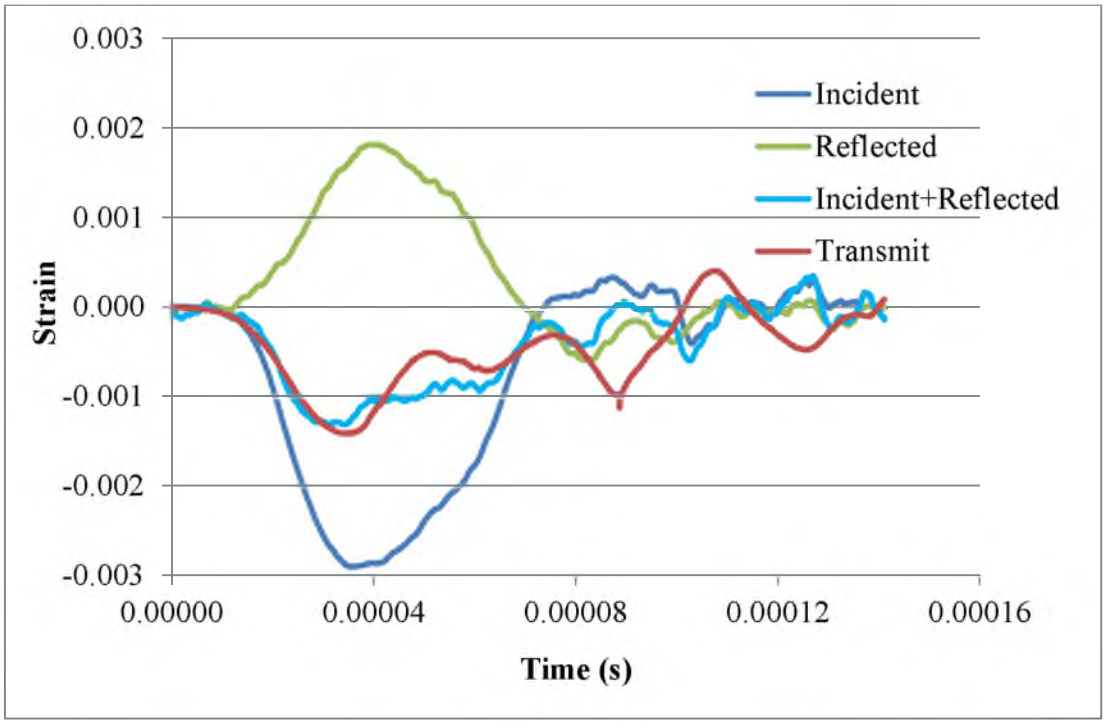

Figure E.17 Strain pulses shifted together for calculations for sample A10

Table E.11 Dynamic compressive strengths – group A

Sample ID	Compressive strength		Dynamic increase factor	Peak strain rate
	MPa	psi		s^{-1}
A07*	236.87	34356	1.1	209
A08	351.77	51020	1.6	287
A09*	268.82	38989	1.2	223
A10	282.94	41037	1.3	281
A11	263.52	38221	1.2	290
A12*	275.28	39926	1.2	270
A13*	270.27	39199	1.2	237
A14	315.32	45733	1.4	299
A15	294.33	42688	1.3	267
Average	301.57	43740	1.4	285

* Tensile failure

E.9 Summary of dynamic strength measurements

Figure E.18 shows a plot of all results for dynamic strength tests, minus those specimens that failed from tensile spalling during compression tests. Note that for the tensile strengths, larger strengths were measured at higher strain rates. This agrees with findings in other rock strength characterization studies that the rate of dynamic loading in a test influences the point of failure. Thus, the dynamic strengths measured in Tables E.10 and E.11 may only be valid at the applied strain rates.

E.10 Calculated rock properties

In addition to the measured and estimated rhyolite properties previously described, a few useful rock properties are calculated here. From the MC failure envelope, the unconfined shear strength τ_0 of the rhyolite is given by $\tau_0 = C_0 \cos\phi\ /2$.

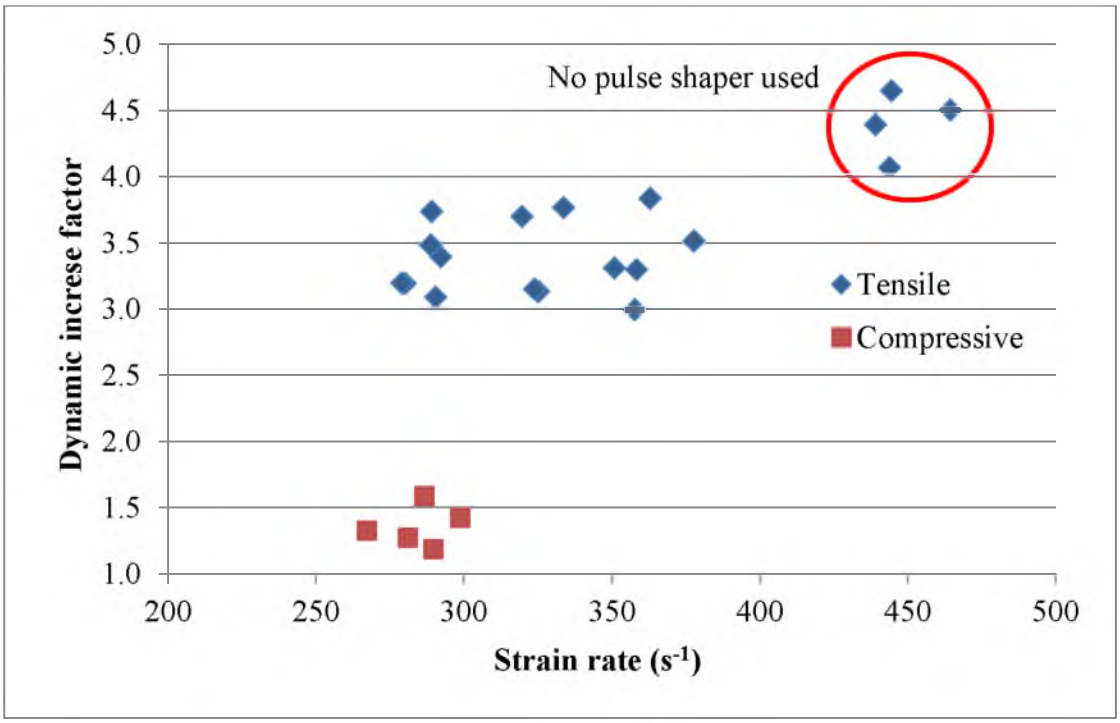

Figure E.18 Strain pulses shifted together for calculations for sample A10

The shear strength was determined to be 47.7 MPa (6,916 psi). The dynamic Young's modulus E_{dyn} and Poisson's ratio ν_{dyn} formulae, as given in ASTM standard D 2845-08 "Standard test method for laboratory determination of pulse velocities and ultrasonic elastic constants of rock," are

$$E_{dyn} = \frac{\rho V_s^2 \left(3V_p^2 - 4V_s^2\right)}{V_p^2 - V_s^2} \tag{E.15}$$

$$\nu_{dyn} = \frac{V_p^2 - 1V_s^2}{2\left(V_p^2 - V_s^2\right)} \tag{E.16}$$

where ρ is the mass density of the rock, and V_p and V_s are the P-wave and S-wave propagation velocities, respectively. The dynamic moduli were calculated to be 47.1 GPa (6,836 ksi) for Young's modulus and 0.23 for Poisson's ratio.

APPENDIX F

PYTHON CODE FOR HOLMBERG–PERSSON MODEL

This appendix provides the Python script written for using the modified Holmberg–Persson vibration prediction approach developed by Smith (2003). The program requires an input text file containing the radial distance, depth from surface, and peak particle velocity (PPV) for each measurement location. A scaling law for α/β must be specified. The search range for an optimum α may need to be adjusted. Values for parameters such as (1) material properties for tensile strength, Young's modulus, wave speed, and rock density; (2) blasthole dimensions; and (3) explosive column height, depth, and density must be entered.

Several options can be turned on or off in the code to vary the output. These are controlled by their Boolean values in the code (*True* or *False*). They are listed as follows:

- Conversion to metric units in the event that the input data file is comprised of imperial units;
- Option to plot the measured, predicted PPV, and estimated tensile damage limit against distance;
- Option to plot vibration contours around the blasthole; and
- Option to plot the estimated tensile damage limit around the blasthole.

The script lists the scaled distance constants α, β, and k as determined using the least squares method incorporated by Smith (2003) in the modified HP model. Measured and predicted PPV values and residuals are also listed as part of the output.

"""
mod_hp_bound.py

Author: Kirk Erickson

Program that reads in an array of PPV vibration data from an explosive charge and returns an approximate damage region based off the tensile strength of the surrounding rock. The damage region is calculated using an empirical vibration model based off a least squares method to estimate scaled-distance vibration levels. The vibration constants are then parsed into a modified adaptation of the Holmberg-Persson approach to calculate vibration contours around the explosive charge. The damage limits are then estimated using the rock's tensile strength as the boundary limits.
   St = eE = PPV*E/c
where St is the tensile strength of the rock, e is the vibration-induced strain, E is Young's modulus, PPV is the peak particle velocity vibration contour at the limit of the failure.

---Theory---
Empirical vibration model is:
   PPV = k*(W^a/R^B)
where W is the charge weight per delay, R is the distance to a point of interest, and k, a, and B are site-specific constants. Applying a constraint of a/B = 1/2 or 1/3, the result is
   PPV = k*(SD)^-B, where SD = R/W^0.5 or R/W^0.333
   The Holmberg-Persson model in discrete format is given by
   PPV = k*[sum from T to H (q*dZ/[r0^2 + (z - z0)^2]^(B/2a))^a]
      = k*(Summation Term)
where q is the linear charge density, dZ is an increment of the explosives column that ranges from the top of the charge T to the bottom H (T and H are expressed as depths below the surface), (r0,z0) is the point of interest at which the PPV is being calulcated, and z is the depth of the current charge increment z.
   The least squares method (LSM) employed in the program 'fit_ppv_lsm.py' is adapted here for the modified Holmberg-Persson model. It performs an iterative search for the minimum sum of residuals squared within a specified range for both k and a (a scaling law for a/B is assumed). By assuming a scaling law, a formula for the sum of the residuals squared (SRS) is
   SRS[j,f] = sum from i=0 to i=M (PPVactual[i]-PPVpredict[i])^2
where PPVactual[i] is the measured PPV, PPVpredict[i] is th PPV predicted by the Holmberg-Persson model, i, j, and f are separate indices (i ranges from 0 to M, j ranges from 0 to n, and f ranges from 0 to m). The derivative with respect to k is taken and dSRS/dk is set equal to zero. Rearranging terms, the following formula can be used to find an optimum k[i] for a given a[f].
   k[j] = (PPVactual[1] + PPVactal[2] + ...) /
   ((Summation Term)[1] + (Summation Term)[2] + ...)

```
Note: Empirical least squares vibration algortihm and the modified Holmberg-
Persson model was originally developed by Amanda Ann Smith, M.S. thesis
published at the University of Utah titled "A Modified Holmberg-Persson
Approach to Predict Blast Damage" (2003)
"""

''' To run code, first set working directory using os.chdir() command, then
execute file using execfile() command.'''
# os.chdir('C:\Users\Kirk\U of U\M.S. thesis\Numerical simulations\Modified HP
model')
# execfile('mod_hp_bound.py')

# Import modules
import numpy as np
import matplotlib.pyplot as plt

# Import data file
'''Imported data file requires 3 columns: radial distance to blasthole, depth
as measured from blasthole collar, and peak particle velocity. Program assumes
1 row of headerlines (column labels). No conversion between units is made.
Progam written for units of either ft and ips or m and mm/s.'''
h_lines = 1     # Number of lines at beginning of file to skip
f_dir = 'C:\Users\Kirk\U of U\M.S. thesis\Numerical simulations\Modified HP
model\\'
filename = f_dir + 'br_data.txt'
R = np.loadtxt(filename,skiprows = h_lines)[:,0]   # radial distance from blasthole
Z = np.loadtxt(filename,skiprows = h_lines)[:,1]   # depth measured from collar
PPV = np.loadtxt(filename,skiprows = h_lines)[:,2] # measured PPV
N = np.size(R)

# Material properties
St = 1638       # Tensile strength in psi - can be static or dynamic
E = 5311        # Young's modulus is ksi
c = 15111       # Wave velocity in ft/s - usually P-wave velocity
units_metric = False # Inform program if input units are metric or imperial
conv_to_m = True    # Convert to metric units of m, Pa, mm/s, kg

# Blasthole parameters
d = 4.75                # Blasthole diameter, inches
d = d/12                # Blasthole diamater, ft
H = 22.                 # Depth of blasthole, ft
T = 14.                 # Stemming height, ft
Le = H - T              # Length of explosive column
pe = 0.85               # Specific gravity of explosive
wg = 62.43              # weight/volume of water, here lb/ft^3
```

```
q = pe*d**2.*wg*np.pi/4.    # Charge density in blasthole, lb/ft

# Conversion to metric units
ft_to_m = 0.3048
in_to_mm = 25.4
psi_to_pa = 6894.757
lbm_to_kg = 0.4535924

if conv_to_m:
    R *= ft_to_m           # ft to m
    Z *= ft_to_m
    PPV *= in_to_mm        # in./s to mm/s
    St *= psi_to_pa*10**-6  # psi to MPa
    E *= psi_to_pa*10**-6   # ksi to GPa
    c *= ft_to_m
    d *= ft_to_m
    H *= ft_to_m
    T *= ft_to_m
    Le *= ft_to_m
    wg *= lbm_to_kg/ft_to_m**3  # lb/ft^3 to g/cm^3
    q *= lbm_to_kg/ft_to_m      # lb/ft to kg/m

    del(ft_to_m,in_to_mm,psi_to_pa,lbm_to_kg)

# Input parameters for vibration model
sc_law = 0.333              # scaling law; equal to a/B
a_min = 0.3
a_max = 2.0
a_inc = 0.001               # number of iterations to perform for a
a_itr = np.int(np.round((a_max - a_min)/a_inc))
# increment to advance a in calculations

# Plotting parameters
disp_PPV = True     # Plot comparison of measured and predicted PPV
disp_vb = True      # Display vibration contours
disp_lim = True     # Display damage limits based off tensile strength
ext_factor = 0.2
r_max = 40*d*(1+ext_factor)  # Estimated radial extent of damage limit to plot

# Define function for calculating summation term in Holmberg-Persson model
def hpsum(R,Z,PPV,d,q,dZ,num_dz,sZ,a,sc_law):
    '''Note: Function assumes that the length of the explosive charge is
    comprised of an integer number num_dz of charge increments dZ.
    Input arguments are:
      R   - array of radial distances from blasthole
      Z   - depths measured from collar
```

```
        PPV - measured PPV
        d   - diamter of blasthole
        q   - loading density of explosive charge per unit length of blasthole
        dZ  - charge increment for calculations
        num_dz - number of charge increments in explosive column
        sZ  - starting depth for calculations
        a   - a constant for vibration model
        sc_law - scaling law

    Output values are:
        SUM - summation term for hp model
        k  - k constant for vibration model'''

    N = np.size(R)
    SUM = np.zeros(N)
    cur_z = sZ - 0.5*dZ

    for j in np.arange(N):
        for l in np.arange(num_dz):
            cur_z += dZ
            SUM[j] += (q*dZ/np.sqrt(R[j]**2+(cur_z-Z[j])**2)**(1./sc_law))**a
        cur_z = sZ - dZ
    k = np.sum(PPV)/np.sum(SUM)

    return SUM,k

# Calculations for determining constants for Holmberg-Persson vibration model
# using the LSM iterative approach
print '\nCalculating vibration constants...'
k = np.zeros(a_itr+2)   # Array for storing k constants
SRS = np.zeros((a_itr+2,N)) # Array for storing individual residuals squared
SRSt = np.zeros(a_itr+2) # Array for storing total residuals squared per iteration
SUM = np.zeros((a_itr+2,N)) # Array for storing summation terms
a_cur = a_min - 2.*a_inc # Counter to track current a constant
dZ = np.sqrt(6)*d/2   # Charge increment based on 'just-touching' sphere model
num_dz = np.int(np.around(Le/dZ)) # Number of charge increments in explosive
column
dZ = Le/num_dz

for i in np.arange(a_itr+2):
    a_cur += a_inc
    SUM[i,:],k[i] = hpsum(R,Z,PPV,d,q,dZ,num_dz,T,a_cur,sc_law)
    # Function call to calculate summation term and constant
    SRS[i,:] = np.power(PPV-k[i]*SUM[i,:],2)
    SRSt[i] = np.sum(SRS[i,:])
SRS_lsm = np.amin(SRSt)
```

```
mindex = np.argmin(SRSt)-1
a_lsm = a_min + a_inc*mindex
k_lsm = k[mindex]
SUM = SUM[mindex,:]
if a_lsm<a_min or a_lsm>a_max:
   print '\nOptimum detected outside of specified limits!\n'

# Print results
print '\nHolmberg-Persson vibration model constants'
print 'Scaling law a/B = {:5.3f}'.format(sc_law)
print 'Constant\tValue    \t'
print 'a    \t{0:>8.3f}\t'.format(a_lsm)
print 'k    \t{0:>7.2f}\t'.format(k_lsm)
print 'SRS  \t{0:>8.3f}\t'.format(SRS_lsm)

# Calcute vibration contour limits
if units_metric or (not(units_metric) and conv_to_m):
   PPV_lim = St*c/E           # PPV in mm/s
   print'\nPPV limit for tensile failure is {:>0.0f} mm/s'.format(PPV_lim)
else:
   PPV_lim = St*c/E*12/1000.   # PPV in ips
   print'\nPPV limit for tensile failure is {:>0.1f} ips'.format(PPV_lim)

# Calculate and plot actual vs predicted PPV
PPV_pred = k_lsm*SUM
rsd = PPV - PPV_pred
if units_metric or (not(units_metric) and conv_to_m):
   print '\nPPV in mm/s are as follows:'
   print 'PPV actual  PPV predicted  Residuals'
   for i in np.arange(N):
      print '{0:>10.0f}  {1:>13.0f}  {2:>9.0f}'.format(PPV[i],PPV_pred[i],\
         rsd[i])
else:
   print '\nPPV in ips are as follows:'
   print 'PPV actual  PPV predicted  Residuals'
   for i in np.arange(N):
      print '{0:>8.1f}  {1:>11.1f}  {2:>7.1f}'.format(PPV[i],PPV_pred[i],\
         rsd[i])

if disp_PPV:
   D = np.sqrt(np.power(R,2)+np.power(T+0.5*Le,2))
   plt.hold(True)          # Toggle hold on for multiply plot commands
   plt.plot(D,PPV,'ms',D,PPV_pred,'cv',markersize=8,zorder=2) # Plot PPV
values
   paxis = np.asarray(plt.axis())      # Axes extents
   D_range = np.amax(D) - np.amin(D)
```

```
    D = np.append(D,np.amax(D)+0.2*D_range)
    D = np.insert(D,0,np.amin(D)-0.2*D_range)
    plt.plot(D,np.ones(N+2)*PPV_lim,'r--',lw=3,zorder=1)
    # Plot PPV tensile damage limit
    plt.axis(tuple(paxis))
    plt.legend(('Measured PPV','Predicted PPV','Tensile damage limit'))
    if units_metric or (not(units_metric) and conv_to_m):
        plt.xlabel('Distance (m)')
        plt.ylabel('PPV (mm/s)')
    else:
        plt.xlabel('Distance (ft)')
        plt.ylabel('PPV (in/s)')
    plt.hold(False)
    print('\nClose plot window to continue...')
    plt.show()

    del(D_range,paxis)

# Function for use in calculating PPV for a point
def hpPPV(r0,z0,q,dZ,num_dz,sZ,k,a,sc_law):
    '''Function that calculates PPV at a point (r0,z0).
    Note: Function assumes that the length of the explosive charge is
    comprised of an integer number num_dz of charge increments dZ.

    Input arguments are:
      z   - depth of current charge increment as measured from collar
      r0  - radial distance from point to blasthole
      z0  - depth of point below collar
      q   - loading density of explosive charge per unit length of blasthole
      dZ  - charge increment for calculations
      num_dz - number of charge increments in explosive column
      sZ  - starting depth for calculations
      k  - k constant for vibration model
      a   - a constant for vibration model
      sc_law - scaling law

    Output values are:
      PPV - peak particle velocity at point'''

    cur_z = sZ - 0.5*dZ
    PPV = 0.0

    for i in np.arange(num_dz):
        cur_z += dZ
        PPV += k*(q*dZ/np.sqrt(r0**2+(cur_z-z0)**2)**(1./sc_law))**a
```

```
    return PPV

# Generate vibration contour grid - origin taken through borehole axis
print '\nGenerating vibration contour grid...'
dx = d/4    # Nominal grid spacings
dy = d/4
num_dx = np.int(np.ceil(0.8*r_max/dx)) # spacing on either side of blasthole
num_dy = np.int(np.ceil((H+r_max/1.5)/dy)) # spacing below blasthole
DX = num_dx*dx  # Grid extents
DY = num_dy*dy
gvib = np.zeros((num_dy,2*num_dx-1)) # PPV vibration grid, laid out so rows
# correspond with y-direction and columns with x-direction
xvib = np.linspace(-DX,DX,2*num_dx-1)
yvib = np.linspace(0.0,DY,num_dy)
ind_top = np.int(np.floor(T/dy)) # Index for grid point directly above blasthole
ind_bot = np.int(np.ceil(H/dy)) # Index for grid point directly below blasthole

cur_x = -dx
cur_y = -dy

for i in np.arange(0,ind_top): # Start calculations at top of model
    cur_y += dy
    for j in (np.arange(num_dx)+num_dx-1): # Start calculations at center of model
        cur_x += dx
        gvib[i,j] = hpPPV(cur_x,cur_y,q,dZ,num_dz,T,k_lsm,a_lsm,sc_law)
    cur_x = -dx

cur_x = 0
x_skip = 0
while cur_x < d/2:
    cur_x += dx
    x_skip += 1
cur_x_temp = cur_x

cur_x -= dx

for i in np.arange(ind_top,ind_bot):
    cur_y += dy
    for j in (np.arange(num_dx-x_skip)+num_dx+x_skip-1):
        cur_x += dx
        gvib[i,j] = hpPPV(cur_x,cur_y,q,dZ,num_dz,T,k_lsm,a_lsm,sc_law)
    cur_x = -dx
    for j in (np.arange(x_skip)+num_dx-1):
        cur_x += dx
        gvib[i,j] = gvib[i,num_dx+x_skip-1]
    cur_x = cur_x_temp
```

```
cur_x = -dx

for i in np.arange(ind_bot,num_dy):
    cur_y += dy
    for j in (np.arange(num_dx)+num_dx-1):
        cur_x += dx
        gvib[i,j] = hpPPV(cur_x,cur_y,q,dZ,num_dz,T,k_lsm,a_lsm,sc_law)
    cur_x = -dx

for j in (np.arange(num_dx)):
    gvib[:,j] = gvib[:,2*num_dx-2-j]

# Routine to plot blasthole layout
def bh_layout(min_x,max_x,min_y,max_y,d,H,T,fig_num,sp_num):
    '''Function that plots blasthole layout.

    Input arguments are:
      min_x   - minimum extent in x-direction
      max_x   - maximum extent in x-direction
      min_y   - minimum extent in y-direction
      max_y   - maximum extent in y-direction
      d       - diameter of blasthole
      H       - hole depth
      T       - distance from collar to explosive charge
      sp_num  - subblot number
      fig_num - figure number

    Output values are:
      fig     - figure handle
      ax      - axes handle'''

    x1 = np.array([min_x,-d/2,-d/2,d/2,d/2,max_x])
    y1 = np.array([0.,0,H,H,0,0])
    x2 = np.array([-d/2,d/2])
    y2 = np.array([T,T])
    e_x = np.array([-d/2,-d/2,d/2,d/2])
    e_y = np.array([T,H,H,T])
    t_x = np.array([-d/2,-d/2,d/2,d/2])
    t_y = np.array([min_y,T,T,min_y])
    fig = plt.figure(fig_num)
    ax = fig.add_subplot(sp_num)
    ax.fill(e_x,e_y,color=(0.3,0.9,0.3)) # Fill explosive region with color
    ax.fill(t_x,t_y,color='w') # Ensure blasthole above explosive remains
    # unfilled in event of contouring
    ax.plot(x1,y1,'k-',x2,y2,'k-',lw=2,zorder=3)
```

```
    p_axis = np.asarray(ax.axis())
    range_y = max_y - min_y
    p_axis[0] = min_x
    p_axis[1] = max_x
    p_axis[2] -= range_y*0.05
    p_axis[3] = max_y
    ax.axis(tuple(p_axis))

    # Draw layout of blasthole
    return fig,ax

# Plot blasthole
plt.hold(True) # Toggle hold on so multiple plots can be made on one figure
fig,ax = bh_layout(-DX,DX,0.0,DY,d,H,T,1,111)
ax.invert_yaxis() # Invert axis so depth is positive downwards

# Display vibration contours
if disp_vb==True:
    # Custom contour levels
    zn = 9  # Number of contours to plot
    zlevels = np.linspace(np.log(np.log(np.amin(gvib))),\
        np.log(np.log(np.amax(gvib))),zn)
    zlevels = np.exp(np.exp(zlevels)) # Exponential grading applied to levels
#    zlevels = np.linspace(np.amin(gvib),np.amax(gvib),zn) # No grading of levels
    # Contour fill plot
#    CS = plt.contourf(xvib,yvib,gvib,levels=zlevels,zorder=1) # Contour fill
    # Contour line plot
    CS = plt.contour(xvib,yvib,gvib,levels=zlevels,colors='k',zorder=1)
    plt.clabel(CS,fmt='%1.0f') # Add labels to contour lines
    del(zn)

# Display damage limit
if disp_lim==True:
#    zlim = np.array([np.amin(gvib),PPV_lim[0],np.amax(gvib)])
    zlim = np.array([PPV_lim])
    CS = plt.contour(xvib,yvib,gvib,levels=zlim,colors='r',linewidths=3,\
        linestyles='dashed',zorder=2)
    plt.clabel(CS,fmt='%1.0f',colors='k') # Add label to damage limit line
    del(zlim)

# Display plot
if units_metric or (not(units_metric) and conv_to_m):
    plt.xlabel('Distance from blasthole axis (m)')
    plt.ylabel('Depth (m)')
else:
    plt.xlabel('Distance from blasthole axis (ft)')
```

```
    plt.ylabel('Depth (ft)')
plt.hold(False)
plt.axes().set_aspect('equal')  # Force axes aspect ratio to be equal
plt.show(ax)

del(dx,dy,ext_factor,cur_x,cur_x_temp,cur_y,x_skip)
del(f_dir,i,j,ind_bot,ind_top,r_max,a_cur,a_itr,a_min,a_max)
```

APPENDIX G

AUTODYN MODEL PARAMETERS

Properties and parameters for each of the materials in the Autodyn™ simulation are provided in Tables G.1, G.2, G.3, and G.4. The vast majority of these are default values in Autodyn's material library.

Table G.1 Rhyolite properties and parameters

Equation of State	**P alpha**
Reference density	2.57000E+00 (g/cm3)
Porous density	2.56000E+00 (g/cm3)
Porous soundspeed	3.24200E+02 (cm/ms)
Initial compaction pressure	9.33000E+02 (bar)
Solid compaction pressure	6.00000E+04 (bar)
Compaction exponent	3.00000E+00 (none)
Solid EOS	Polynomial
Bulk Modulus A1	3.52700E+05 (bar)
Parameter A2	3.95800E+05 (bar)
Parameter A3	9.04000E+04 (bar)
Parameter B0	1.22000E+00 (none)
Parameter B1	1.22000E+00 (none)
Parameter T1	3.52700E+05 (bar)
Parameter T2	0.00000E+00 (bar)
Reference Temperature	3.00000E+02 (K)
Specific Heat	6.54000E+00 (Merg/gK)
Thermal Conductivity	0.00000E+00 ()
Compaction Curve	Standard
Strength	**RHT Concrete**
Shear Modulus	1.44200E+05 (bar)
Compressive Strength (fc)	2.22300E+02 (bar)
Tensile Strength (ft/fc)	5.10000E-02 (none)
Shear Strength (fs/fc)	2.15000E-01 (none)
Intact Failure Surface Constant A	1.60000E+00 (none)
Intact Failure Surface Exponent N	6.10000E-01 (none)
Tens./Comp. Meridian Ratio (Q)	6.80500E-01 (none)
Brittle to Ductile Transition	1.05000E-02 (none)
G (elas.)/(elas.-plas.)	2.00000E+00 (none)
Elastic Strength / ft	7.00000E-01 (none)
Elastic Strength / fc	5.30000E-01 (none)
Fractured Strength Constant B	1.60000E+00 (none)
Fractured Strength Exponent M	6.10000E-01 (none)
Compressive Strain Rate Exp. Alpha	9.09000E-03 (none)
Tensile Strain Rate Exp. Delta	1.25000E-02 (none)
Max. Fracture Strength Ratio	1.00000E+20 (none)
Use CAP on Elastic Surface?	Yes

Table G.1 Continued

Failure	**RHT Concrete**
Damage Constant, D1	4.00000E-02 (none)
Damage Constant, D2	1.00000E+00 (none)
Minimum Strain to Failure	1.00000E-02 (none)
Residual Shear Modulus Fraction	1.30000E-01 (none)
Tensile Failure	Hydro (Pmin)
Erosion	**Geometric Strain**
Erosion Strain	5.00000E-01 (none)
Type of Geometric Strain	Instantaneous
Material Cutoffs	-
Maximum Expansion	1.00000E-01 (none)
Minimum Density Factor (Euler)	1.00000E-04 (none)
Minimum Density Factor (SPH)	2.00000E-01 (none)
Maximum Density Factor (SPH)	3.00000E+00 (none)
Minimum Soundspeed	1.00000E-07 (cm/ms)
Maximum Soundspeed	1.01000E+15 (cm/ms)
Maximum Temperature	1.01000E+20 (cm/ms)

Table G.2 Sand properties and parameters

Equation of State	**Compaction**
Reference density	2.64100E+00 (g/cm3)
Density #1	1.67400E+00 (g/cm3)
Density #2	1.73950E+00 (g/cm3)
Density #3	1.87380E+00 (g/cm3)
Density #4	1.99700E+00 (g/cm3)
Density #5	2.14380E+00 (g/cm3)
Density #6	2.25000E+00 (g/cm3)
Density #7	2.38000E+00 (g/cm3)
Density #8	2.48500E+00 (g/cm3)
Density #9	2.58500E+00 (g/cm3)
Density #10	2.67130E+00 (g/cm3)
Pressure #1	0.00000E+00 (bar)
Pressure #2	4.57700E+01 (bar)
Pressure #3	1.49800E+02 (bar)
Pressure #4	2.91510E+02 (bar)
Pressure #5	5.91750E+02 (bar)
Pressure #6	9.80980E+02 (bar)
Pressure #7	1.79443E+03 (bar)
Pressure #8	2.89443E+03 (bar)
Pressure #9	4.50198E+03 (bar)
Pressure #10	6.50660E+03 (bar)
Density (Soundspeed) #1	1.67400E+00 (g/cm3)
Density (Soundspeed) #2	1.74560E+00 (g/cm3)
Density (Soundspeed) #3	2.08630E+00 (g/cm3)
Density (Soundspeed) #4	2.14680E+00 (g/cm3)
Density (Soundspeed) #5	2.30000E+00 (g/cm3)
Density (Soundspeed) #6	2.57200E+00 (g/cm3)
Density (Soundspeed) #7	2.59800E+00 (g/cm3)
Density (Soundspeed) #8	2.63500E+00 (g/cm3)
Density (Soundspeed) #9	2.64100E+00 (g/cm3)
Density (Soundspeed) #10	2.80000E+00 (g/cm3)
Soundspeed #1	2.65200E+01 (cm/ms)
Soundspeed #2	8.52100E+01 (cm/ms)
Soundspeed #3	1.72170E+02 (cm/ms)
Soundspeed #4	1.87550E+02 (cm/ms)
Soundspeed #5	2.26480E+02 (cm/ms)

Table G.2 Continued

Soundspeed #6	2.95610E+02 (cm/ms)
Soundspeed #7	3.11220E+02 (cm/ms)
Soundspeed #8	4.60000E+02 (cm/ms)
Soundspeed #9	4.63400E+02 (cm/ms)
Soundspeed #10	4.63400E+02 (cm/ms)
Strength	**MO Granular**
Pressure #1	0.00000E+00 (bar)
Pressure #2	3.40100E+01 (bar)
Pressure #3	3.48980E+02 (bar)
Pressure #4	1.01324E+03 (bar)
Pressure #5	1.84650E+03 (bar)
Pressure #6	5.00000E+03 (bar)
Pressure #7	0.00000E+00 (bar)
Pressure #8	0.00000E+00 (bar)
Pressure #9	0.00000E+00 (bar)
Pressure #10	0.00000E+00 (bar)
Yield Stress (zero plastic strain)	0.00000E+00 (bar)
Yield Stress #2	4.23500E+01 (bar)
Yield Stress #3	4.46950E+02 (bar)
Yield Stress #4	1.24035E+03 (bar)
Yield Stress #5	2.26000E+03 (bar)
Yield Stress #6	2.26000E+03 (bar)
Yield Stress #7	0.00000E+00 (bar)
Yield Stress #8	0.00000E+00 (bar)
Yield Stress #9	0.00000E+00 (bar)
Yield Stress #10	0.00000E+00 (bar)
Density #1	1.67400E+00 (g/cm3)
Density #2	1.74570E+00 (g/cm3)
Density #3	2.08630E+00 (g/cm3)
Density #4	2.14680E+00 (g/cm3)
Density #5	2.30000E+00 (g/cm3)
Density #6	2.57200E+00 (g/cm3)
Density #7	2.59800E+00 (g/cm3)
Density #8	2.63500E+00 (g/cm3)
Density #9	2.64100E+00 (g/cm3)
Density #10	2.80000E+00 (g/cm3)
Yield Stress (zero plastic strain)	0.00000E+00 (bar)

Table G.2 Continued

Yield Stress #2	0.00000E+00 (bar)
Yield Stress #3	0.00000E+00 (bar)
Yield Stress #4	0.00000E+00 (bar)
Yield Stress #5	0.00000E+00 (bar)
Yield Stress #6	0.00000E+00 (bar)
Yield Stress #7	0.00000E+00 (bar)
Yield Stress #8	0.00000E+00 (bar)
Yield Stress #9	0.00000E+00 (bar)
Yield Stress #10	0.00000E+00 (bar)
Density #1	1.67400E+00 (g/cm3)
Density #2	1.74570E+00 (g/cm3)
Density #3	2.08630E+00 (g/cm3)
Density #4	2.14680E+00 (g/cm3)
Density #5	2.30000E+00 (g/cm3)
Density #6	2.57200E+00 (g/cm3)
Density #7	2.59800E+00 (g/cm3)
Density #8	2.63500E+00 (g/cm3)
Density #9	2.64100E+00 (g/cm3)
Density #10	2.80000E+00 (g/cm3)
Shear Modulus #1	7.69000E+02 (bar)
Shear Modulus #2	8.69400E+03 (bar)
Shear Modulus #3	4.03170E+04 (bar)
Shear Modulus #4	4.90690E+04 (bar)
Shear Modulus #5	7.76900E+04 (bar)
Shear Modulus #6	1.48009E+05 (bar)
Shear Modulus #7	1.65710E+05 (bar)
Shear Modulus #8	3.67180E+05 (bar)
Shear Modulus #9	3.73470E+05 (bar)
Shear Modulus #10	3.73470E+05 (bar)
Failure	**Hydro (Pmin)**
Hydro Tensile Limit	-1.00000E-02 (bar)
Reheal	Yes
Crack Softening	No
Stochastic failure	No
Erosion	**Geometric Strain**
Erosion Strain	1.00000E+00 (none)
Type of Geometric Strain	Instantaneous

Table G.2 Continued

Material Cutoffs	-
Maximum Expansion	1.00000E-01 (none)
Minimum Density Factor (Euler)	1.00000E-04 (none)
Minimum Density Factor (SPH)	2.00000E-01 (none)
Maximum Density Factor (SPH)	3.00000E+00 (none)
Minimum Soundspeed	1.00000E-07 (cm/ms)
Maximum Soundspeed	1.01000E+15 (cm/ms)
Maximum Temperature	1.01000E+20 (cm/ms)

Table G.3 ANFO properties and parameters

Equation of State	**JWL**
Reference density	8.50000E-01 (g/cm3)
Parameter A	4.94600E+05 (bar)
Parameter B	1.89100E+04 (bar)
Parameter R1	3.90700E+00 (none)
Parameter R2	1.11800E+00 (none)
Parameter W	3.33333E-01 (none)
C-J Detonation velocity	4.16000E+02 (cm/ms)
C-J Energy / unit volume	2.48400E+04 (kerg/mm3)
C-J Pressure	5.15000E+04 (bar)
Burn on compression fraction	0.00000E+00 (none)
Pre-burn bulk modulus	0.00000E+00 (bar)
Adiabatic constant	0.00000E+00 (none)
Auto-convert to Ideal Gas	Yes
Strength	**None**
Failure	**None**
Erosion	**None**
Material Cutoffs	-
Maximum Expansion	1.00000E-01 (none)
Minimum Density Factor (Euler)	1.00000E-04 (none)
Minimum Density Factor (SPH)	2.00000E-01 (none)
Maximum Density Factor (SPH)	3.00000E+00 (none)
Minimum Soundspeed	1.00000E-07 (cm/ms)
Maximum Soundspeed	1.01000E+20 (cm/ms)
Maximum Temperature	1.01000E+20 (cm/ms)

Table G.4 Air properties and parameters

Equation of State	**Ideal Gas**
Reference density	1.22500E-03 (g/cm3)
Gamma	1.40000E+00 (none)
Adiabatic constant	0.00000E+00 (none)
Pressure shift	0.00000E+00 (bar)
Reference Temperature	2.88200E+02 (K)
Specific Heat	7.17600E+00 (Merg/gK)
Thermal Conductivity	0.00000E+00 ()
Strength	**None**
Failure	**None**
Erosion	**None**
Material Cutoffs	-
Maximum Expansion	1.00000E-01 (none)
Minimum Density Factor (Euler)	1.00000E-04 (none)
Minimum Density Factor (SPH)	2.00000E-01 (none)
Maximum Density Factor (SPH)	3.00000E+00 (none)
Minimum Soundspeed	1.00000E-03 (cm/ms)
Maximum Soundspeed	1.01000E+15 (cm/ms)
Maximum Temperature	1.01000E+20 (cm/ms)

APPENDIX H

PYTHON CODE FOR LEAST SQUARES

VIBRATION MODEL

This appendix contains scripts written in Python for computing best fit, scaled-distance vibration models using the iterative least squares methodology proposed by Smith (2003). For the plots shown in Figures B.15 and B.16, the data presented in Table H.1 was used. These data were randomly generated using the script named "gen_sd_data.py."

Table H.1 Randomly-generated vibration data

Random peak particle vibration (PPV) data set		
W - explosive weight (lb), D - distance (ft), PPV (in./s)		
W	D	PPV
756	788	2.42
466	436	2.55
161	568	1.52
690	1172	1.21
747	686	2.74
804	708	1.7
282	534	1.42
170	549	0.89
829	212	15.57
396	273	5.66
425	498	3.41
179	526	0.9
834	670	2.65
271	196	8.86
563	241	6.47
361	668	1.66
297	352	3.91
154	295	2.67
461	566	2.63
508	386	3.21

H.1 Python script for randomly generating vibration data

```
"""
gen_sd_data.py

Author: Kirk Erickson

Program to randomly generate scaled distance data for blast vibration
analysis. Based on the empirical equation PPV = k(SD)^-B, where SD =
R/W^(a/B).
"""
''' To run code, first set working directory using os.chdir() command, then
execute file using execfile() command.'''
# os.chdir('C:\Users\Kirk\U of U\M.S. thesis\LSM vibration model')
# execfile('gen_sd_data.py')

# Import modules
import numpy as np

# Input parameters
'''Note: Program originally written for units of lb, ft, and ips'''
sc_law = 0.4                    # Scaling law
B = 1.6
a = B*sc_law
k = 700.
W_range = np.array([100.,900.])   # Range of charge weights
SD_range = np.array([10.,90.])    # Range of scaled distance values
N = 20                          # size of data set
factor = 1.2                    # Amount by which data can randomly vary

# Generate random data
SD = np.random.random(N)*(SD_range[1]-SD_range[0])+SD_range[0]
# Generate scaled distances
W = np.random.random(N)*(W_range[1]-W_range[0])+W_range[0]
# Generate charge weights
R = np.multiply(SD,np.power(W,sc_law)) # Calulate distances
PPV = np.multiply(k,np.power(SD,-B)) # Calculate PPV values
PPV += np.multiply(np.random.random(N),PPV)*factor  # Randomize PPV data

# Write values to file
savedir = 'C:\Users\Kirk\U of U\M.S. thesis\LSM vibration model\\'
filename = savedir + 'rnd_data.txt' # File name to write data to
fid = open(filename,'w')
fid.write('Random peak particle vibration (PPV) data set\n')
fid.write('W - explosive weight (lb), D - distance (ft), PPV (ips)\n')
fid.write('W\tD\tPPV\n')
```

```
for i in np.arange(N):
    fid.write('{0:5.0f}\t{1:5.0f}\t{2:5.2f}\n'.format(W[i],R[i],PPV[i]))
fid.close()
```

H.2 Python script for LSM vibration model using 1D approach

```
"""
fit_ppv_lsm.py

Author: Kirk Erickson

Program that reads in an array of vibration data and returns an empirical
vibration model using a least squares method. Results are compared with the
conventional method for estimating a vibration model using a least squares
linear regression of logarithmically-transformed data.

Note: Method was originally developed by Amanda Ann Smith, M.S. thesis
published at the University of Utah titled "A Modified Holmberg-Persson
Approach to Predict Blast Damage" (2003)

---Theory---
Empirical vibration model is:
   PPV = k*(W^a/R^B)
where W is the charge weight per delay, R is the distance to a point of
interest, and k, a, and B are site-specific constants. Applying a constraint
of a/B = 1/2 or 1/3, the result is
   PPV = k*(SD)^-B, where SD = R/W^0.5 or R/W^0.333

The conventional method for fitting a vibration model is to linearize the
equation using logarithms, then apply a simple linear regression.
   log PPV = log K + B*log(SD) --> y = B0 + B1*x
The advantage of this approach is mathematical expediency; the disadvantage is
that the linear regression minimizes the sum of the squares of the logarithm
of the residuals, rather than the actual residuals themselves. This can lead
to erroneous predictions towards or beyond the limits of the data or when the
data range is large.

The least squares method (LSM) employed in this program performs an iterative
search for the minimum sum of residuals squared within a specified range for
both k and B (a scaling law for a/B is assumed). By assuming a scaling law, a
2D formula for the sum of the residuals squared (SRS) is
   SRS[j,f] = sum from i=0 to i=M (PPV[i]-k[j]*(SD[i])^-B[f])^2
where i, j, and f are separate indices (i ranges from 0 to M, j ranges from 0
to n, and f ranges from 0 to m). This formula requires computation in two
dimensions, since both k and B are varied. By taking the derivative with
respect to one of these constants and setting it equal to zero, the problem
can be reduced to one dimensional. It is easier to differentiate with respect
to k. The result is
   dSRS[j,f]/dk[j] = sum from i=0 to i=M (0 - 2*PPV[i]*(SD[i])^-B[f] +
      2*k[j]*(SD[i])^-2B[f])
```

```
    --> k[j] = (PPV[1]*(SD[1])^-B[f] + PPV[2]*(SD[2])^-B[f] + ...) /
    ((SD[1])^-2B[f] + SD[2])^-2B[f] + ...)

"""
''' To run code, first set working directory using os.chdir() command, then
execute file using execfile() command.'''
# os.chdir('C:\Users\Kirk\U of U\M.S. thesis\LSM vibration model')
# execfile('C:\Users\Kirk\U of U\M.S. thesis\LSM vibration model\\fit_ppv_lsm.py')

# Import modules
import numpy as np
import matplotlib.pyplot as plt

# Import data file
'''Imported data file requires 3 columns: explosive weight, distance,
and peak particle velocity. Program assumes 3 row of headerlines (column
labels). No conversion between units is made. Program originally written for
units of lb, ft, and ips'''
h_lines = 3     # Number of lines at beginning of file to skip
f_dir = 'C:\Users\Kirk\U of U\M.S. thesis\LSM vibration model\\'
filename = f_dir + 'rnd_data_final.txt'     # location and name of file
W = np.loadtxt(filename,skiprows = h_lines)[:,0]    # explosive weights
R = np.loadtxt(filename,skiprows = h_lines)[:,1]    # distance from
PPV = np.loadtxt(filename,skiprows = h_lines)[:,2]  # measured PPV
N = np.size(W)  # Number of data points

# Input parameters
display = True              # Boolean to plot results
sc_law = np.array([1./2,1./3],dtype=np.float) # scaling law; equal to a/B
L = np.size(sc_law)
W.shape = (N,1)             # Reshape input data arrays to 2 dimensions
R.shape = (N,1)
PPV.shape = (N,1)
B_min = 0.5     # Minimum extent of B
B_max = 3.      # Maximum extent of B
B_inc = 0.001   # increment to advance B in calculations
B_itr = (B_max - B_min)/B_inc # number of iterations to perform for B

# Scaled distance calculations
SD = np.zeros((N,L))

for i in np.arange(L):
    for k in np.arange(N):
        SD[k,i] = R[k]/W[k]**sc_law[i]

# Compute conventional vibration model, using logarithmic transform and linear
```

```
# regression
SD_log = np.log(SD)
PPV_log = np.log(PPV)
B_conv, k_conv = np.zeros(L), np.zeros(L)

for i in np.arange(L):
    x_mean = np.mean(SD_log[:,i])
    y_mean = np.mean(PPV_log)
    Sxy = np.sum((PPV_log-y_mean)*(SD_log[:,i].reshape((N,1))-x_mean))
    Sxx = np.sum(np.power(SD_log[:,i].reshape((N,1))-x_mean,2))
    B_conv[i] = -Sxy/Sxx                    # conventionally-obtained B
    k_conv[i] = np.exp(y_mean - Sxy/Sxx*x_mean) # conventionally-obtained k

# Calculate residuals squared for conventional vibration model
PPV_conv = np.zeros((N,L))
SRS_conv = np.zeros(L)

for i in np.arange(L):
    for k in np.arange(N):
        PPV_conv[k,i] = k_conv[i]*np.power(SD[k,i],-B_conv[i])
    SRS_conv[i] = np.sum((PPV-PPV_conv[:,i].reshape((N,1)))**2)

# Compute LSM iterative vibration model
SD_lsm = np.zeros((N,1))
k = np.zeros((B_itr+2,L))
SRS = np.zeros((B_itr+2,L))
B_lsm = np.zeros(L)
k_lsm = np.copy(B_lsm)
SRS_lsm = np.zeros(L)

for i in np.arange(L):
    B_cur = B_min-B_inc
    for f in np.arange(B_itr+2):
        SD_lsm = np.power(SD[:,i],-B_cur).reshape((N,1))
        k[f,i] = np.sum(np.multiply(PPV,SD_lsm))/np.sum(np.power(SD_lsm,2))
#       k[f,i] = np.sum(PPV)/np.sum(SD_lsm)    # Original formula; incorrect
        B_cur = B_cur + B_inc
        SRS[f,i] = np.sum(np.power(PPV-k[f,i]*SD_lsm,2))
    SRS_lsm[i] = np.amin(SRS[:,i])
    B_lsm[i] = B_min + B_inc*(np.argmin(SRS[:,i])-1)
    k_lsm[i] = k[np.argmin(SRS[:,i])-1,i]
    if B_lsm[i]<B_min or B_lsm[i]>B_max:    # Check check for poor constraints
        print 'Optimum detected outside of specified limits!\n'

# Print results
print 'Vibration model constants are as follows:\n'
```

```
for i in range(L):
    print 'Scaling law a/B = {:5.3f}'.format(sc_law[i])
    print 'Value  \tLog    \tLSM    \t'
    print 'B    \t{0:>8.3f}\t{1:>8.3f}'.format(B_conv[i],B_lsm[i])
    print 'k    \t{0:>7.2f}\t{1:>7.2f}'.format(k_conv[i],k_lsm[i])
    print 'SRS  \t{0:>8.3f}\t{1:>8.3f}'.format(SRS_conv[i],SRS_lsm[i])
    print '\n'


del(Sxy,Sxx,x_mean,y_mean,SD_log,PPV_log)
del(B_cur,B_min)

# Display results
if display:
    plt.close()

    if L>16:    # No plot generated if more than 16 figures to be plotted
        print 'Number of subplots exceeds maximum of 16!'
    else:
        s1 = np.int(np.ceil(np.sqrt(L))) # Determine arrangement of subplots
        s2 = np.int(L-s1)
        if s2==0:
            s2 = 1
        elif s2*s1<L:
            s2 += 1
        s_cur = 1 # Current subplot number

        for i in np.arange(L):
            plt.subplot(s1,s2,s_cur)    # Subplot number
            xaxis = np.linspace(np.amin(SD[:,i]),np.amax(SD[:,i]))
            yaxis1 = k_conv[i]*np.power(xaxis,-B_conv[i])
            yaxis2 = k_lsm[i]*np.power(xaxis,-B_lsm[i])
            plt.plot(SD[:,i],PPV,'rs',xaxis,yaxis1,'--k',xaxis,yaxis2,'-k')
            if s_cur==1:
                plt.suptitle('Comparison of vibration models',fontsize=18)
#           sc_show = '{0:0.3f}'.format(sc_law[i])  # For showing superscript
#           plt.xlabel('Scaled distance 'r'$R/W^{'+sc_show+'}$')
            plt.xlabel('Scaled distance 'r'$R/W$^${0:5.3f}$'.format(sc_law[i]))
            plt.ylabel('PPV, 'r'$\alpha/\beta={0:5.3f}$'.format(sc_law[i]))
            plt.legend(('Data','Log','LSM'))
            s_cur = s_cur + 1

        mng = plt.get_current_fig_manager()
        mng.window.showMaximized()  # Maximize figure window
        plt.show()
```

```
        del(s1,s2,s_cur,xaxis,yaxis1,yaxis2)
del(display,SD_lsm)
```

H.3 Python script for LSM vibration model that generates 2D surface of residuals

```
"""
fit_ppv_lsm_2D.py

Author: Kirk Erickson

This program uses the same approach as that applied in the script
fit_ppv_lsm.py, except that the approach in fitting a least squares vibration
model uses a brute-force approach of the residuals squared algorithm
    SRS[j,f] = sum from i=0 to i=M (PPV[i]-k[j]*(SD[i])^-B[f])^2
where i, j, and f are separate indices (i ranges from 0 to M, j ranges from 0
to n, and f ranges from 0 to m). This program also produces a contour graph
for each scaling law within the domains specified for the site-specific
constants k and B.
"""
''' To run code, first set working directory using os.chdir() command, then
execute file using execfile() command.'''
# os.chdir('C:\Users\Kirk\U of U\M.S. thesis\LSM vibration model')
# execfile('fit_ppv_lsm_2D.py')

# Import modules
import numpy as np
import matplotlib.pyplot as plt
import matplotlib

# Import data file
'''Imported data file requires 3 columns: explosive weight, distance,
and peak particle velocity. Program assumes 3 row of headerlines (column
labels). No conversion between units is made. Program originally written for
units of lb, ft, and ips'''
h_lines = 3     # Number of lines at beginning of file to skip
f_dir = 'C:\Users\Kirk\U of U\M.S. thesis\LSM vibration model\\'
filename = f_dir + 'rnd_data_final.txt'     # location and name of file
W = np.loadtxt(filename,skiprows = h_lines)[:,0]    # Explosive weights
R = np.loadtxt(filename,skiprows = h_lines)[:,1]    # Distance from
PPV = np.loadtxt(filename,skiprows = h_lines)[:,2]  # Measured PPV
N = np.size(W)  # Number of data points

# Input parameters
display = True              # Boolean to plot results
sc_law = np.array([1./2,1./3],dtype=np.float) # scaling law; equal to a/B
L = np.size(sc_law)
W.shape = (N,1)             # Reshape input data arrays to 2 dimensions
R.shape = (N,1)
PPV.shape = (N,1)
```

```
B_min = [1.4,1.5]       # Minimum extents of B
B_max = [2.0,2.0]       # Maximum extents of B
B_itr = 200.            # Number of iterations to perform for B
B_inc = np.zeros(L)
for i in range(L):
    B_inc[i] = (B_max[i] - B_min[i])/B_itr
    # Increment to advance B in calculations
k_min = [200.,1200.]    # Minimum extents of k
k_max = [700.,3000.]    # Maximum extents of k
k_itr = 600.            # Number of iterations to perform for k
k_inc = np.zeros(L)
for i in range(L):
    k_inc[i] = (k_max[i] - k_min[i])/k_itr
    # Increment to advance k in calculations
zn = 20         # No. of colors to use for contour plot
zg = True       # Flag for grading contours to match large changes in
                # topography and provide ample resolution near minimum
gcolor = False  # Use gray-scaled coloring between contours
grev = True     # Flag to reverse gray scale colors
gcmap = True    # Use custom gray-scale color map for contour plot

# Scaled distance calculations
SD = np.zeros((N,L))

for i in np.arange(L):
    for k in np.arange(N):
        SD[k,i] = R[k]/W[k]**sc_law[i]

# Compute conventional vibration model, using logarithmic transform and linear
# regression
SD_log = np.log(SD)
PPV_log = np.log(PPV)
B_conv, k_conv = np.zeros(L), np.zeros(L)

for i in np.arange(L):
    x_mean = np.mean(SD_log[:,i])
    y_mean = np.mean(PPV_log)
    Sxy = np.sum((PPV_log-y_mean)*(SD_log[:,i].reshape((N,1))-x_mean))
    Sxx = np.sum(np.power(SD_log[:,i].reshape((N,1))-x_mean,2))
    B_conv[i] = -Sxy/Sxx                    # conventionally-obtained B
    k_conv[i] = np.exp(y_mean - Sxy/Sxx*x_mean) # conventionally-obtained k

# Calculate residuals squared for conventional vibration model
PPV_conv = np.zeros((N,L))
SRS_conv = np.zeros(L)
```

```
for i in np.arange(L):
    for k in np.arange(N):
        PPV_conv[k,i] = k_conv[i]*np.power(SD[k,i],-B_conv[i])
    SRS_conv[i] = np.sum((PPV-PPV_conv[:,i].reshape((N,1)))**2)

# Compute LSM iterative vibration model
SD_lsm = np.zeros((N,1))
SRS = np.zeros((L,B_itr+2,k_itr+2))
B_lsm = np.zeros(L)
k_lsm = np.copy(B_lsm)
SRS_lsm = np.zeros(L)
SRS_max = np.copy(SRS_lsm)

for i in np.arange(L):
    B_cur = B_min[i]-B_inc[i]
    for f in np.arange(B_itr+2):
        SD_lsm = np.power(SD[:,i],-B_cur).reshape((N,1))
        k_cur = k_min[i] - k_inc[i]
        for j in np.arange(k_itr+2):
            SRS[i,f,j] = np.sum(np.power(PPV-k_cur*SD_lsm,2))
            k_cur += k_inc[i]
        B_cur += B_inc[i]
    SRS_lsm[i] = np.amin(SRS[i,1:B_itr+1,1:k_itr+1])
    SRS_max[i] = np.amax(SRS[i,1:B_itr+1,1:k_itr+1])
    mindex = np.unravel_index(np.argmin(SRS[i,:,:]),(B_itr+2,k_itr+2))
    B_lsm[i] = B_min[i] + B_inc[i]*(mindex[0]-1)
    k_lsm[i] = k_min[i] + k_inc[i]*(mindex[1]-1)
    if B_lsm[i]<B_min[i] or B_lsm[i]>B_max[i] or k_lsm[i]<k_min[i] or \
            k_lsm[i]>k_max[i]:  # Check check for poor constraints
        print 'Optimum detected outside of specified limits!'

# Print results
print '\nVibration model constants are as follows:\n'
for i in range(L):
    print 'Scaling law a/B = {:5.3f}'.format(sc_law[i])
    print 'Value  \tLog    \tLSM    \t'
    print 'B    \t{0:>8.3f}\t{1:>8.3f}'.format(B_conv[i],B_lsm[i])
    print 'k    \t{0:>7.2f}\t{1:>7.2f}'.format(k_conv[i],k_lsm[i])
    print 'SRS  \t{0:>8.3f}\t{1:>8.3f}'.format(SRS_conv[i],SRS_lsm[i])
    print '\n'

del(Sxy,Sxx,x_mean,y_mean,SD_log,PPV_log)
del(B_cur,k_cur)

# Custom grayscale colormap for plotting exponentially-increasing contour
# levels
```

```
def exp_cmap(num_l=0.2,max_g=0.5,grev=True):    # Function definition
    '''Note: the variable num_l adjusts the rate of exponential increase in the
    darkness of gray colors in the map, and can be any value.
    The variable max_g dictates the darkest shade of gray to be used, and
    ranges between 0 and 1.'''
    g_scale = max_g*(np.exp(np.linspace(0,num_l,zn+1))-1)/(np.exp(num_l)-1) + \
        (1.0-max_g)
    if grev==False: # If reversed array is not to be used
        g_scale = g_scale[::-1]
    l_scale = np.linspace(0,1,zn)
    c_color = np.zeros((zn,3))

    for i in range(zn):
        c_color[i,0] = l_scale[i]
        c_color[i,1] = g_scale[i]
        c_color[i,2] = g_scale[i+1]
    c_color = tuple(c_color)

    g_dict = {'red': c_color,'green': c_color,'blue': c_color}
    g_exp_map =
matplotlib.colors.LinearSegmentedColormap('grey_exp_colormap',\
        g_dict,256)

    return g_exp_map

# Display results
if display:
    plt.close()

    if L>16:    # No plot generated if more than 16 figures to be plotted
        print 'Number of subplots exceeds maximum of 16!'
    else:
        s1 = np.int(np.ceil(np.sqrt(L))) # Determine arrangement of subplots
        s2 = np.int(L-s1)
        if s2==0:
            s2 = 1
        elif s2*s1<L:
            s2 += 1
        s_cur = 1 # Current subplot number

        for i in np.arange(L):
            B_plot = np.linspace(B_min[i]-B_inc[i],B_max[i]+B_inc[i],B_itr+2)
            k_plot = np.linspace(k_min[i]-k_inc[i],k_max[i]+k_inc[i],k_itr+2)
            # Plotting axes
            plt.hold(True)  # Hold plot on for overlaying contour plots
            plt.subplot(s1,s2,s_cur)    # Subplot number
```

```
    zaxis = np.transpose(SRS[i,:,:]) # Transpose SRS to match axes
    if zg:  # Graded contour levels
       zlevels = np.linspace(np.log(SRS_lsm[i]),np.log(SRS_max[i]),\
          zn+1)
       zlevels = np.exp(zlevels)
    else:
       zlevels = np.linspace(SRS_lsm[i],SRS_max[i],zn+1)
    if gcolor: # Apply grayscale shading
       if gcmap:   # Custom grayscale
          g_exp_map = exp_cmap(0.01,0.4,grev)
          plt.contourf(B_plot,k_plot,zaxis,levels=zlevels,\
             cmap=g_exp_map)
       else:   # Built-in grayscale
          if grev:
             plt.contourf(B_plot,k_plot,zaxis,levels=zlevels,\
                cmap=plt.cm.gray_r)
          else:
             plt.contourf(B_plot,k_plot,zaxis,levels=zlevels,\
                cmap=plt.cm.gray)
    # Plot contour lines and labels
    CS = plt.contour(B_plot,k_plot,zaxis,levels=zlevels,colors='k')
    plt.clabel(CS,fmt='%1.0f')
    p_axis = np.asarray(plt.axis())
    p_hrange = p_axis[1] - p_axis[0]
    p_vrange = p_axis[3] - p_axis[2]
    # Plot minimum with label
    plt.plot(B_lsm[i],k_lsm[i],'bo',markersize=10)
    plt.text(B_lsm[i]+p_hrange*0.008,k_lsm[i]+p_vrange*0.008,\
       'Minimum',fontsize=12)
    plt.title('LSM contour surface for scaling law 'r'$\alpha/' + \
       r'\beta={0:5.3f}$'.format(sc_law[i]),fontsize=12)
    plt.xlabel(r'$\beta$-values')
    plt.ylabel('k-values')
    plt.hold(False)
    s_cur = s_cur + 1

mng = plt.get_current_fig_manager()
mng.window.showMaximized()  # Maximize figure window
plt.show()
del(s1,s2,s_cur,B_plot,k_plot,p_axis)
```

APPENDIX I

THE FAST FOURIER TRANSFORM

During the course of the author's studies, a considerable amount of time and effort was spent on learning and applying the basics of digital signal analysis with the Fourier transform to apply in research for this thesis. It is only reasonable that at least an overview of the knowledge acquired should be passed on for other individuals to use. For those who are unfamiliar with digital signal processing and wish to expand their knowledge beyond the contents of this appendix, *Fundamentals of Signals and Systems* by Cha and Molinder (2006) is highly recommended for both its accessibility and brevity.

In this appendix, a basic overview of the Fast Fourier Transform (FFT) is presented. Python code is attached for calculating and plotting a frequency spectrum from an input vibration waveform.

I.1 Background theory of the FFT

Frequency analysis plays an important role in a variety of fields such as signal analysis, filtering, probability and statistics, cryptology, numerical analysis, and digital data compression, to name a few. When studying a waveform signal, whether it is acoustic or electrical or seismic, spectral analysis is often needed. The FFT has become a revolutionary algorithm for its computational efficiency and ability to manipulate digital data.

A signal can be represented either in time domain or frequency domain. Time domain gives information such as the signal's duration, its behavior at various points in its history, and the occurrence of peak amplitudes. Frequency domain presents the overall frequency content of the signal and what frequencies are dominant. The FFT can be used to transform data between both domains. To understand how this works, consider the case of a simple sinusoid.

I.1.1 Frequency content of a simple sinusoid

Recall that frequency is the number of cycles, or revolutions, per second that a wave oscillates at. The frequency f of a cycle and its duration, or period T, are related using the relationship

$$f = \frac{1}{T} \tag{I.1}$$

For a simple sinusoid, the rate of oscillation is specified in this general equation of motion:

$$f(t) = A\sin\left(\frac{2\pi t}{T} + \phi\right) = A\sin(2\pi f t + \phi) = A\sin(\omega t + \phi) \tag{I.2}$$

where A is the amplitude of the sine wave, ϕ is the phase, and $\omega = 2\pi f$ is the angular frequency and is measured in radians/second. Consider the sine wave specified by the equation $f(t) = \sin t$, with amplitude $A = 1$ and phase $\phi = 0$. Figure I.1 shows a graph of $f(t)$.

To plot a frequency spectrum of $f(t)$, all that is needed is to determine its frequency. From Equation I.2, $f(t)$ can be expanded as

$$f(t) = 1.0 \cdot \sin\left(2\pi \cdot \frac{1}{2\pi} t\right) \tag{I.3}$$

where here $f = 1/2\pi$. Figure I.2 shows a graph of the frequency spectrum, which is here represented as a unit impulse function.

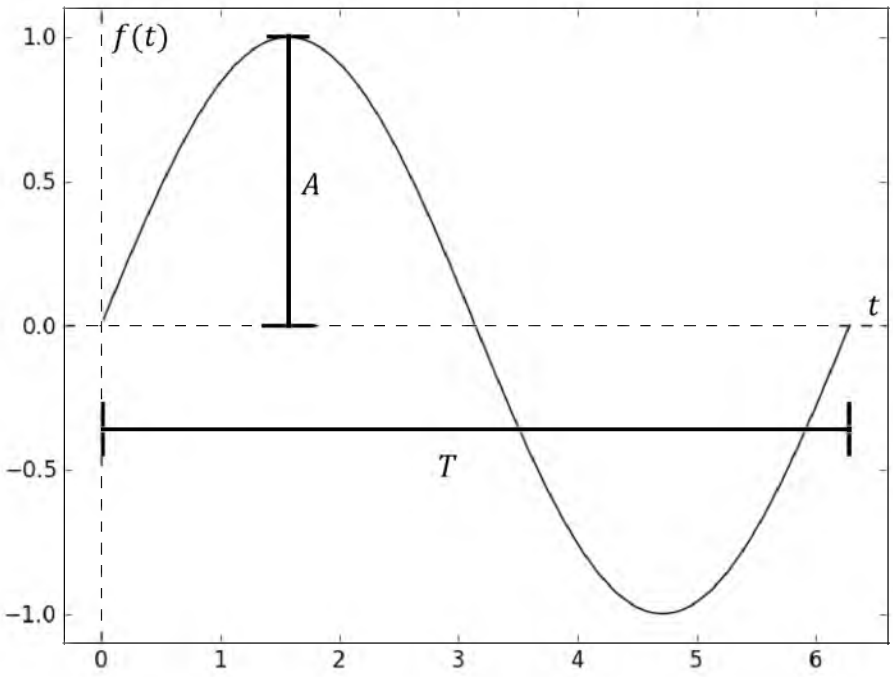

Figure I.1 Graph of $f(t) = \sin t$

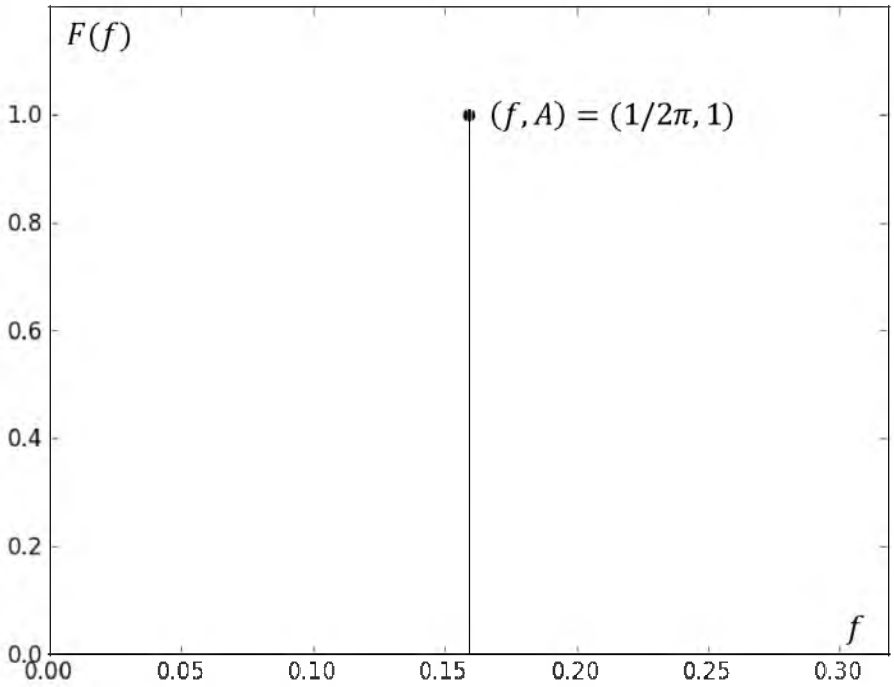

Figure I.2 Frequency spectrum of $f(t) = \sin t$

I.1.2 Frequency content of two superimposed sinusoids

Consider two different sinusoids superimposed with each other. Sinusoid 1 has amplitude $A_1 = 1$ and frequency $f_1 = 1/2\pi$, and sinusoid 2 has amplitude $A_2 = 0.5$ and frequency $f_2 = 1/\pi$. The combined waveform has the equation of

$$f(t) = 1.0 \cdot \sin\left(2\pi \cdot \frac{1}{2\pi} t\right) + 0.5 \cdot \sin\left(2\pi \cdot \frac{1}{\pi} t\right) = \sin t + 0.5 \sin 2t \qquad (I.4)$$

Figures I.3 and I.4 show Equation I.4 in both the time and frequency domains. Note that the amplitude of the second sine term in Equation I.4 is one-half that of the first in the spectral plot.

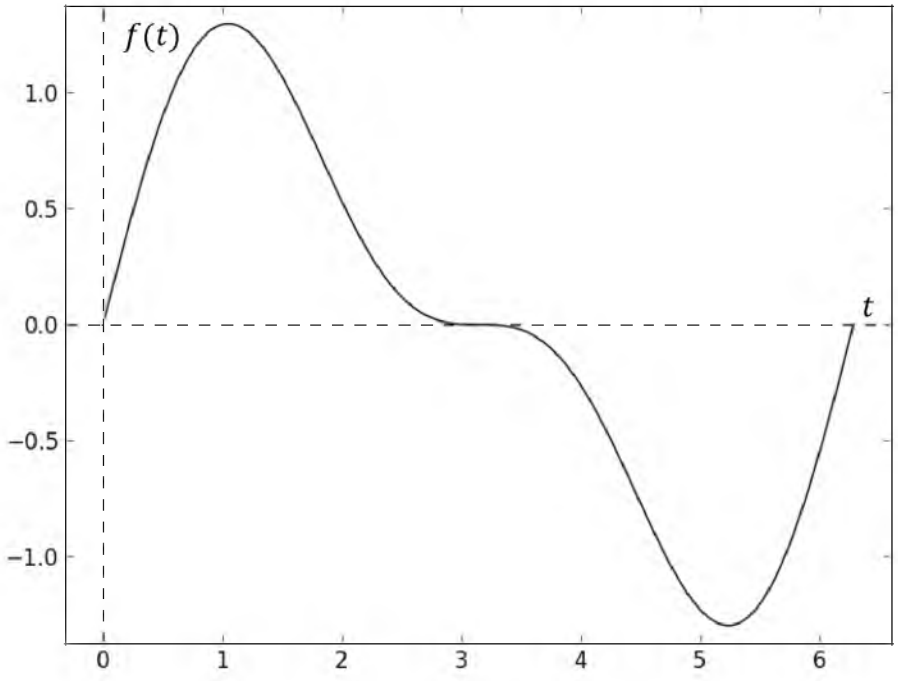

Figure I.3 Graph of $f(t) = \sin t + 0.5 \sin 2t$

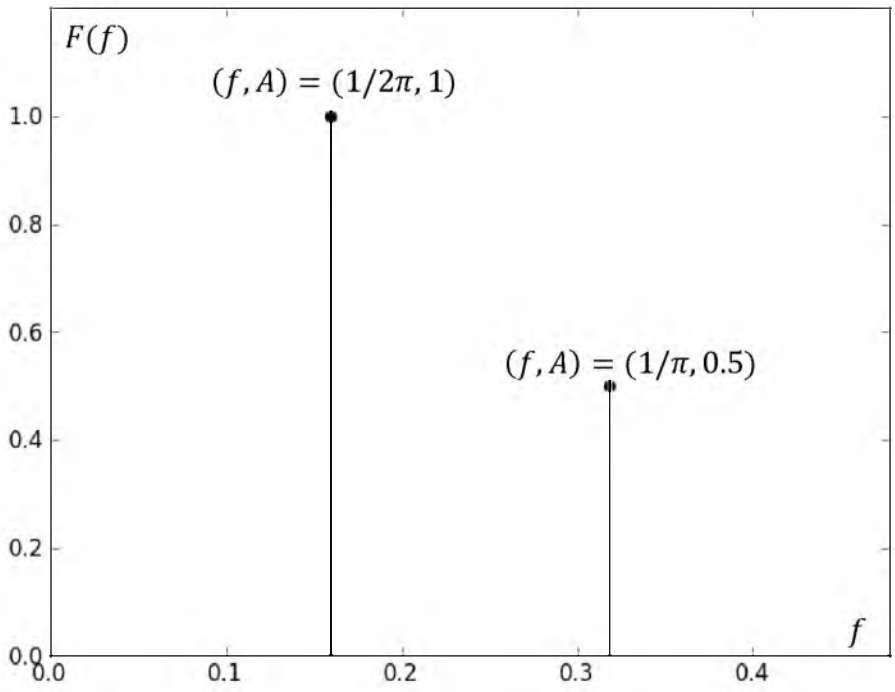

Figure I.4 Frequency spectrum of $f(t) = \sin t + 0.5 \sin 2t$

I.1.3 Fourier series

The previous two examples demonstrate how to construct a frequency spectrum from simple sinusoidal functions. However, most functions do not directly incorporate a frequency term in their formulations and most experimentally-obtained vibration waveforms are rather complex in nature. The Fourier series tool, developed by the mathematician Joseph Fourier in the 19th century, bridges the gap between simple sine waves and virtually any function. The Fourier series formulation allows essentially any arbitrary function to be expressed as a series of sine and cosine functions (Asmar 2005). The formula is presented in Equation I.5.

$$f(t) = a_0 + \sum_{n=1}^{\infty} (a_n \cos nt + b_n \sin nt) \tag{I.5}$$

where a_0, a_n, and b_n are coefficients that can be determined using these integral formulas:

$$a_0 = \frac{1}{2\pi}\int_{-\pi}^{\pi} f(t)dt \tag{I.6}$$

$$a_n = \frac{1}{\pi}\int_{-\pi}^{\pi} f(t)\cos nt\, dt \tag{I.7}$$

$$b_n = \frac{1}{\pi}\int_{-\pi}^{\pi} f(t)\sin nt\, dt \tag{I.8}$$

Note that these integrals are evaluated over the interval $[-\pi, \pi]$. For arbitrary periods, a more detailed formulation is used.

Two conditions must be met by the function $f(t)$ for Equation I.5 to be valid (Asmar 2005):

1. $f(t)$ must be periodic over a constant interval.
2. $f(t)$ must be piecewise-smooth, meaning that no discontinuities are present except at the ends.

These conditions, especially condition 1, may seem like a significant limitation. However, in most cases, only a finite interval of a function is necessary. As an example, consider the periodic function $f(t) = e^t$, evaluated from $t = 0$ to $t = 1$ and shifted by the period $T = 1$. Figure I.5 displays a graph of this function. From Equation I.5, the Fourier series formulation for $f(t) = e^t$ is

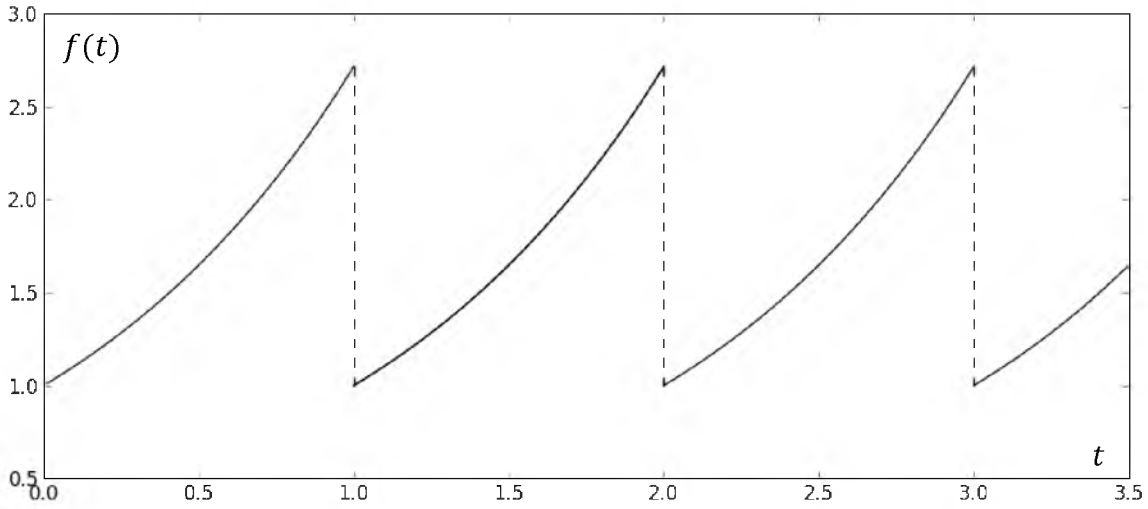

Figure I.5 Periodic, piecewise-smooth function of $f(t) = e^t$ from $t = 0$ to 1

$$f(t) = e^t = e - 1 + 4\sum_{n=1}^{\infty}\left(\frac{e-1}{8n^2\pi^2+2}\cos 2n\pi t + \frac{n\pi - n\pi e}{4n^2\pi^2+1}\sin 2n\pi t\right) \quad (I.9)$$

Figures I.6 and I.7 show partial sums of Equation I.9 overlaying $f(t) = e^t$. In theory, the approximation presented increases in accuracy as more sums are added. In reality, though, some overshoot of the oscillating lobes occurs at discontinuities, as can be seen in Figure I.7. This undesired effect is known as Gibb's phenomenon and is a numerical artifact of the Fourier series formulation (Asmar 2005).

I.1.4 Alternate formulations of Fourier series

The Fourier series equation can be reformulated so it will only contain sine or cosine terms. It can also be reformulated in terms of complex exponentials, a form that later will be shown analogous to the formula for the discrete Fourier transform. Under special cases where the input function is odd or even, either the sine or cosine term in Equation I.5 can be omitted because the multiplying coefficient becomes zero (Asmar

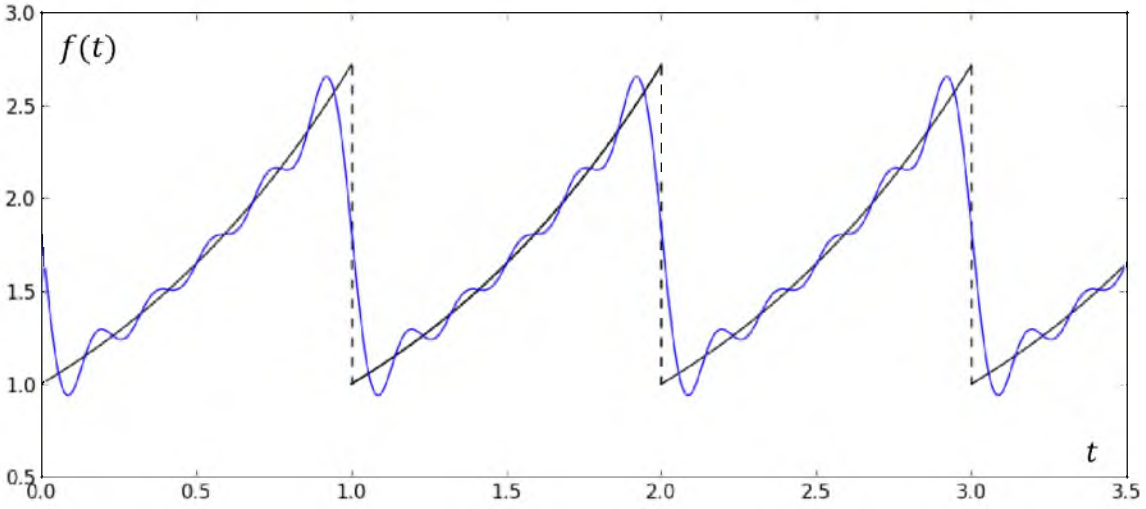

Figure I.6 Fourier series approximation of $f(t) = e^t$ from $t = 0$ to 1 using $n = 5$ sums

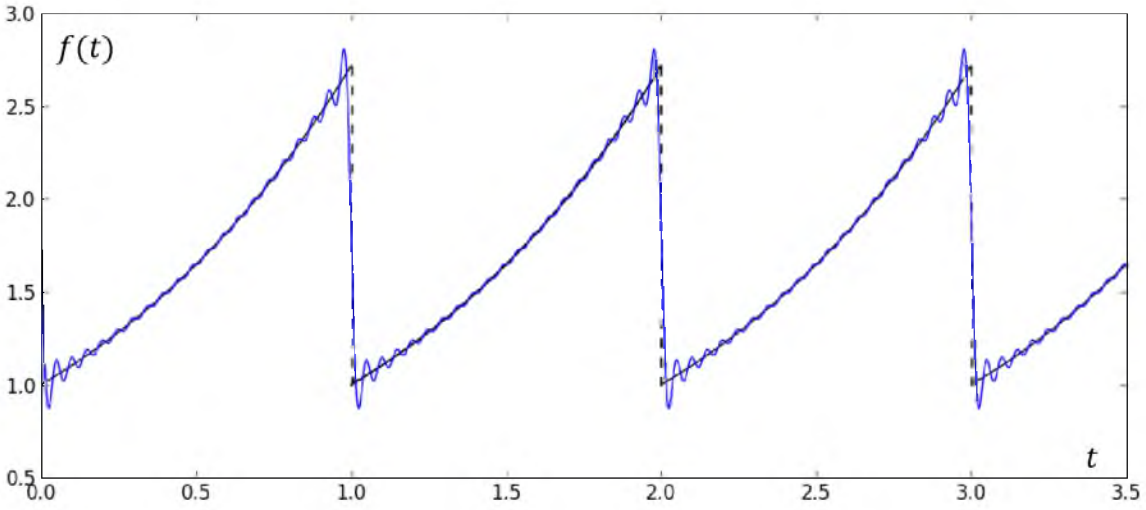

Figure I.7 Fourier series approximation of $f(t) = e^t$ from $t = 0$ to 1 using $n = 20$ sums

2005). Using the following relationships provided by Edwards et al. (2010), Equation I.5 can be rearranged in the following fashion with the aid of Figure I.8.

$$c_n = \sqrt{a_n^2 + b_n^2} \tag{I.10}$$

$$\frac{a_n}{c_n} = \sin \phi_n \tag{I.11}$$

$$\frac{b_n}{c_n} = \cos \phi_n \tag{I.12}$$

$$\phi_n = \begin{cases} \tan^{-1}(a_n/b_n) & for\ a_n > 0, b_n > 0 \\ \pi + \tan^{-1}(a_n/b_n) & for\ a_n < 0 \\ 2\pi + \tan^{-1}(a_n/b_n) & for\ a_n > 0, b_n < 0 \end{cases} \tag{I.13}$$

Equation I.5 then becomes

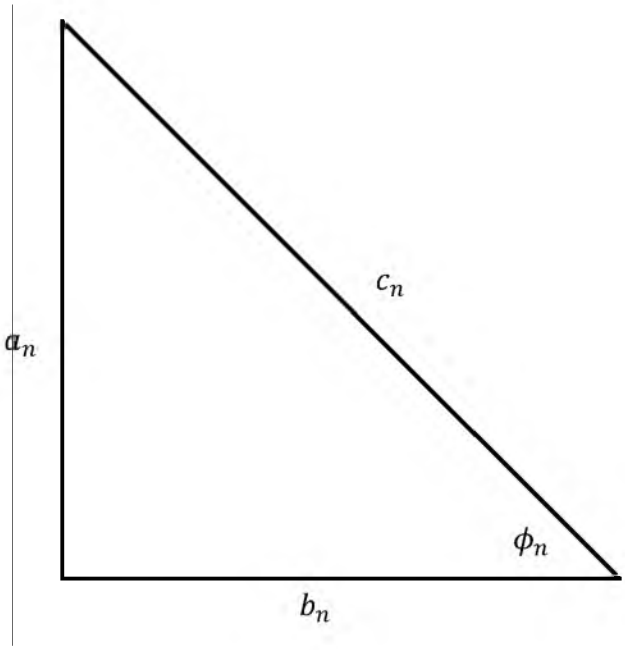

Figure I.8 Right triangle illustrating relation of Fourier coefficients

$$f(t) = a_0 + \sum_{n=1}^{\infty} c_n \left(\frac{a_n}{c_n}\cos nt + \frac{b_n}{c_n}\sin nt\right)$$

$$= a_0 + \sum_{n=1}^{\infty} c_n(\sin \phi_n \cos nt + \cos \phi_n \sin nt)$$

$$= a_0 + \sum_{n=1}^{\infty} c_n \sin(nt + \phi_n) \tag{I.14}$$

To cast Equation I.5 in terms of complex exponentials, Euler's identity must be employed:

$$e^{jnt} = \cos nt + j \sin nt \tag{I.15}$$

where $j = \sqrt{-1}$ is an imaginary number. The complex exponential Fourier series is

$$f(t) = \sum_{n=-\infty}^{\infty} c_n e^{jnt} \tag{I.16}$$

$$c_n = \frac{1}{T}\int_{-T/2}^{T/2} f(t)e^{jnt}dt \tag{I.17}$$

where T is the interval over which $f(t)$ is piecewise smooth. This formulation is useful in that it shows for each frequency given by n, the corresponding magnitude of the input function at that frequency is the constant coefficient c_n.

I.1.5 The Fourier transform

A mathematic transform is a formula that converts a function or set of data from one domain to another. The Fourier transform converts a continuous function or a set of

data, representing a signal in the time domain, to the frequency domain. Conversely, the inverse Fourier transform will do the opposite. The Fourier series is a generalization of the Fourier series that can be applied over the entire domain of a function or data set, not just a periodic interval (Asmar 2005).

For analytical functions, the Fourier and inverse Fourier transforms are integrals of the form

$$\hat{f}(\omega) = \frac{1}{\sqrt{2\pi}} \int_{-\infty}^{\infty} f(t) e^{-j\omega t} dt \quad (-\infty < \omega < \infty) \tag{I.18}$$

$$f(t) = \frac{1}{\sqrt{2\pi}} \int_{-\infty}^{\infty} \hat{f}(\omega) e^{j\omega t} dt \quad (-\infty < t < \infty) \tag{I.19}$$

where, in applying to a waveform signal, ω may be considered the angular frequency. The Fourier transform is a special case of the Laplace transform.

For discrete data, the Fourier transform is called the discrete Fourier Transform (DFT). For a set of N points, the DFT and its inverse are given by

$$X[k] = \frac{1}{N} \sum_{n=0}^{N-1} x[n] e^{-j2\pi k \frac{n}{N}} \tag{I.20}$$

$$x[n] = \sum_{k=0}^{N-1} X[k] e^{j2\pi k \frac{n}{N}} \tag{I.21}$$

where k and n are indices of discrete points in the time and frequency domains, respectively (Cha and Molinder 2006). The values of $X[k]$ are discrete approximations of

the c_n coefficients presented in Equation I.17. Thus, for a waveform signal given by the set of points $x[n]$, the frequency amplitude at each frequency kn/N is given by $X[k]$.

For a real-valued input data set, the DFT returns a complex-valued data set in which each point is of the form $a_k + b_k j$. This output can be separated into frequency magnitude $c_k = \sqrt{a_k^2 + b_k^2}$ and phase $\phi_k = \tan^{-1}(b_k/a_k)$. A plot of c_k against its corresponding frequency axis gives the frequency spectrum; a plot of ϕ_k gives the phase spectrum. Both provide potentially useful data about the frequency characteristics of a signal. However, while the frequency spectrum plot yields visually-discernible information, the phase spectrum for a complex signal often appears incoherent (Birch et al. 2013). Figure I.9 displays this.

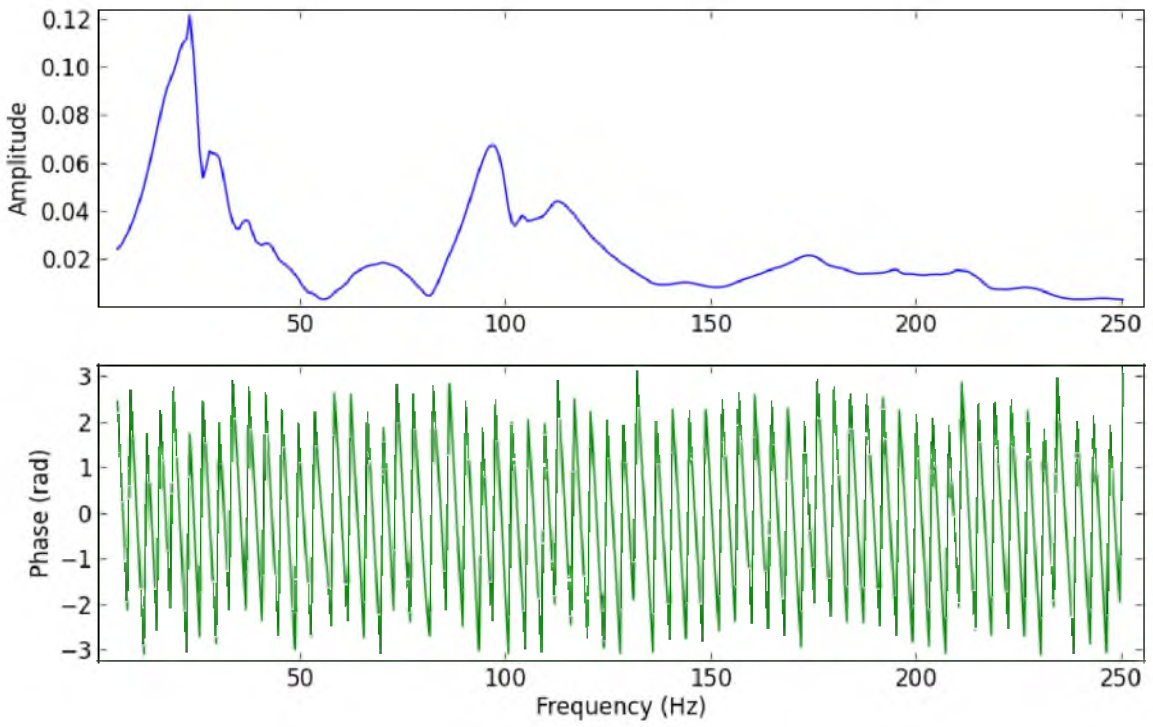

Figure I.9 Frequency and phase spectrums

One important detail to note is the construction of the frequency axis that corresponds with the DFT transform. Digital sampling theory dictates that the highest measurable frequency of a signal is only one-half of the sampling frequency, or Nyquist rate (Cha and Molinder 2006). Thus, if the sampling rate of a discrete data set is f, the maximum measureable frequency is $0.5f$.

The frequency terms of the DFT have a slightly unusual order. The frequencies start at zero and climb to $0.5f$, then suddenly drop to $-0.5f$ and climb back up to zero. The exact order depends on whether the input data set contains an even or odd number of values. The frequency domain arrangement, expressed mathematically for a data set with N values, is (Cha and Molinder 2006)

$$\text{Even: } f[n] = \frac{f}{N}\left[0, 1, 2, \ldots, \frac{N}{2} - 1, -\frac{N}{2}, -\frac{N}{2} + 1, \ldots, -2, -1\right] \quad (I.22)$$

$$\text{Odd: } f[n] = \frac{f}{N}\left[0, 1, 2, \ldots, \frac{N-1}{2}, -\frac{(N-1)}{2}, -\frac{(N-1)}{2} + 1, \ldots, -2, -1\right] \quad (I.23)$$

This behavior can be corrected by shifting both the frequencies and the DFT output about the origin. However, not all applications involving signal analysis need to do this, for two reasons. First, when only the frequency or phase spectrum is needed, only nonnegative frequencies are useful—negative frequencies do not make any physical sense. Second, the DFT possesses a property that if a real-valued data set is transformed, the second half of the transformed data set is the complex conjugate of the first half. This means that the frequency magnitudes on both sides of the origin are virtually symmetrical, although the phases are 180° opposite. Thus, unless phases on both sides of the origin become important, all the useful data is contained within the first half of the transformed data set.

I.1.6 The FFT algorithm

Through the use of a computer language, the DFT is easily implemented. The formulas presented in Equations I.20 and I.21, however, have a major drawback that becomes apparent with large data arrays. For a data set with N values, the number of operations to compute the DFT is on the order of N^2. This rapidly becomes inefficient for large volumes of data. The FFT algorithm is a computationally-efficient implementation of the DFT that can decrease the number of operations to the order of $N \log_2 N$. This results in substantial savings with large data sets. The FFT, originally discovered in 1965 by J.W. Turkey and J.W. Cooley, is considered to be among one the most important contributions in numerical mathematics (Asmar 2005).

A drawback to the FFT is its level of complexity. The underlying principle of the FFT is to factor out "roots of unity", or the factors $e^{j2\pi k_i n_l/N}$, where k_i and n_l are specific indices shared by a group of values within the larger data body (Asmar 2005). The difficulty lies in determining how to factor out these roots with an arbitrarily-sized data set. The mathematics and logic involved can become rather complicated. The simplest way to compute the FFT is to only accept data sets that contain 2^m points, with m being arbitrary. Certain shortcuts can then be taken in the FFT formulation, reducing complexity and increasing computational speed. FFT algorithms that employ this approach are termed radix-2 FFTs. Constraining the size of the input data array to a power of 2 may seem like a ridiculous limitation, but as will be shown in the next section, a technique called zero padding can be employed to bring any data set to the necessary size.

I.1.7 Resolution and zero-padding

The formulas for the DFT presented in Equations I.20 and I.21 do not explicitly specify the ranges for the indices k and n. It is only implied within the formulation that they range from 0 to $N-1$ for N values. In reality, k and n can have differently-sized ranges. The conditions of the DFT do not constrain k and n to be equal in size. A technique called zero-padding can be used, in which extra zeros are added to a data array (Cadzow 1987). Zero-padding can be employed to artificially increase the resolution of a frequency spectrum plot or ensure the input data set meets FFT algorithm size requirements. Consider the frequency spectrum plot shown in Figure I.10. The top graph shows a portion of the spectrum calculated from a record of 4,000 data points, and the bottom graph shows that same portion padded with zeros to contain 2^{14} = 16,348 data points. The differences may seem minor, but when using high sampling rates, zero-

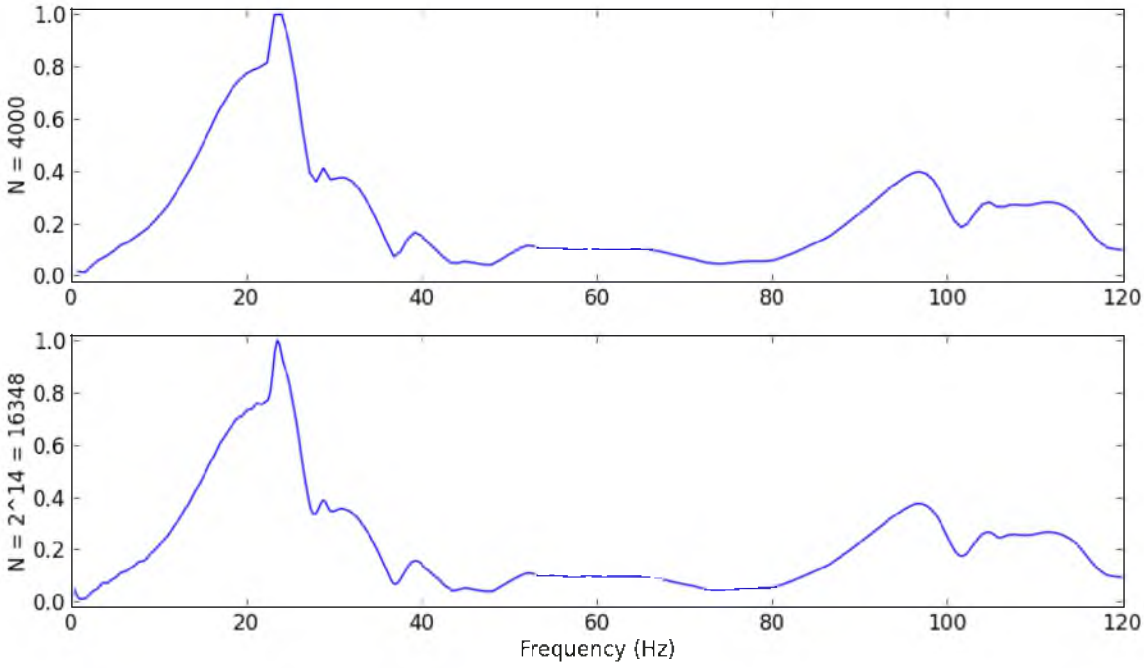

Figure I.10 Comparison of original and zero-padded frequency spectrums

padding can be beneficial for analyzing lower frequency patterns in sharper detail. Care must be taken when zero-padding, though, as high-frequency artifacts can sometimes appear in the spectrum.

If zero-padding is needed in order to reach a size requirement of 2^m data points, the following formula can be used. For a data array of N values, the minimum power m to raise 2 to such that 2^m is greater than N equals

$$m = \left\lceil \frac{\ln N}{\ln 2} \right\rceil \tag{I.24}$$

where $\lceil\ \rceil$ is the ceiling function.

I.1.8 Windowing and spectral leakage

Sometimes when a frequency spectrum is computed from a set of experimentally measured data, a large frequency magnitude will appear near 0 Hz. Usually this is a numerical artifact from the Fourier transform. A key assumption in Fourier analysis with finite data sets (or functions on a finite interval) is that the input data set repeats itself periodically. If the endpoints of the data set do not meet at the same amplitude, the Fourier transform assumes that a discontinuity has occurred and thus calculates a frequency value at a frequency approximately equal to the reciprocal of the duration of the input data set. This is the lowest frequency on the frequency axis. As an example, observe the periodic functions in Figures I.11 and I.12. Figure I.11 has no discontinuities and thus will not generate a large spike near 0 Hz. Figure I.12, on the other hand, has a large discontinuity that will be accounted for in the Fourier transform.

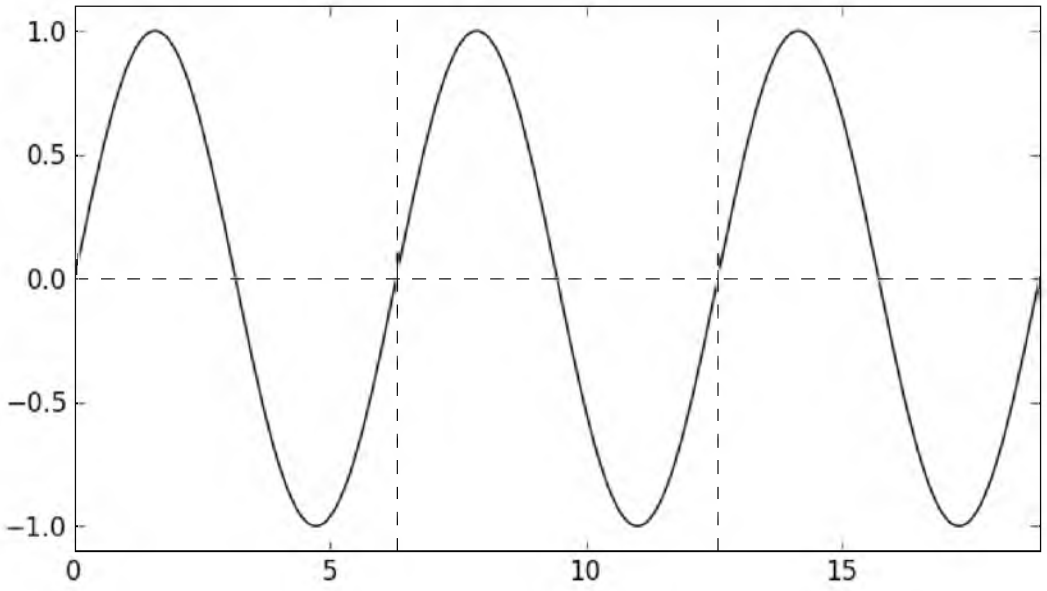

Figure I.11 Periodic signal with no discontinuity

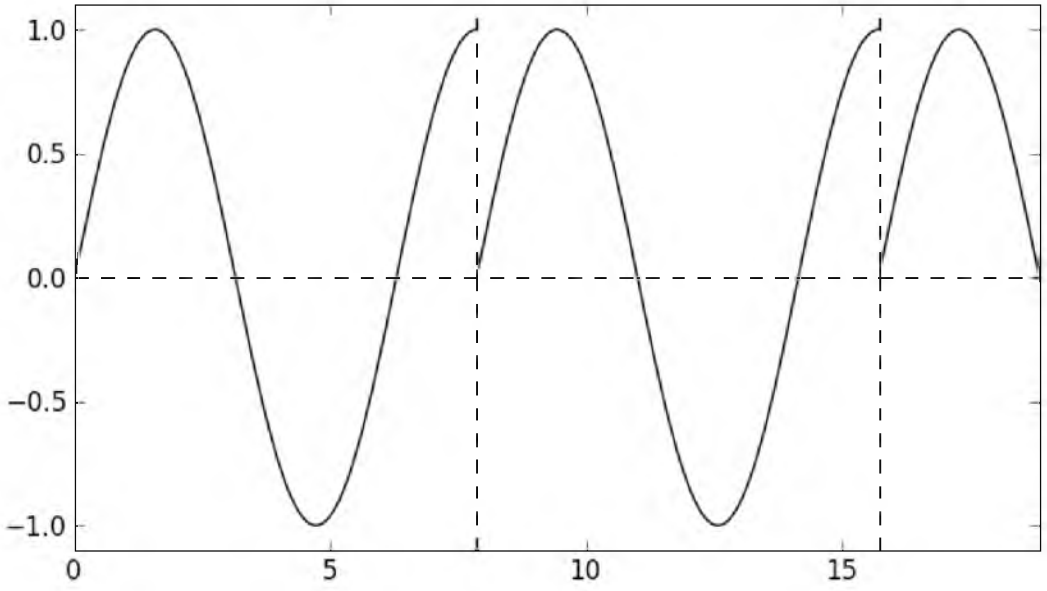

Figure I.12 Periodic signal with a discontinuity at every new cycle

There are two ways to deal with this undesirable effect. One is to ignore the large frequency amplitude near 0 Hz by not graphing it. This simple solution can only be employed with limited success, as the undesired frequency value can "bleed off" into the rest of the spectrum in a phenomenon called spectral leakage. A more rigorous approach is to use a set of tools called windows (Cha and Molinder 2006). Various types of windows can be convolved with the input data set to force the edges of the waveform towards zero. Using an appropriate window will minimize the effect of spectral leakage while leaving the signal largely intact. This approach is more complicated and subject to the judgment of the user.

I.2 Python code for computing and plotting a frequency spectrum

```
"""
fft_sample.py

Author: Kirk Erickson

Program that reads in digital signal data from a text file and computes the
frequency spectrum using FFT analysis.

Alternatively, a power spectrum may be calculated, which is simply the square
of the frequency spectrum. The power spectrum is useful in that it provides a
visual comparison of the energy content of the waveform at each frequency.

The option to plot a normalized spectrum is available.

The input file requires two columns:
   Column 1 - time increments
   Column 2 - amplitude data
Both columns must contain the same number of points.
"""
''' To run code, first set working directory using os.chdir() command, then
execute file using execfile() command.'''
# os.chdir('C:\Users\Kirk\U of U\M.S. thesis\Illustrations')
# execfile('fft_sample.py')

# Import modules
```

```
import numpy as np
import matplotlib.pyplot as plt

# Read in data file to numeric arrays
h_lines = 0     # Number of rows to skip in input file before reading data
f_dir = 'C:\Users\Kirk\U of U\M.S. thesis\Illustrations\\'  # File location
f_name = 'fft_data.txt'   # File name
filename = f_dir + f_name
time = np.loadtxt(filename,skiprows = h_lines)[:,0]
data = np.loadtxt(filename,skiprows = h_lines)[:,1]
N = len(time)

# Calculation and plotting parameters
tstart = 0.0    # Starting time value for time-domain plot
tlen = 0.5      # Ending time value for time-domain plot
k = N           # Number of increments to use in calculating the FFT
# k = 2**np.ceil(np.log(N)/np.log(2))    # find next power of 2 above N
f_low = 0       # Lower cut-off frequency for filtering
f_hi = 250      # Upper cut-off frequency for filtering
# f_low = None  # Setting both variables to None plots the full frequency
# f_high = None # spectrum
norm = False    # Flag to normalize spectrum data
power = False   # Flag to calculate power spectrum instead of normal frequency
                # spectrum
factor = 0.02   # Factor for expanding plotting extents

# Array size check
if not(np.size(time)==np.size(data)):
    raise ValueError('\nTime and data vectors must be of equal size!\n')

# Time-domain plotting extends check
if not(tstart==None) and (tstart < time[0] or tstart > time[-1]):
    print '\nSpecified starting time outside of time interval bounds; ' + \
        'setting equal to first time step\n'
    tstart = time[0]
if not(tlen==None) and (tlen > time[-1] - time[0]):
    print '\nSpecified time range exceeds time interval bounds; setting ' + \
        'equal to remaining time interval\n'
    if tstart==None:
        tlen = 0 # To be altered at a later step
    else:
        tlen = time[-1] - time[0] - max(tstart-time[0],0)

dt = np.abs((time[-1]-time[0])/(k-1))  # Time step

# Calculate frequency amplitude spectrum
```

```
'''Note: Python's implementation of the FFT does not divide the transform by
the number of data points. To stay consistent with the conventional
formulation, the FFT output is divided by k.'''
fft_data = np.fft.fft(data,k)/k         # Comput complex-values FFT
fft_data = np.fft.fftshift(fft_data)    # Shift frequencies about the origin of
                                        # frequency axis
if power==True: # Take absolute power of fft tranform data
   fft_abs = np.power(np.abs(fft_data),2)
else:
   fft_abs = np.abs(fft_data)

# Frequency bins
'''Frequency domain vectors for fft are:
Even #: f(n) = fs/N*[0,1,2,...,N/2-1,-N/2,-N/2+1,...,-2,-1]
           = fs*(n-1)/N for 1 <= n <= N/2
           = fs*[(n-1)/N-1] for N/2+1 <= n <= N
Odd #:  f(n) = fs/N*[0,1,2,...,(N-1)/2,-(N-1)/2,-(N-1)/2+1,...,-2,-1]
           = fs*(n-1)/N for 1 <= n <= (N+1)/2,
           = fs*[(n-1)/N-1] for (N+1)/2+1 <= n <= N'''
# f_axis = np.fft.fftfreq(N,dt)  # Python function for performing the same
                                 # task shown below
fs = 1/dt
if np.mod(k,2)==0: # Even number of frequency bins
   f_axis = np.hstack((fs/k*np.arange(0,int(k/2)),fs/k*\
      np.arange(int(-k/2),0)))
elif np.mod(k,2)==1: # Odd number of frequency bins
   f_axis = np.hstack((fs/k*np.arange(0,int((k-1)/2)+1),fs/k*\
      np.arange(int(-(k-1))/2,0)))
else:
   pass

f_axis = np.fft.fftshift(f_axis)    # Shift frequency spectrum about origin

# Frequency limit plotting limit check
if f_low < 0:
   print '\nNonnegative lower frequency bound detected; setting to zero\n'
   f_low = 0
elif f_low > f_axis[-1]:
   print '\nLower frequency bound exceeds frequency range; setting to zero\n'
   f_low = 0

if f_hi < 0:
   print '\nNonnegative upper frequency bound detected; setting to ' + \
      'maximum frequency\n'
   f_hi = f_axis[-1]
elif f_hi > f_axis[-1]:
```

```
    print '\nUpper frequency bound exceeds frequency range; setting to ' + \
        'maximum frequency\n'
    f_hi = f_axis[-1]

if f_low > f_hi:
    print '\nLower frequency bound greater than upper frequency bound; ' + \
        'switching bounds\n'
    f_low,f_hi = f_hi,f_low

# Determine plotting extents for time-domain plot based on user-specified
# start time and duration
if not(tstart==None): # Ensure that tstart and tlen are floating point types
    tstart = np.float(tstart)
if not (tlen==None):
    tlen = np.float(tlen)

if tstart==None:
    tstart = time[0] # Set starting time to first value of time array if not
                     # specified
if tlen==None or tlen<=0:
    print '\nCannot use negative or zero-length time range; setting equal ' + \
        'to remaining time interval\n'
    tlen = time[-1] - time[0] - max(tstart-time[0],0) # Set time plot length to
    # the remainder of the time array if not specified or is less than or
    # equal to zero

# Determine plotting extents for frequency spectrum based on user-specified
# frequency limits
if not(f_low==None): # Ensure that f_low and f_hi are floating point types
    f_low = np.float(f_low)
if not(f_hi==None):
    f_hi = np.float(f_hi)

if f_low==None or f_low==0:
     f_p1 = f_axis.searchsorted(0) + 1 # Determine array index of origin
     f_low = 0.0
else:
     f_p1 = f_axis.searchsorted(f_low) # Determine array index of f_low

if f_hi==None:
    f_p2 = k-1
    f_hi = f_axis[-1]
else:
    f_p2 = f_axis.searchsorted(f_hi)   # Determine array index of f_hi

# Normalize data if specified, set plotting axes extends of frequency spectrum
```

```
# and vertical axis label
if norm==False:
    f_range = np.amax(fft_abs[f_p1:f_p2+1])
    fr_axis = (f_low,f_hi,-factor*f_range,(1.0+factor)*f_range)
    ylabel2 ='Amplitude'
else:
    fr_axis = (f_low,f_hi,-factor,(1.0+factor))
    fft_abs = fft_abs/np.amax(fft_abs)  # Normalize fft transform data
    ylabel2='Relative amplitude'

# Plot results
plt.subplot(2,1,1)  # Time domain plot of signal
plt.plot(time,data,'k')
plt.title('Signal and frequency spectrum')
plt.xlabel('Time (sec)')
plt.ylabel('Amplitude')
plt.axis('tight')   # Set axes extents to tightly fit data
p_axis = np.asarray(plt.axis()) # Modify axes extends to slightly expand
range1 = tlen
range2 = p_axis[3] - p_axis[2]
p_axis[0] = tstart - factor*range1
p_axis[2] -= factor*range2
p_axis[1] = tstart + (1.0+factor)*range1
p_axis[3] += factor*range2
plt.axis(tuple(p_axis))

plt.subplot(2,1,2)  # Frequency spectrum plot
plt.plot(f_axis[f_p1:f_p2+1],fft_abs[f_p1:f_p2+1],'b')
plt.xlabel('Frequency (Hz)')
plt.ylabel(ylabel2)
plt.axis(fr_axis)

mng = plt.get_current_fig_manager() # Maximize figure window
mng.window.showMaximized()
plt.show()
```

REFERENCES

Abo-Zena, A.M. 1977. Radiation from a finite cylindrical explosive source. *Geophys*. 42(7):1384–1393.

Adams, D.J., Gay, N.C., and Cross, M. 1993. Preconditioning – A technique for controlling rockbursts. In *Rockbursts and Seismicity in Mines 93*. Edited by R.P. Young. Brookfield, VT: A.A. Balkema. pp. 29–33.

Adamson, W.R., and Scherpenisse, C.R. 1998. The measurement and control of blast induced damage of final pit walls in open pit mining. In *Proceedings of the Fourteenth Annual Conference on Explosives and Blasting Research*, New Orleans, LA, February 8–11. Cleveland, OH: International Society of Explosives Engineers. pp. 539–555.

AEMC Instruments. 2004. What is a TDR? Chauvin Arnoux Group. http://www.aemc.com/techinfo/appnotes/CableTesters/APP-CableTesters-WhatIsATDR. Accessed May 2013.

AEMC Instruments. 2011a. Fault Mapper Pro Telephone/Coaxial/Parallel Cable Tester Graphical TDR Model CA7026. Chauvin Arnoux Group. http://www.aemc.com/products/pdf/2127.81.pdf. Accessed May 2013.

AEMC Instruments. 2011b. User manual for CA7026 Fault Mapper Pro. Chauvin Arnoux Group. http://www.chauvin-arnoux.us/pdfs_aemc/user-manuals/CA7026_EN_ES_PO.pdf. Accessed May 2013.

Álvarez-Vigil, A.E., González-Nicieza, C., López Gayarre, F., and Álvarez-Fernández, M.I. 2012. Predicting blasting propagation velocity and vibration frequency using artificial neural networks. *Int. J. Rock Mech. Min. Sci*. 55(2012):108–116.

Anderson, D., Ott, K., Campo, D., and Haq, S. 2004. Strain and peak particle velocity as vibration criteria: Some thoughts. In *Proceedings of the Thirtieth Annual Conference on Explosives and Blasting Technique*, Vol. 2, New Orleans, LA, February 1–4. Cleveland, OH: International Society of Explosives Engineers. pp. 133–145.

Andrieux, P., McKenzie, C., Heilig, J., and Drolet, A. 1994. The impact of blasting of excavation design – A geomechanics approach. In *Proceedings of the Tenth Annual Conference on Explosives and Blasting Research*, Austin, TX, January 30–February 3. Cleveland, OH: International Society of Explosives Engineers. pp.

107–119.

Arora, S., and Dey, K. 2013. Comparison of two near-field blast vibration estimation models: A theoretical study. In *Rock Fragmentation by Blasting – Fragblast 10*. Edited by P.K. Singh and A. Sinha. Boca Raton, FL: CRC Press. pp. 465–471.

Asmar, N.H. 2005. *Partial Differential Equations with Fourier Series and Boundary Value Problems*. Upper Saddle River, NJ: Pearson Education, Inc.

Atchison, T.C., and Pugliese, J.M. 1964. *Comparative studies of explosives in granite – third series of tests*. Report of Investigation RI-6693. Washington, DC: U.S. Bureau of Mines.

Atchison, T.C., and Roth, J. 1961. *Comparative studies of explosives in marbl*e. Report of Investigation RI-5797. Washington, DC: U.S. Bureau of Mines.

Atchison, T.C., and Tournay, W.E. 1959. *Comparative studies of explosives in granite*. Report of Investigation RI-5509. Washington, DC: U.S. Bureau of Mines.

Atchison, T.C., Duvall, W.I., and Pugliese, J.M. 1964. *Effect of decoupling on explosion-generated strain pulses in rock*. Report of Investigation RI-6333. Washington, DC: U.S. Bureau of Mines.

Atlas Powder Company. 1987. *Explosives and Rock Blasting*. Dallas, TX: Explosives company.

Badger, A.A., Beecroft, A.D., and Stienstra, A. 1990. Seismic data recording: The limiting component. Presented at the 1990 Annual Meeting for the Society of Exploration Geophysicists, September 23–27, San Francisco, CA.

Banadaki, M.M.D. 2010. Stress-wave induced fracture in rock due to explosive action. Ph.D. dissertation, University of Toronto, ON.

Bastante, F.G., Alejano, L., and González-Cao, J. 2012. Predicting the extent of blast-induced damage in rock masses. *Int. J. Rock Mech. Min. Sci*. 56(2012):44–53.

Birch, W.J., Bermingham, L., Hosein, S, White, T.J., and Farnfield, R. 2013. Phase – The forgotten problem of blast vibration prediction. In *Rock Fragmentation by Blasting – Fragblast 10*. Edited by P.K. Singh and A. Sinha. Boca Raton, FL: CRC Press. pp. 425–432.

Blair, D.P. 1987. The measurement, modelling, and control of ground vibrations due to blasting. In *Second International Symposium on Rock Fragmentation by Blasting*, Keystone, CO, August 23–26. Edited by W.L. Fourney and R.D. Dick. Bethel, CT: Society for Experimental Mechanics. pp. 88–101.

Blair, D., and Minchinton, A. 1996. On the damage zone surrounding a single blasthole. In *Rock Fragmentation by Blasting – Fragblast-5*. Edited by B. Mohanty.

Brookfield, VT: A.A. Balkema. pp. 21–130.

Blair, D.P., and Spathis, A.T. 1982. Attenuation of explosion-generated pulse in rock masses. *J. Geophys. Res.* 87(B5):3885–3892.

Bollinger, G.A. 1971. *Blast Vibration Analysis*. Carbondale, IL: Southern Illinois University Press.

Born, W.T. 1941. The attenuation constant of earth materials. *Geophys.* 6(2):132–148.

Bradley, W. Jr., and Eller, E.E. 1961. Introduction to shock and vibration measurements. In *Shock and Vibration Handbook*. Vol. 1, Basic Theory and Measurements. Edited by C.M. Harris and C.E. Crede. New York: McGraw-Hill.

Brent, G.F., and Smith, G.E. 1996. Borehole pressure measurements behind blast limits as an aid to determining the extent of rock damage. In *Rock Fragmentation by Blasting – Fragblast-5*. Edited by B. Mohanty. Brookfield, VT: A.A. Balkema. pp. 103–112.

Brent, G.F,. and Smith, G.E. 1999. The detection of blast damage by borehole pressure measurement. In *Sixth International Symposium for Rock Fragmentation by Blasting – Fragblast 6*. Johannesburg, Republic of South Africa: The South African Institute of Mining and Metallurgy. pp. 9–13.

Brinkman, J.R. 1990. An experimental study of the effects of shock and gas penetration in blasting. *Third International Symposium on Rock Fragmentation by Blasting*, Brisbane, Australia, August 26–31. Brisbane, Qld., Australia: The Australasian Institute of Mining and Metallurgy. pp. 55–66.

Cadzow, J.A. 1987. *Foundations of Digital Signal Processing and Data Analysis*. New York: Macmillan.

Cha, P.D., and Molinder, J.I. 2006. *Fundamentals of Signals and Systems*. New York: Cambridge University Press.

Cho, S., Ogata, Y., and Kaneko, K. 2003. Strain-rate dependency of the dynamic tensile strength of rock. *Int. J. Rock Mech. Min. Sci.* 40(5):763–777.

Curbach, M., and Eibl, J. 1990. Crack velocity in concrete. *Eng. Fract. Mech.* 35(1–3):321–326.

Darling, P. 2011. Mining: Ancient, modern, and beyond. In *SME Mining Engineering Handbook*, 3rd ed. Vol. 1. Edited by P. Darling. Littleton, CO: Society for Mining, Metallurgy, and Exploration.

Davidson, L. 2008. *Fundamentals of Shock Wave Propagation in Solids*. Berlin: Springer-Verlag.

Dehghani, H., and Ataee-pour, M. 2011. Development of a model to predict peak particle velocity in a blasting operation. *Int. J. Rock Mech. Min. Sci*. 48(1):51–58.

Devine, J.F., Beck, R.H., Meyer, A.V.C., and Duvall, W.I. 1965. *Vibration levels transmitted across a presplit fracture plane*. Report of Investigation RI-6695. Washington, DC: U.S. Bureau of Mines.

Dey, K., and Murthy, V.M.S.R. 2013. Monitoring ground vibrations for predicting overbreak threshold levels in underground drivages. In *Rock Fragmentation by Blasting – Fragblast 10*. Edited by P.K. Singh and A. Sinha. Boca Raton, FL: CRC Press. pp. 787–791.

Dowding, C.H. 1985. *Blast Vibration Monitoring and Control*. Englewood Cliffs, NJ: Prentice-Hall, Inc.

Dowding, C.H., and Aimone, C.T. 1992. Rock breakage: Explosives. In *SME Mining Engineering Handbook*, 2nd ed. Vol. 1. Edited by H.L. Hartman. Littleton, CO: Society for Mining, Metallurgy, and Exploration.

Drukovanyi, M.F., Kravtsov, V.S., Chernyavskii, Y.E., Shelenok, V.V., Reva, N.P., and Zver'kov, S.N. 1976. Calculation of fracture zones created by exploding cylindrical charges in ledge rocks. *J. Min. Sci*. 12(3):292–295.

Duvall, W.I., and Petkof, B. 1959. *Spherical propagation of explosion-generated strain pulses in rock*. Report of Investigation RI-5483. Washington, DC: U.S. Bureau of Mines.

Dyno Nobel. n.d. DYNOMIX. http://www.dynonobel.com/files/2010/04/1Dynomix.pdf. Accessed May 2013.

Edwards, C.G., Penney, D.E., and Calvis, D. 2010. *Differential Equations and Linear Algebra*, 3rd ed. Upper Saddle River, NJ: Pearson Prentice Hall.

Faber, K., and Maxwell, P.W. 1997. Geophone spurious frequency: What is it and how does it affect seismic data quality? *Can. J. Explor. Geophys*. 33(1–2):46–54.

Farnfield, R.A. 1996. So you think you are monitoring peak particle velocity. In *Proceedings of the Twelfth Symposium on Explosives and Blasting Research*, Orlando, FL, February 4–8. Cleveland, OH: International Society of Explosives Engineers. pp. 13–20.

Favreau, R.F. 1969. Generation of strain waves in rock by an explosion in a spherical cavity. *J. Geophys. Res*. 74(17):4267–4280.

Floyd, J. 2008. *Efficient Blasting Techniques*. Course notes. Blast Dynamics, Inc.

Fogelson, D.E., Duvall, W.I., and Atchison, T.C. 1959. *Strain energy in explosion-generated strain pulses*. Report of Investigation RI-5514. Washington, DC: U.S.

Bureau of Mines.

Furtney, J.K., Cundall, P.A., and Chitombo, G.P. 2010. Development in numerical modeling of blast induced rock fragmentation: Updates from the HSBM project. In *Rock Fragmentation by Blasting – Fragblast 9*. Edited by J.A. Sanchidrián. New York: CRC Press. pp. 355–342.

Geospace Technologies. 2012. GS-20DM. http://www.geospace.com/tag/gs-20dm/. Accessed April 2013.

Gohkle, C. n.d. Unofficial Windows binaries for Python extension packages. http://www.lfd.uci.edu/~gohlke/pythonlibs/. Accessed May 2013.

Graizer, V.M. 1979. Determination of true ground displacement by using strong motion records. *Izvestiya Phys. Solid Earth*. 15(12):875–885.

Hagedoorn, A.L., Kruithof, E.J., and Maxwell, P.W. 1988. A practical set of guidelines for geophone element testing and evaluation. *First Break*. 6(10):325–331.

Hamdi, E., Audiguier, M., Mauza, J., and Fjäder, K. 2003. Blast induced micro cracks assessment in muckpile blocks: P-wave velocity and porosity measurements. In *Proceedings of the EFEE Second World Conference on Explosives and Blasting Technique*, Prague, Czech Republic, September 10–12. Edited by R. Holmberg. Lisse, The Nethelands: A.A. Balkema. pp. 389–399.

Hamdi, E., Romdhanea, N.B., and Le Cléac'h, J.M. 2011. A tensile damage model for rocks: Application to blast induced damage assessment. *Comput. Geotech*. 38(2):133–141.

Harries, G. 1983. The modelling of long cylindrical charges of explosive. In *Proceedings of the First International Symposium on Rock Fragmentation by Blasting*, Luleå, Sweden, August 23–26. Edited by R. Holmberg and A. Rustan. Luleå, Sweden: Luleå, University of Technology. pp. 419–431.

Heelan, P.A. 1953. Radiation from a cylindrical source of finite length. *Geophys*. 18(3):685–696.

Herrmann, W. 1969. Constitutive equation for the dynamic compaction of ductile porous materials. *J. Appl. Phys*. 40(6):2490–2499.

Hinzen, K.G. 1998. Comparison of seismic and explosive energy in five smooth blasting test rounds. *Int. J. Rock Mech. Min. Sci*. 35(7):957–967.

Hoffman, J.E. 2003. A search for alternative electronic order in the high temperature superconductor $Bi_2Sr_2CaCu_2O_{8+\delta}$ by scanning tunneling microscopy. Ph.D. dissertation, University of California, Berkeley, CA. p.136.

Holcomb, D.J., Stone, C.M., and Costin, L.S. 1990. Combining acoustic emission

locations and a microcrack damage model to study development of damage in brittle materials. In *Rock Mechanics Contributions and Challenges: Proceedings of the 31st U.S. Symposium*. Edited by W.A. Hustrulid and G.A. Johnson. Brookfield, VT: A.A. Balkema. pp. 645–651.

Hustrulid, W. 1999. *Blasting Principles for Open Pit Mining*. Vol. 2: Theoretical Foundations. Brookfield, VT: A.A. Balkema.

Hustrulid, W., and Johnson, J. 2008. A gas pressure-based drift round blast design methodology. Washington, DC: National Institute for Occupational Safety and Health.

Hustrulid, W., and Lu, W. 2002. Some general design concepts regarding the control of blast-induced damage during rock slope excavation. In *Rock Fragmentation by Blasting – Fragblast 7*. Edited by W. Xuguang. Beijing, China: Metallurgical Industry Press. pp. 95–100.

Hustrulid, B., Iverson, S., Furtney, J., Cundall, P., and Torres, M. 2009. Developments in the numerical modeling of rock blasting: Updates from the HSBM project. Presented at the 2009 Annual Meeting and Exhibit of the Society for Mining, Metallurgy, and Exploration, Denver, CO, February 22–25, 2009.

International Society of Explosives Engineers. 2011. Fragmentation and heave process. In *ISEE Blasters' Handbook*, 18th ed. Edited by J.F. Stiehr. Cleveland, OH: ISEE.

Iverson, S.R., Hustrulid, W.A., Johnson, J.C., Tesarik, D., and Akbarzadeh, Y. 2010. The extent of blast damage from a fully coupled explosive charge. In *Rock Fragmentation by Blasting – Fragblast 9*. Edited by J.A. Sanchidrián. New York: CRC Press. pp. 459–468.

Iverson, S., Kerkering, C., and Hustrulid, W. 2008. Application of the NIOSH–Modified Holmberg–Persson approach to perimeter blast design. Washington, DC: National Institute for Occupational Safety and Health. http://www.cdc.gov/niosh/mining/UserFiles/works/pdfs/aotnm.pdf. Accessed March 2012.

Jimeno, C.L., Jimeno, E.L., and Carcedo, F.J.A. 1995. *Drilling and Rock Blasting*. Geomining Technological Institute of Spain. Brookfield, VT: A.A. Balkema.

Johnson, J.C. 2010. The Hustrulid bar – A dynamic strength test and its application to the cautious blasting of rock. Ph.D. dissertation, University of Utah, Salt Lake City, UT.

Johnson, G.R., and Holmquist, T.J. 1993. An improved computational constitutive model for brittle materials. In *High-Pressure Science and Technology – 1993*, Colorado Springs, CO, June 28–July 2. American Institute of Physics. pp. 981–984.

Jordan, D.W. 1962. The stress wave from a finite cylindrical explosive. *J. Math. Mech.* 11(4):503–552.

Katsabanis, P.D. 2001. Applications of numerical modeling to examine damage in wall control operations. In *Proceedings of the Twenty-Seventh Annual Conference on Explosives and Blasting Technique*, Vol. 2, Orlando, FL, January 28–31. Cleveland, OH: International Society of Explosives Engineers. pp. 25–37.

Katsabanis, P.D. 2005. Application of air decking to blasting – Findings from numerical modelling. In *Proceedings of the Thirty-First Annual Conference on Explosives and Blasting Technique*, Vol. 1, Orlando, FL, February 6–9. Cleveland, OH: International Society of Explosives Engineers. pp. 217–228.

Kelsall, P.C., Case, J.B., and Chabannes, C.R. 1984. Evaluation of excavation-induced changes in rock permeability. *Int. J. Rock Mech. Min. Sci. Geomech. Abstr.* 21(3):123–135.

Khandelwai, M., and Singh, T.N. 2009. Prediction of blast-induced ground vibration using artificial neural network. *Int. J. Rock Mech. Min. Sci.* 46(7):1214–1222.

Kilebrant, M., Norrgård, T., and Jern, M. 2010. The size of the damage zone in relation to the linear charge concentration. In *Rock Fragmentation by Blasting – Fragblast 9*. Edited by J.A. Sanchidrián. New York: CRC Press. pp. 449–457.

Kim, D.S., and McCarter, M.K. 1993. Assessment of damage in rock subjected to explosive loading. In *Proceedings of the Ninth Annual Symposium on Explosives and Blasting Research*, San Diego, CA, January 31–February 4. Cleveland, OH: International Society of Explosives Engineers. pp. 163–177.

Kjartansson, E. 1979. Constant Q-wave propagation and attenuation. *J. Geophys. Res.* 84(B9):4737–4748.

Kolsky, H. 1963. *Stress Waves in Solids*. Mineola, NY: Dover Publications, Inc.

LeBlanc, T.M., Ryan, J.M., and Heilig, J.H. 1996. Predicting the envelope of damage from the detonation of a confined charge. In *Proceedings of the Twenty-Second Annual Conference on Explosives and Blasting Technique*, Vol. 2, Orlando, FL, February 4–8. Cleveland, OH: International Society of Explosives Engineers. pp. 11–31.

Lee, E.L., Hornig, H.C., and Kury, J.W. 1968. Adiabatic expansion of high explosive detonation products. UCRL–50422. Lawrence Radiation Laboratory, University of California, Livermore.

Liu, L., and Katsabanis, P.D. 1997. Development of a continuum damage model for blasting analysis. *Int. J. Rock Mech. Min. Sci.* 34(2):217–231.

Liu, Q., Hung, T., Counter, D., and Andrieux, P. 1998. A case study of blast damage evaluation in open stope mining at Kidd Creek Mines. In *Proceedings of the Fourteenth Annual Conference on Explosives and Blasting Research*, New Orleans, LA, February 8–11. Cleveland, OH: International Society of Explosives

Engineers. pp. 323–336.

Lizotte, Y.C. 1996. Controlled blasting at the CANMET experimental mine. *Min. Eng.* 48(6):74–78.

Lu, P., and Latham, J.P. 1999. Investigation into the relationship between fractal dimension and the blastability of rock masses. In *Sixth International Symposium for Rock Fragmentation by Blasting – Fragblast 6*. Johannesburg, Republic of South Africa: The South African Institute of Mining and Metallurgy. pp. 191–198.

Lundborg, N. 1972. A statistical theory of the polyaxial compressive strength of materials. *Int. J. Rock Mech. Min. Sci. Geomech. Abstr*. 9(5):617–624.

McHugh, S. 1983. Crack extension caused by internal gas pressure compared with extension caused by tensile stress. *Int. J. Fract*. 21(3):163–176.

McKenzie, C.K. 1999. A review of the influences of gas pressure on block stability during rock blasting. In *EXPLO '99*. Edited by C. Workman-Davies. Carlton, Vic., Australia: The Australasian Institute of Mining and Metallurgy. pp. 173–179.

McKenzie, C.K., and Holley, K.G. 2004. A study of damage profiles behind blasts. In *Proceedings of the Thirtieth Annual Conference on Explosives and Blasting Technique*, Vol. 2, New Orleans, LA, February 1–4. Cleveland, OH: International Society of Explosives Engineers. pp. 203–214.

McKown, A. 1986. Perimeter control blasting for underground excavations in fractured and weathered rock. *Bull. Assoc. Eng. Geol*. 23(4):461–478.

Mencacci, S., and Farnfield, R. 2003. The measurement and analysis of near-field pressure transients in production blasting. In *Proceedings of the EFEE Second World Conference on Explosives and Blasting Technique*, Prague, Czech Republic, September 10–12. Edited by R. Holmberg. Lisse, The Nethelands: A.A. Balkema. pp. 467–473.

Meyer, R., Kohler, J., and Homburg, A. 2002. *Explosives*, 5th ed. Weinheim, Germany: Wiley-VCH Verlag GmbH & Co. KGaA.

Micro-Measurements. 2010. Strain gauge selection: Criteria, procedures, recommendations. Vishay Precision Group. http://www.vishaypg.com/docs/11055/tn505.pdf. Accessed April 2013.

Mohammadnejad, M., Gholami, R., Sereshki, F., and Jamshidi, A. 2013. A new methodology to predict backbreak in blasting operation. *Int. J. Rock Mech. Min. Sci*. 60(2013):75–81.

Monjezi, M., Rezaei, M., and Yazdian, A. 2009. Prediction of backbreak in open-pit

blasting using fuzzy set theory. *Expert Syst. Appl*. 37(3):2637–2643.

Montgomery, D.C., and Runger, G.C. 2007. *Applied Statistics and Probability for Engineers*, 4th ed. Hoboken, NJ: John Wiley & Sons, Inc.

Murthy, V.M.S.R., Dey, K., and Mohanty, P.R.. 2004. Predicting tunnel overbreak thresholds from acceleration measurements – An Indian case study. In *Proceedings of the Thirtieth Annual Conference on Explosives and Blasting Technique*, Vol. 2, New Orleans, LA, February 1–4. Cleveland, OH: International Society of Explosives Engineers. pp. 389–399.

National Oceanic and Atmospheric Administration (NOAA). n.d. How hydrodynamic models are used. http://www.nauticalcharts.noaa.gov/csdl/learn_models.html. Accessed March 2012.

Neiman, I.B. 1979. Determination of dimensions of the zone of crushing of rock in place by blasting. *J. Min. Sci*. 15(5):480–485.

Neiman, I.B. 1983. Mathematical model of the explosive action of a fracturing charge in a ledge rock mass. *J. Min. Sci*. 19(6):494–499.

Neiman, I.B. 1986. Volume models of the action of cylindrical-charge explosion in rock. *J. Min. Sci*. 22(6):455–463.

Nicholls, H.R., Johnson, C.F., and Duvall, W.I. 1971. *Blasting vibrations and their effects on structures*. Bulletin 656. Washington, DC: U.S. Bureau of Mines.

Onederra, I., Chitombo, G.P., Cundall, P.A., and Furtney, J.K. 2010. Towards a complete validation of the lattice scheme in the Hybrid Stress Blasting Model (HSBM). In *Rock Fragmentation by Blasting – Fragblast 9*. Edited by J.A. Sanchidrián. New York: CRC Press. pp. 343–351.

Onederra, I., Furtney, J.K., and Sellers, E. 2013a. Modelling the extent of damage from fully coupled explosive charges. In *Rock Fragmentation by Blasting – Fragblast 10*. Edited by P.K. Singh and A. Sinha. Boca Raton, FL: CRC Press. pp. 267–274.

Onederra, I., Furtney, J.K., Sellers, E., and Iverson, S. 2013b. Modelling blast induced damage from a fully coupled explosive charge. *Int. J. Rock Mech. Min. Sci*. 58(2013):73–84.

Oriard, L.L. 1972. Blasting effects and their control in open pit mining. In *Geotechnical Practice for Stability in Open Pit Mining: Proceedings of the Second International Conference on Stability in Open Pit Mining*, Vancouver, BC, November 1–2. Ann Arbor, MI: Bell Howell Information and Learning Co.

Oriard, L.L. 1982. Blasting effects and their control. In *Underground Mining Methods Handbook*. Edited by W.A. Hustrulid. New York, NY: Society for Mining, Metallurgy, and Exploration. pp. 1590–1603.

Ouchterlony, F. 1995. Review of rock blasting and explosives engineering research at SveBeFo. In *EXPLO '95*. Carlton, Vic., Australia: The Australasian Institute of Mining and Metallurgy. pp. 133–146.

Ouchterlony, F. 1997. Prediction of crack lengths in rock after cautious blasting with zero inter-hole delay. *Int. J. Blasting and Fragmentation*. 1(4):417–444.

Ouchterlony, F., Nie, S., Nyberg, U., and Deng, J. 1996. Monitoring of large open cut rounds by VOD, PPV and gas pressure measurements. In *Rock Fragmentation by Blasting – Fragblast-5*. Edited by B. Mohanty. Brookfield, VT: A.A. Balkema. pp. 167–176.

Ouchterlony, F., Nyberg, U., Olsson, M., Bergqvist, I., Granlund, L., and Grind, H. 2004. Where does the explosive energy in rock blasting rounds go? *Sci. Technol. Energetic Mater*. 65(2):54–63.

Ouchterlony, F., Olsson, M., and Bergqvist, I. 2001. Towards new Swedish recommendations for cautious perimeter blasting. In *EXPLO 2001*. Edited by A. Marton. Carlton, Vic., Australia: The Australasian Institute of Mining and Metallurgy. pp. 169–181.

Ouchterlony, F., Sjöberg, C., and Jonsson, B.A. 1993. Blast damage predictions from vibration measurements at the SKB underground laboratories at Aspo in Sweden. In *Proceedings of the Ninth Annual Symposium on Explosives and Blasting Research*, San Diego, CA, January 31–February 4. Cleveland, OH: International Society of Explosives Engineers. pp. 189–197.

Pariseau, W.G. 2007a. *Design Analysis in Rock Mechanics*. Philadelphia, PA: Taylor and Francis. pp. 473–501.

Pariseau, W.G. 2007b. Fitting failure criteria to laboratory strength tests. *Int. J. Rock Mech. Min. Sci*. 44(2007):637–646.

Park, D., and Jeon, S. 2010. Reduction of blast-induced vibration in the direction of tunneling using an air-deck at the bottom of a blasthole. *Int. J. Rock Mech. Min. Sci*. 47(5):752–761.

Paventi, M., Lizotte, Y., Scoble, M., and Mohanty, B. 1996. *Measuring rock mass damage in drifting. In Rock Fragmentation by Blasting – Fragblast-5*. Edited by B. Mohanty. Brookfield, VT: A.A. Balkema. pp. 131–138.

PCB Piezotronics. 2002. Model 353B32 – Installation and operating manual. http://www.pcb.com/contentstore/docs/PCB_Corporate/Vibration/Products/Manuals/353B32.pdf. Accessed November 2012.

PCB Piezotronics. 2013. Introduction to Piezoelectric Accelerometers. http://www.pcb.com/techsupport/. Accessed May 2013.

PCB Piezotronics. 2013. General piezoelectric theory. http://www.pcb.com/TechSupport/tech_gen#.UcJyUJwyyxg. Accessed May 2013.

Persson, P.A., Holmberg, R., and Lee, J. 1994. *Rock Blasting and Explosives Engineering*. Boca Raton, FL: CRC Press, Inc.

Peterson, J.A. 2001. Blast damage mechanisms at Ekati™ Mine. M.Sc. thesis, University of Alberta, Edmonton, AB.

Prasad, U. 2000. Dynamic fracture characteristics of selected rocks. Ph.D. dissertation, McGill University, Montreal, QC.

Preece, D.S., and Chung, S.H. 2003. Blast induced rock fragmentation prediction using the RHT constitutive model for brittle materials. In *Proceedings of the Twenty-Ninth Annual Conference on Explosives and Blasting Technique*, Vol. 2, Nashville, TN, February 2–5. Cleveland, OH: International Society of Explosives Engineers. pp. 375–381.

Preece, D.S., and Lownds, C.M. 2008. 3D computer simulation of bench blasting with precise delay timing. In *Proceedings of the Thirty-Fourth Annual Conference on Explosives and Blasting Technique*, Cleveland, OH, January 27–30. Cleveland, OH: International Society of Explosives Engineers. pp. 191–200.

Pusch, R., and Stanfors, R. 1996. Disturbance of rock around blasted tunnels. In *Rock Fragmentation by Blasting – Fragblast-5*. Edited by B. Mohanty. Brookfield, VT: A.A. Balkema. pp. 153–159.

Python Software Foundation. 2013. About Python. http://www.python.org/about/. Accessed May 2013.

Qian, W.Z., and Hui, L. 1997. A fractal and damage model for rock-breaking by blasting. In *Proceedings of the Twenty-Third Annual Conference on Explosives and Blasting Technique*, Las Vegas, NV, February 2–5. Cleveland, OH: International Society of Explosives Engineers. pp. 327–331.

Rathore, S.S., Jain, S.C., and Parik, S. 2013. ANN approach for blast vibration control in limestone quarry. In *Rock Fragmentation by Blasting – Fragblast 10*. Edited by P.K. Singh and A. Sinha. Boca Raton, FL: CRC Press. pp. 495–500.

Riedel, W., Thoma, K., Hiermaier, S., and Schmolinske, E. 1999. Penetration of reinforced concrete by BETA-B-500 numerical analysis using a new macroscopic concrete model for hydrocodes. In *Proceedings of the 9th International Symposium on the Interaction of the Effects of Munitions with Structures*, Berlin-Strausberg, Germany, March 3–7.

Rorke, A.J., and Milev, A.M. 1999. Near field vibration monitoring and associated rock damage. In *Sixth International Symposium for Rock Fragmentation by Blasting –*

Fragblast 6. Johannesburg, Republic of South Africa: The South African Institute of Mining and Metallurgy. pp. 19–22.

Rosenthal, M.F., and Morlock, G.L. 1987. *Blasting Guidance Manual*. Washington, DC: Office of Surface Mining Reclamation and Enforcement. http://www.osmre.gov/lrg/docs/directive315.pdf. Accessed April 2011.

Russel, D.A. 2013. Longitudinal and transverse wave motion. Pennsylvania State University. http://www.acs.psu.edu/drussell/Demos/waves/wavemotion.html. Accessed March 2013.

Ryu, C.H., Choi, B.H., and Jeong, J.H. 2013. Assessment of blast-induced damaged zone and its control. In *Rock Fragmentation by Blasting – Fragblast 10*. Edited by P.K. Singh and A. Sinha. Boca Raton, FL: CRC Press. pp. 725–730.

Sanchidrián, J.A., Segarra, P., and López, L.M. 2007. Energy components in rock blasting. *Int. J. Rock Mech. Min. Sci*. 44(1):130-147.

Scoble, M.J., Lizotte, Y.C., Paventi, M., and Mohanty, B.B. 1997. Measurement of blast damage. *Min. Eng*. 49(6):103–108.

Scott, J.H., Lee, F.T., Carroll, R.D., and Robinson, C.S. 1968. The relationship of geophysical measurements to engineering and construction parameters in the Straight Creek tunnel pilot bore, Colorado. *Int. J. Rock Mech. Min. Sci. Geomech. Abstr*. 5(1):1–30.

Segarra, P., Sanchidrián, J.A., López, L.M., and Llamas, A. 2013. Measurement errors in vibrations from blasting. In *Rock Fragmentation by Blasting – Fragblast 10*. Edited by P.K. Singh and A. Sinha. Boca Raton, FL: CRC Press. pp. 349–356.

Seto, M., Nag, D.K., and Vutukuri, V.S. 1996. Evaluation of rock mass damage using acoustic emission technique in the laboratory. In *Rock Fragmentation by Blasting – Fragblast-5*. Edited by B. Mohanty. Brookfield, VT: A.A. Balkema. pp. 139–145.

Singer, J.A., Link, C.A., and Iverson, S.R. 2010. High resolution seismic refraction tomography for determining depth of blast induced damage in a mine wall. *J. Explos. Eng*. 27(1):34–43.

Singh, S.P., and Lamond, R.D. 1993. Investigation of blast damage and underground stability. In *Proceedings of the 12th Conference on Ground Control in Mining*, Morgantown, WV, August 3–5. pp. 366–372.

Singh, T.N., Dontha, L.K., and Bhardwaj, V. 2008. Study into blast vibration and frequency using ANFIS and MVRA. *Min. Technol*. 117(3):116–121.

Siskind, D.E., Stagg, M.S., Kopp, J.W., and Dowding, C.H. 1980. *Structure response and damage produced by ground vibration from surface mine blasting*. Report of

Investigation RI-8507. Washington, DC: U.S. Bureau of Mines.

Smith, A.A. 2003. A modified Holmberg–Persson approach to predict blast damage. M.S. thesis, University of Utah, Salt Lake City, UT.

Spathis, A.T. 1999. On the energy efficiency of blasting. In *Sixth International Symposium for Rock Fragmentation by Blasting – Fragblast 6*. Johannesburg, Republic of South Africa: The South African Institute of Mining and Metallurgy. pp. 81–90.

Spathis, A.T., Blair, D.P., and Grant, J.R. 1987. Blast damage assessment of rock by using the high frequency cross hole seismic method. In *Second International Symposium on Rock Fragmentation by Blasting*, Keystone, CO, August 23–26. Edited by W.L. Fourney and R.D. Dick. Bethel, CT: Society for Experimental Mechanics. pp. 488–497.

Starfield, A.M., and Pugliese, J.M. 1968. Compression waves generated in rock by cylindrical explosive charges: A comparison between a computer model and field measurements. *Int. J. Rock Mech. Min. Sci*. 5(1):65–77.

Stewart, I. 2002. *Does God Play Dice? The New Mathematics of Chaos*, 2nd ed. Malden, MA: Blackwell Publishing. pp. 201–227.

Sun, C. 2013. Damage zone prediction for rock blasting. Ph.D. dissertation, University of Utah, Salt Lake City, UT.

Sutherland, M. 1990. Improving mine safety through perimeter blasting at Inco Limited's Thompson T-3 mine. *Can. Inst. Min. Metall. Pet. Bull*. 83(940):45–48.

Tawardrous, A.S., Preece, D.S., and Gelnville, J.P. 2013. Modification of the RHT model for enhanced tensile response predictions of geological materials. In *Rock Fragmentation by Blasting – Fragblast 10*. Edited by P.K. Singh and A. Sinha. Boca Raton, FL: CRC Press. pp. 309–323.

Tose, S.S.J. 2006. A review of the design criteria and practical aspects of developing a successful pre-split. In *Stability of Rock Slopes in Open Pit Mining and Civil Engineering Situations*. Johannesburg, Republic of South Africa: The South African Institute of Mining and Metallurgy. pp. 525–546.

Trivino, L.F., and Mohanty, B. 2013. Estimation of blast-induced damage through cross-hole seismometry in single-hole blasting experiments. In *Rock Fragmentation by Blasting – Fragblast 10*. Edited by P.K. Singh and A. Sinha. Boca Raton, FL: CRC Press. pp. 685–695.

U.S. Gypsum Corporation. 1999. Hydro-Stone® gypsum cement. http://www.usg.com/rc/data-submittal-sheets/industrial-plasters-cements/hydrostone/hydro-stone-gypsum-cement-data-en-IG1379.pdf. Accessed January 2013.

Wang, R., Schurr, B., Milkereit, C., Shao, Z., and Jin, M. 2011. An improved automatic scheme for empirical baseline correction of digital strong-motion records. *Bull. Seismol. Soc. Am.* 101(5):2029–2044.

Wheeler, R. 2004. The importance of proper seismometer coupling. In *Proceedings of the Thirtieth Annual Conference on Explosives and Blasting Technique*, Vol. 2, New Orleans, LA, February 1–4. Cleveland, OH: International Society of Explosives Engineers. pp. 147–160.

Xia, K., Huang, S., and Jha, A.K. 2010. Dynamic tensile test of coal, shale and sandstone using split Hopkinson pressure bar: a tool for blast and impact assessment. *Int. J. Geotech. Earthquake Eng.* 1(2):24–37.

Yang, R., and Ray, K. 2013. A method to determine 3-D dynamic strain tensor based on displacement gradients from blast vibration and field test results. In *Rock Fragmentation by Blasting – Fragblast 10*. Edited by P.K. Singh and A. Sinha. Boca Raton, FL: CRC Press. pp. 341–348.

Yang, R., and Scovira, S. 2010. A model for near and far field blast vibration based on multiple seed waveforms and transfer functions. In *Proceedings of the Thirty-Sixth Annual Conference on Explosives and Blasting Technique*, Vol. 2, Orlando, FL, January 7–10. Cleveland, OH: International Society of Explosives Engineers. pp. 223–242.

Yang, J., and Wang, S. 1996. A new constitutive model for rock fragmentation by blasting - fractal damage model. In *Rock Fragmentation by Blasting – Fragblast-5*. Edited by B. Mohanty. Brookfield, VT: A.A. Balkema. pp. 95–100.

Yang, J., Jin, Q., and Gao, W. 2002. A new damage model for rock fragmentation by blasting based on stress wave attenuation and its application. In *Rock Fragmentation by Blasting – Fragblast 7*. Edited by W. Xuguang. Beijing, China: Metallurgical Industry Press. pp. 139–143.

Yang, R., Bawden, W.F., and Katsabanis, P.D. 1996. A new constitutive model for blast damage. *Int. J. Rock Mech. Min. Sci. Geomech. Abstr.* 33(3):245–254.

Yang, R.L., Rocque, P., Katsabanis, P., and Bawden, W.F. 1993. Blast damage study by measurement of blast vibration and damage in the area adjacent to blast hole. In *Rock Fragmentation by Blasting – Fragblast-4*. Edited by H.P. Rossmanith. Brookfield, VT: A.A. Balkema. pp. 137–144.

Zhang, J.C., and Chang, C. 1999. On damage mechanism of microcrack zone in rock blasting and its measurement. In *Sixth International Symposium for Rock Fragmentation by Blasting – Fragblast 6*. Johannesburg, Republic of South Africa: The South African Institute of Mining and Metallurgy. pp. 359–363.

Zhou, Y.X., Xia, K., Li, X.B., Li, H.B., Ma, G.W., Zhao, J., Zhou, Z.L., and Dai, F. 2012.

Suggested methods for determining the dynamic strength parameters and mode-I fracture toughness of rock materials. *Int. J. Rock Mech. Min. Sci*. 49(2012):105–112.

Zhou, Y., and Zhoa, J. 2011. *Advances in Rock Dynamics and Applications*. Boca Raton, FL: CRC Press.

Zhu, Z., Mohanty B., and Xie, H. 2007. Numerical investigation of blasting-induced crack initiation and propagation in rocks. *Int. J. Rock Mech. Min. Sci*. 44(3):412–424.

Zhu. Z., Xie, H., and Mohanty, B. 2008. Numerical investigation of blasting-induced damage in cylindrical rocks. *Int. J. Rock Mech. Min. Sci*. 45(2):111–121.